

UC Irvine

UC Irvine Electronic Theses and Dissertations

Title

DYNAMIC ANALYSIS OF A PROTON EXCHANGE MEMBRANE ELECTROLYZER INTEGRATED WITH A NATURAL GAS COMBINED CYCLE POWER PLANT FOR POWER-TO-GAS APPLICATIONS

Permalink

<https://escholarship.org/uc/item/9ww7g5nf>

Author

Stansberry, John

Publication Date

2018

Peer reviewed|Thesis/dissertation

UNIVERSITY OF CALIFORNIA
IRVINE

Dynamic Analysis of a Proton Exchange Membrane
Electrolyzer Integrated with a Natural Gas Combined Cycle
Power Plant for Power-to-Gas Applications

THESIS

Submitted in partial satisfaction of the requirements for the
degree of

MASTER OF SCIENCE

in Mechanical and Aerospace Engineering

by

John Michael Stansberry

Thesis Committee:
Professor Jacob Brouwer, Chair
Professor Scott Samuelsen
Assistant Professor Jaeho Lee

2019

DEDICATION

This thesis is dedicated to the two most influential people I am fortunate to have had in my life; my fiancé Amber, for her incredible love and support in all my endeavors, and the late Eric Pedersen, whose memory stays with me in everything that I do.

Amber's steadfast loyalty and incredible drive inspire me every day to create a better future for us together. I look forward to the years to come because I know we will spend them together, and together we can accomplish anything. I am amazed every day that we were able to find each other so easily, and I suspect our meeting will remain the luckiest thing to ever happen to me in my life. I have learned so much from you and yet still have so much left to learn.

Eric Pedersen's passion for life had a profound influence on me in the relatively short time that I was able to spend with him. Without Eric's influence, I would not be where I am today. While he is not physically with me anymore, I still feel his passion and love for doing anything and everything in all that I do.

Table of Contents

LIST OF FIGURES	v
LIST OF TABLES	xv
NOMENCLATURE & SYMBOLS.....	xvii
ACKNOWLEDGEMENTS	xxiii
ABSTRACT.....	xxvi
1 INTRODUCTION	1
1.1 Goals	2
1.2 Objectives	3
2 BACKGROUND	4
3 Integration of PEM Electrolyzer System with the UC Irvine Central Plant (Objective 1)	12
3.1 UC Irvine Central Plant.....	12
3.2 Electrolyzer System	14
3.2.1 Electrolysis Cell Stack	16
3.2.2 Hydrogen Management Subsystem.....	18
3.2.3 Oxygen Management Subsystem.....	19
3.2.4 Deionized Water Management Subsystem	19
3.3 Data Acquisition Systems	20
3.4 Chiller System.....	21
3.5 DI Water System.....	22
3.6 Mass Flow Controller & Control System	24
3.7 VRES Dynamic Data	25
3.7.1 UC Irvine Microgrid & Melrok Metering Network - MSTB PV Array	26
3.8 Natural Gas Pipeline & Gas Turbine	27
4 Dynamic Operation of PEM Electrolyzer System (Objectives 2, 3, & 4)	28
4.1 Electrolyzer Steady State Operation & Benchmarking.....	28
4.2 Electrolyzer Sustained Part Load Performance Characterization	42
4.3 VRES Load Following – Solar Photovoltaic Array	54
4.4 VRES Load Following – Wind Turbine Farm.....	63
4.5 Effects of Operating Conditions on Electrolysis.....	72
4.5.1 Effects of Operating Conditions on Electrolysis Stack.....	72
4.5.2 Effects of Operating Condition on Electrolyzer System Efficiency	80
4.5.3 Effects of Operating Conditions on H ₂ losses	87
4.5.4 Effects of Operating Conditions on AC/DC Power Electronics	91

4.5.5	Synthesis of System Efficiency and Specific Energy Analysis	94
4.5.6	Degradation.....	97
5	Hydrogen Injection & Combustion Turbine Impacts.....	99
5.1	Variation of Natural Gas Properties with Blended Hydrogen.....	100
5.2	Effects of Hydrogen Addition to Natural Gas on Gas Turbine Operation.....	106
5.3	Statistical Analysis (ANOVA) of Injection of Hydrogen produced by the Electrolyzer System to the Natural Gas Fired Combustion Turbine.....	111
5.3.1	Effects of Hydrogen Addition on Gravimetric Gas Flow to Turbine	114
5.3.2	Effects of Hydrogen Addition on Carbon Monoxide (CO) Emissions	118
5.3.3	Effects of Hydrogen Addition on Emissions of Nitrogen Oxides (NO _x).....	120
5.4	High Throughput Hydrogen Injection Test.....	122
5.4.1	High Throughput Hydrogen Injection System	124
5.4.2	Test Results	129
5.4.3	Effects of Hydrogen Addition on Gravimetric Gas Flow to Turbine	133
5.4.4	Effects of Hydrogen Addition on Carbon Monoxide (CO) Emissions	136
5.4.5	Effects of Hydrogen Addition on Emissions of Nitrogen Oxides (NO _x).....	138
6	Semi-empirical Thermodynamic Model of PEM Stack.....	140
6.1	Steady State Electrochemical Model	143
6.1.1	Water Transport	151
6.1.2	Hydrogen Gas Transport.....	155
6.1.3	Oxygen Gas Transport	156
6.1.4	Overall Molar Balance	156
6.2	Electrochemical Parameter Identification	158
6.3	Membrane Species Transport Parameters Identification	163
6.3.1	Water Transport	163
6.3.2	Product Hydrogen Loss & Gas Cross-Over.....	174
6.4	Model Validation	188
6.4.1	Winter & Spring Load Following	189
6.4.2	Wind Load Following	193
6.5	Electrochemical Compression.....	197
7	Summary, Conclusions & Recommendations	205
7.1	Summary & Observations.....	205
7.2	Conclusions.....	218
7.3	Recommendations.....	222
8	Bibliography	224

LIST OF FIGURES

Figure 1. CAISO’s ‘Duck Curve’ highlighting the growing ramp demands and risks of over-generation occurring today and projected in the upcoming years [18].	7
Figure 2. Power-to-gas-to-power at the UC Irvine Central Plant Power-to-Gas Demonstration. Hydrogen utilization pathway is highlighted in green. Two pathways of power utilization are differentiated; uncontrolled ‘full load condition’ power draw (red) and simulated VRES load profiles (purple).	12
Figure 3. UC Irvine Central Plant simplified process flow diagram [61].	13
Figure 4. C10 electrolyzer system. Fluids cabinet containing mechanical systems and cell stack on the left, electrical cabinet containing the power electronics on the right.	15
Figure 5. C10 Electrolyzer system proton exchange membrane cell stack.	16
Figure 6. Dynamic dispatch control of the mass flow controller.	24
Figure 7. Calibration curves for the two mass flow controllers using a laminar flow element.	25
Figure 8. Hydrogen injection line at UCI Central Plant.	27
Figure 9. Start-up j-V curves during ‘break-in’ period with measurement error bars.	28
Figure 10. Stack power, system power, and hydrogen production pre- and post-drying process across different stages of steady state characterization of the electrolyzer system.	30
Figure 11. Comparison of stack & system efficiencies (HHV basis) across different stages of steady state characterization of the electrolyzer system.	32
Figure 12. Hydrogen Dryer Efficiency across different stages of steady state characterization of the electrolyzer system.	33
Figure 13. AC/DC power electronics efficiency across different stages of steady state characterization of the electrolyzer system.	34

Figure 14. AC/DC power electronics efficiency and ambient temperature over two and a half days at full throughput.	35
Figure 15. AC/DC power electronics efficiency vs. ambient temperature across the benchmarking test period.	35
Figure 16. Maximum observed stack current on a given day versus net hours of operation on the electrolyzer system, break-in period observed in the first 800 hours.....	37
Figure 17. Maximum observed stack current on a given day versus ambient temperature for ‘normal operation’ data in Figure 16 (above).....	37
Figure 18. Energy consumption at the 100 hours of operation regime (Top) and 600 hours of operation regime (Bottom).....	39
Figure 19. Step-wise ramp of electrolyzer system net hydrogen production vs. control signal.	43
Figure 20. Calculated wet hydrogen gas output from measured stack current versus stepwise mass flow controller control signal.	44
Figure 21. Electrolyzer system power consumption versus control signal of expected power consumption set point for step-wise ramp.	45
Figure 22. Percentage part load condition of dry hydrogen output, stack current, and system power consumption.....	46
Figure 23. Box plot of system power consumption dispatch versus flow controller signal. Red bars show the average value, with 95% confidence intervals in blue, and the entire range of observed responses in black.....	47
Figure 24. j-V curve generated from step-wise ramp sustained part load operation with temperature correlation.	48
Figure 25. 1-hour system and stack efficiencies for sustained part load operation.....	49
Figure 26. Ancillary power consumption in kilowatts and as a % share of total power consumption vs. sustained part load conditions.	50

Figure 27. Percentage of measured hydrogen flow post-dryer to expected hydrogen output from electrolysis vs. sustained part load condition.....	51
Figure 28. Efficiency of AC/DC power electronics vs. sustained part load condition.	52
Figure 29. Electrolyzer system energy consumption across different levels of part load condition.....	53
Figure 30. MSTB Rooftop Solar Photovoltaic Array Output – Seasonal Variation.....	54
Figure 31. Seasonal differences in output from MSTB solar PV array for relatively ‘clear’ days.....	55
Figure 32. Hydrogen flow control signal vs. hydrogen flow output for winter (top) and spring (bottom) solar PV load following test.....	56
Figure 33. System power consumption control signal vs. measured power consumption for winter (top) and spring (bottom) solar PV load following test.	57
Figure 34. Hydrogen flow control signal vs. hydrogen flow output for fall solar PV load following test.	58
Figure 35. System power consumption control signal vs. measured power consumption for fall solar PV load following test.	58
Figure 36. Hydrogen flow control signal vs. hydrogen flow output for summer solar PV load following test.....	59
Figure 37. System power consumption control signal vs. measured power consumption for summer solar PV load following test.....	59
Figure 38. Stack power slew rate for spring and winter solar PV load following run.	61
Figure 39. System power slew rate for spring and winter solar PV load following run vs. control signal on 2-minute and 10-minute intervals.	62
Figure 40. Tehachapi 1-month wind farm output profile utilized in wind load following test.....	63
Figure 41. Normalized wind farm output for wind load following test.	64
Figure 42. Wind load following test week one, hydrogen output versus control signal.....	65
Figure 43. Wind load following test week two, hydrogen output versus control signal.....	65
Figure 44. Wind load following test week three, hydrogen output versus control signal.....	66
Figure 45. Wind load following test week one, system power consumption versus control signal.....	67

Figure 46. Wind load following test week two, system power consumption versus control signal.	67
Figure 47. Wind load following test week three, system power consumption versus control signal.	68
Figure 48. Wind load following test, stack power consumption slew rate 1-second time scale.	69
Figure 49. Wind load following test, system power consumption slew rate versus control signal two and ten-minute intervals.....	70
Figure 50. j-V curve across the breadth of electrolyzer testing, parsed by stack temperature.....	74
Figure 51. j-V curve across the breadth of electrolyzer testing, parsed by H ₂ pressure (left) and O ₂ pressure (right).	75
Figure 52. Contour plot of ANOVA prediction model for cell voltage as a function of stack temperature and current density.....	77
Figure 53. Contour plot of ANOVA prediction model for cell voltage as a function of H ₂ pressure and current density.....	78
Figure 54. Contour plot of ANOVA prediction model for cell voltage as a function of H ₂ pressure and current density.....	79
Figure 55. System efficiency versus current density with stack temperature distribution, all data (left) and orthogonalized data for ANOVA analysis (right).	81
Figure 56. ANOVA prediction of stack temperature influence on system efficiency, dashed lines depict 95% confidence intervals ($j = 1 \text{ A/cm}^2$, $P_{\text{H}_2} = 30 \text{ barg}$, $P_{\text{O}_2} = 1.5 \text{ barg}$).....	82
Figure 57. System efficiency versus current density with H ₂ pressure distribution.....	83
Figure 58. System efficiency versus current density with O ₂ pressure distribution.....	83
Figure 59. ANOVA prediction of H ₂ pressure influence on system efficiency, dashed lines depict 95% confidence intervals ($P_{\text{O}_2} = 1.5 \text{ barg}$).	85
Figure 60. ANOVA prediction of O ₂ pressure influence on system efficiency, dashed lines depict 95% confidence intervals ($P_{\text{H}_2} = 30 \text{ barg}$).....	86
Figure 61. %H ₂ loss versus current density with H ₂ pressure distribution.....	87
Figure 62. %H ₂ loss versus current density with O ₂ pressure distribution.....	88

Figure 63. ANOVA prediction of H ₂ pressure influence on H ₂ efficiency, dashed lines depict 95% confidence intervals (P _{O₂} = 1.5 barg).....	89
Figure 64. ANOVA prediction of O ₂ pressure influence on system efficiency, dashed lines depict 95% confidence intervals (P _{H₂} = 30 barg).....	90
Figure 65. AC/DC power electronics efficiency versus current density with ambient temperature distribution.....	91
Figure 66. ANOVA prediction of ambient temperature on H ₂ efficiency, dashed lines depict 95% confidence intervals.....	93
Figure 67. Specific energy cost of electrolyzer system versus current density.....	94
Figure 68. Specific energy consumption of electrolyzer system broken down by sources of energy consumption versus current density.....	95
Figure 69. Percentage share of total specific energy consumption of hydrogen production by the electrolyzer system.....	96
Figure 70. System efficiency versus hours of operation, 95% confidence intervals shown in dashed lines (j = 1.92 A/cm ² , P _{H₂} = 30 barg, P _{O₂} = 1.5 barg).....	97
Figure 71. Cell voltage (Top Right), Ancillary Power Consumption (Top Left), AC/DC Efficiency (Bottom Left), %H ₂ Loss (Bottom Right) versus hours of operation (j = 1.92 A/cm ² , P _{H₂} = 30 barg, P _{O₂} = 1.5 barg, T _{Stack} = 55 Celsius, T _{Ambient} = 28 Celsius).....	98
Figure 72. National average for higher heating value of natural gas balanced volumetrically with increasing amounts of hydrogen versus the observed limits of natural gas variation in higher heating value and rule 30 limits.....	103
Figure 73. National average for Wobbe Index of natural gas balanced volumetrically with increasing amounts of hydrogen versus observed limits of natural gas variation in Wobbe Index and rule 30 limits.....	104
Figure 74. Heat rate (Top) and efficiency (Bottom) versus electrical load curve for UC Irvine Central Plant combustion turbine.....	107

Figure 75. Combustion turbine fuel gas flow versus electrical load and % volume H ₂	108
Figure 76. Combustion turbine natural gas offset versus electrical load and % volume H ₂	108
Figure 77. Combustion turbine carbon dioxide offset versus electrical load and % volume H ₂	110
Figure 78. Expected natural gas flow offset with addition of hydrogen gas to the gas turbine fuel input.	111
Figure 79. Population of turbine operation data versus hydrogen addition via injection from electrolyzer system throughout test period, all points (left) and orthogonalized input used for ANOVA (right).	113
Figure 80. Observed correlation for turbine injection of hydrogen from electrolyzer system and turbine load against total fuel gas flow, NO _x , and CO emissions using ANOVA analysis.....	114
Figure 81. Contour plot of ANOVA predictive model for combined influence of turbine load and hydrogen injection on total fuel gas flow.....	115
Figure 82. ANOVA predicted model with 95% confidence interval versus fixed heat rate prediction for offset of natural gas flow with the addition of hydrogen within range of testing (Turbine Load = 11.8 MW _{el}).	117
Figure 83. ANOVA predicted model versus fixed heat rate prediction for offset of natural gas flow with the addition of hydrogen up to 100% hydrogen (Turbine Load = 11.8 MW _{el}).	117
Figure 84. Contour plot of ANOVA predictive model for combined influence of turbine load and hydrogen injection on carbon monoxide emissions (SCR Temperature = 592 Celsius).	119
Figure 85. Contour plot of ANOVA predictive model for combined influence of turbine load and hydrogen injection on nitrogen oxides (NO _x) emissions (SCR Temperature = 592 Celsius).	121
Figure 86. Planned hydrogen injection rates for high throughput hydrogen injection.....	123
Figure 87. Sierra Hi-Trak 840 mass flow controller utilized in high throughput hydrogen injection testing.....	124
Figure 88. Siting of the six-pack hydrogen cylinders at the UCI Central Plant on concrete pad space....	126
Figure 89. Pressure regulator and cylinder manifold used in high throughput hydrogen testing.	127

Figure 90. Injection system simplified process flow diagram.	128
Figure 91. Hydrogen output (kg/hr) from mass flow controller for high throughput hydrogen injection test on June 22 nd , 2018.	129
Figure 92. Turbine electrical load and gas flow during high throughput hydrogen injection test on June 22 nd , 2018.	131
Figure 93. Percentage of hydrogen in fuel gas flow to combustion turbine at UCI Central Plant during high throughput hydrogen injection test on June 22 nd , 2018.	132
Figure 94. Contour plot of ANOVA predictive model for combined influence of turbine load and hydrogen injection on total fuel gas flow for high throughput hydrogen testing.	134
Figure 95. Predicted natural gas offset due to hydrogen injection from ANOVA analysis with 95% confidence intervals versus expected natural gas offset on a lower heating value basis for high throughput hydrogen testing.	135
Figure 96. Contour plot of ANOVA predictive model for combined influence of turbine load and hydrogen injection on carbon monoxide emissions for high throughput hydrogen testing.	137
Figure 97. Contour plot of ANOVA predictive model for combined influence of turbine load and hydrogen injection on nitrogen oxide emissions for high throughput hydrogen testing.	139
Figure 98. Semi-Empirical PEM Stack Model with Possible Applications for future studies.	142
Figure 99. Energy requirement for dissociation of water reaction versus temperature.	144
Figure 100. Species Transport in PEM Electrolyzer.	150
Figure 101. Fitted polarization curve agreement with input experimental data.	159
Figure 102. Dependence of electrochemical parameters on temperature	160
Figure 103. Breakdown of additive overvoltage contributions to polarization curve using experimentally determined parameters, concentration omitted as contribution was negligible ($T_{stk} = 55 \text{ C}$, $P_{cath} = 30 \text{ barg}$, $P_{anode} = 1.6 \text{ barg}$).	162
Figure 104. Water consumption of electrolysis process and observed total system water consumption. .	164
Figure 105. A300 hydrogen-water phase separator schematic.	166

Figure 106. A300 fill time vs. current density.	167
Figure 107. Cathode water out molar flow rate – estimate from A300 fill time.	167
Figure 108. Estimated hydraulic transport of water across cell stack with 95% confidence intervals.	169
Figure 109. Electro-osmotic drag transport versus current density at different stack operating temperatures with linear regression trend lines.	171
Figure 110. Electro-osmotic drag coefficient as a function of current density and operating temperature.	171
Figure 111. Comparison of electro-osmotic drag coefficient vs. current density measurements in this study to values found in literature.	173
Figure 112. Comparison of electro-osmotic drag coefficient vs. temperature measurements in this study to values found in literature.	173
Figure 113. Product hydrogen loss pathways.	175
Figure 114. Hydrogen loss & hydrogen transport to the anode due to dissolved hydrogen entrained in water recovered from the cathode outlet.	176
Figure 115. Estimated percentage of hydrogen content in anode due to solubility versus observed values.	177
Figure 116. Comparison of net generated hydrogen at stack versus predicted hydrogen output after dryer and solubility losses versus observed hydrogen output.	178
Figure 117. Observed percentage of hydrogen gas in the anode product stream.	180
Figure 118. Observed ‘unaccounted’ for hydrogen losses, with stable points utilized for the top-down estimate of hydrogen cross-over.	181
Figure 119. Top-down estimate of H ₂ cross-over, function of cathodic H ₂ pressure; $\epsilon_{H2} = 1.76 \times 10^{-10} \text{ mol} \cdot \text{seccm} \cdot \text{bar}$. 95% confidence intervals in dashed lines.	182
Figure 120. Percentage of hydrogen gas in anode predicted by top-down estimate of hydrogen gas cross-over.	183
Figure 121. Bottom-up estimate for H ₂ cross-over in kg/hr, with pressure correlation.	184

Figure 122. Bottom-up estimate of H ₂ cross-over, function of cathodic H ₂ pressure and current density; $\epsilon_{H_2} = 4.47 \times 10^{-13} \left[\frac{\text{mol}\cdot\text{sec}}{\text{cm}\cdot\text{bar}} \right]$ and $A_{H_2} = 154.34 \left[\frac{\text{bar}\cdot\text{cm}^2}{\text{amp}} \right]$. 95% confidence intervals in dashed lines.	185
Figure 123. Stack power consumption for winter solar load following, observed data versus analytical model fit.	190
Figure 124. Stack power consumption for spring solar load following, observed data versus analytical model fit.	191
Figure 125. Polarization curve fits for winter and spring solar load following, observed data versus analytical model fit.	191
Figure 126. System hydrogen output versus stack current density for winter and spring solar load following, observed data versus model fit with 1-hour averaged observed data.	192
Figure 127. Stack power consumption for first half of wind load following, observed data versus analytical model fit.	194
Figure 128. Stack power consumption for second half of wind load following, observed data versus analytical model fit.	194
Figure 129. Polarization curve fits for wind load following, observed data versus analytical model fit.	195
Figure 130. System hydrogen output versus stack current density for wind load following, observed data versus model fit with 1-hour averaged observed data.	196
Figure 131. Work requirements for adiabatic vs. isothermal compression of hydrogen gas.	199
Figure 132. Specific work for electrochemical compression of hydrogen gas in PEM electrolyzer stack versus isothermal compression. ($T_{\text{stack}} = 55$ Celsius, $P_{\text{anode}} = 0$ barg, $j = 1$ A/cm ²).	200
Figure 133. Predicted overvoltage due to increasing hydrogen pressure versus observed average variation using ANOVA on cell voltage measurements.	200
Figure 134. Specific energy of hydrogen production for increasing pressures in the PEM electrolyzer system at several load conditions.	201

Figure 135. Integration of state-of-the-art H ₂ centrifugal compressor design with electrolysis plant for pipeline end-use versus compression solely performed during electrolysis step for ideal and actual electrochemical compression ($j = 2 \text{ A/cm}^2$, $T_{\text{stack}} = 55 \text{ Celsius}$).	203
Figure 136. Compression work for HyET electrochemical compressor vs. hydrogen mass flow rate [135]......	204
Figure 137. Performance comparison for electrolyzer system with compression in supplying 200 kg/day H ₂ at 450 barg intended to be representative of a hydrogen fueling station.....	205

LIST OF TABLES

Table 1. Summary of full throughput benchmarking on electrolyzer system.....	41
Table 2. Seasonal comparison for results of solar photovoltaic load following tests.....	60
Table 3. Summary of wind load following tests.....	69
Table 4. Wind load following test with electrolyzer power cycling below minimum power set point.....	71
Table 5. List of factors utilized in ANOVA analysis for electrolyzer system study.....	73
Table 6. Results of ANOVA analysis on cell voltage.....	76
Table 7. Results of ANOVA analysis on system efficiency; input data orthogonalized for stack temperature effects.....	82
Table 8. Results of ANOVA analysis on system efficiency, all data points & stack temperature excluded.....	84
Table 9. Results of ANOVA analysis on %H ₂ loss.....	89
Table 10. Results of ANOVA analysis on AC/DC power electronics efficiency.....	92
Table 11. Mole fraction of natural gas constituents for Engineering Laboratory Facility – 1993.....	100
Table 12. Hydrogen and Natural Gas Characteristics (1 atm, 20 Celsius).....	102
Table 13. Allowable percentage of hydrogen by volume in natural gas for complying with Rule 30 standards on higher heating value and Wobbe Index.....	105
Table 14. Summary of ANOVA analysis of the effects of hydrogen injection from the electrolyzer system, turbine electrical load, and SCR temperature on emissions of carbon monoxide post catalytic reduction from the combustion turbine.....	115
Table 15. Summary of ANOVA analysis of the effects of hydrogen injection from the electrolyzer system, turbine electrical load, and SCR temperature on emissions of carbon monoxide post catalytic reduction from the combustion turbine.....	118

Table 16. Summary of ANOVA analysis of the effects of hydrogen injection from the electrolyzer system, turbine electrical load, and SCR temperature on emissions of nitrogen oxides (NO _x) post catalytic reduction from the combustion turbine.	121
Table 17. Summary of ANOVA analysis of the effects of hydrogen injection from the high throughput hydrogen injection testing on net gravimetric fuel gas flow.....	133
Table 18. Summary of ANOVA analysis of the effects of hydrogen injection from the high throughput hydrogen injection testing on post catalytic clean-up carbon monoxide emissions.....	136
Table 19. Summary of ANOVA analysis of the effects of hydrogen injection from the high throughput hydrogen injection testing on post catalytic clean-up nitrogen oxide emissions.	138
Table 20. Identified Stack Parameters associated with species transport	157
Table 21. ANOVA Results for cathode water flow rate.	168
Table 22. ANOVA results for influencing factors on electro-osmotic water transport in the membrane.	170
Table 23. Solar load following cases with analytical model using set points and input current versus actual system behavior.....	189
Table 24. Wind load following case with analytical model using set points and input current versus actual system behavior.....	193

NOMENCLATURE & SYMBOLS

$\epsilon_{H_2,diff}$: Diffusive permeability of hydrogen gas through Nafion 117

$\epsilon_{H_2,perm}$: Permeability coefficient of hydrogen gas through Nafion 117

$\epsilon_{O_2,diff}$: Diffusive permeability of hydrogen gas through Nafion 117

η_{act} : Activation overvoltage

η_{conc} : Mass transport overvoltage

η_{ohmic} : Ohmic overvoltage

E_{OCV} : Open-circuit voltage

ΔG° : Change in Gibbs Free Energy at Standard Conditions (T = 25 Celsius, P = 1 atm)

∇P : Pressure gradient

A : Active area of cell

A200 : DI Water Fill Tank

A300 : Oxygen-water phase separator tank

A500 : Hydrogen-water phase separator tank

AC : Alternating Current

Adeq. Precision : Signal-to-noise ratio in ANOVA model. Comparison of range of predicted values to average prediction error – larger values are better.

Adjusted R² : Strength of ANOVA model in explaining the mean, adjusted for number of terms

A_{H2} : Hydrogen partial pressure enhancement coefficient

a_{H2O} : Activity of liquid water

Anode : The electrode of an electrochemical cell where oxidation takes place.

ANOVA : Statistical method comparing population means of several groups, allowing a generalized t-test to greater than two groups.

APEP : Advanced Power & Energy Program, University of California, Irvine

ASTM : American Society for Testing and Materials

Bar : Atmospheric pressure in Bar

Barg : Gauge pressure in Bar

Btu : British Thermal Unit

C. V. % : Standard deviation as a percentage of the sample mean.

C10 : Proton Exchange Membrane Electrolyzer system produced by Proton Onsite

CaCO₃ : Calcium Carbonate

Cathode : The electrode of an electrochemical cell at which reduction occurs.

C_d : Discharge coefficient of a valve.

CHP : Combined Heat and Power

cm² : Square centimeters

CO₂ : Carbon Dioxide

CP : Central Plant

csv : Comma-separated file

C_x : Concentration of a species

DAQ : Data Acquisition System

DC : Direct Current

D_{eff} : Effective diffusion coefficient

Degrees of Freedom : number of independent variables influencing a system

D_{H₂} : Diffusion coefficient of hydrogen gas

DI : Deionized

DMFC : Direct methanol fuel cell

D_{O₂} : Diffusion coefficient of oxygen gas

D_w : Diffusive permability of water in randomized porous fiber membranes

ERCOT : Electric Reliability Council of Texas

E_{rev} : Reversible voltage of an electrochemical cell

F : Faraday's Constant

F-Value : Test comparing the mean square of the data to the residual mean square

Fe²⁺/Fe³⁺ : Ions of iron

ft³ : cubic feet

GWh : Gigawatt-hour

H : Enthalpy

H^+ : Hydrogen ion

H_2 : Hydrogen gas

HER : Hydrogen evolution reaction

HHV : Higher Heating Value

hp : Horsepower

hr : Hour

HRSG : Heat recovery steam generator

HyET : High yield Energy Technologies

I : Current

IC : Integrated Circuit

IRWD : Irvine Ranch Water District

j : Current density

j_0 : Exchange current density

j_L : Limiting current density

j-V : Relation of current density and voltage, also known as ‘polarization curve’

K : Temperature in Kelvin

k : Ratio of specific heats

K_D : Darcy constant

kg : Kilogram

K_H : Henry’s Law constant

kJ : Kilojoule

kV : Kilovolt

kVa : kilovolt-amp

kW : Kilowatt

kWh : Kilowatt-hour

L : Liter

LEL : Lower explosive limit

LHV : Lower heating value
LNG : Liquefied natural gas
 M_x : Molecular weight of species 'x'
mA : Milliamp
MEA : Membrane electrode assembly
Mean Square : Estimate of population variance based on variability
MFC : Mass flow controller
mg : Milligram
min : Minute
Modbus : Software protocol for serial communication processes
MW : Megawatt
M Ω -cm : Resistivity of deionized water, measured in megaohms-centimeters
n : Number of electrochemical cells
 N_x : mol of species 'x'
N₂ : Nitrogen gas
 n_{eo} : Electro-osmotic drag coefficient
NFCRC : National Fuel Cell Research Center, University of California, Irvine
NG : Natural gas
NGCC : Natural gas combined cycle
Nm³ : Normal cubic meters (standard conditions T = 25 Celsius, P = 1 atm)
NO_x : Oxides of nitrogen, NO and NO₂.
 n_p : Polytropic compression coefficient
NPT : American National Standard Pipe Thread
O₂ : Oxygen gas
°C : Degrees celsius
OD : Outer Diameter
OEM : Original Equipment Manufacturer
OER : Oxygen evolution reaction

P-Value : Probability that f-value in ANOVA test is observed when considering the null hypothesis

P2G : Power-to-gas

P2G2P : Power-to-gas-to-power

PAFC : Phosphoric acid fuel cell

P_{An} : Absolute pressure in anode compartment of electrochemical cell

P_{cat} : Absolute pressure in cathode compartment of electrochemical cell

PEM : Proton exchange membrane

PEMEZ : Proton exchange membrane electrolyzer

PEMFC : Proton exchange membrane fuel cell

ppm : Parts per million

Predicted R^2 : Ability of regression model to predict responses for new data.

PSA : Pressure-swing adsorption

Psi : Atmospheric pressure in pounds per square inch

Psig : Gauge pressure in pounds per square inch

PV : Photovoltaic

P_x : Partial pressure of species 'x'

R : Ideal gas constant

R^2 : Coefficient of determination detailing how well observed data fit a regression model

S : Entropy

SCFM : Standard cubic feet per minute (standard conditions $T = 25$ Celsius, $P = 1$ atm)

SCG : Southern California Gas Company

SCR : Selective Catalytic Reduction

SS316 : Stainless steel grade 316

STC : Standard Testing Condition for solar systems

Std. Dev. : Standard Deviation

Sum of Squares : Sum of the squared difference between a population average and the variation of the data.

T : Temperature (degrees Kelvin unless otherwise specified)

TET : Turbine exit temperature

Trust Region : Optimization technique for unconstrained non-linear problems

UCI : University of California, Irvine

US DoE : United States Department of Energy

USGS : United States Geological Survey

VAC : Voltage Alternating Current

VDC : Voltage Direct Current

VRES : Variable Renewable Energy Sources

y_x : Molar fraction of species 'x'

α : Symmetry coefficient of electrochemical reaction

δ : Thickness

ε : Porosity

λ : Membrane water content in mol of water per mol of sulfonic acid groups

μ : Dynamic viscosity

ρ : Density

σ : Conductivity

φ : Void ratio

η : Efficiency

ACKNOWLEDGEMENTS

It is necessary to take a moment and acknowledge the number of individuals and entities to which I owe a great amount of gratitude in contributing to and supporting to this work.

The Advanced Power & Energy Program (APEP) and by extension the National Fuel Cell Research Center (NFCRC) has created an environment unlike any other where a passion for sustainable innovation in energy has met incredible mentorship and vision. I owe an incredible debt of gratitude to my advisors Professor Jacob Brouwer and Professor Scott Samuelsen for creating this space and inviting me to contribute to it and benefit so immensely from it. Professor Brouwer exhibits incredibly sharp insight, and has been a source of invaluable and tireless guidance, through which many challenges faced in this work were overcome. Professor Brouwer's endless optimism for the future of power and energy engineering has been an endless fount of inspiration for me. In combination with Professor Samuelsen's steadfast and pragmatic leadership of the APEP program, they have undoubtedly had a huge positive impact on the direction of my life.

I would like to share my immense gratitude towards Professor Jaeho Lee for all the knowledge he has imparted on me in my Masters studies and for graciously agreeing to review this work as a member of my thesis committee. Dr. Li Zhao assisted directly in the installation of the electrolyzer system and provided immense technical insight throughout the process. Dr. Robert Flores contributed his invaluable expertise in the operation of the Central Plant and shared a large burden of the work associated with the high throughput hydrogen injection testing, working with me throughout the 12-hour test period. Gabrielle Cobos, Alejandra Hormaza and Jeremiah Blackburn contributed a great amount of assistance at various stages of the electrolyzer

installation and operation. I would also like to thank Yan Zhao and Ryan Ehlig for their patience in fielding numerous questions regarding combustion science. Max Venaas perhaps is owed the greatest thanks here for technical assistance, due to the large amount of time spent fielding my questions or generally being a sounding board for the more novel technical approaches taken in this study.

A huge debt of gratitude is owed to the facilities management personnel that run the UC Irvine Central Plant. The engineers of UCI Central Plant consistently went above and beyond to provide invaluable assistance to the project, and displayed an incredible candor while doing so. A special thanks is owed to the leadership at Central Plant; Gerry Nearhoof, Tamela Kelleher, and Neal Edwards. Their incredible command of the plant's operations and their concise and easy to follow directions could not have made my time working in their facilities any easier or more enjoyable than it already was. Neal Edwards also directly contributed to maintenance and repairs of the electrolyzer system, offering vital insight through a highly refined technical intuition. I learned an incredible amount from my hours working on-site at the Central Plant, and I owe it all to them.

A huge thanks to the memory of Rich Hack, who played a significant role in the early stages of this study in the planning of the electrolyzer installation. More importantly, Rich Hack was critical in the development of the skills that I used in carrying out this study. From my earliest days at the Advanced Power & Energy Program, Rich Hack instilled in me an appreciation for tackling new challenges head on, with a careful and precise approach that I strive to match every day. Without Rich Hack's tutelage, I would not be where I am today, and for that I am immeasurably grateful.

I would like to recognize the technical contributions of Proton OnSite's Steve Szymanski and Dr. Kathy Ayers, who provided incredible support on the electrolyzer system. I would also like to recognize the leadership, vision, and contributions of Southern California Gas's Ron Kent, Matt Gregori, and Dr. Jeffrey Reed. They represent the organizations that made this work possible, and went far beyond simply providing the funding for the project, taking part in the work along the way.

ABSTRACT

DYNAMIC ANALYSIS OF A PROTON EXCHANGE MEMBRANE ELECTROLYZER INTEGRATED WITH A NATURAL GAS COMBINED CYCLE POWER PLANT FOR POWER-TO-GAS APPLICATIONS

By

John M. Stansberry

Master of Science in Mechanical and Aerospace Engineering

University of California, Irvine, 2019

Professor Jacob Brouwer, Chair

Proton exchange membrane electrolyzers (PEMEZ) are an attractive technology choice as the principal piece of equipment in power-to-gas (P2G), however their usage within the context of P2G has not yet been thoroughly investigated, and no pilot plants for power-to-gas with PEMEZ have as yet been realized in the United States. In this study, a PEM electrolyzer was modified to have dynamic dispatch capabilities, then subsequently operated and studied in detail as a part of the UC Irvine P2G demonstration. The system operated at sustained part load conditions and load followed variable renewable energy resources. Furthermore, the impact on emissions due to the addition of hydrogen to the high pressure natural gas fuel feed to the University of California Irvine (UCI) Central Plant's combustion turbine is analyzed.

Solar PV load following was found to have minimal impact on system efficiency in producing hydrogen from electrolysis, however wind load following did result in sustained low load conditions that did impact system efficiency significantly. Reduced efficiency due to sustained low part load conditions could be circumvented by cycling PEMEZ off completely and starting up as the load signal reached the minimum effective point again. The effective

compression of hydrogen electrochemically in the PEMEZ was demonstrated to nearly match the efficiency of ideal isothermal compression using a semi-empirical model developed from sustained part load operation testing of the PEMEZ.

Addition of hydrogen to the natural gas fired combustion turbine showed very little likelihood of impact on emissions of criteria pollutants (CO, NO_x). A slightly significant correlation between reduction in natural gas usage, and by extension emissions of CO₂, was noted.

1 INTRODUCTION

Power-to-gas is an emerging technology concept in which electrical energy storage is provided in the form of compressed gaseous fuel. The principal step in this process is water electrolysis, which utilizes inputs of electricity and water to create hydrogen and oxygen gas. Hydrogen gas can be utilized as fuel for power generation or transportation, or it can be stored. Produced hydrogen gas can also be stored in tanks or sent to natural gas infrastructure via blending with natural gas or methanation. The existence of expansive natural gas infrastructures in conjunction with electrical grids portends a large potential energy capacity for power-to-gas.

Proton Exchange Membrane (PEM) electrolyzers have a number of attributes that make them an attractive option for the water electrolysis step of power-to-gas. They are highly dynamic, and thus able to ramp their output from very low capacities to full throughput in seconds and are able to ‘cold start’ in minutes. Additionally, their efficiency does not depend greatly on part load capacity. These characteristics make these systems a promising for load following applications of power-to-gas, one example being the diurnal patterns in solar energy overproduction on high solar penetration electrical systems. Current power-to-gas demonstrations primarily employ alkaline electrolyzer systems, and as such not many studies assess the performance of PEM electrolyzer systems in power-to-gas applications. This thesis seeks to assess the performance and characteristics of a PEM electrolyzer system uniquely coupled with a natural gas combined cycle power plant (NGCC) in power-to-gas to power demonstration.

1.1 Goals

The goals of the research are to

- Demonstrate proof of concept for the power-to-gas pathway concerning the conversion of renewable sourced electricity to hydrogen by PEM electrolysis and the later conversion of hydrogen back to electricity through combustion in a gas turbine.
- Determine performance characteristics of a PEM electrolyzer system with regards to power-to-gas applications and assess possible alternatives or recommend improvements.
- Ascertain impacts, if any, that hydrogen addition has on the performance of a natural gas fired combustion turbine system used for combined heat and power (CHP).

1.2 Objectives

The following objectives are met to fulfill the goal of the thesis:

1. Integrate a commercial scale (60 kW) PEM Electrolyzer system with the UC Irvine Central Plant for injection of hydrogen gas to the natural gas infrastructure upstream of the gas turbine. Carry out proof of concept operation of the hydrogen injection process and discern any impacts on gas turbine performance.
2. Develop and evaluate a control strategy for dynamic operation.
3. Operate the integrated PEM electrolyzer system through sustained part load condition cycles to assess part load performance.
4. Use solar photovoltaic and wind turbine output data to operate the PEM electrolyzer system in a load following fashion to support variable renewable energy resources (VRES).
5. Analyze the dynamic performance characteristics of PEM electrolysis in power-to-gas applications for energy storage and load balancing services.
6. Determine the electrical work requirements concerning the pressurization of generated hydrogen in the electrolyzer system.
7. Characterize system performance using acquired experimental data and model any system components that impact dynamic performance.
8. Develop an analytical model for further studies involving the integration of PEMEZ electrolyzer systems with other power-to-gas utilization pathways.

2 BACKGROUND

Increasing amounts of variable renewable electricity sources such as solar and wind in conventional electrical grids are predicted to lead to a diminishing return in benefits due to dynamics of uncontrollability and intermittency and operational constraints associated with their integration into electrical systems [1]. This is becoming apparent in electrical grids that already have relatively large shares of solar and wind, such as in California and Germany. Current efforts to expand the penetration of renewable energy resources are being impeded by the challenging dynamics associated with the intermittency of solar and wind – the two fastest growing sources of renewable electricity in the United States [2]. In 2014, wind energy comprised 27% of total electricity generation capacity additions, and large solar energy installations (greater than 1MW capacity) comprised 22% [2]. Other renewable resources that are more dispatchable, such as geothermal or biomass are limited. The intermittency of these wind and solar resources means that the periods of electrical generation does not necessarily match the periods of demand. The challenge of maintaining the supply of variable renewable energy to meet the actual instantaneous demand for energy results in challenges for utilizing large amounts of renewable energy compared to controllable conventional energy sources, such as fossil fuel-based power plants. This has consequences for the economics and reliability of electrical grid networks seeking to implement more renewable energy sources. Ultimately wind and solar energy resources have been identified as essential to meet high renewable electricity generation long term goals such as those of California’s SB350, which mandates 50% electrical generation from renewable resources by 2030 [3] [4].

Over-generation of variable renewable energy resources occur typically during periods of low demand when conventional energy resources are unable to turn down any further due to

frequency regulation requirements, or due to electricity transmission congestion [6]. Given the minimum generation requirements of many long-start resources and the need to accommodate the technical and economic limits of turning down or turning off other power plants such as thermal or hydro, over-generation from solar and wind is a necessity for any highly renewable electricity system [6]. This was the case discovered in a study considering an RPS of 50% in California [7], a high RPS case for the United States eastern interconnection regional transmission organization PJM [8], and a study of 100% RPS cases in the Australian National Electricity Market [9].

Wind energy production is both spatially and temporally intermittent. Locally, spatial variation can be attributed to the topography of the area. At a given location wind energy can vary dramatically on time scales that range from years down to seconds. One review found multiple studies concluding that over a twenty-year period, the standard deviation of mean wind power output from one turbine to the next was at most 10% [10]. Thus, there can be a fairly consistent forecast for the wind energy production in the long term for a given turbine. Furthermore turbulence events related wind energy variations on the timescale of minutes to seconds can be smoothed to a degree by the use of variable speed wind turbines as well as distributing generators in a ‘wind farm’ configuration [10] [11]. It is diurnal variations of wind power generation and synoptic variations, related to weather events such as storm conditions, that ultimately can affect power balancing requirements [10]. Increasing additions of wind energy resources could negatively impact electrical grid operation on the load following time scale, due to diurnal variations, as well as on the scheduling time scale, due to synoptic variations [12]. Electrical systems with appreciable amounts wind penetration will encounter operational constraints due to these intermittency characteristics, forcing curtailment events of

wind energy resources [13]. Curtailment of as much as 10% annually has been observed in regions of relatively high wind integration already, such as China, Italy, and The Electric Reliability Council of Texas (ERCOT) service area [1]. To integrate increasing amounts of wind energy resources to an electrical system, there is need for greater operational flexibility in energy resource dispatch and/or energy storage.

Solar energy resources tend to be more predictable than wind, however their potential impact on an electrical grid system still makes for challenging load balancing conditions. The diurnal variation of solar energy is well understood as a result of the earth's rotation and orbit, varying cyclically by season and location. Non-cyclical variability can occur in the event of intermittent cloud cover or weather events. This non-cyclical variability has the potential to create unfavorable forecasting conditions that leads to curtailment events in favor of controllable energy resources. The potential impact of this variability can be dramatically reduced by dispersing the solar energy resources geographically [14] [15]. The glaring challenge in large scale integration of solar energy to an electrical system is the dramatic difference in output between peak solar production time and off-peak hours. Once solar capacity levels are such that peak solar generation periods result in excess generation, greater and greater incremental solar capacity additions and eventually massive energy storage are needed to increase overall solar contribution [16]. This effect is exacerbated by different peak demand periods, such as in the case of California. In the California day-to-day electrical load demand there is a residential demand increase starting at 4AM, well before solar begins to kick in, and a late evening residential demand peak increasing from 5PM up to 7PM which corresponds to a steep drop in solar concurrently [17]. The consequences of this can be seen in the California Independent System Operator's (CAISO) 'duck curve' analysis that predicts an increasingly dramatic ramp

requirement for meeting the evening electrical demand, predicting that an increase in dispatchable generators of as much as 13,000MW from 3PM to 6PM could be needed by 2020, compared to the 2013 requirement of 5,000MW, already up from 2012's 3,000MW ramp requirement over that time period [17] [18].

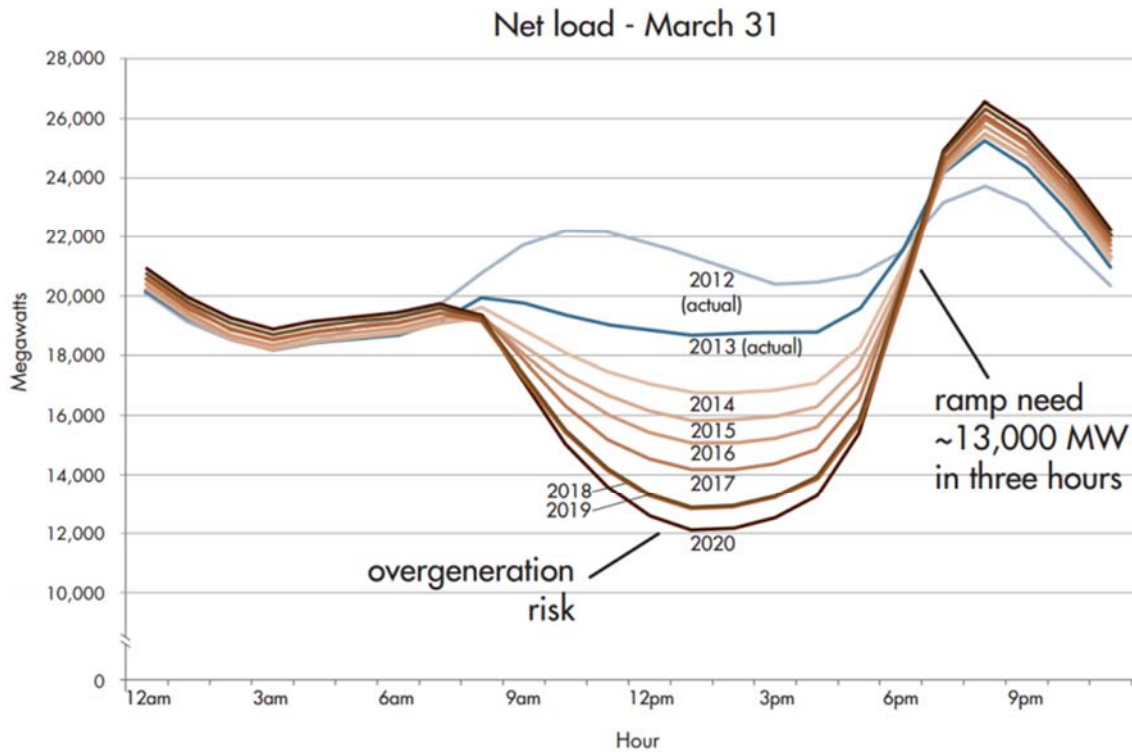


Figure 1. CAISO's 'Duck Curve' highlighting the growing ramp demands and risks of over-generation occurring today and projected in the upcoming years [19].

Tarroja et al. determined that high renewable penetration levels would impose severe challenges for load balancing costs and operation in lieu of any energy management strategies [20]. The consequences of such a scenario include low net load capacity factors resulting in oversized generators with small relative returns to their capital costs [20]. To achieve zero excess renewable generation, dispatchable generator resources may need to turn off more often, which can cause significant degradation in combustion engines, introducing potentially higher electricity costs [20] [21].

Management strategies for increasing flexibility in load balance include the reduction of spatial supply and demand differences by increased transmission interconnections, energy storage, addition of flexible generation such as natural gas turbines and hydroelectric, and demand response type technologies such as ‘smart’ micro-grid demand shifting or controllable load additions such as electric vehicle charging.

A promising strategy to mitigate the intermittency of wind and solar is energy storage [22]. Energy storage brings to the electrical grid the capability to decouple the temporal aspects of electrical generation versus demand. Conventional energy storage technologies include battery, fly wheel, compressed air, and pumped hydro. Due to the potentially massive scale of required energy storage to effectively implement large numbers of variable renewable energy sources, newer strategies with higher energy densities are being considered. One such technology is power-to-gas.

Power-to-gas is a concept wherein a chemical energy carrier is produced during peak renewable power production periods. Power-to-gas is a relatively new technology concept that has come about with the increased apparent need for long term and massive energy flexibility. A 2012 review of power-to-gas pilot plants found 26 demonstration plants in operation worldwide, 95% of which were found in either Europe or North America [23]. A more recent 2017 survey of European power-to-gas plants found over 70 power-to-gas plants in operation with a combined electrolyzer system capacity of 30 MW [24].

The primary electrochemical conversion process in many power-to-gas concepts is water electrolysis. In water electrolysis, an electric potential across two electrodes drives a water splitting process that generates hydrogen and oxygen. The electrodes and products are separated by an electrolytic layer that conducts ions across from one electrode to the other. Hydrogen is

produced in the cathode compartment and oxygen is produced in the anode compartment. There are a number of different electrolyzer technologies available today, distinguished by the type of electrolyte employed.

Hydrogen energy storage has the capability to deliver large energy capacities and/or power in and out over long periods of time, making it an attractive solution for grid scale energy storage. Maton et al. simulated salt cavern based compressed hydrogen energy storage and suggested that load shifting on daily time scales up to as long as seasonal time scales could be accomplished [25]. For solar energy the capability of load shifting on seasonal time scales to offset the dramatic difference in generation from summer to winter is particularly attractive [26]. Over long time periods, the self-discharge of chemical energy storage in the form of hydrogen or carbon neutral methane is close to zero, whereas most other energy storage technologies deal with self-discharge rates too high to accommodate the seasonal time scale [27] [28] [29] [30]. Hydrogen produced in this renewable manner can be sent to a number of different pathways. Hydrogen can be injected directly into pre-existing natural gas infrastructure up to acceptable concentration levels or used in methanation processes to generate carbon neutral methane for injection into natural gas infrastructure without concern for the concentration. Alternatively, hydrogen can be stored separately for end use in fueling stations for transportation use in fuel cell electric vehicles or for power generation in a fuel cell or combustion engine.

To realize the benefits of power-to-gas, the electrolysis system needs to be able to meet a number of criteria. Due to the intermittent nature of the renewable energy inputs, a wide range of load condition operation and rapid dynamic response in a load following manner are desired. High efficiencies are needed to effectively capture renewable energy inputs and keep operating

costs down. Economic viability is a concern, with electrolyzer capital costs relatively high compared to similar sized energy storage options with more maturity behind them [31].

Proton exchange membrane (PEM) electrolyzers are a relatively young electrolyzer technology, having been in development for only the last 20 years [32]. The electrolyte membrane for which it is named consists of a solid polymer of the perfluorosulfonic acid family, with carbon-supported platinum electrocatalyst layers on each side, which allows for dissociation of water when wet and the subsequent transport of hydrogen ions (H^+) across the membrane [33]. PEM electrolyzers are low temperature systems that are typically operated below 100°C as the membrane must be hydrated to facilitate ion conduction. In lab environments, PEM stack efficiencies have been demonstrated as high as 85% higher heating value [34] [35]. State of the art commercial PEM electrolyzer system efficiencies at large scale are found typically between 67% and 75% of higher heating value [36].

Publications on PEM technology are more often concerned with Proton Exchange Membrane fuel cell systems, but within the last decade an increase in interest towards PEM electrolyzer can be observed in the greater proportion of publications concerning PEM electrolyzer systems [37]. A number of modeling approaches have been able to analytically characterize the theoretical effects of varying operating conditions and physical design characteristics on cell and stack performance and shown good agreement with experimental data [38] [39] [40] [41] [42] [43] [44] [45]. Other efforts have also successfully characterized system level performance, incorporating the balance-of-plant into their models and having similar success with matching experimental system data [46] [47]. Further analytical studies have demonstrated the suitability of PEM electrolyzer systems integrated with variable renewable energy for the production of renewable hydrogen [48] [49] [50] [51], and further applied to a

self-sustaining renewable hydrogen fueling station [52], reversible or ‘regenerative’ PEM fuel cell systems [53] [54] [55], and large scale power-to-gas scenarios [56]. Experimental studies have demonstrated the application of these systems for integration with variable renewable energy resources [57], in providing ancillary grid services [58], and have investigated the ability to electrochemically compress hydrogen in the electrolyzer stack, reducing or negating the requirement of additional compression equipment [59].

Proton Exchange Membrane electrolyzers show promising qualities for implementation within the power-to-gas concept. These systems can operate at part load capacities as low as 5% up to 100% without interruption [60]. They have shown the capability to load follow highly dynamic power inputs, as would be necessary for integration with solar or wind energy sources [60]. These are important qualities for successful power-to-gas integration with solar due to the likely need for relatively low capacity factors of the electrolyzer systems when utilized for absorbing large amounts of solar over-generation [26]. There exists the capability for hybrid ‘reversible’ PEM systems. These are systems that can run in both a fuel cell mode, generating electricity with hydrogen fuel input, and an electrolysis mode, generating hydrogen fuel for storage with electrical input. Maclay et al. was able to demonstrate the technological feasibility of such a system at a residential scale integrated with dynamic PV solar inputs as well as residential loads [61].

3 Integration of PEM Electrolyzer System with the UC Irvine Central Plant (Objective 1)

The initial task of this thesis was concerned with the successful implementation of a proof of concept power-to-gas process. This power-to-gas demonstration involves the integration of an electrolyzer system with the UC Irvine Central Plant. Hydrogen produced from the electrolyzer system is mixed into the high-pressure natural gas pipeline upstream of the gas turbine and subsequently combusted to complete a power-to-gas-to-power ('P2G2P') utilization pathway. Figure 2 provides an illustration of this specific utilization pathway within the greater power-to-gas framework.

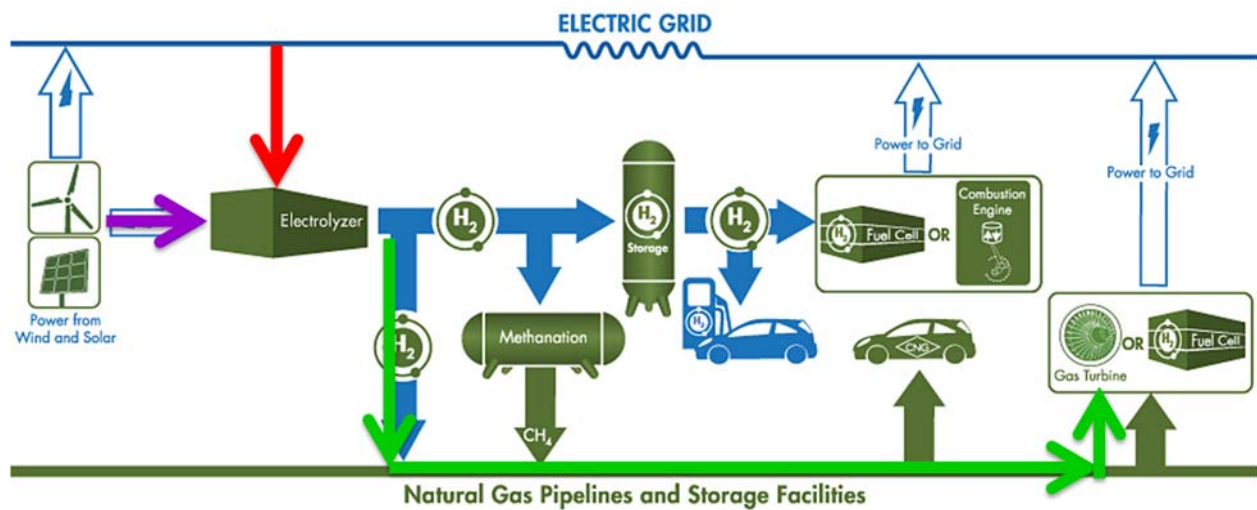


Figure 2. Power-to-gas-to-power at the UC Irvine Central Plant Power-to-Gas Demonstration. Hydrogen utilization pathway is highlighted in green. Two pathways of power utilization are differentiated; uncontrolled 'full load condition' power draw (red) and simulated VRES load profiles (purple).

3.1 UC Irvine Central Plant

The UC Irvine Central Plant (UCI CP) contains a combined heat and power (CHP) plant that has been in operation since 2007. It is a natural gas fired combined cycle power plant (NGCC)

system, utilizing a 13.5 MW Solar Turbines Titan 130 gas turbine integrated via a Heat Recovery Steam Generator (HRSG) that can send steam to either the bottoming cycle 5.6 MW Dresser-Rand Murray Steam Turbine, or directly to the UCI campus heat load, or to a steam turbine chiller to help meet the campus chilling load. The UCI CP also incorporates boilers and electric chillers for meeting additional heating and cooling requirements as needed, as well as an extensive cold water thermal energy storage (TES) system and district heating and cooling loops that serve all of the major buildings on campus. Figure 3 presents a more detailed graphical representation of the UCI CP itself.

Combined Heat and Power Plant

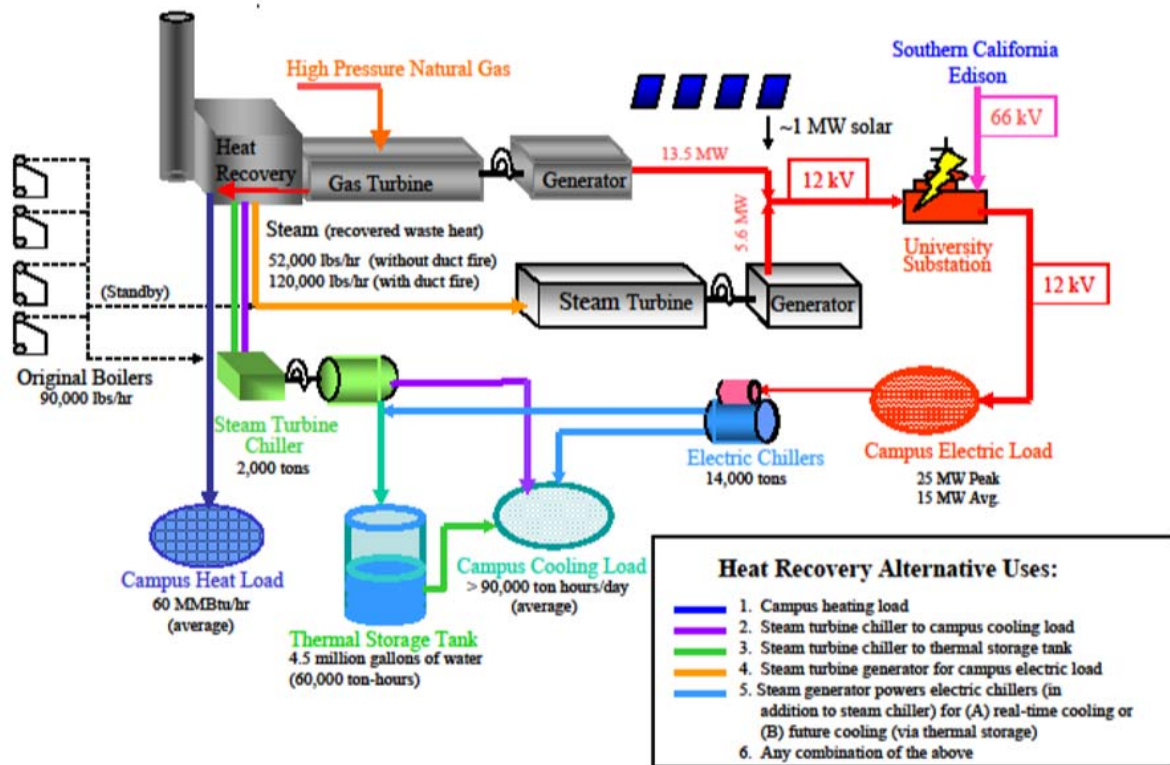


Figure 3. UC Irvine Central Plant simplified process flow diagram [62].

3.2 Electrolyzer System

The PEM electrolyzer deployed was a Proton Onsite Model C10 electrolyzer, which was purchased through an agreement with Southern California Gas Company to enable our demonstration of power-to-gas concepts on campus. For ease of access to the high-pressure natural gas pipeline, the electrolyzer was sited at the UCI CP compressor yard. To meet siting requirements, a concrete pad was laid down in the compressor yard for the system, a 480 VAC 3-phase 200-amp breaker added to the gas turbine motor control center (MCC) was added with a circuit run to the electrolyzer skid, and a deionized (DI) water line was plumbed from a pre-existing DI water system.

The C10 system is a differential pressure proton exchange membrane (PEM) electrolyzer system. The '10' in C10 comes from the rated hydrogen gas (H_2) output rate of 10 normal cubic meters per hour (Nm^3/hr) at 30 barg and a purity of $> 99.9998\%$ H_2 . Proton Onsite reports that detectable impurities come in the form of water vapor ($H_2O(g) < 2$ ppm), nitrogen gas ($N_2 < 2$ ppm), and oxygen gas ($O_2 < 1$ ppm). The system is rated for a 480VAC 3-phase 100kVa breaker, with a power consumption of 60kW and a specific energy consumption rate of 68.9 kilowatt-hours of electricity (kWh_{el}) per kg of H_2 , for a higher heating value (HHV) system efficiency of 58.1%.

The C10 system is comprised of two separate cabinets, a 'fluids cabinet' containing the electrolysis stack and mechanical systems while an electrical cabinet houses the power conditioning equipment. This is done to prevent the introduction of relatively volatile hydrogen gas, which has a lower explosive limit (LEL) of 4% in air, to electrical components which could produce a spark and cause ignition in the presence of relatively small concentrations of hydrogen. The cabinets are connected by a wire way track the runs the direct current (DC) cables

to the electrolysis stack in the fluids cabinet from the AC/DC rectifying power supply in the electrical cabinet (see Figure 4). Both cabinets in the C10 system are oversized, as the system architecture is intended to be upgradeable, allowing the addition of up to two more C series PEM stacks, for a total of three stacks in the fluids cabinet. Each stack would require an additional AC/DC rectifying power supply in the electrical cabinet.



Figure 4. C10 electrolyzer system. Fluids cabinet containing mechanical systems and cell stack on the left, electrical cabinet containing the power electronics on the right.

3.2.1 Electrolysis Cell Stack

The C Series PEM electrolysis cell stack is built in-house by Proton Onsite for their C10/C20/C30 systems. The stack is rated at roughly 60 kW_{el} of electrical input, at a maximum current of 410 amps DC. Within typical operating parameters of the C10 system this power rating is not ever reached, though conditions resulting in higher cell potentials (lower temperature primarily) could more than likely hit the 60kW_{el} number. The maximum pressure ratings are 34.5 barg H₂ gas on the hydrogen electrode and 2.76 barg O₂ gas on the wet electrode, and an operational temperature range of 5 to 65 C°.

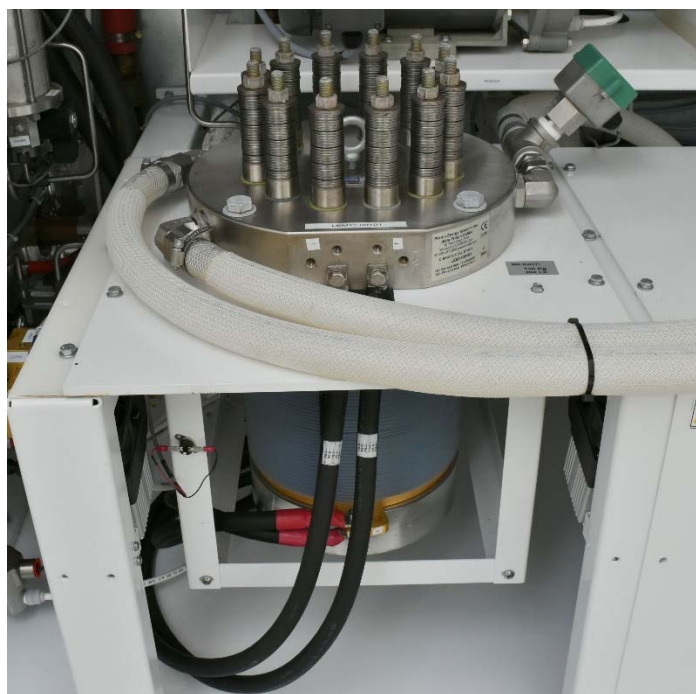


Figure 5. C10 Electrolyzer system proton exchange membrane cell stack.

The stack itself is comprised of 65 cells, with the negative potential endplate on the top, and the positive potential endplate on the bottom (Figure 5). There is one DI water inlet to the wet electrode, and a ‘wye’ configuration two hose outlet from the wet electrode to reduce the pressure drop coming out of the stack on the recirculating DI water feed. From the hydrogen

electrode side, a 3/8" OD SS316 line carries wetted hydrogen out to the hydrogen management subsystem. Further information was provided for the purposes of this study by Proton Onsite concerning the cells structure and active cell area, which was given as 213.68 cm². Further details on the electrolysis cell known parameters and their values are given in section 6.1.

3.2.2 Hydrogen Management Subsystem

Generated hydrogen gas goes through a hydrogen management subsystem that maintains hydrogen pressure in the system up to the process connection, as well as removes to a high degree and recovers to some extent entrained water in the hydrogen gas stream. As hydrogen gas exits the cell stack, it enters a hydrogen water phase separator vessel where system-side hydrogen pressure is monitored and maintained. Water is dropped out by gravity in this vessel, and intermittently ‘flushed’ to send the water back into the DI water loop. From the hydrogen water phase separator, hydrogen gas passes through a heat exchanger before entering a secondary larger volume hydrogen water phase separator vessel, which prevents sudden buildup of hydrogen pressure on the system side.

After passing through the heat exchanger, hydrogen gas enters a pressure swing adsorption dryer system. The system is comprised of two dryer beds, each full of desiccant beads that selectively adsorb water at elevated pressure, drying the hydrogen gas to the high degree of purity the system is rated for, > 99.9998% H₂. One dryer bed flows hydrogen gas at a time, the ‘dry bed’, while the other bed depressurizes to allow adsorbed water to drop out, which is then purged out of the bed by a continuous slipstream of the dry hydrogen from the other bed. Upon this ‘purge’, the beds swap and the process repeats.

After the drying process a, a series of check valves, pressure transducers, and a back-pressure regulator control the output pressure of the hydrogen gas to the end process. This pressure feedback control loop is the primary control concerning the amount of electrical power delivered to the electrolysis process.

3.2.3 Oxygen Management Subsystem

Generated oxygen gas is entrained in the water electrode and exits through the return DI water hose. This mixture goes to a water-oxygen phase separator, which separates the two through gravity. Oxygen gas exits to an exterior vent with a small amount of water. Sensors on this subsystem monitor the gas pressure and for the presence of hydrogen gas to prevent a flammable mixture. The pressure of the oxygen gas does not exceed 2.76 barg.

3.2.4 Deionized Water Management Subsystem

The electrolyzer consumes DI water at a rate of 9 L/hr and requires a delivery pressure of 1 to 4.1 barg. DI water quality must be at minimum ASTM Type II, resistivity $> 1 \text{ M}\Omega\text{-cm}$, but ASTM Type I, resistivity $> 10 \text{ M}\Omega\text{-cm}$ is recommended to maximize the lifetime of the stack. Incoming water quality to the system is monitored at the system inlet, before a primary DI water tank that holds up to 56 L of DI water. Incoming water below $1 \text{ M}\Omega\text{-cm}$ for a sustained period (> 30 seconds) triggers a system failure even if recirculating water quality is maintained.

DI water from the main tank is introduced to the recirculating water loop through a secondary feed water pump (1.1 hp) to an internal DI water polishing bed, housing a mixed bead resin filter. A recirculating system water pump (3 hp) drives the DI water through a heat exchanger and then to the cell stack. When water is not being added from the main DI water tank, a portion of the recirculating water stream is diverted through the internal DI water polishing bed.

3.3 Data Acquisition Systems

An onsite Lenovo laptop serves as the data acquisition (DAQ) and control personal computer (PC) for the test bed. The C10 electrolyzer system has an internal data stream that provides high resolution, accurate data concerning the operation and control of the system through Modbus protocol. These metrics are collected in real time from the system by connection through an ethernet switch with proprietary software provided by Proton Onsite. Onboard metrics of interest to the study of the system include the system hydrogen pressure at the outlet of the hydrogen electrode (barg), oxygen pressure at the oxygen-water phase separator (barg), system water temperature at the outlet of the DI water subsystem heat exchanger (C°), hydrogen gas temperature at the hydrogen management subsystem heat exchanger (C°), the stack voltage (volts), and the stack current command signal (amps). The state of the system solenoid valves, water levels, coolant temperature at the heat exchangers, DI water quality at the inlet and in the recirculating water loop is also monitored and recorded.

To complement the on-board data acquisition and provide verification of some measurements, some external sensing was implemented. Power meters (Dent ElitePro®) at the electrolyzer system connection to the grid, on the electrolyzer system breaker to the ancillary power demands, and at the grid connection to the chiller system, recorded the net power consumption (kW), voltage across the 3-phases (volts AC), amperage across the 3-phases (amps AC), and the power factor. Having power monitoring on both the overall system consumption and on the ancillary systems circuit allowed for the characterization of the AC electricity consumption of the electrolysis process separate from the electrical power needed to run the pumps, blowers, valves, etc.; that make up the ancillary power demands.

An additional Dent ElitePro® system was connected to the cell stack to independently measure the stack voltage at a higher resolution than the internal data stream and also served to verify the on-board system measurements.

The stack current was measured using two split-core current transducers (CR Magnetics CR5220S Split Core Current Transducers) rated for 0-300 amps DC. Verification on the current reading was accomplished intermittently with a Fluke split-core current transformer (Fluke i410 AC/DC Current Clamp). Hydrogen gas mass flow from the system to the end process was measured using a Sierra Instruments 840H Hi-Trak Mass Flow Controller. 4-20 mA analog output logic from the split-core current transducers and mass flow controller was logged on a Dent DataLogger Pro.

All Dent power meters and the Dent data logger are read from by way of an USB-RS232 adapter at regular intervals depending on their memory capacity. The Dent data logger is connected at all times during system operation so that real-time hydrogen flow and current throughput data can be accessed for diagnostic purposes.

3.4 Chiller System

The C10 electrolyzer system has three water cooling loops that serve heat exchangers with the electrolysis process DI water, the hydrogen gas before the drying process, and the blowers in the power electronics cabinet. The cooling demand is served by a co-located chiller system, shown below in. The net cooling water requirement of the C10 is a max heat load of 114,307 Btu/hr, at a flow rate 90 L/min at 3 barg. The chiller system used is an Accuchiller® air-cooled chiller (PN#: NQA13C1E213C) which provides up to 190,000 Btu/hr.

3.5 DI Water System

A deionized water polishing system was implemented to upgrade municipal water supply from the Irvine Ranch Water District (IRWD) to a high-quality DI water stream. This was accomplished through service deionization provided by Evoqua Water Technologies. The skid is comprised of a 4 ft³ water softener, followed by two 3.6 ft³ mixed bed deionizer tanks rated for 36 LPM.

The expected service life of such a system is 2000 gallons of delivered DI water. For the C10 consumption rate of the system, this would give a replacement cycle of ~35 days or roughly a monthly filter exchange on mixed bed deionizer tanks. Two mitigating factors led to a replacement cycle of every 10-14 days for the DI water system.

Much of the IRWD water delivered comes from groundwater sources, which leads to measured hardness values as high as 394 mg CaCO₃/Liter [63]. The US Geological Survey (USGS) defines hardness values higher than 250 mg CaCO₃/Liter as ‘very hard’ [64]. This has a direct impact on the longevity of ion exchange-based resin filters, as the total amount of ions removed per liter of water delivered is much higher than what is typically expected. The water softener bed does assist in mitigating the high hardness of the water by removing problematic cations such as Iron (Fe²⁺ and Fe³⁺), however it does so by exchange with salts that will still need to be removed by the downstream deionizer beds and as such does not ultimately reduce the ‘work’ done by the DI beds.

Due to the relatively low DI water consumption rate of the C10 system, the system only ‘fills’ from the DI water feed intermittently. At full load conditions, this fill occurs every ~3 hours and fills for about 3 minutes. Resin-based ion exchanger beds are rated for specific flow ranges at a constant flow. When there is a non-constant flow, or the flow rate is too low, the resin beds can

lose their compaction, allowing some water to flow through ‘channels’ bypassing the resin. This ‘channeling’ event effectively reduces the overall capacity of the tanks. Oftentimes, these drawbacks are prevented by implementing a recirculation pump in the DI system. To keep system complexity down, a water bleed line was introduced to keep a constant flow through the beds.

3.6 Mass Flow Controller & Control System

To control the dispatch of the C10 system for dynamic response, a mass flow controller was installed on the hydrogen product line. The mass flow controller is able to dispatch the electrolyzer system by choking the hydrogen flow, simulating a reduced hydrogen demand downstream of the system. The pressure feedback loop in the hydrogen management subsystem senses the higher downstream pressure and reduces the current throughput to the electrolysis stack accordingly.

For dynamic dispatch, a dispatch profile from a selected data source, or a general load profile such as a stepwise ramp, is converted to comma-separated (.csv) file format. The .csv file is read by a Python script, which outputs the signal value through serial communication to a Seed Studio Seeeduino microcontroller. The microcontroller reads the serial value and then outputs an equivalent 0-5V DC analog signal through pulse width modulation. This signal is converted to a 4-20mA signal by way of a signal conditioning circuit comprised of an RC circuit for conditioning the Volts DC signal which then goes through a Texas Instruments XTR110 precision Voltage-to-Current converter IC. This 4-20mA signal is then communicated to the mass flow controller which controls the hydrogen flow from the system.

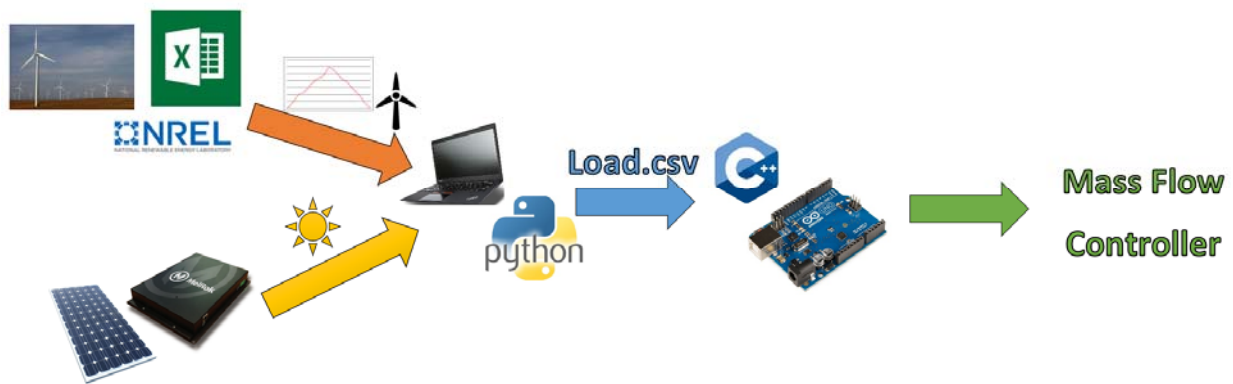


Figure 6. Dynamic dispatch control of the mass flow controller.

Hydrogen mass flow was measured and controlled using Sierra Instruments Hi-Trak 840H mass flow controllers (P/N#: 840H-4-OV1-SV1-D-V4-S4-HP). Two separate mass flow controllers (MFC) were employed throughout the duration of testing. Both MFCs were the same model, with separate factory calibrations set for 0-10 SCFM H₂ and 0-10 SCFM carbon monoxide (CO). Initially, the MFC calibrated for hydrogen gas was used, but a critical failure of the valve spring adjustment screw took the MFC out of service. While that MFC was being repaired, the CO configured flow controller was put into service. Before flow controllers were put into service, an in-situ calibration was performed using a laminar flow element (Meriam: Model 50MJI-6410). The calibrations for the two mass flow controllers are shown below in Figure 7.

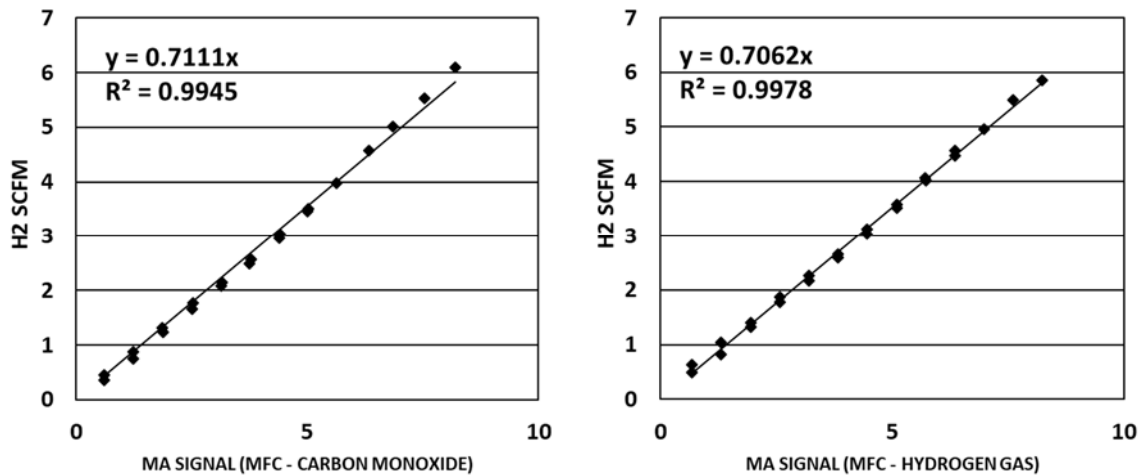


Figure 7. Calibration curves for the two mass flow controllers using a laminar flow element.

3.7 VRES Dynamic Data

For the dynamic dispatch testing, two different electrical power sources of variable renewable energy were considered; solar photovoltaic and aggregated wind turbine resources (wind farm). The solar photovoltaic dispatch comes from local resources on the UC Irvine microgrid. Lack of nearby wind resources required the use of wind generation data from NREL's database.

3.7.1 UC Irvine Microgrid & Melrok Metering Network - MSTB PV Array

The UC Irvine microgrid is centrally operated by a central UCI substation that serves a 12kV circuit, which radially distributes electrical power throughout the campus. The substation is connected by a 66kV circuit to the nearby Edison MacArthur substation. Major sources of electrical generation resources on the microgrid include the 18 MW UC Irvine Central Plant, 4 MW of rooftop solar photovoltaic, as well as a 250kW Amonix tracking solar photovoltaic array.

An extensive network of power meters throughout the UCI microgrid provides real-time and historic data concerning electricity consumption and production on almost three quarters of UCI's buildings and on all generation assets. For the purposes of this study, the rooftop photovoltaic array located on the roof of the Multipurpose Science and Technology Building (MSTB) was chosen as source for the solar load following dispatch profiles. This is due to the relatively high temporal resolution of the available historical data (1 min time-step) and the scale of the array (75 kW standard testing conditions - STC) being comparable to the 60kW electrolyzer system. Melrok's Energistream™ software was used to search through and obtain the historical data.

3.8 Natural Gas Pipeline & Gas Turbine

The hydrogen from the electrolyzer system is fed into a natural gas bypass line located at the Central Plant's external natural gas compressor skid. The hydrogen 'injection' line is 70' of 3/8" OD SS316 tube that connects to a 1/2" NPT access port on the 4" iron pipe bypass line. A stainless-steel check valve was put in place to prevent any backflow of natural gas from the bypass line to the hydrogen injection line. The hydrogen injection line is shown in Figure 8.

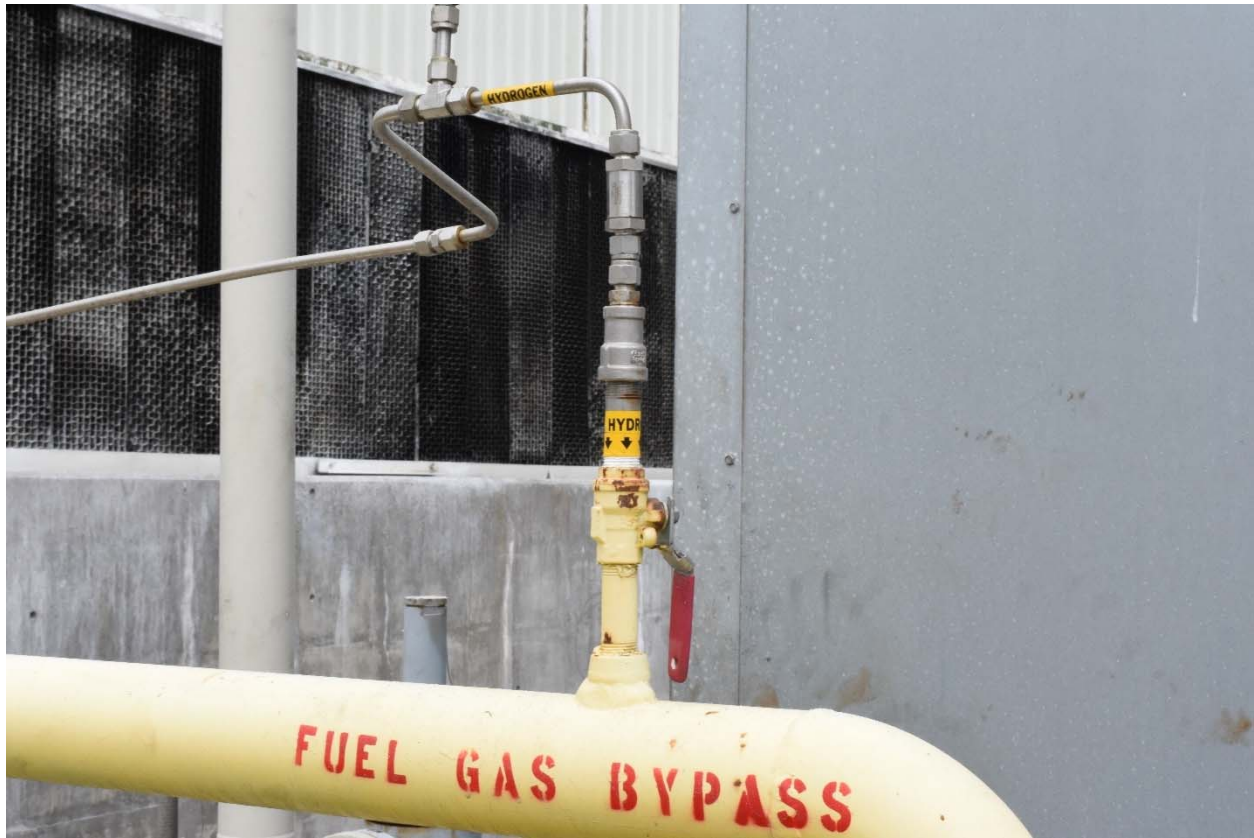


Figure 8. Hydrogen injection line at UCI Central Plant

The pressure of the natural gas delivered by Southern California Gas Company (SCG) to the Central Plant line varies as much as 20 barg up to 34.5 barg, though typically varies in a range between 26 to 27.5 barg. When the line pressure drops below 25 barg, which tends to occur when SCG refills their gas storage facilities in late summer, the external gas compressor kicks on, boosting the pressure to at least 30 barg.

4 Dynamic Operation of PEM Electrolyzer System (Objectives 2, 3, & 4)

4.1 Electrolyzer Steady State Operation & Benchmarking

For the first 1000 hours of operation at the demonstration site, the C10 electrolyzer system was operated at full throughput to establish baseline operation characteristics and performance. Total system power consumption, stack power consumption, and the production of hydrogen before and after the drying process was analyzed and compared at 100, 600, and 1000 hours of operation.

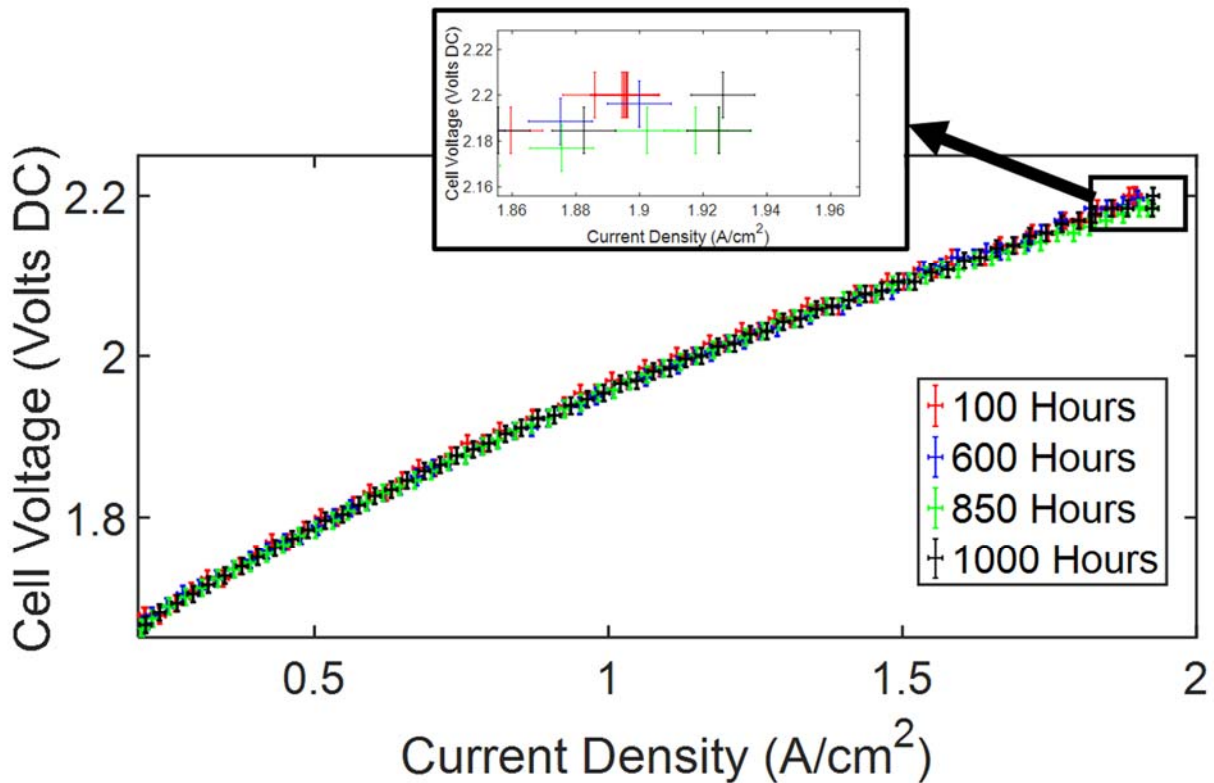


Figure 9. Start-up j - V curves during 'break-in' period with measurement error bars.

Figure 9 demonstrates the slight variations observed in the measured j - V values outside of the rated error of our current and voltage sensors, specifically current density. These curves were

generated at the same average feed water temperature and stack pressures, highlighting a ‘break-in’ period for stack performance that occurred within the first 800 hours. After 800 hours, a consistent maximum current density of approximately 1.93 A/cm^2 was established. At 600 hours of operation, the AC/DC power supply failed, and was replaced by the OEM with a new power supply. No immediate notable change in maximum current density and general j-V behavior was observed on replacement of the power supply, suggesting that the ‘break-in’ period was not related to the power supply and rather due to changes in the stack. In PEM electrolyzers, the membrane electrode assembly (MEA) typically undergoes an activation process immediately after manufacturing that can last anywhere from several hours to several days, resulting in progressively better cell performance that ultimately plateaus [65]. Generally, ‘break-in’ periods are more commonly observed in studies of high temperature proton exchange membranes for application in phosphoric acid fuel cells (PAFC) and direct methanol fuel cells (DMFC) [66] [67], but are not unheard of for PEM fuel cell MEAs [68] [69]. An increase in current density without an increase in applied potential is typical of these ‘break in’ or activation processes, which involve cycling of the cell [70].

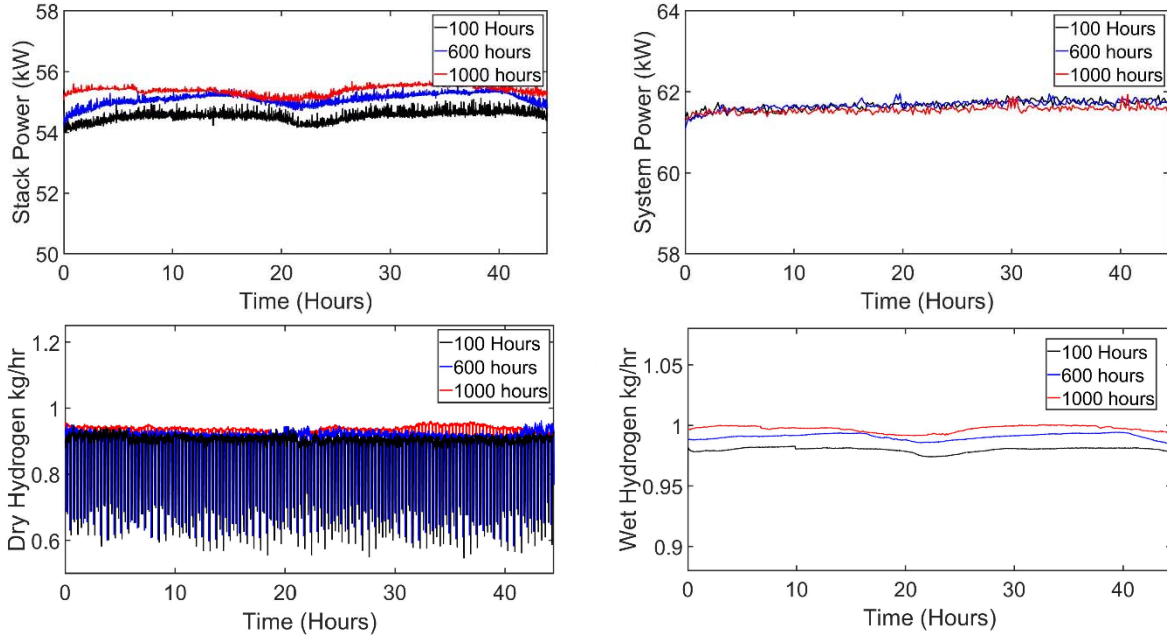


Figure 10. Stack power, system power, and hydrogen production pre- and post-drying process across different stages of steady state characterization of the electrolyzer system.

Figure 10 demonstrates the slight variation in system operation across the first 1000 hours of operation for three separate periods of continuous two-day operation. The constant dips observed in post-dryer hydrogen output is due to the swing-bed operation of the PSA dryer system, while a generally ‘unsteady’ flow rate is observed related to the pressure regulation manifold managing the hydrogen pressures on the system and ‘product’ (downstream of the electrolyzer) sides. Measured stack power consumption and dry hydrogen production increased over the test period as a direct result of the increase in maximum current density. Wet hydrogen production also increased, and is a quantity derived directly from measured stack current using the mol balance of electrons to hydrogen gas. The calculation is shown below in equation (1) where F is the Faraday constant, n is the number of cells in the stack, M_{H_2} is the molar mass of hydrogen, and

$\eta_{Faraday}$ is the Faradaic efficiency. Faradaic efficiency is the ratio of current that participates in the production of hydrogen to the total amount of current delivered to the stack. This quantity reflects the magnitude of parasitic losses in the stack, due to either leakage and crossover of species or short circuits. It is often assumed to have a value of 0.99 [45] [71], or ignored all together [43] [72]. In this case we neglected this loss term ($\eta_{Faraday} = 1$).

$$H_{2,Wet}[gram/sec] = \frac{I_{Stack}}{2F} nM_{H_2} \eta_{Faraday} \quad (1)$$

System level power consumption did not increase relative to the increases observed in stack power consumption and hydrogen output, resulting in an increasing improvement in system efficiency as the electrolyzer was exercised in these first 1000 hours of operation. A diurnal trend is apparent in stack power consumption as well as hydrogen production, and absent in system power consumption. The time of day at which the minimum and maximum of this trend occurs is midday and midnight respectively, meaning that system efficiency varies an observable amount with the time of day. The maximum system efficiency was typically observed near midnight and the minimum was observed near midday, most likely due to the ambient temperature variations associated with these times of day. Highest efficiency was correlated with lowest ambient temperature.

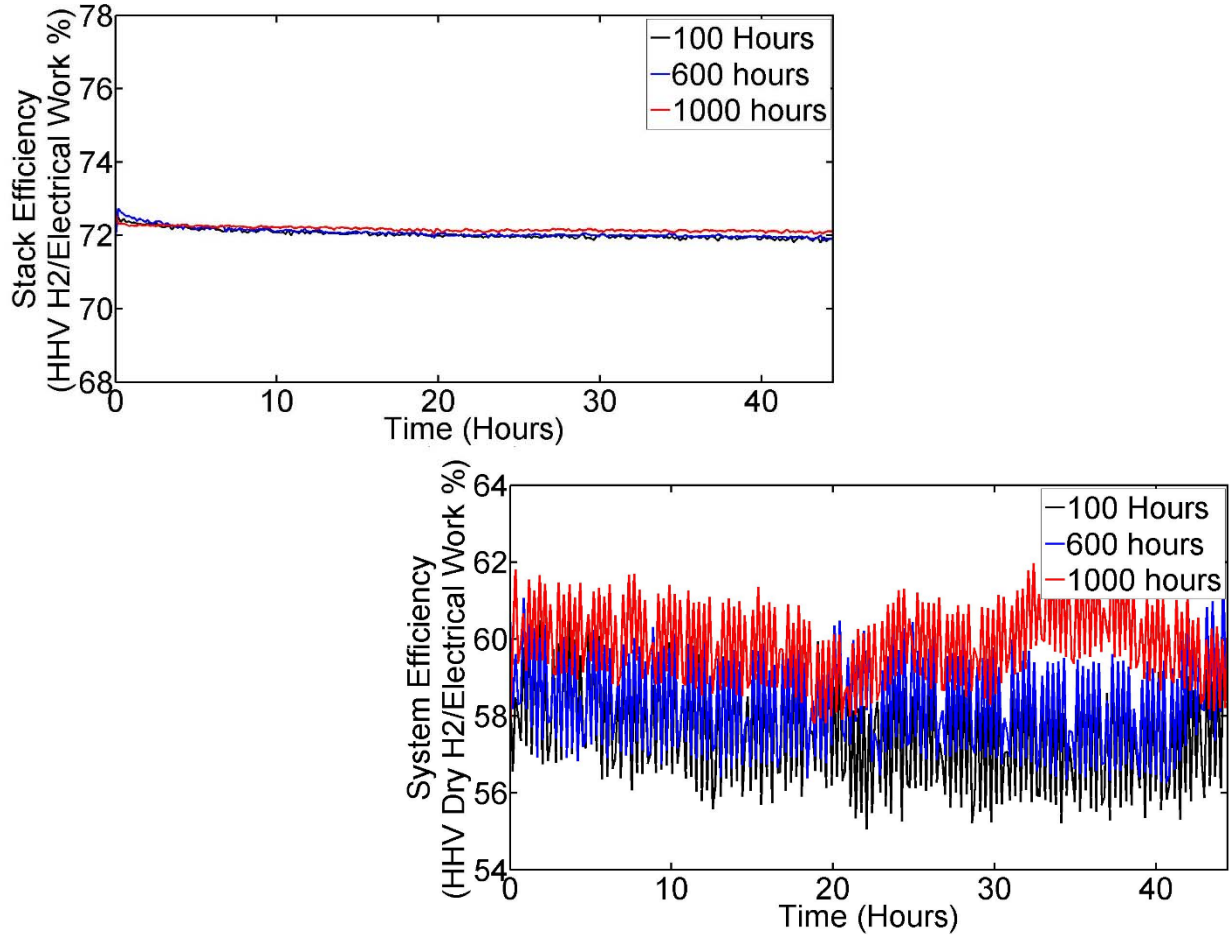


Figure 11. Comparison of stack & system efficiencies (HHV basis) across different stages of steady state characterization of the electrolyzer system.

The efficiency at the stack and system levels are shown in Figure 11 on a higher heating value (HHV) basis for hydrogen. These efficiencies are calculated as shown in equations (2) and (3) below.

$$\eta_{Stack} = \frac{HHV_{H2}[kJ/kg]H_{2,Wet}[g/s]}{Stack\ Power[kW]} \quad (2)$$

$$\eta_{System} = \frac{HHV_{H2}[kJ/kg]H_{2,Dry}[g/s]}{System\ Power[kW]} \quad (3)$$

Figure 11 indicates that both the stack and system level efficiency did improve over time. The spiking behavior in system efficiency is a result of the intermittent dry hydrogen flow due to dryer operation. The stack level efficiency did not demonstrate any of the diurnal trends associated with the stack power consumption, while the system efficiency did. This eliminates the cell stack as the source of this variation and points to a balance of plant component. Two major balance of plant components that can influence the system efficiency are the hydrogen dryer and the AC/DC power electronics. The performance of these systems for these runs are shown below in figures Figure 12 and Figure 13.

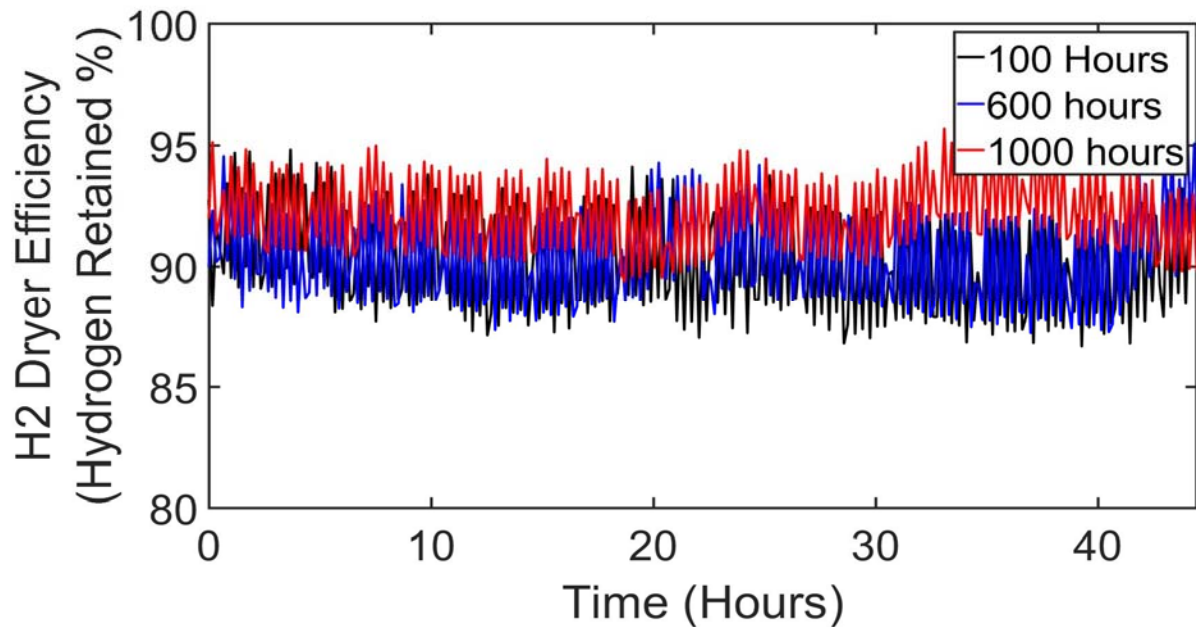


Figure 12. Hydrogen Dryer Efficiency across different stages of steady state characterization of the electrolyzer system.

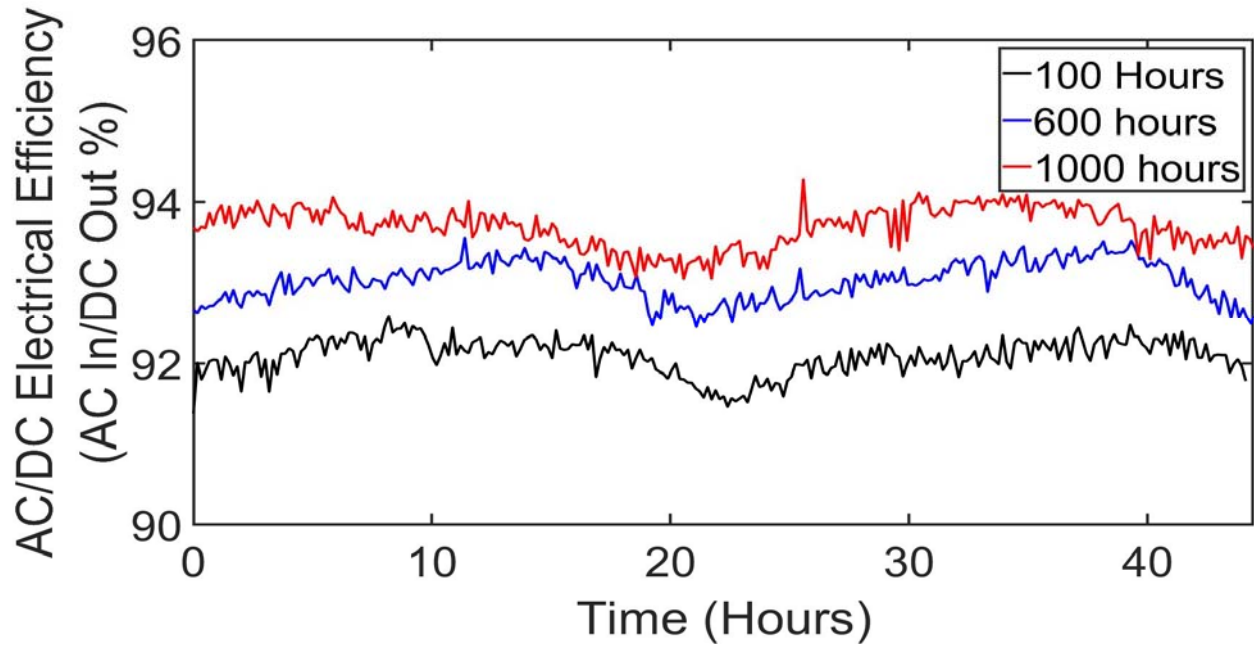


Figure 13. AC/DC power electronics efficiency across different stages of steady state characterization of the electrolyzer system.

Hydrogen dryer efficiency improved as maximum operating current increased. The diurnal trend in Figure 12 also correlates with the diurnal trend in current density and by extension, wet hydrogen output. Figure 13 shows a much clearer diurnal trend associated with AC/DC power electronics efficiency, correlating with the previously observed trends towards higher efficiencies around midnight, and lower efficiencies in the afternoon.

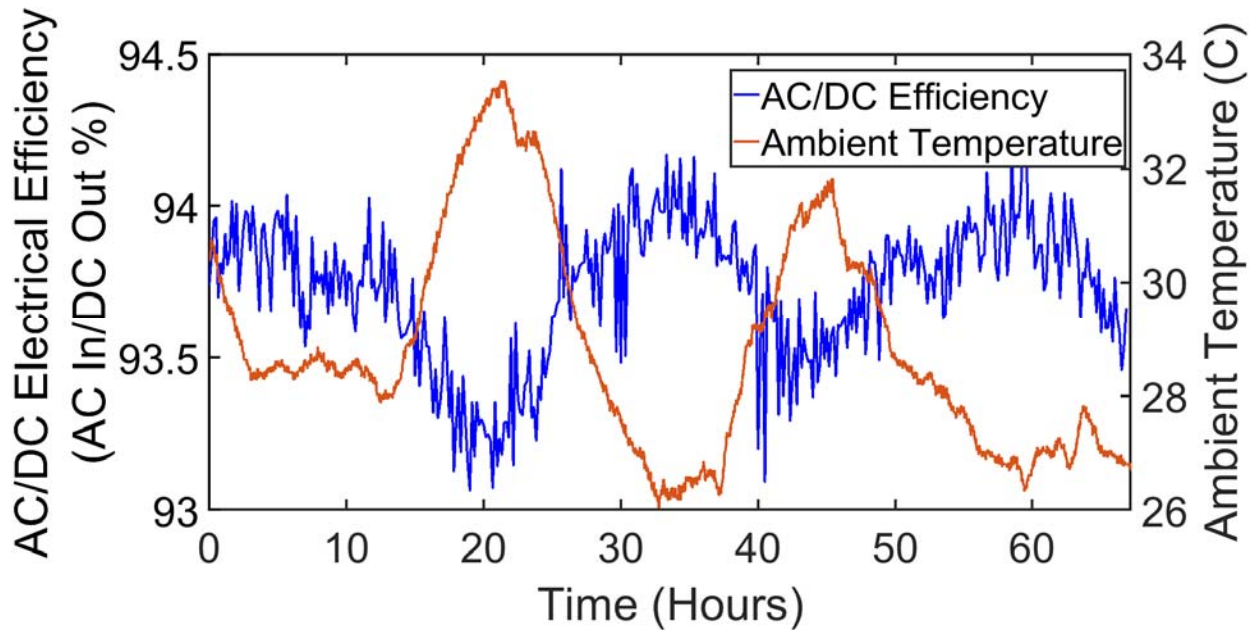


Figure 14. AC/DC power electronics efficiency and ambient temperature over two and a half days at full throughput.

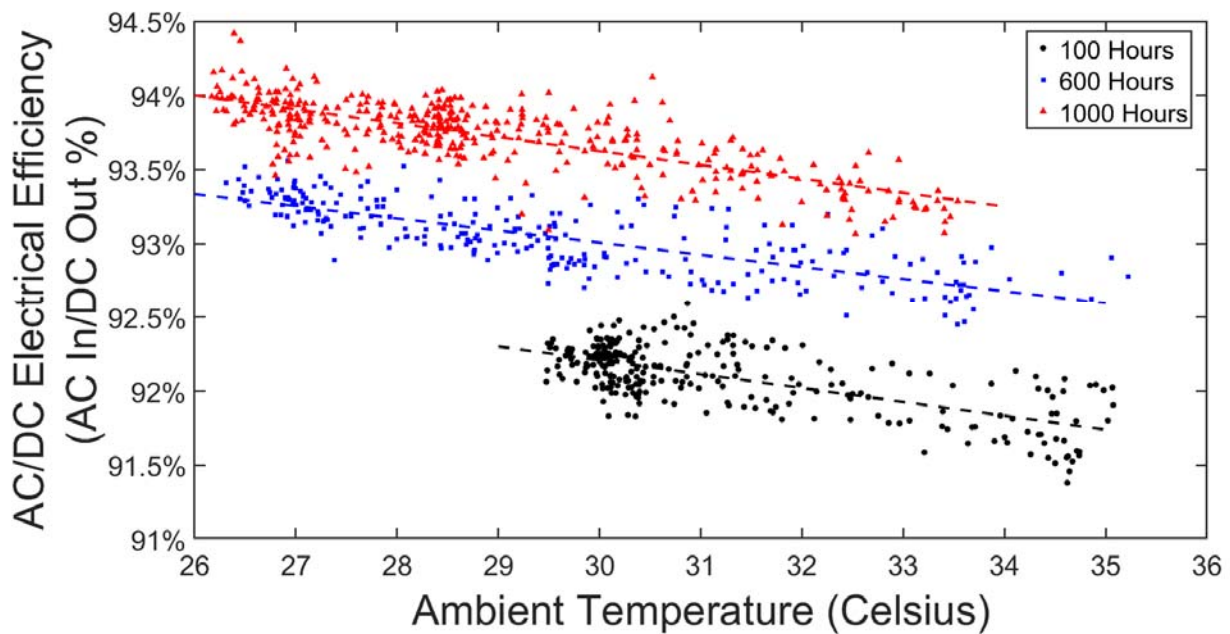


Figure 15. AC/DC power electronics efficiency vs. ambient temperature across the benchmarking test period.

The reoccurring diurnal trend points to a potential correlation in ambient temperatures and the efficiency of the AC/DC power electronics. The inverse correlation between ambient temperature and efficiency is shown above at the ~1000 hours of operation mark for a two and a half day run in Figure 14. The correlation with ambient temperature does not entirely account for the increased output from the AC/DC power electronics; Figure 15 shows a clear improvement in efficiency as test hours progressed for a given ambient temperature. The overall negative correlation in power electronics efficiency with ambient temperature still holds. This could be the result of power output derating, where the amount of power dissipation lost in the form of heat in AC/DC rectifier power supplies increases as ambient temperature increases [73] [74].

The correlation between AC/DC power supply efficiency and low ambient temperatures assists in explaining the variation in operating current observed post ‘break-in’ period of operation.

Across the first 800 hours of operation, a steady climb in DC current output to the stack was observed during this “break-in period.” For the remainder of the operation period (1000 - 4000 hours of operation), the maximum observed operating current for a given day of continuous operation varied within a consistent range (see Figure 16). The correlation between AC/DC power electronics and ambient temperature (Figure 15) holds as well for this variation in maximum stack current past the ‘break-in’ period (Figure 17).

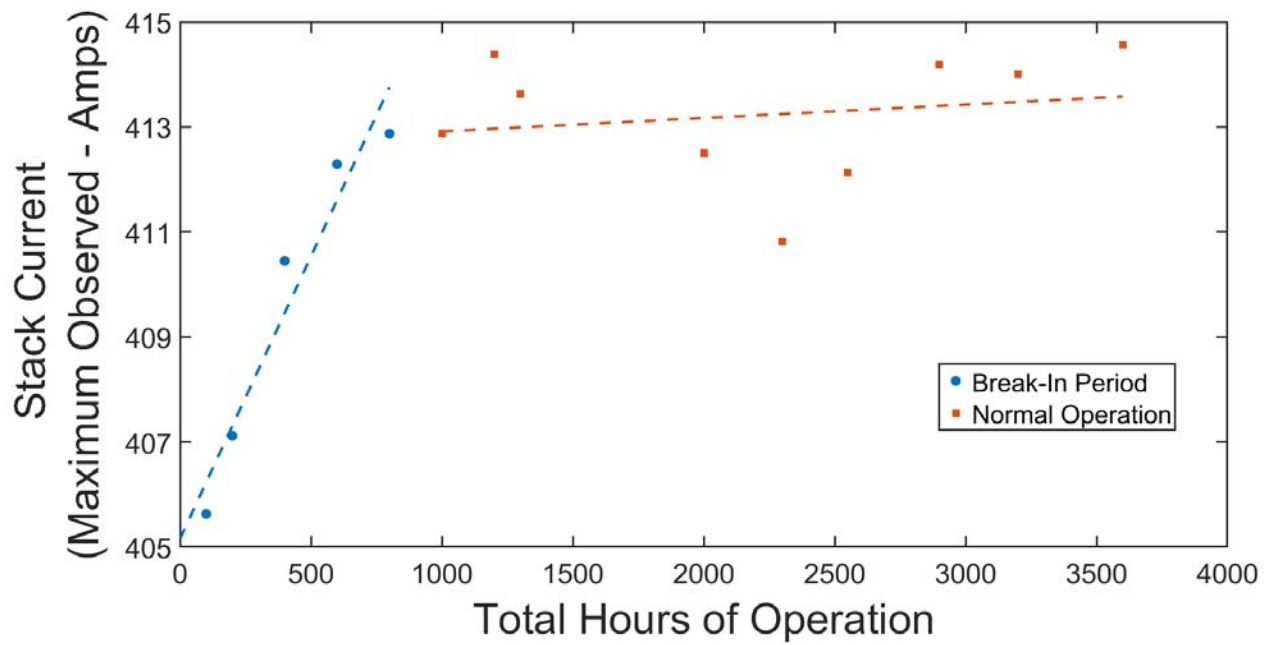


Figure 16. Maximum observed stack current on a given day versus net hours of operation on the electrolyzer system, break-in period observed in the first 800 hours.

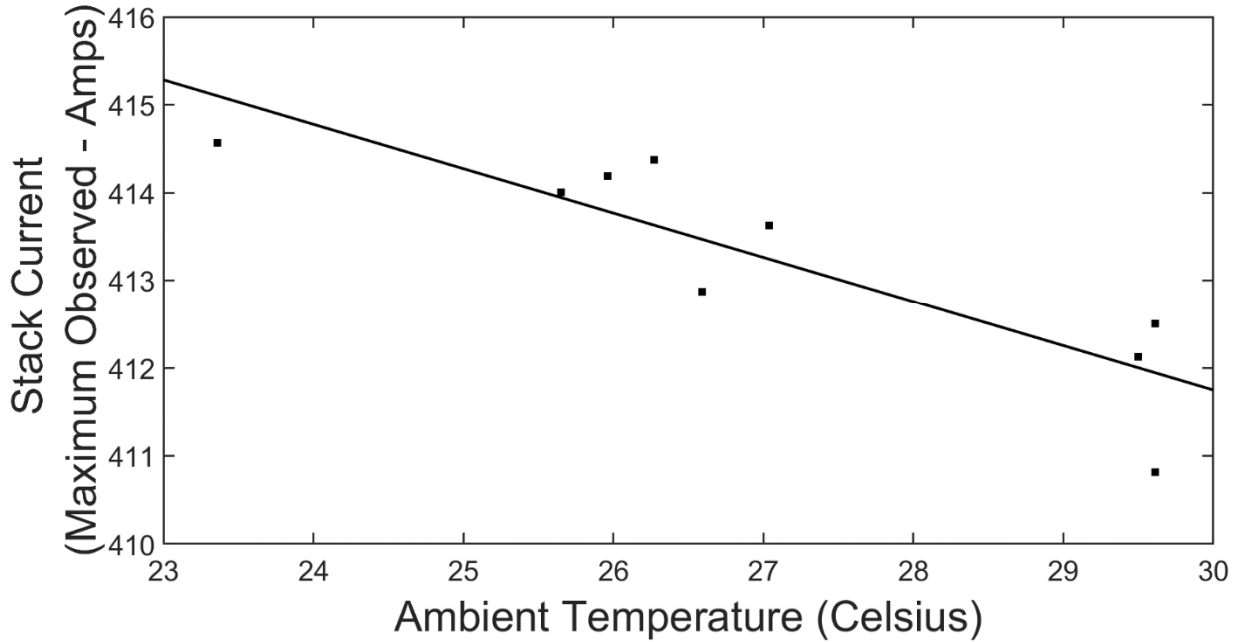


Figure 17. Maximum observed stack current on a given day versus ambient temperature for 'normal operation' data in Figure 16 (above).

The power consumption of the air-cooled chiller that provided the thermal management for the electrolyzer system was monitored for the duration of the benchmarking tests. The full power consumption of the electrolyzer system including the power demand of the chiller is shown below for the 100- and 600-hour operating cases. Figure 18 shows the energy ‘steps’ leading to the ultimate product of hydrogen gas, allowing insight into the relative magnitude of electrical energy loss. The 1000-hour case is not included as the power meter associated with the chiller failed around the ~800 operating hours mark. As the power consumption of the chiller was not of major interest to this study, the meter was not replaced.

The magnitude of energy consumption that goes to the chiller is more than twice the amount lost to the rest of the balance of plant, including power electronics. In terms of hydrogen production, a quarter of the electricity consumption is directed to the chiller system, equivalent to 17 kWh of electricity per kg of hydrogen produced.

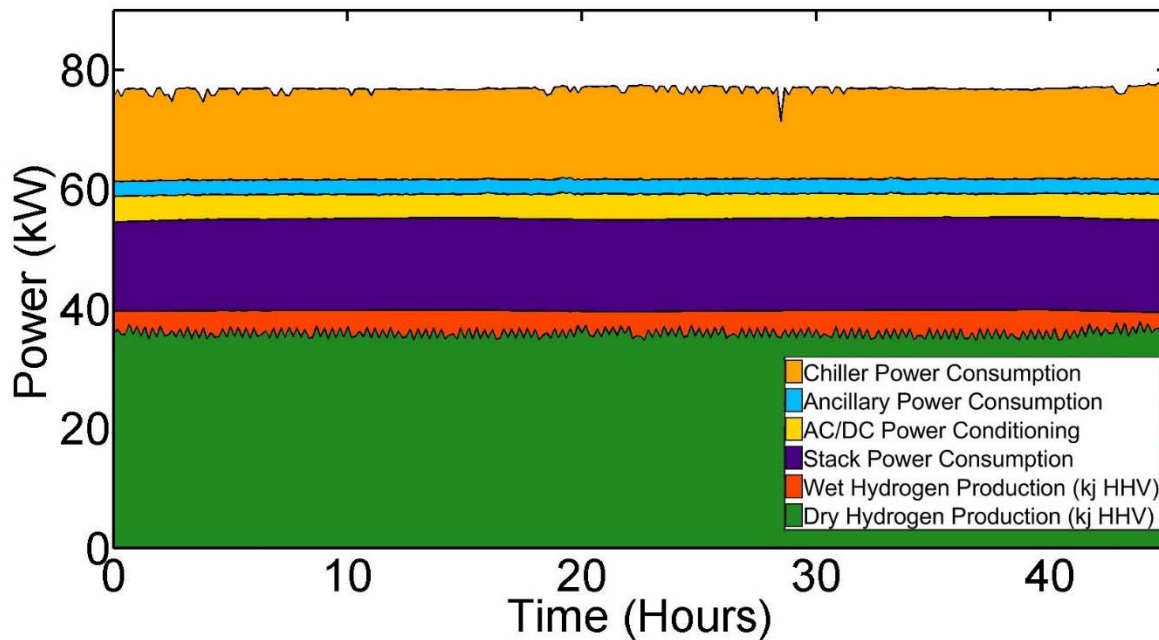
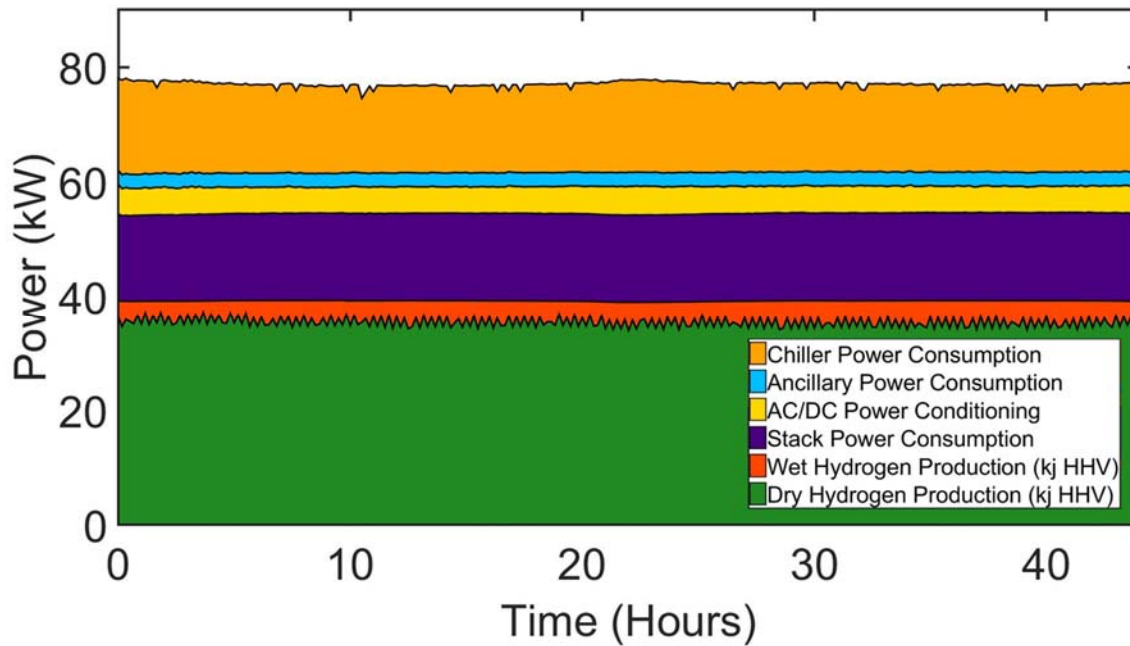


Figure 18. Energy consumption at the 100 hours of operation regime (Top) and 600 hours of operation regime (Bottom).

The rated water consumption is given as ‘roughly’ 2.4 gallons per hour at full output. For molar balance alone, the electrolysis reaction would consume 2.37 gallons per hour at the rated current

of 410 Amps. The OEM's rated water consumption does not seem to account for other sources of water loss. For widespread implementation of electrolyzer technology, it is important to consider the total water consumption of these systems.

The water consumption of the system at full throughput was determined by analyzing the fluctuations in water level in the A500 primary feed water tank over time. The A500 tank is not part of the recirculating DI water loop, and only intermittently fills to the A300 water tank that is part of the stack water loop. The A500 serves as a buffer tank that ensures the system always has an excess of DI water available. A float-based level switch system maintains the water level between two states, opening a feed water inlet valve when the level switch reaches an 'L1' level state and closing the valve once an 'L3' level state is reached.

Due to the intermittent nature of the transfer of DI water from the A500 buffer tank to the recirculating DI water loop, it is rare that the filling of the A500 tank coincides with the outflow of water from the A500. Using this fact, in conjunction with the dimensions of the A500 tank and the height change in water level going from L1 to L3, the amount of water added to the A500 tank during each fill event is determined as 9.85 gallons of DI water.

Using only the fill events where no other flows of water occurred, the average flow rate of water from the external DI water system to the A500 is found to be 1.602 gallons per minute. Using valve state data, net water consumption of the electrolyzer system (not including the chiller) was found for the 100-, 600-, and 1000- hours of operation for full throughput operation. Actual water consumption was approximately 3.1 gallons per hour for full throughput across all cases.

Table 1. Summary of full throughput benchmarking on electrolyzer system.

	Run 1 100 Hours	Run 2 600 Hours	Run 3 1000 Hours
Avg. H2 (kg/hr)	0.899	0.912	0.936
Avg. Current (Amps)	401.52	407.99	411.30
Avg. Water Consumption (Gal/hr)	3.095	3.031	3.116
Avg. Stack Power (kW)	54.54	55.09	55.38
Avg. System Power (kW)	61.67	61.68	61.56
H2 Dryer Efficiency (%)	90.85%	90.49%	92.24%
AC/DC Efficiency (%)	92.09%	93.03%	93.69%
Stack Efficiency (%HHV H2)	72.03%	72.06%	72.17%
System Efficiency (%HHV H2)	57.47%	58.25%	59.88%
System Efficiency w/ Chiller (%HHV H2)	45.99%	46.79%	N/A

Table 1 summarizes the results of key parameters for benchmarking the electrolyzer system performance and maximum load condition. Overall system performance increased as testing went on. The increase in current output from the AC/DC power electronics lead to a proportional increase in hydrogen output, improving efficiency across the board. Water consumption did not vary a significant amount. The values obtained provide a reference of expected system performance when operating as intended for a commercial electrolyzer system as opposed to the modified dispatch approach explored in the following sections.

4.2 Electrolyzer Sustained Part Load Performance Characterization

A step-wise ramp up and ramp down load profile was employed to study sustained part load performance. These tests held the hydrogen output at a fixed amount in one-hour intervals, establishing a steady-state part load condition in the electrolyzer system as it load follows the hydrogen ‘demand’ downstream, allowing for the characterization of the electrolyzer performance and the efficacy of the control scheme in modulating electrolyzer power consumption.

The control signal profile and system response in kg of hydrogen produced per hour, averaged over 15 second- and 10-minute intervals, is shown below in Figure 19. The dramatic swings in flow that are characteristic of the transfer of pressure from the active PSA dryer bed to the other are absent below the 0.6 kg/hr mark (65% of full output). The unsteady flow characteristic of the full throughput operation begins to appear at the 0.88 kg/hr output set point (95% of full output) but is not fully in effect until the 100% set point, when the flow controller is fully opened.

Observing the 10-minute averages for the measured flow rate, it is clear that the unsteady flow occurs as the average flow rate drops below the flow set point on the flow controller, with the

effect becoming more pronounced as the disparity increases.

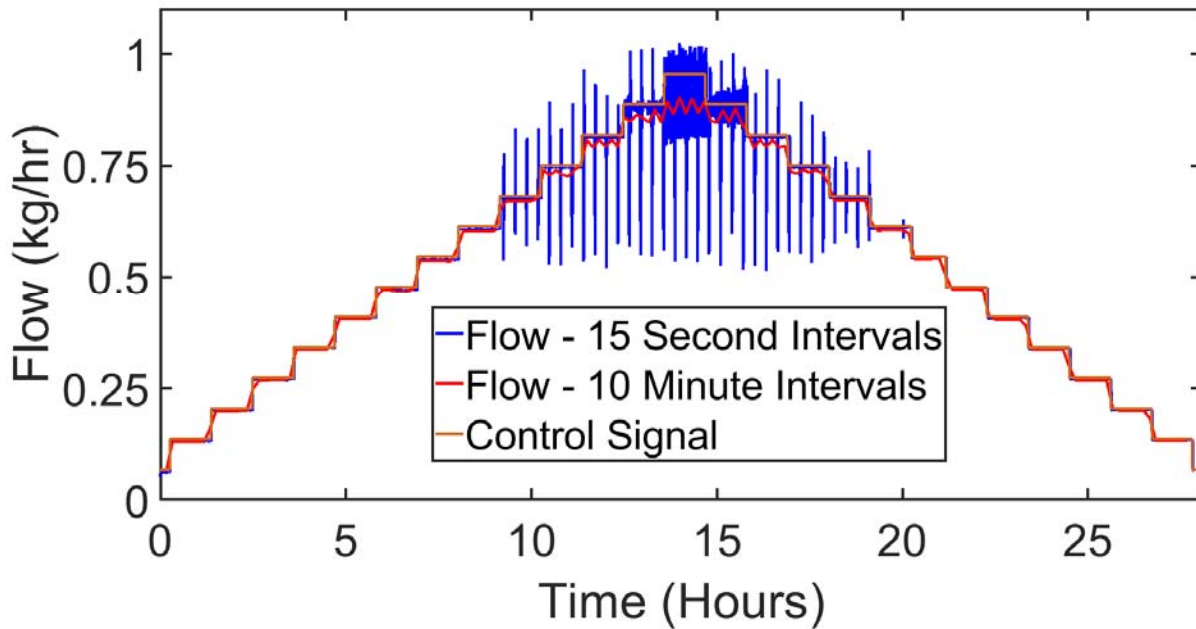


Figure 19. Step-wise ramp of electrolyzer system net hydrogen production vs. control signal.

Using again the relation from equation (1), and using a Faradaic efficiency of $\eta_{Faraday} = 1$, the expected output of ‘wet’ or total product hydrogen from the electrolysis process as a function of the measured current through the electrolyzer stack is shown below versus the control signal in Figure 20. The large spikes in current correspond to the switching of dryer beds in the PSA system and is present across all load conditions. This demonstrates that the timer-based dryer operation is not modified by the load condition of the electrolyzer as the hydrogen output does ramp up to pressurize the new bed and purge the bed being regenerated. The constant unsteady current can be explained as the response to the choked downstream flow condition as the pressure-based controls attempt to keep the hydrogen production pressure higher than the downstream pressure.

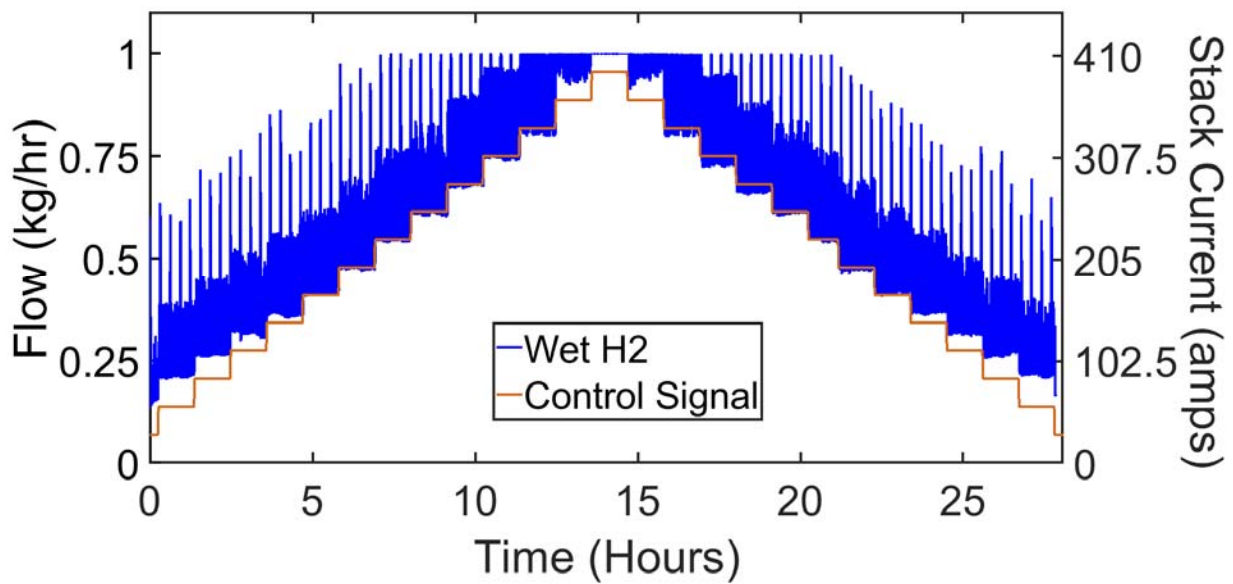


Figure 20. Calculated wet hydrogen gas output from measured stack current versus stepwise mass flow controller control signal.

Of particular interest is the efficacy of the mass flow controller in controlling the system power consumption. Ultimately, the ability of the electrolyzer system to load-follow variable renewable energy resources on a minute-to-minute time scale is key to its implementation in a power-to-gas system. In the future, the ability for these systems to participate in demand response on a second-to-second time scale, and potentially even in the time scale of milliseconds for frequency regulation, could become attractive depending upon the emergence of pricing mechanisms that value such services. Certainly the power electronics for inversion and conversion of the electricity, which are very similar to those of photovoltaic and battery systems, are capable of providing such responses with proper design.

Figure 21 shows the response in system power consumption versus the expected power consumption for the given mass flow controller set point. The set point in terms of power consumption was calculated by taking a 1:1 ratio between full scale hydrogen output and full-

scale power consumption assessed in the benchmarking phase of testing. For general load following, the system power consumption on ten-minute intervals shows that the power consumption is converging to the expected set point at power consumption load factors of 50% and greater, although generally the power consumption is higher than expected. The current cycling observed in Figure 20 has a visible impact on the power consumption response, causing an undesirable power consumption profile on the two-minute time scale.

Using the benchmarked values for maximum hydrogen output, stack current, and system power consumption, the percentage of maximum output (% load condition) that was observed is shown below in Figure 22. Fairly precise control of hydrogen output was achieved across most load conditions, while system power consumption follows the desired step-wise trend albeit in an unsteady fashion. The unsteady power consumption is a direct result of the stack current controls responding to the downstream flow controller.

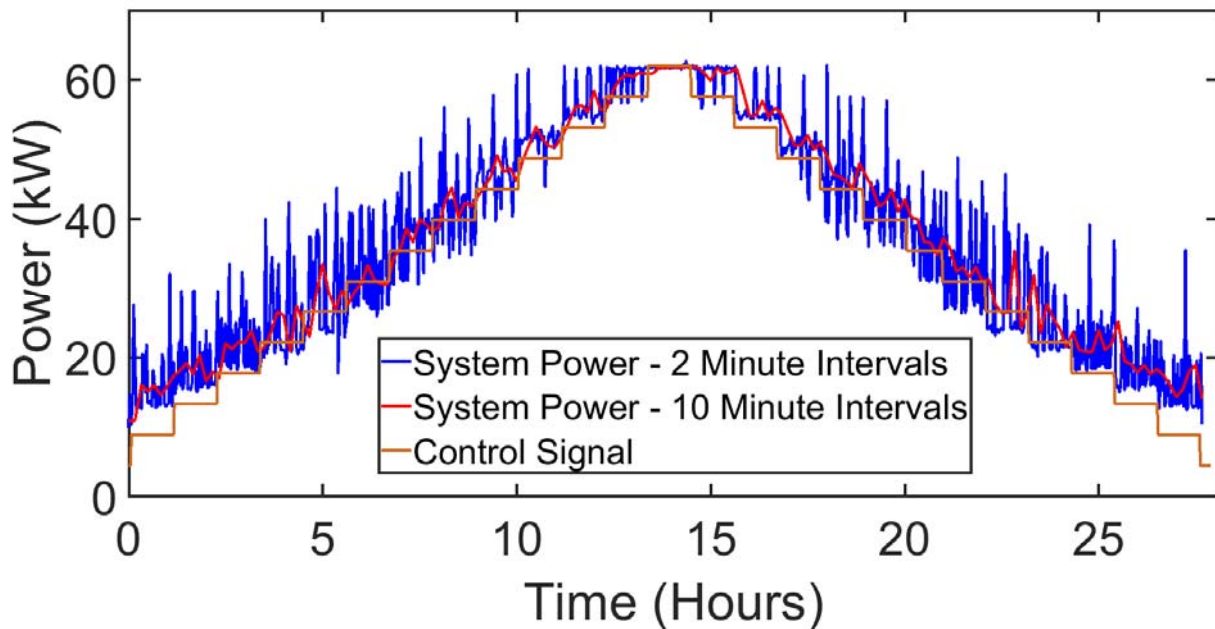


Figure 21. Electrolyzer system power consumption versus control signal of expected power consumption set point for step-wise ramp.

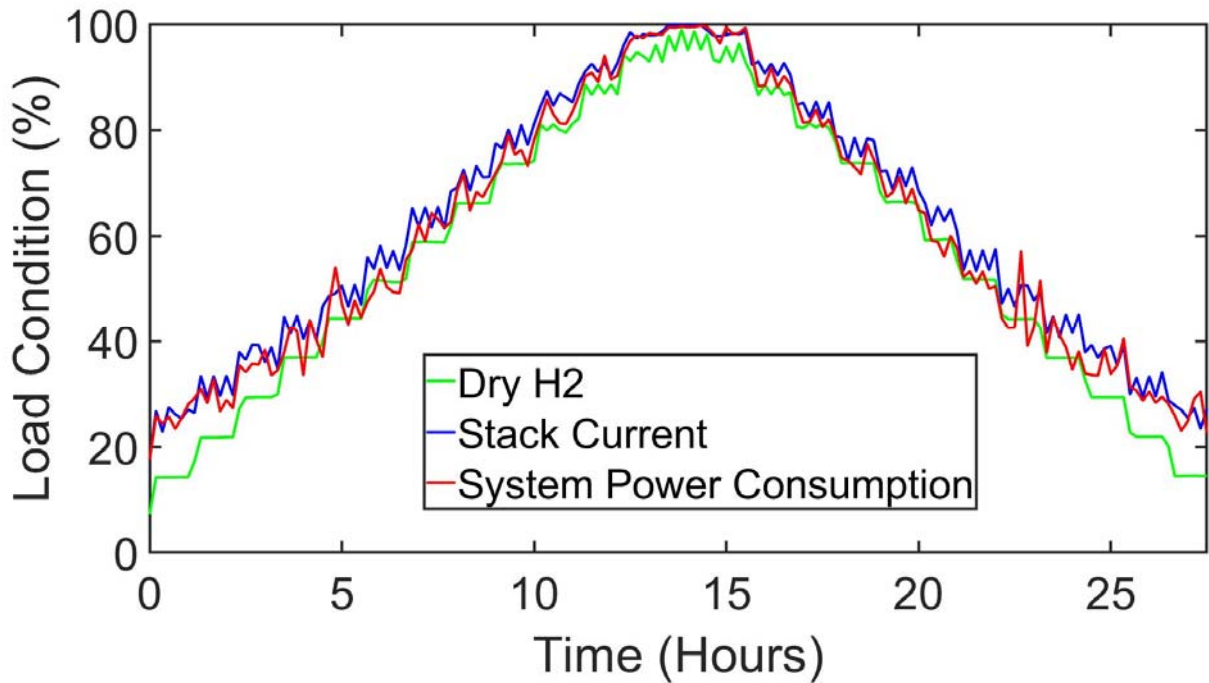


Figure 22. Percentage part load condition of dry hydrogen output, stack current, and system power consumption.

The efficacy of the mass flow controller in dispatching the system in a load following manner was assessed during the sustained part load testing. Figure 23 outlines response in system power consumption as a function of flow controller control signal. The flow controller results in a linear response in system power consumption on average, with a non-linearity occurring from the 0.41 to 0.48 kg/hr H₂ set point. This non-linearity characterizes when the electrolyzer system begins to see higher pressures downstream (choking from the flow controller) than the system pressure. Additionally, the actual power consumption still varied appreciably from the average by a few kW, and the full range of observed power consumption is very large due to the erratic stack current ramping.

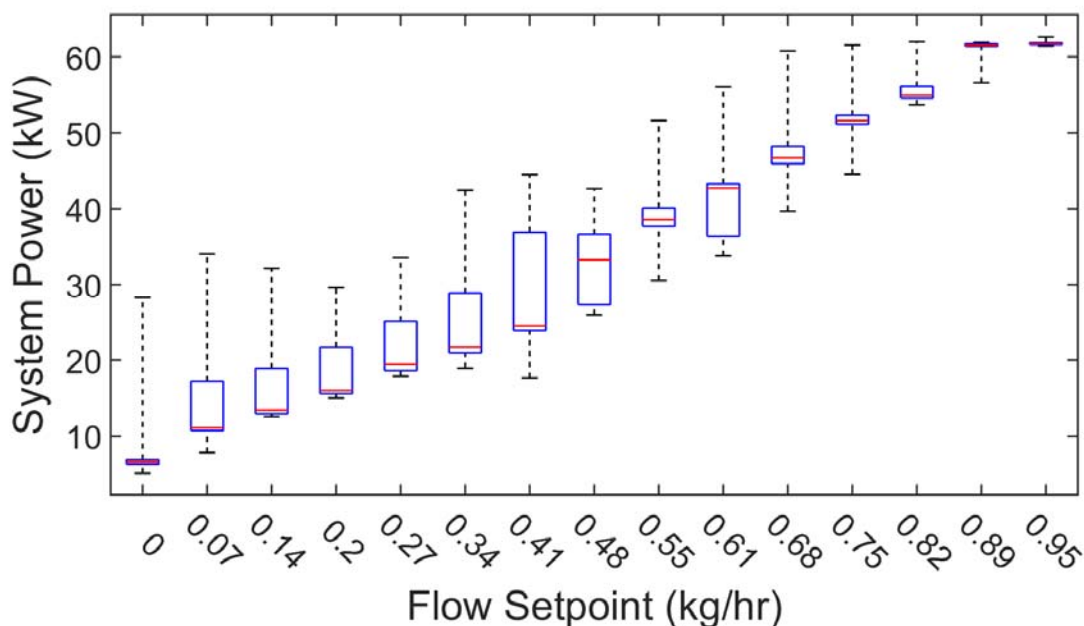


Figure 23. Box plot of system power consumption dispatch versus flow controller signal. Red bars show the average value, with 95% confidence intervals in blue, and the entire range of observed responses in black.

The current and voltage behavior of the cell stack during the test is displayed in a j-V plot (Figure 24). Variations observed in cell voltage response to the stack current consumption can be correlated to the stack temperature, measured in the recirculating DI water feed on the exit side of the stack. Lower variation in temperature from the set point (55 °C) is observed as current density goes down, due to the direct reduction in joule heating.

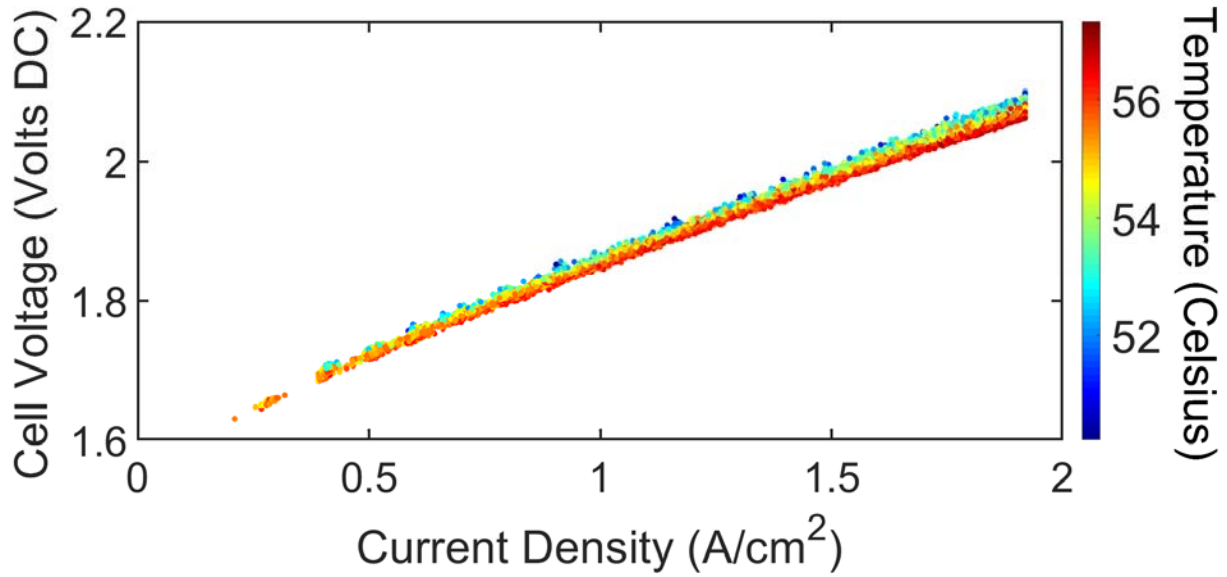


Figure 24. j-V curve generated from step-wise ramp sustained part load operation with temperature correlation.

The net efficiency at the stack and system level for each load condition (from this point on to be taken as % of maximum system power consumption, rather than hydrogen production or stack current) is presented below in Figure 25, according to the net energy consumption and net hydrogen production for each one hour period. As expected, the stack efficiency, the efficiency of the electrolysis process itself, improves at lower load conditions. System efficiency remains relatively constant until roughly 40% of maximum power consumption (24.8 kW_{el}), below 40% the system efficiency falls off quickly.

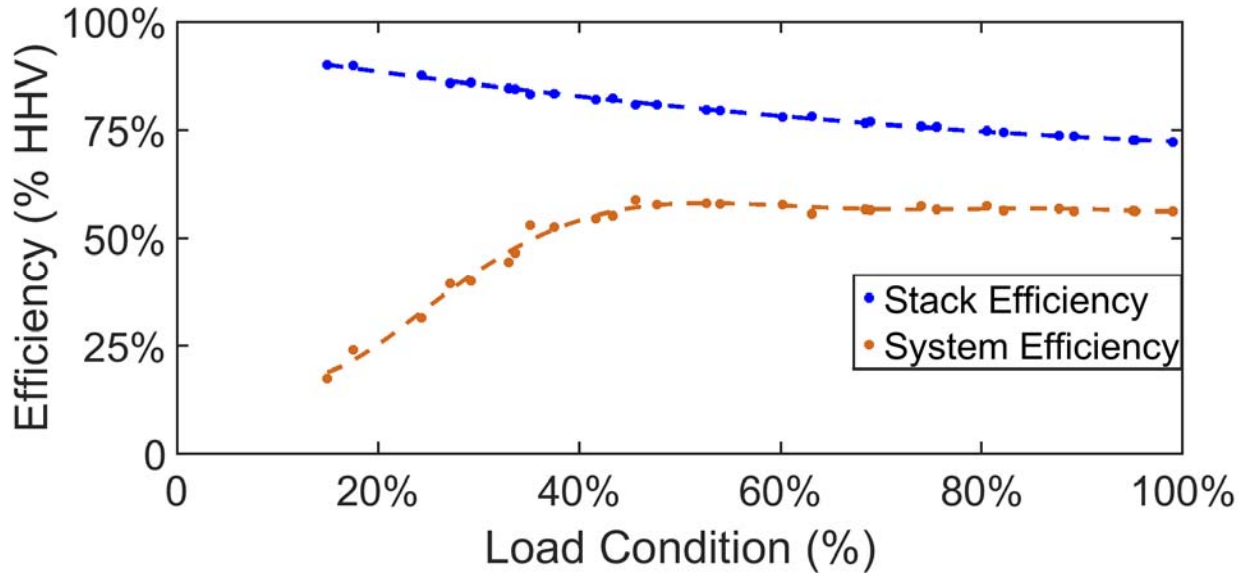


Figure 25. 1-hour system and stack efficiencies for sustained part load operation.

Ancillary power demand to mechanical balance of plant does not vary with lower load conditions. System efficiency does decrease with load condition due in part to this constant balance of plant demand. The flat trend down to 40% load condition is partially a result of the increasing electrolysis efficiency trading off with the increasing share of power going to the constant balance of plant load. Figure 26 shows the behavior of the ancillary power consumption.

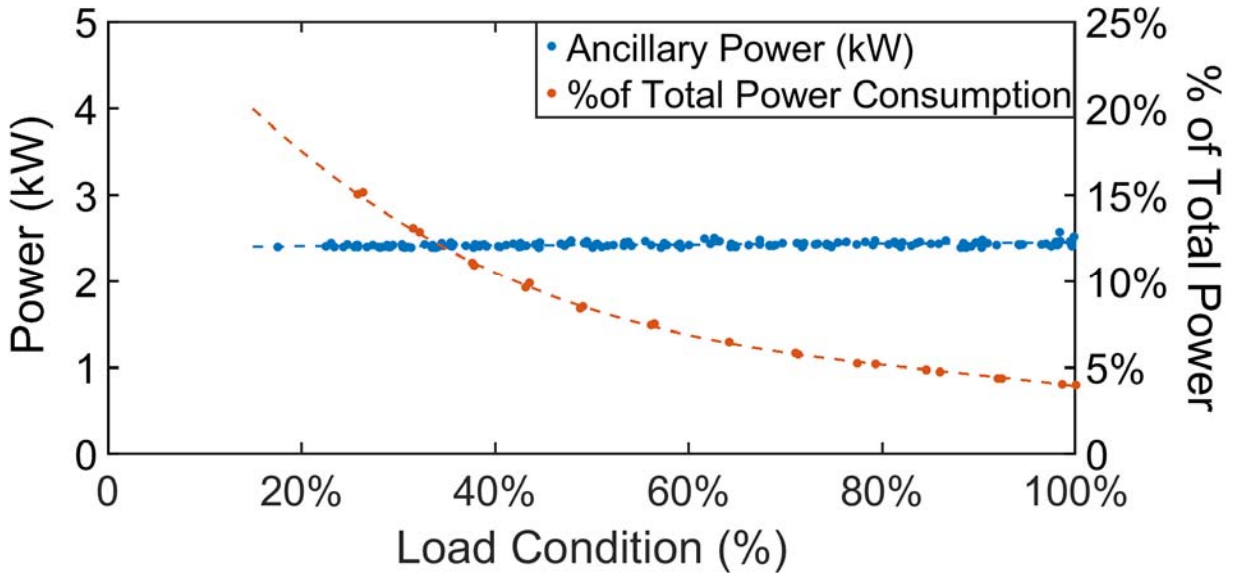


Figure 26. Ancillary power consumption in kilowatts and as a % share of total power consumption vs. sustained part load conditions.

The difference in measured hydrogen production versus the total, or ‘wet’ hydrogen production from equation (1), slowly increases in magnitude up to the 40% load condition and then climbs dramatically. This trend, shown below in Figure 27, explains the sharp drop-off in system efficiency at the 40% and below load conditions. This trend suggests that either the assumption of a efficiency of 1 is invalid, especially at lower current densities, or that the hydrogen dryers operate less efficiently at lower hydrogen throughputs, or some combination of the two. As the electrolyzer system idles at roughly 18%-part load condition (zero hydrogen output), the hydrogen loss trend with load condition shown below would continue the sharp up trend up to the 18% load condition regime. Similarly, system efficiency would effectively drop to zero at that point.

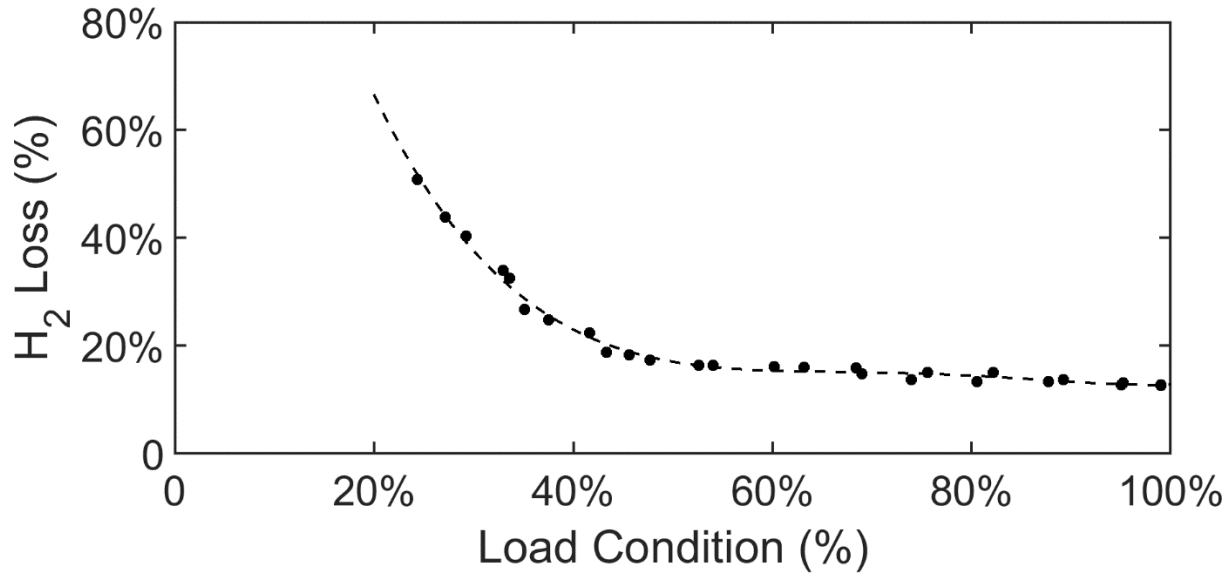


Figure 27. Percentage of measured hydrogen flow post-dryer to expected hydrogen output from electrolysis vs. sustained part load condition.

The efficiency of the AC/DC power electronics remains on average around 92-94%, regardless of load condition (Figure 28). Increasingly low load conditions lead to increasingly inconsistent performance from the AC/DC power electronics. This might have been due to the erratic stack current behavior observed at the lower part load conditions (Figure 20) but can be better explained as due to the step-wise nature of the test. The load condition points at higher loads were recorded at times closer to one another, and as such the ambient temperatures were relatively even for those data points. As previously established in the benchmarking tests, ambient temperature is the best predictor for the performance of the electrolyzer system AC/DC power electronics at full throughput. Additionally, the higher efficiency lower part load condition points occurred on the ramp up. The ramp up occurred in late afternoon to nighttime hours with lower ambient temperatures relative to the ramp up, which took place from mid-morning to early

afternoon. This reinforces the trend of improved performance at lower ambient temperatures for the AC/DC power electronics established in the benchmarking tests.

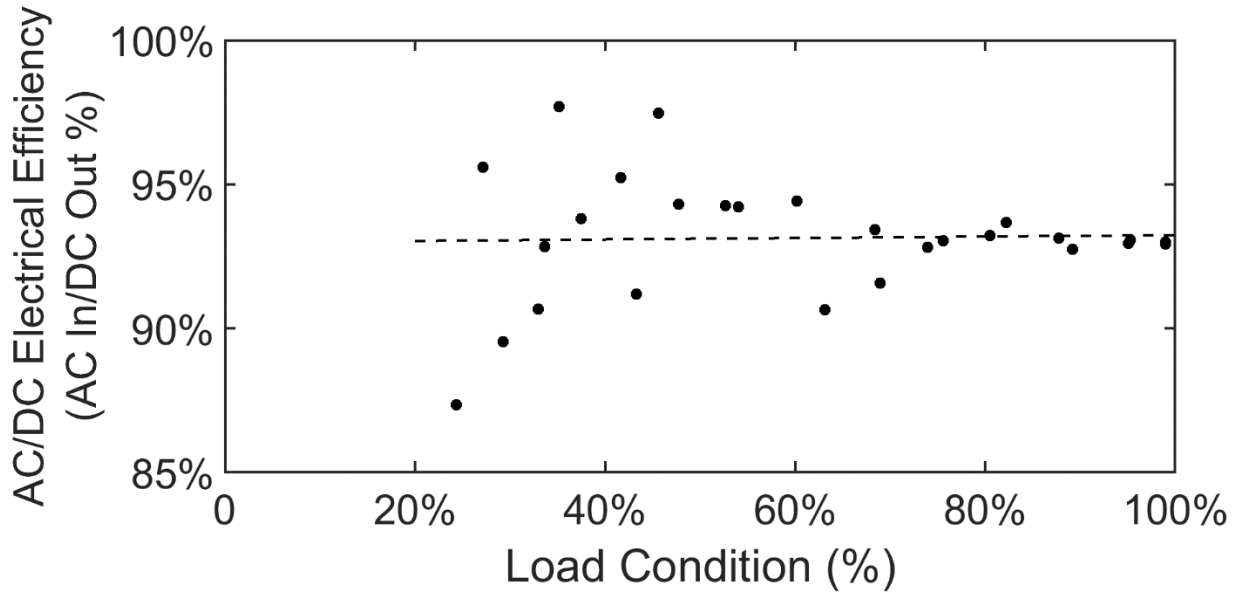


Figure 28. Efficiency of AC/DC power electronics vs. sustained part load condition.

The net effect of these energy losses across the system across the different sustained load conditions is summarized below in Figure 29. The constant ancillary power demand, system power consumption in the figure below, takes a larger portion of the total energy throughput at lower loads. The AC/DC power electronics performed better on the ramp up due to the lower ambient temperatures at the time relative to the ramp down. Stack power consumption relative to the wet, expected hydrogen production as well as the measured dry hydrogen production decreases in proportion at lower loads due to the increasing efficiency of the electrolysis process at lower throughput. The visibly fixed difference in wet hydrogen and dry hydrogen production suggests that the dryer system could be venting a fixed amount of hydrogen gas, leading to the increasingly large percentage of hydrogen loss observed in Figure 27.

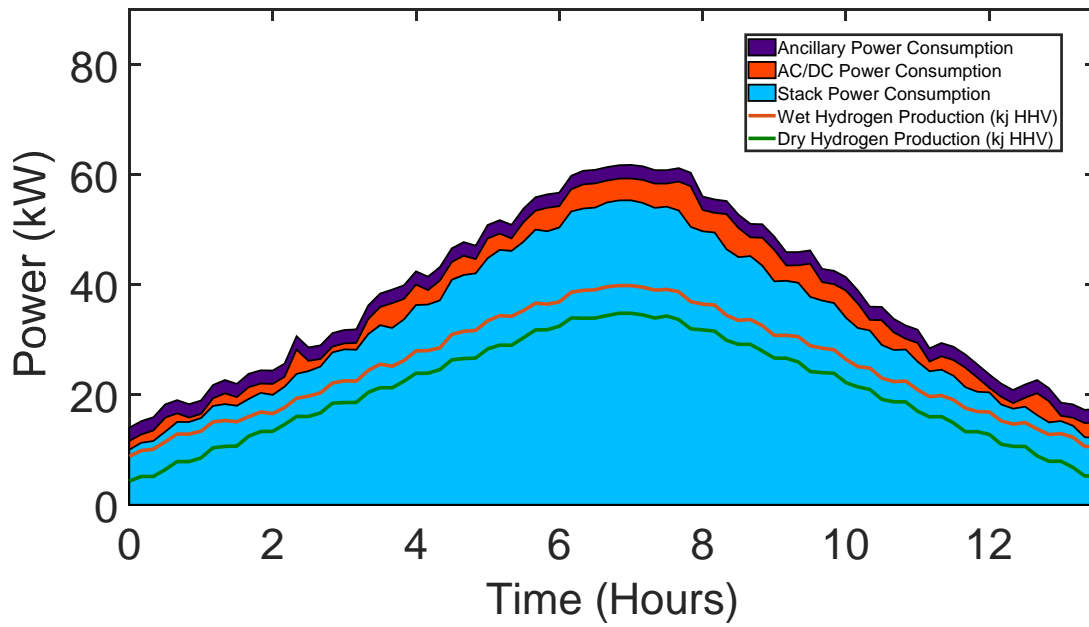


Figure 29. Electrolyzer system energy consumption across different levels of part load condition.

4.3 VRES Load Following – Solar Photovoltaic Array

Figure 30 displays the historical generation data from the MSTB photovoltaic array utilized in the electrolyzer solar load following tests concerning the seasonal variations in output from a solar PV resource.

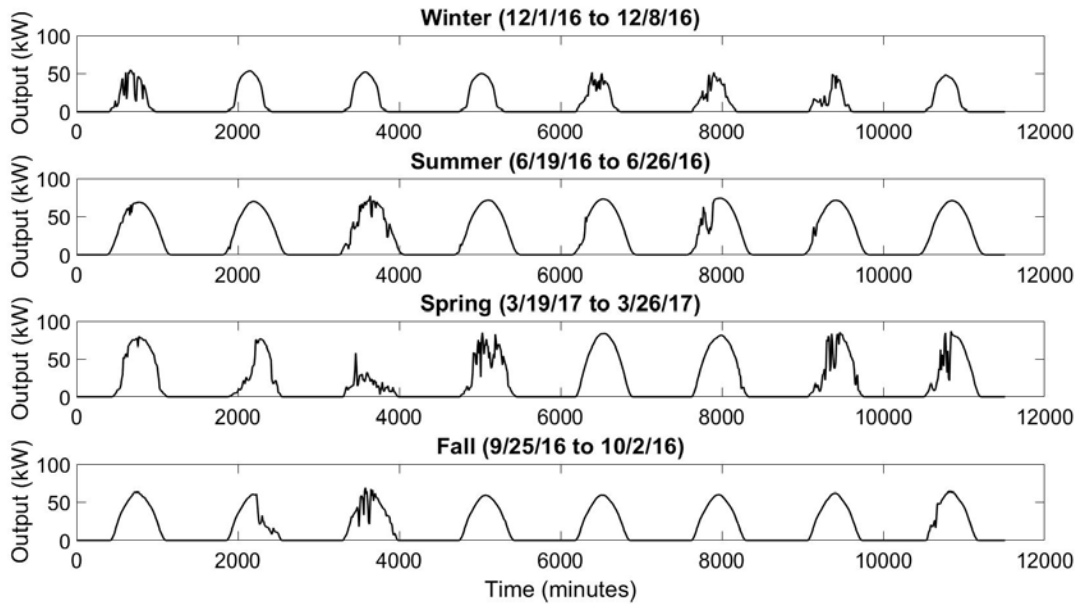


Figure 30. MSTB Rooftop Solar Photovoltaic Array Output – Seasonal Variation

The selected solar profiles demonstrate many of the expected changes in output of a fixed solar photovoltaic system due to seasonal and weather variations in the southern California region. The highest capacity factors of the system are experienced in the summer and spring, the lowest in the winter. Greater intermittency is experienced in the spring and winter when weather events such as rain and cloud cover are more common. The highest peak outputs are observed in the spring, due to the confluence of high solar irradiation giving greater throughput with lower ambient temperatures resulting in a higher PV module efficiency. Figure 31 highlights this season to season variation for clear days exhibiting the typical diurnal solar generation patterns.

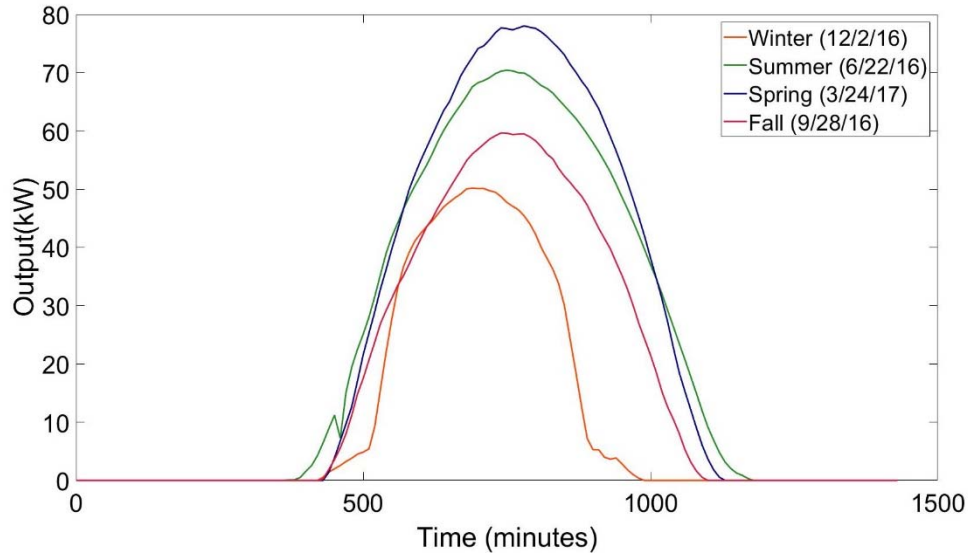


Figure 31. Seasonal differences in output from MSTB solar PV array for relatively ‘clear’ days.

For purposes of expedience, solar ‘downtime’ (ie; nighttime) was cut from the control signal sent to the electrolyzer system for these tests. The winter and spring PV cases were the first two solar PV load following runs accomplished and were accomplished successively. These two cases provide the two ‘extremes’ for comparison in capacity factor and transient weather effects.

Figure 32 and Figure 33 below show the hydrogen output response and the system power consumption for the two runs respectively. In both cases the hydrogen flow controller was able to follow the dynamics effectively (Figure 32). From the system power consumption perspective, there were two points in the spring case where the extreme transience in the control signal was not effectively matched by the system (Figure 33). This occurred on each occasion on a down-

ramp event, specifically for a local minima or ‘valley’. In each case electrolyzer system did not reduce its power consumption low enough to match the signal.

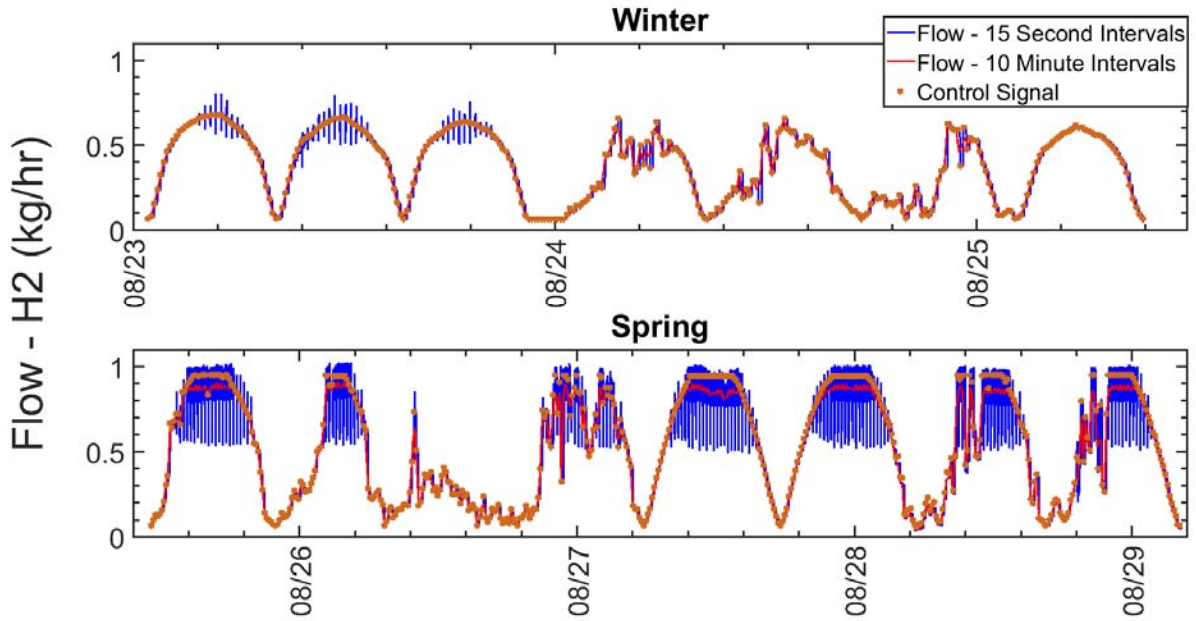


Figure 32. Hydrogen flow control signal vs. hydrogen flow output for winter (top) and spring (bottom) solar PV load following test.

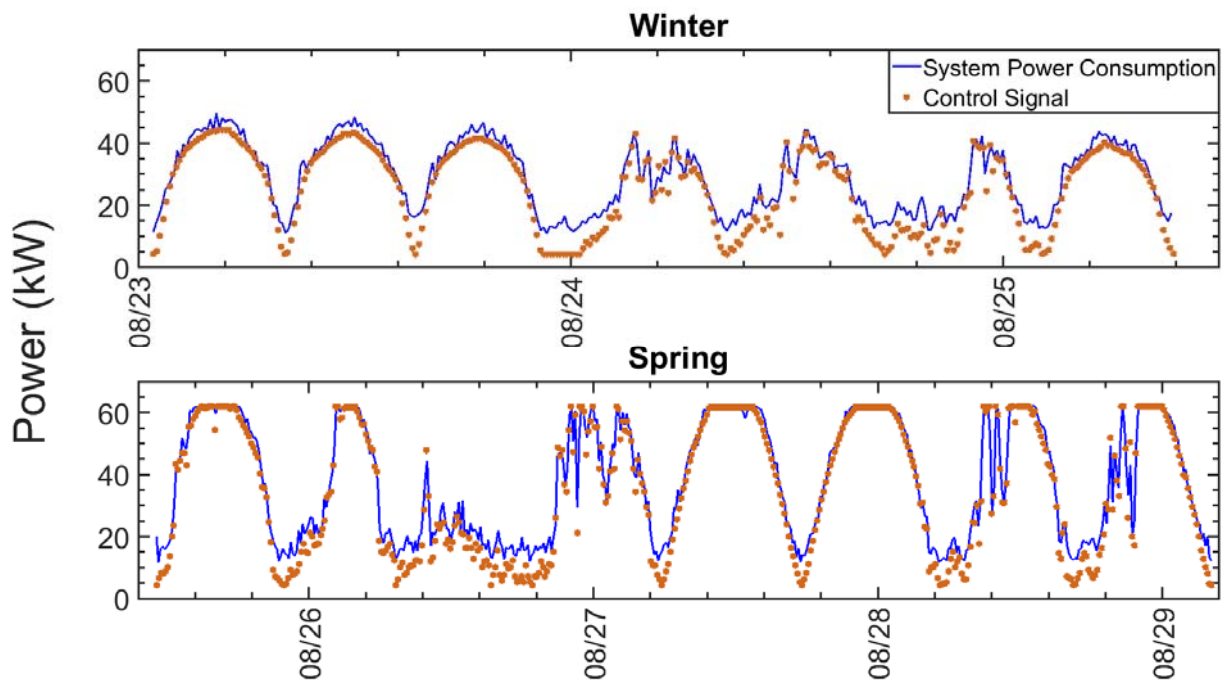


Figure 33. System power consumption control signal vs. measured power consumption for winter (top) and spring (bottom) solar PV load following test.

Both the summer and fall PV load following cases ran into issues that made them incomplete to an extent. The results of the most successful runs for these two cases still provided valuable information for the load following studies and are included below. The fall solar PV load following case was accomplished two weeks following the winter and spring cases. Testing was interrupted by drift in the valve spring tension on the mass flow controller, requiring disassembly and multiple readjustments of the spring tension. As a result of these adjustments, the fall run was a ‘special case’ in terms of the minimum load conditions that could be reached. The upside of this was an overall increased range in hydrogen output and power consumption, which reached minimums of 0.029 kg/hr and 6.6 kW respectively. The downside of this was lower reliability, as operation at lower and lower hydrogen flow rates led to an increased risk of the valve closing entirely.

One of these zero flow events did occur in the fall run (Figure 34), resulting in an increasingly dramatic departure from the load following signal. The valve does not open again with increasing flow signals until the electrolyzer starts sending the appropriate hydrogen flow through the pressure regulation manifold, which may not readily occur in the event of low-pressure differential from the flow controller outlet to the natural gas injection point. An integration of the flow controller into the electrolyzer system controls could easily circumvent this issue, but due to the ‘external’ control approach employed here, the flow controller required regular and careful adjustment to avoid these events.

The fall season did encounter some transients that proved challenging from a power consumption control perspective, similar to what was observed in the spring case, but to a lesser extreme.

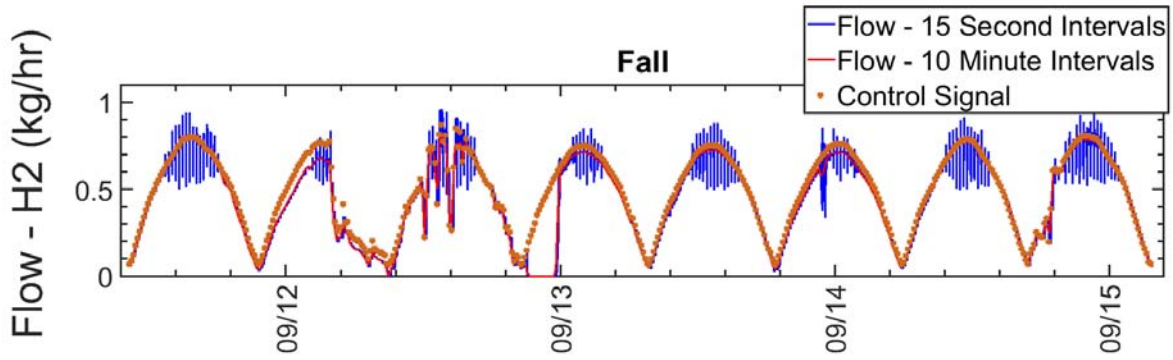


Figure 34. Hydrogen flow control signal vs. hydrogen flow output for fall solar PV load following test.

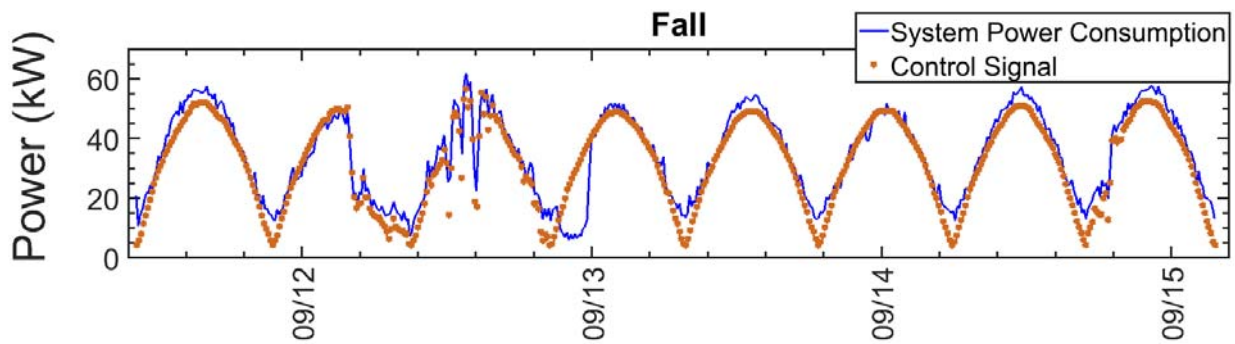


Figure 35. System power consumption control signal vs. measured power consumption for fall solar PV load following test.

The summer PV load following was completed successfully but was broken up into three parts due to similar flow controller issues experienced during the fall solar PV load following test. The flow controller valve assembly was rebuilt with a new valve spring and adjustment screw on October 15, 2017 and flow controller issues were largely taken care of, except for some initial re-adjustments.

Flow and system power consumption response for the summer case is displayed below in figures Figure 36 and Figure 37. For the most part, the transients in load following in summer are relatively smooth.

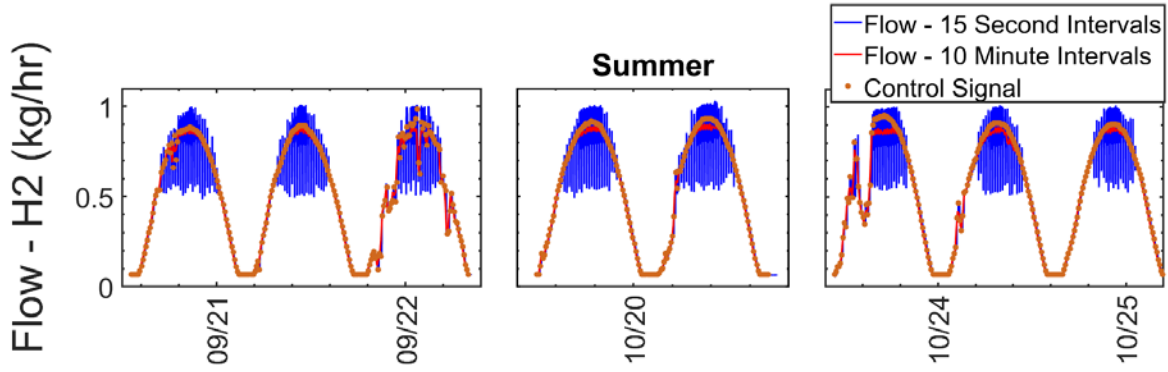


Figure 36. Hydrogen flow control signal vs. hydrogen flow output for summer solar PV load following test.

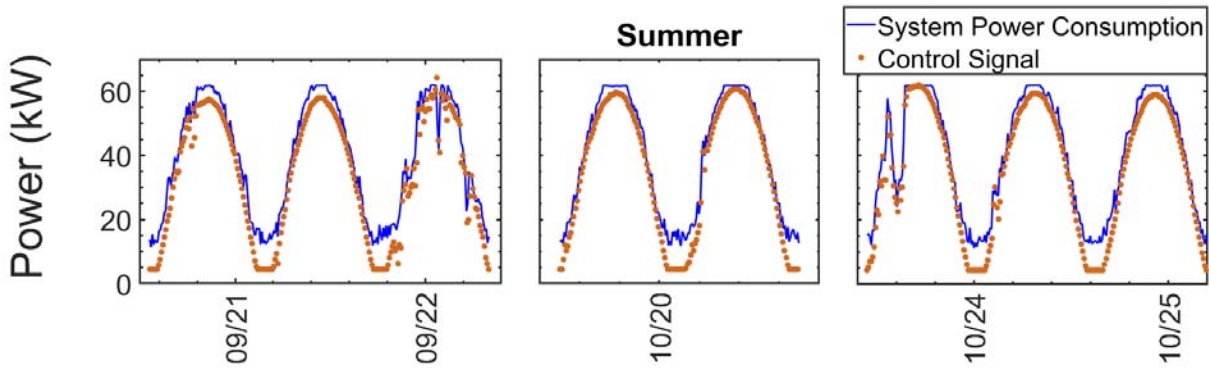


Figure 37. System power consumption control signal vs. measured power consumption for summer solar PV load following test.

Table 2 below summarizes the results of interest with respect to the seasonal differences. Included below is both the capacity factor of the system as the tests were run (zero downtime due to lack of solar radiation at night) and including the down time. The latter result serves to highlight an issue encountered by many energy storage strategies when being paired with solar PV systems, low capacity factors. To maximize the electricity arbitrage capabilities of the energy storage system and prevent curtailment from the PV system, the power capacity of the energy storage system is typically sized close to the peak over-generation of the PV system. With a peak

power capacity of 75kW on the PV system and 62 kW on the electrolyzer system, the two systems are relatively well matched. The result is a capacity factor of at most 38.07% during peak solar activity in the summer season, and as low as 15.89% in the winter.

An encouraging result is the consistent overall system efficiency for all cases in the range of 51-53% higher heating value basis. In retrospect this is perhaps not surprising; system efficiency was observed to remain relatively flat with decreasing load condition until around 40% and below (Figure 25). In all cases, the total capacity factor of each run, considering only actual operating hours ('Test Only' - Table 2), was well above this number, meaning that the system typically operated in the optimal system efficiency regime of greater than 40% load condition.

Table 2. Seasonal comparison for results of solar photovoltaic load following tests.

	Winter	Spring	Fall	Summer
Capacity Factor -Test Only (%System Power Consumption)	47.25%	62.49%	55.88%	63.48%
Capacity Factor - Overall (%System Power Consumption)	15.89%	28.97%	26.05%	38.07%
Hydrogen production (Average kg/day)	3.10	5.75	5.03	7.39
System Efficiency (%HHV H2)	51.60%	52.55%	51.08%	51.37%
Stack Efficiency (%HHV H2)	77.70%	73.92%	75.53%	73.92%
Maximum Slew Rate Up/Down - Stack (kW/sec)	40.81/ -54.53	45.86/ -55.15	41.85/ -54.74	45.14/ -54.74

Also of interest is the extremity of power transients that the electrolyzer is subjected to when load following solar PV dynamics. Due to limitations in sampling rate for the system power consumption metering, and combined with the fact that the stack accounts for the entirety of the variable power consumption (barring very slight variation in losses to the AC/DC power electronics), the maximum slew rates are defined in Table 2 in terms of stack power change on a

second to second basis. The maximum up ramp rates varied slightly, with the higher capacity factor seasons (winter and fall) experiencing lower up ramps than the higher capacity factor cases. The maximum down ramp rate observed was essentially the same across all cases, and in fact was a 100% turndown in the span of a second based off the previously established ~55kW maximum stack power in the benchmarking tests (Table 1).

The stack power slew rate behavior for the winter and spring cases in one second resolution is shown below in Figure 38. The more extreme slew rates occurred more often during the high transient events for both cases but did not follow the solar trend. Instead what is observed is the stack current cycling previously observed in the part load condition testing.

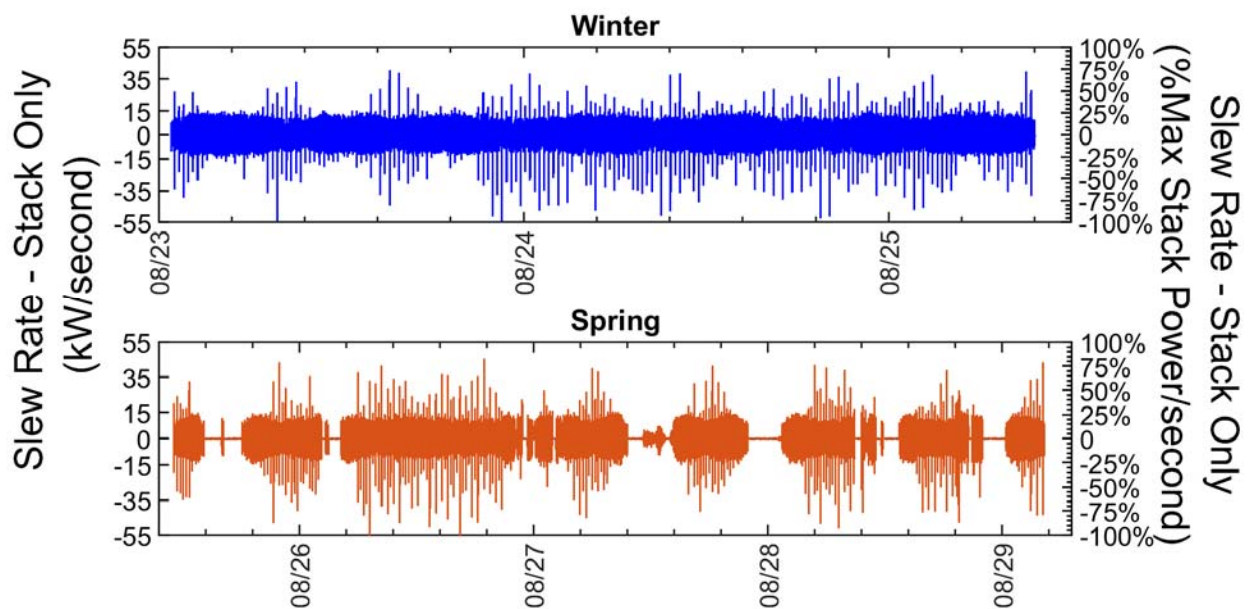


Figure 38. Stack power slew rate for spring and winter solar PV load following run.

Taking the measured system power consumption slew rates and the required slew rates from the solar PV signal to the electrolyzer system we can observe the disparity in trend at the higher 2-minute sampling rate (Figure 39). When comparing the ten-minute power consumption slew rate against the signaled slew rate, the match is much stronger. The electrolyzer system still

introduces transients in power consumption outside the load following signal, but the trend is clearly being followed and the most extreme step changes are followed successfully.

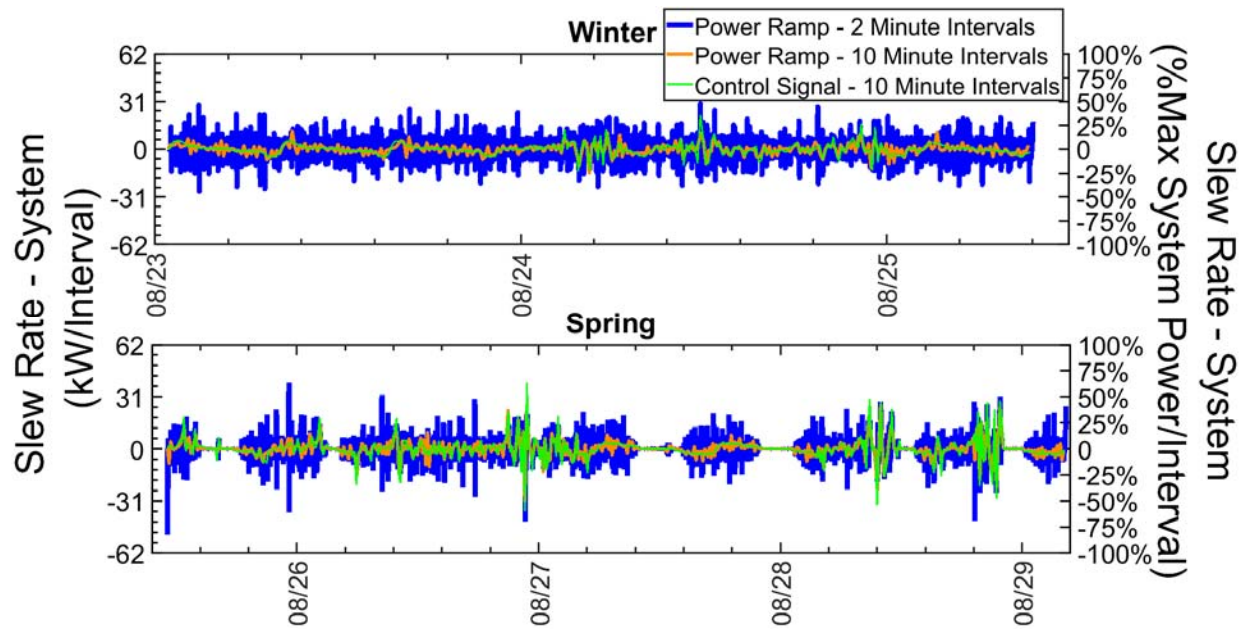


Figure 39. System power slew rate for spring and winter solar PV load following run vs. control signal on 2-minute and 10-minute intervals.

4.4 VRES Load Following – Wind Turbine Farm

The wind load following test utilized 3 weeks of measured net electrical power output from the Tehachapi wind farm on a 5-minute resolution (Figure 40). Due to the order of magnitude difference between the electrolyzer system and the wind farm data, normalization was applied to match the wind farm output scale 1:1 with the electrolyzer system capacity (Figure 41). A minimum flow setpoint was determined, where the flow controller would not shut the valve completely, at 0.03 kg/hr H₂. This is half the previously used minimum flow setpoint of 0.06 kg/hr H₂ and was achieved by increasing the H₂ pressure output from 30 barg to 32 barg in an effort to increase the reliability of the mass flow controller for the longer duration wind load following run.

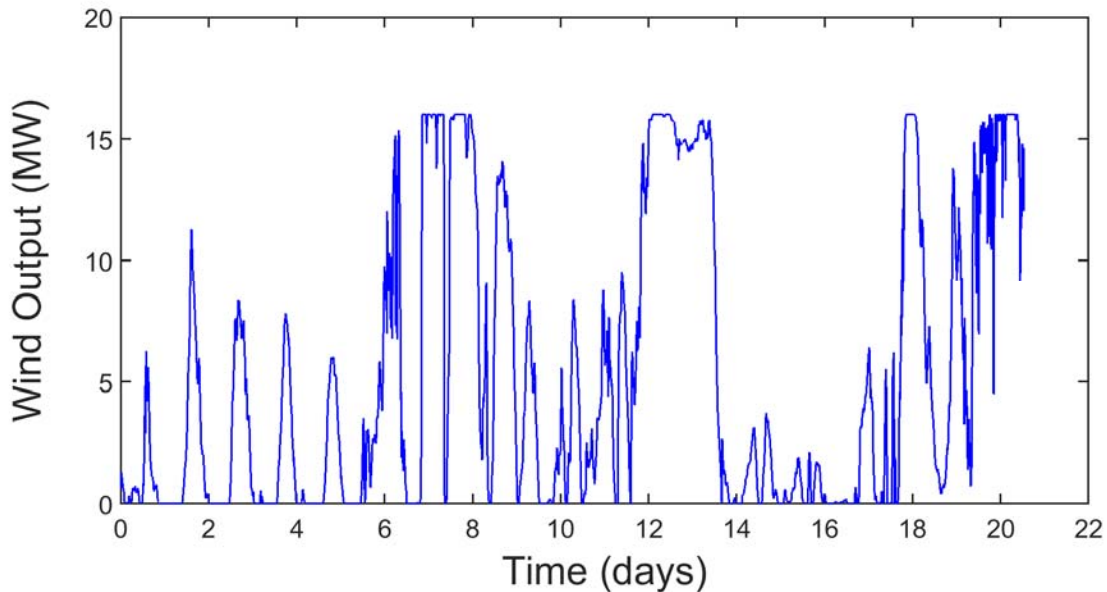


Figure 40. Tehachapi 1-month wind farm output profile utilized in wind load following test.

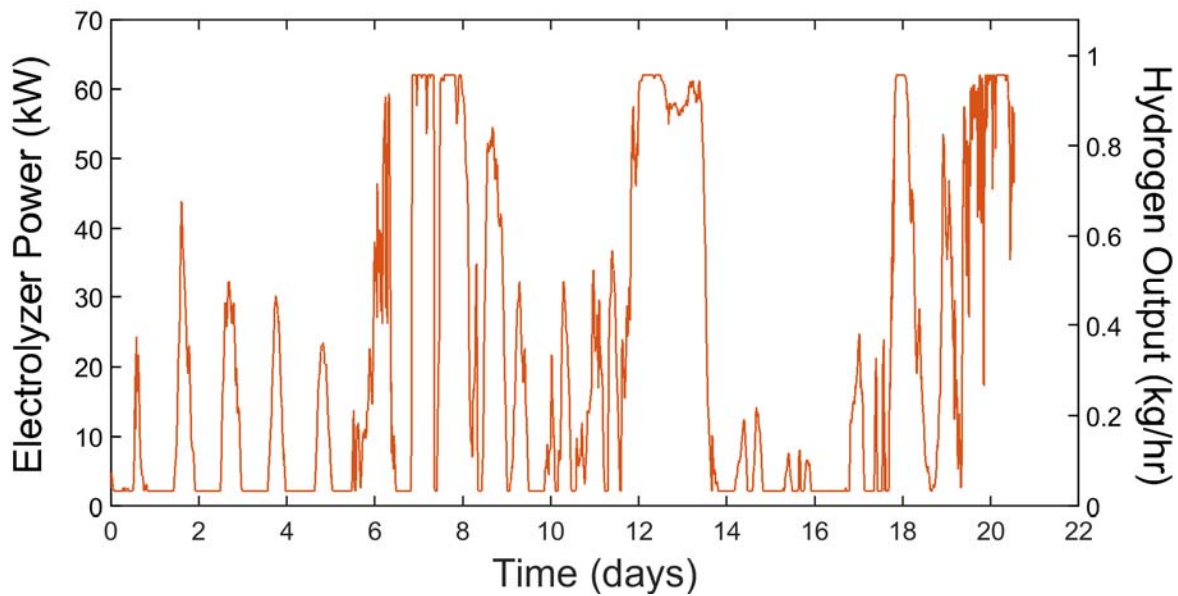


Figure 41. Normalized wind farm output for wind load following test.

Figure 42, Figure 43, and Figure 44 show the hydrogen output response for weeks one, two, and three, respectively. In contrast to the solar load following runs, the wind load following involved prolonged minimum H₂ output operation (~0.03 kg/hr H₂), representative of an idling state.

Particularly throughout week one, and the first half of week three. As observed previously, at near full output, the hydrogen flow rate begins to fluctuate dramatically, but otherwise remained smooth.

Up until week 3, hydrogen output did not deviate from the control signal. Early into week 3, there were two high-transience flow events due to the flow controller valve closing and then ‘searching’ for the flow set point again, both of which rectified themselves. This was followed by a somewhat extended zero-flow (~3 hours) event that required operator intervention in the form of an in-situ valve spring adjustment. Otherwise, operation of the electrolyzer system went uninterrupted for the duration of the test.

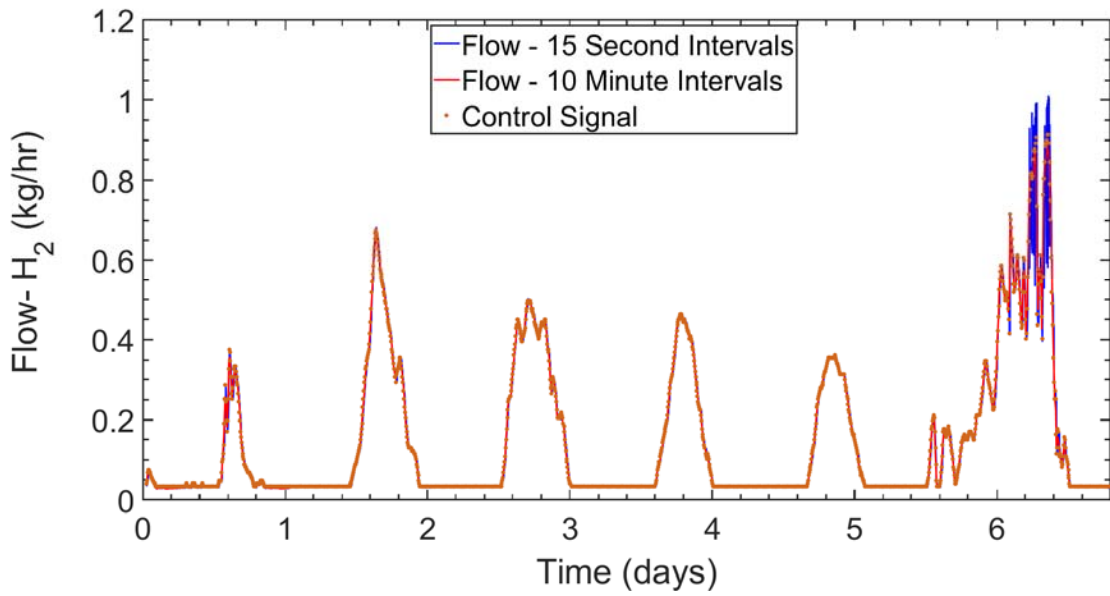


Figure 42. Wind load following test week one, hydrogen output versus control signal.

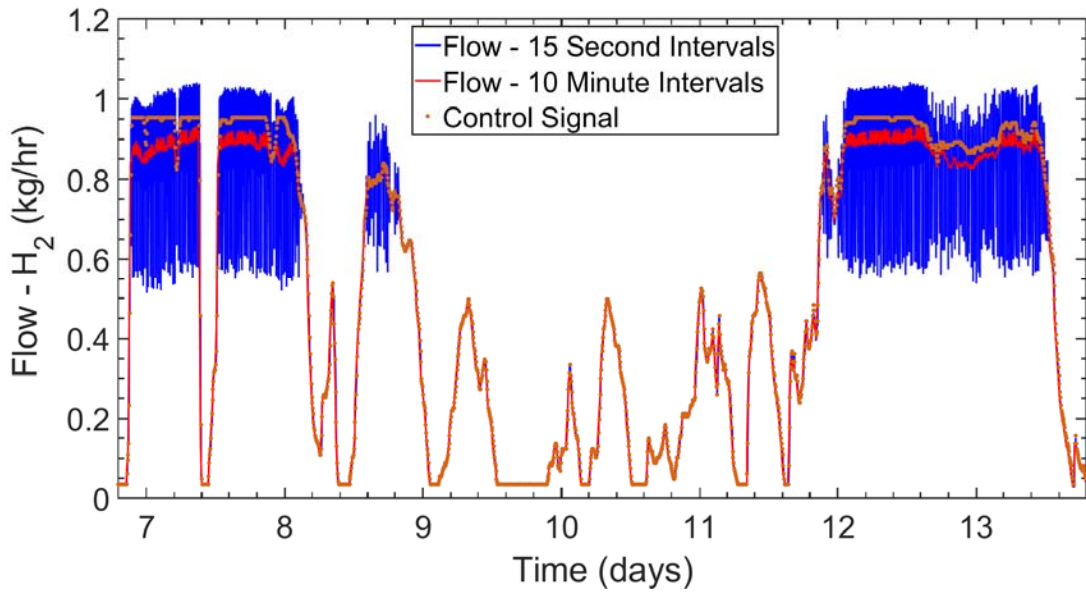


Figure 43. Wind load following test week two, hydrogen output versus control signal.

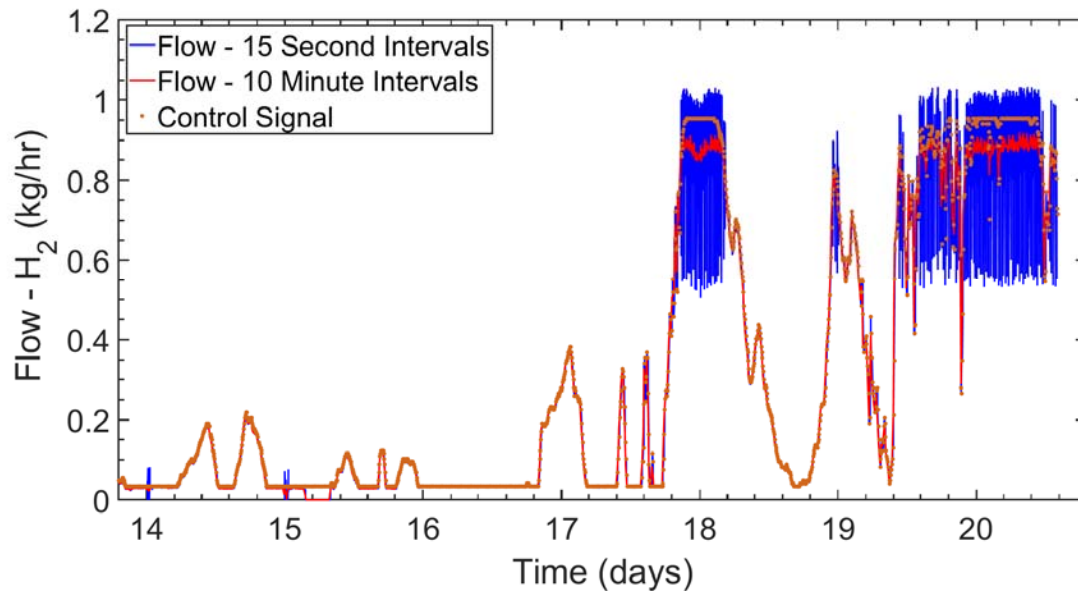


Figure 44. Wind load following test week three, hydrogen output versus control signal.

Figure 45, Figure 46, and Figure 47 display the electrolyzer system's power consumption relative to the expected control signal for weeks one, two and three respectively. The results of which are encouraging, as the electrolyzer system had no issue following the rapid power consumption transients called for by the wind farm profile.

There are two clear trends of interest in the system power consumption. First and most significant is the clear 'minimum' power consumption set point of roughly $\sim 14\text{kW}_{\text{el}}$ when the hydrogen output is at the 0.03 kg/hr H_2 minimum set point up to approximately 0.15 kg/hr . This suggests that the electrolyzer system controls do not reduce power consumption below this point and instead hydrogen is vented beyond this point. For this reason, the flow controller minimum setpoint should not be used, but rather the 0.15 kg/hr setpoint. At 0.03 kg/hr H_2 , the specific energy cost of hydrogen production is $433.3\text{ kWh}_{\text{el}}/\text{kg H}_2$, and at 0.15 kg/hr H_2 , it is $93.3\text{ kWh}_{\text{el}}/\text{kg H}_2$, four-fold improvement in efficiency. By extension, the 14-kW system power consumption setpoint (22.5% load condition) is the true minimum at which the electrolyzer system produces hydrogen at a reasonable efficiency.

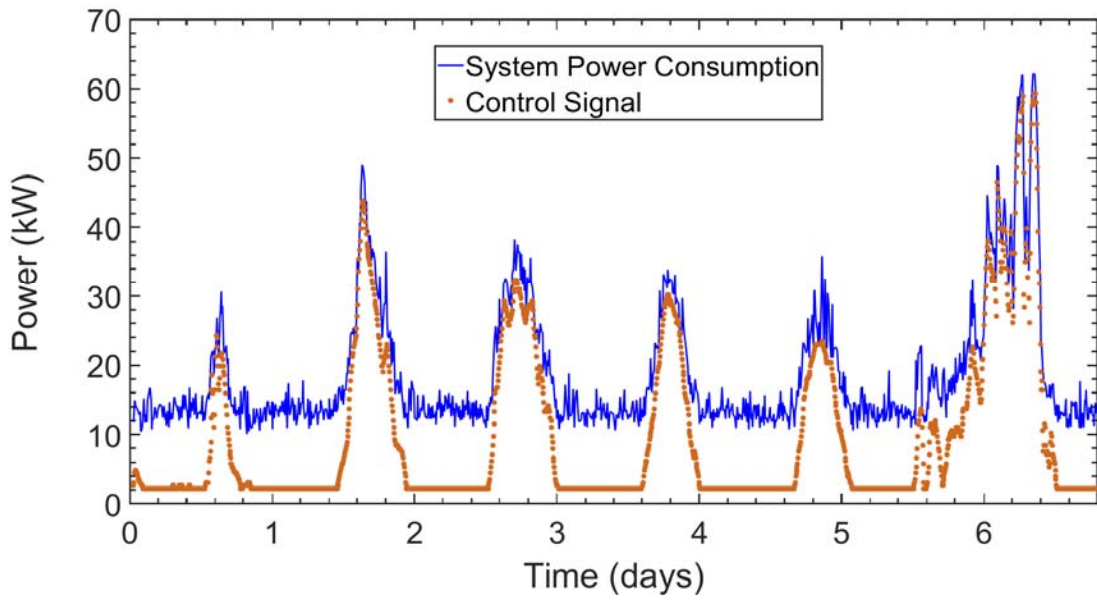


Figure 45. Wind load following test week one, system power consumption versus control signal.

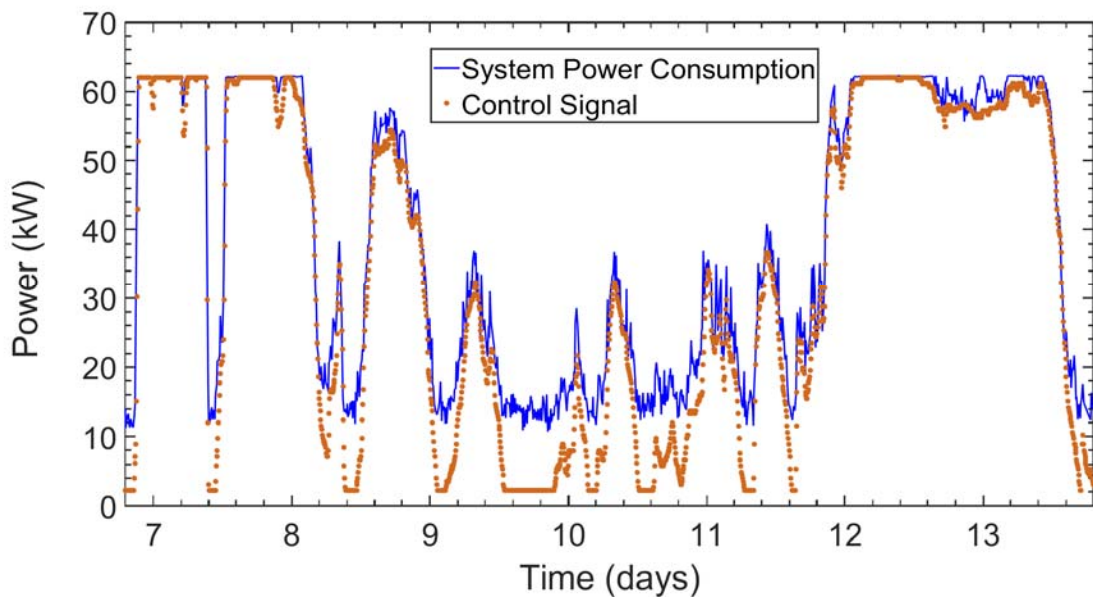


Figure 46. Wind load following test week two, system power consumption versus control signal.

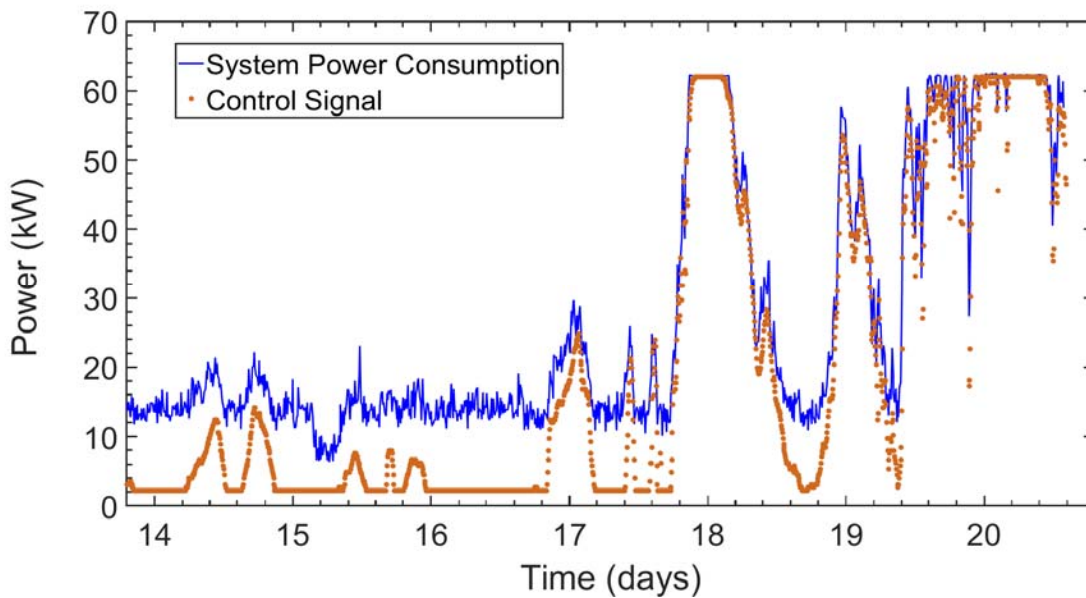


Figure 47. Wind load following test week three, system power consumption versus control signal.

The results of the three separate weeks and the overall performance are tabulated in Table 1.

Splitting the runs up helps highlight the effects that the dynamic nature of wind power, even in an aggregated wind farm format averaged over a week-long period, has on the electrolyzer system, with capacity factors as low as 30% in week one up to 62% the next week. System efficiency suffers at these lower capacity factors, even as stack efficiency climbs, as previously observed in the sustained part load operation as well as the solar load following tests. More dramatic, is the observed slew rates, with the stack ramping up as much as 54.75 kW in a second. Stack maximum power varies with operating conditions, but typically is in the range of 53 to 56kW. For the conditions at that time, this was essentially a 100% up-ramp in power from zero. Similar down-ramps were observed more regularly throughout testing. Figure 48 shows the stack power slew rates throughout the duration of testing. Figure 49 shows the system power consumption slew rates versus the slew rate requirements of the wind load following profile. As previously demonstrated the required slew rate is far less dramatic than the observed variations in power consumption.

Table 3. Summary of wind load following tests.

	Week 1	Week 2	Week 3	Overall
Capacity Factor (%System Power Consumption)	30.24%	62.09%	44.15%	45.68%
Hydrogen production (Average kg/day)	3.5509	12.0486	7.0373	7.5962
System Efficiency (%HHV H2)	31.07%	51.35%	42.06%	43.96%
Stack Efficiency (%HHV H2)	80.96%	73.48%	75.73%	75.73%
Maximum Slew Rate Up/Down - Stack (kW/sec)	46.436/ -55.154	44.672/ -55.154	54.746/ -55.154	---

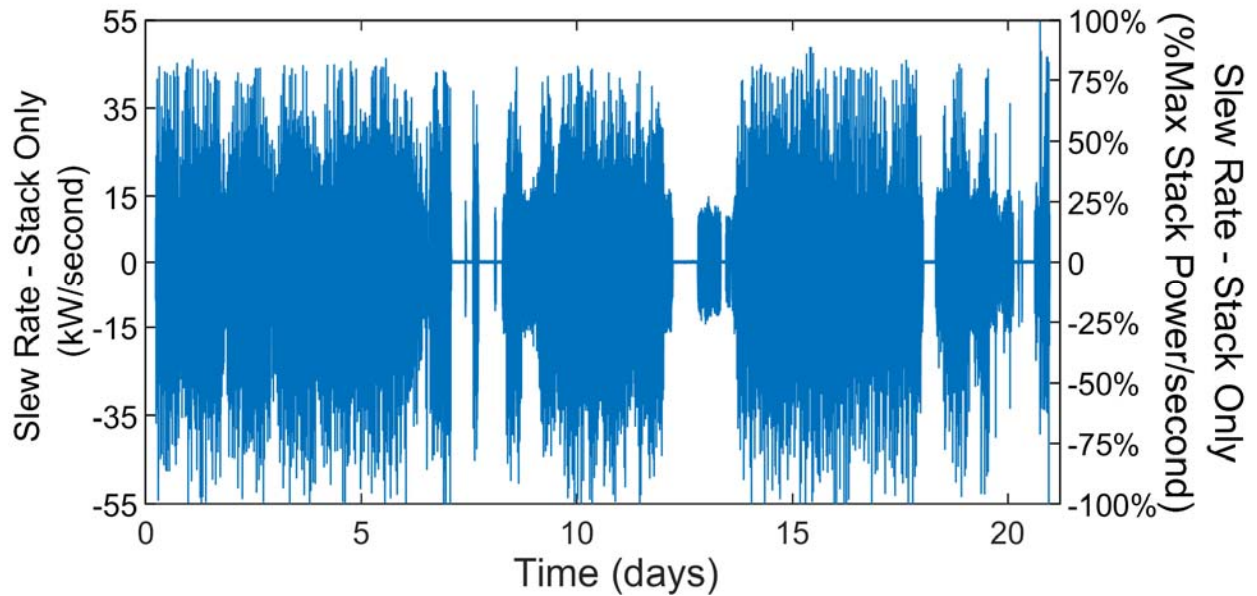


Figure 48. Wind load following test, stack power consumption slew rate 1-second time scale.

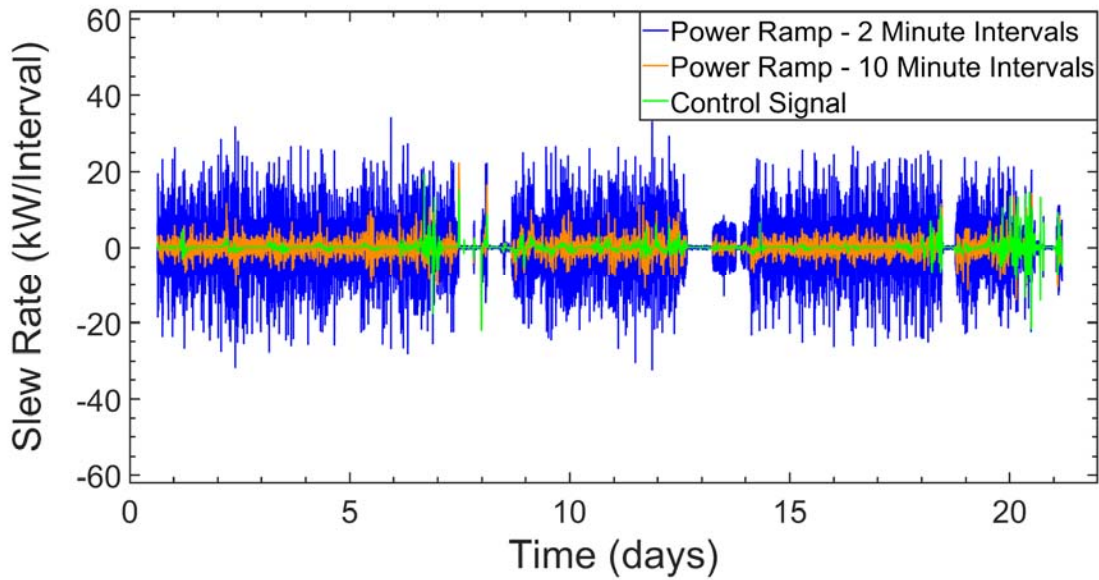


Figure 49. Wind load following test, system power consumption slew rate versus control signal two and ten-minute intervals

Also of interest with wind load following applications is the capability to cycle the electrolyzer system on/off as the load following demand falls below the minimum power requirement of the electrolyzer system. To simulate this idea, the three-week period studied above is pruned of any system activity below a 14 kW system power consumption signal. A start-up period of roughly 4 minutes is added to each on cycle based upon previously collected start-up data as well hydrogen lost on system off cycles when the onboard hydrogen is purged. Power consumption on shutdown was not considered as the system shutdown takes less than a minute in its entirety and only ancillary systems are using power. Table 4 below summarizes the results.

The electrolyzer system cycles power on average one to two times a day, and overall spends over half the time turned off. This highlights once again the expected issue of sizing these energy storage systems for meeting the needs of balancing variable renewable energy resources. On the other hand, system efficiency does improve to a much more reasonable 55% HHV H₂.

Table 4. Wind load following test with electrolyzer power cycling below minimum power set point.

	Week 1	Week 2	Week 3	Overall
Power Cycles (# of)	10	11	10	31
Downtime (% Hours off/Hours Total)	73.43%	30.07%	60.38%	54.62%
Capacity Factor (%System Power Consumption)	14.44%	55.72%	31.16%	33.77%
Hydrogen production (Average kg/day)	3.03	11.78	6.62	7.14
System Efficiency (%HHV H2)	55.55%	55.95%	56.19%	55.90%

4.5 Effects of Operating Conditions on Electrolysis

Electrolysis, and the electrolyzer system that carries out the process, can be heavily influenced by the dynamic operating conditions present. Using the nearly four thousand hours of operation data collected, in addition to controlled tests where only parameters of interest were allowed to vary, the influence of several significant operating parameters on the electrolyzer system are assessed. Due to the large number of data being compared, data is analyzed using analysis of variance (ANOVA) by way of the Design Expert statistical software package. In this case, ANOVA is applied to largely non-randomized experiments and as such the results are largely useful for suggesting hypotheses and identifying trends.

4.5.1 Effects of Operating Conditions on Electrolysis Stack

The cell voltage at which electrolysis is carried out for a given current density is known to vary with several parameters, including variable operating conditions. Lower cell voltages are desirable for a given current density as it results in lower power consumption for the same amount of hydrogen production. In our case, the temperature of the environment and the partial pressures of the species involved can be varied, and the effect on cell voltage observed. In the case of species pressure, the partial pressure contribution of water vapor and gas cross-over is assumed to be minimal on each side of the cell stack such that the measured anode pressure is described here as the O₂ pressure and the cathode pressure described here as the H₂ pressure. Uncontrolled variable operating conditions are considered as well, such as the resistivity of the feed water and the ambient temperature conditions. The full list of factors considered are displayed below in Table 5.

Table 5. List of factors utilized in ANOVA analysis for electrolyzer system study.

Factors	Units	Minimum	Maximum	Mean	Std. Dev
A - Current Density	Amps/cm ²	0.1869	1.9338	1.0885	0.5906
B - H2	kg/hr	0.0000	0.9318	0.4342	0.3318
C - Hours of Operation	Hours	1000	3800	2470.8918	605.8384
D - H2 Pressure	Barg	27.1724	31.9987	30.6286	1.2757
E - Inj Pressure	Barg	20.1081	32.1675	30.0672	2.4482
F - O2 Pressure	Barg	1.1085	2.0876	1.7506	0.1731
G - Stack Temperature	Celsius	41.5095	57.0630	55.1612	0.8623
H - Ambient Temperature	Celsius	22.6785	42.5343	29.5606	3.0419
J - H2 Temperature	Celsius	17.1274	26.7815	20.4037	1.4230
K - DI Water	MΩ-cm	1.1440	17.5408	11.1567	5.5405

Figure 24 previously displayed the effects of temperature change on cell voltage correlated to normal temperature in the stack. More focused testing was carried out to vary the stack temperature across a wider range, better establishing the correlation. Figure 50 below shows the input current density versus cell voltage data including the temperature correlation for the wider range of temperatures studied. It is evident that stack temperature is a strong predictor for cell voltage at a given current density.

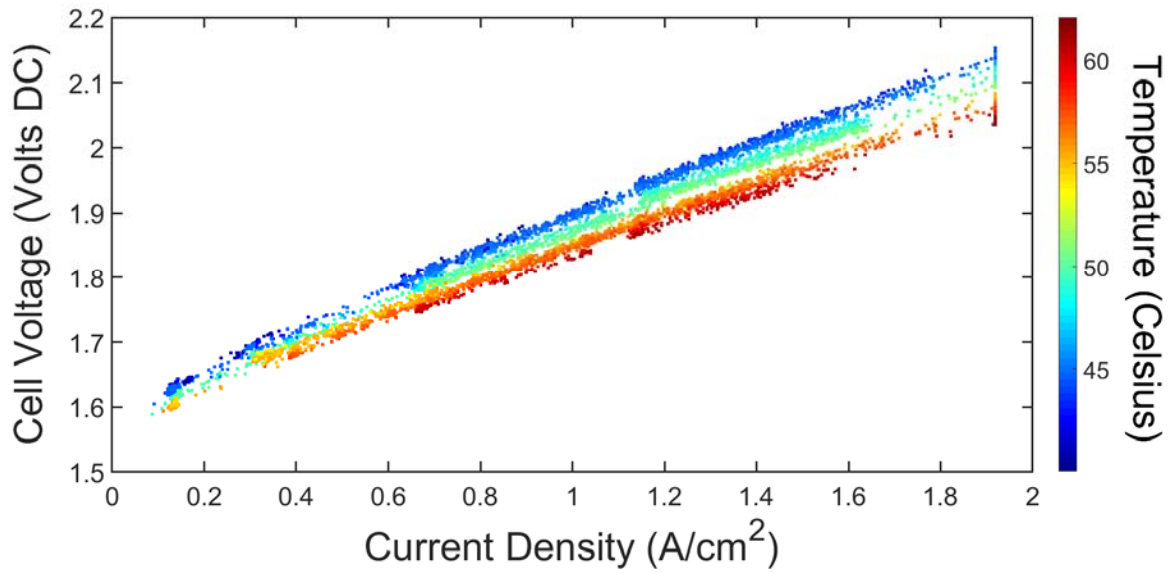


Figure 50. j-V curve across the breadth of electrolyzer testing, parsed by stack temperature.

In the case of species pressures, the effects are less obvious from a cursory observation of the j-V curve behavior. Figure 51 shows the j-V curve behavior with respect to hydrogen (cathode side) and oxygen (anode side) pressures. In the case of H₂ pressure, there is a healthy distribution of data to use albeit in the limited range of roughly 28 to 32 barg. There is no pressure regulation on the oxygen-side, and as a consequence oxygen pressure is less evenly distributed.

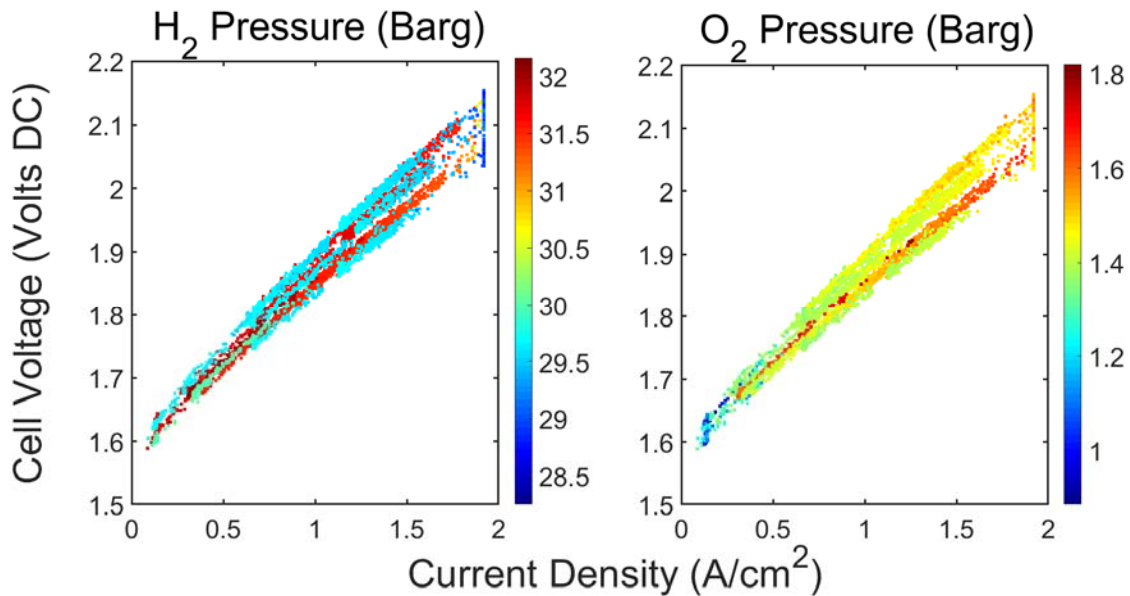


Figure 51. j-V curve across the breadth of electrolyzer testing, parsed by H₂ pressure (left) and O₂ pressure (right).

The most significant predictors of cell voltage in order of significance were current density, stack temperature, and hydrogen pressure. Overall the model is a strong predictor of j-V behavior with an R² value greater than 0.99. A linear model was used as the j-V region considered was in the largely ‘linear’ region of the relation, although nonlinearities would begin to appear at lower current densities that were not included. The results of the ANOVA analysis on cell voltage is displayed below in Table 6.

Table 6. Results of ANOVA analysis on cell voltage.

Std. Dev.	0.0331	R ²	0.9936
Mean	3.2808	Adjusted R ²	0.9935
C.V. %	1.0094	Predicted R ²	0.9932
		Adeq Precision	639.5880

	Sum of Squares	Degrees of Freedom	Mean Square	F Value	P-value (Prob > F)
A-Current Density	82.5536	1	82.5536	75271.2063	< 0.0001
D-H₂ Pressure	0.0099	1	0.0099	9.0030	0.0028
G-Stack Temperature	0.0849	1	0.0849	77.4291	< 0.0001
Model	110.1166	3	36.7055	33467.5768	< 0.0001

The trend predictions match up with what was observed for current density and stack temperature in the j-V curve; higher temperatures result in lower cell voltages. Figure 52 shows the contour plot of the ANOVA model prediction for the combined effects of temperature and current density.

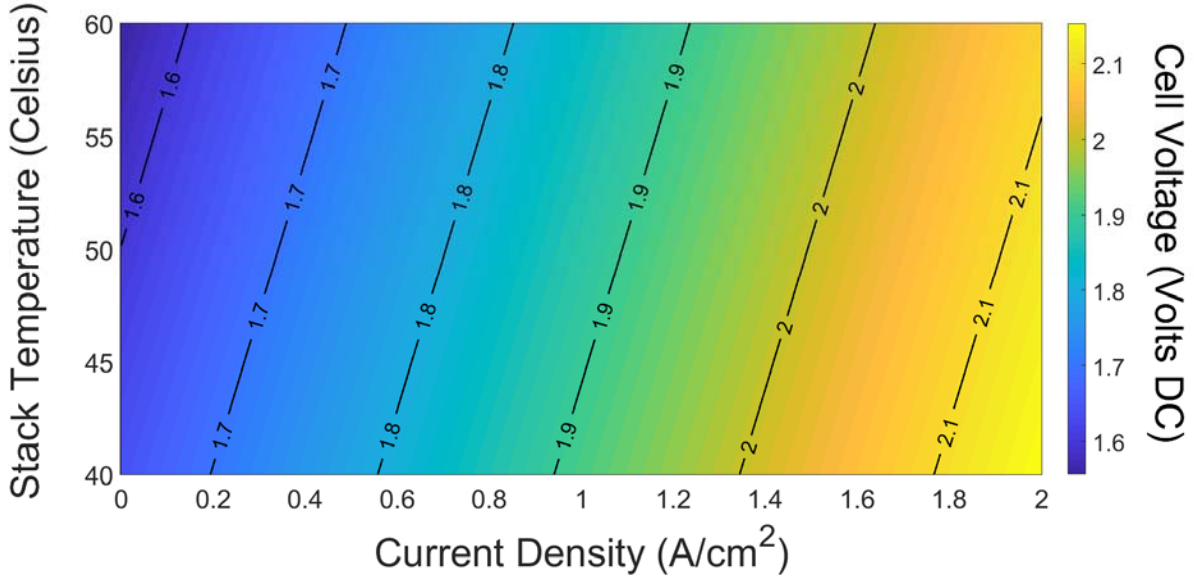


Figure 52. Contour plot of ANOVA prediction model for cell voltage as a function of stack temperature and current density.

The ANOVA analysis allows less apparent relationships between certain variables and cell voltage to become visible, such as the effects of H₂ pressure on cell voltage. Increasing pressures on the hydrogen side increase cell voltage slightly, which is the expected trend. According to the ANOVA model, going from 28 barg to 32 barg hydrogen incurs an overvoltage of 4.64 ± 3.48 mV per cell. The overvoltage incurred by pressurization of the hydrogen side is not well understood but is typically attributed to the predicted change in Nernst (reversible) voltage as described in equation (4) below.

$$E_{OCV}(T, P) = 1.228 - 0.0009(T_{avg} - 298.15) + \frac{RT}{2F} \left[\ln \left(\frac{P_{H_2, cathode} P_{O_2, anode}^{0.5}}{a_{H_2O, anode}} \right) \right] \quad (4)$$

Our ANOVA model prediction for hydrogen pressurization is in line with the predicted change in voltage by the Nernst equation of 2 mV going from 28 to 32 barg. The losses due to

pressurization of hydrogen in this fashion are of great interest due to the potentially much higher compression efficiency relative to traditional mechanical based methods. Electrochemical compression is explored further in section 6.5.

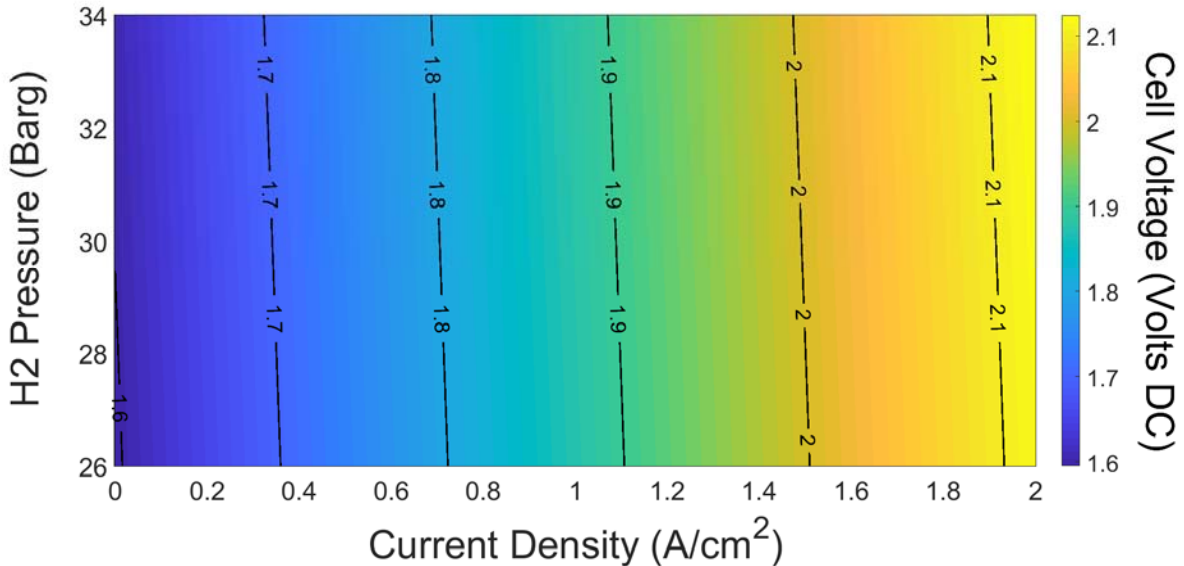


Figure 53. Contour plot of ANOVA prediction model for cell voltage as a function of H₂ pressure and current density.

While the effect of varying O₂ pressure was not found to be significant across cell voltage measurements according to the ANOVA analysis, the general predicted trend was still of interest. Figure 54 shows that increasing oxygen pressure was generally correlated with higher cell voltages, which also agrees with the expected result. However, the overvoltage prediction is higher than would be expected, with a 1 barg increase in pressure from 1 barg O₂ to 2 barg O₂ predicted to incur a 16.33 ± 5.72 mV overvoltage. According to the Nernst equation this should only incur a ~ 4.79 mV overvoltage. Given the poor distribution of oxygen pressure data across all other operating conditions, this incongruence is unsurprising.

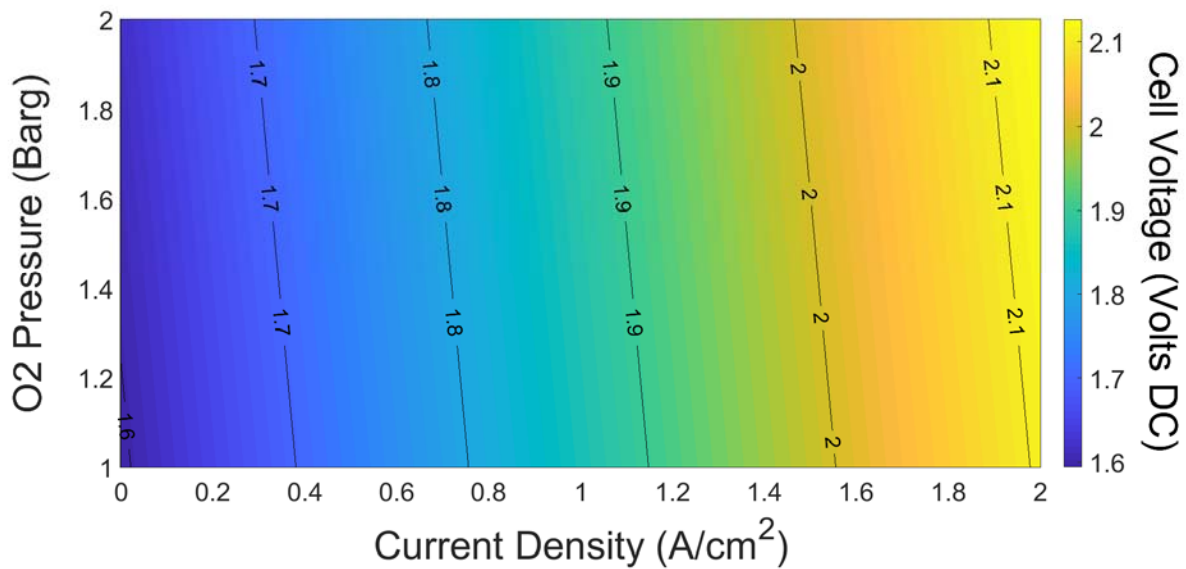


Figure 54. Contour plot of ANOVA prediction model for cell voltage as a function of H₂ pressure and current density.

4.5.2 Effects of Operating Condition on Electrolyzer System Efficiency

From a system level perspective, the same operating conditions considered in Table 5 are of interest. Overall system efficiency is likely influenced greatly by those same factors that influence cell voltage due to the high percentage of power consumption attributed to the electrolysis process alone.

For the effects of stack temperature on system efficiency, data had to be orthogonalized to exclude a region of current density (up to 0.8 A/cm^2) that was only gathered at 55 Celsius. Stack temperature was only modified for focused part load operation tests that did not go below a sustained 0.8 A/cm^2 . The bulk of tests were accomplished using a 55 Celsius stack temperature set point to avoid thermal degradation trips (stack temperature > 60 Celsius for an extended period) while minimizing chiller operation, and as a consequence the ANOVA analysis on the effects of stack temperature on system efficiency was limited to 0.8 A/cm^2 operation and above. Figure 55 shows the distribution of all data on the left and the input to ANOVA on the right.

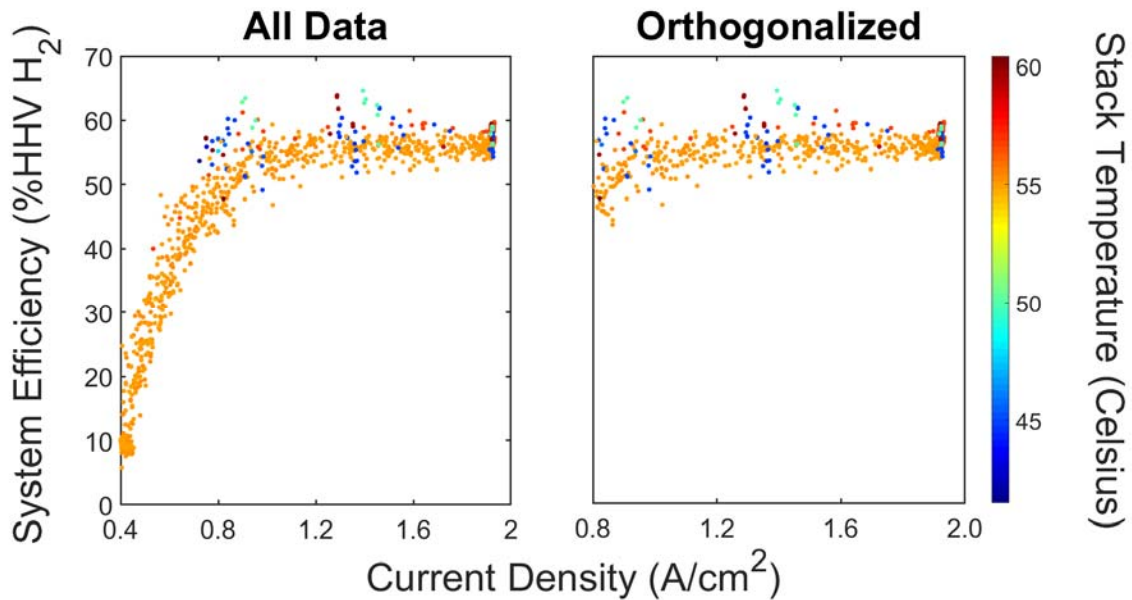


Figure 55. System efficiency versus current density with stack temperature distribution, all data (left) and orthogonalized data for ANOVA analysis (right).

For the range considered, stack efficiency overall did not vary appreciably with stack temperature. Further pruning the data to achieve an equivalent amount of data at 55 Celsius did not change the result. Ultimately, for the data input to analyze the effects of stack temperature, stack temperature was the least significant factor in system efficiency (Table 7). Although a slight positive correlation with system efficiency was observed, likely as a consequence of its effects on cell voltage, overall no significant variation was observed outside of the 95% confidence intervals (Figure 56). Given the R^2 value of 0.15, the overall ANOVA model is poor.

Table 7. Results of ANOVA analysis on system efficiency; input data orthogonalized for stack temperature effects.

	Sum of Squares	Degrees of Freedom	Mean Square	F Value	P-value (Prob > F)
A-Current Density	118.0852	1	118.0852	18.9636	<0.0001
D-H₂ Pressure	21.2888	1	21.28875	3.4188	0.0656
F-O₂ Pressure	60.7287	1	60.72868	9.7526	0.0020
G-Stack Temperature	10.4060	1	10.40599	1.6711	0.1972
Model	285.2926	4	71.32314	11.4540	<0.0001

Std. Dev.	2.4954	R ²	0.1479
Mean	56.9807	Adjusted R ²	0.1350
C.V. %	4.3794	Predicted R ²	0.1009
		Adeq Precision	13.7671

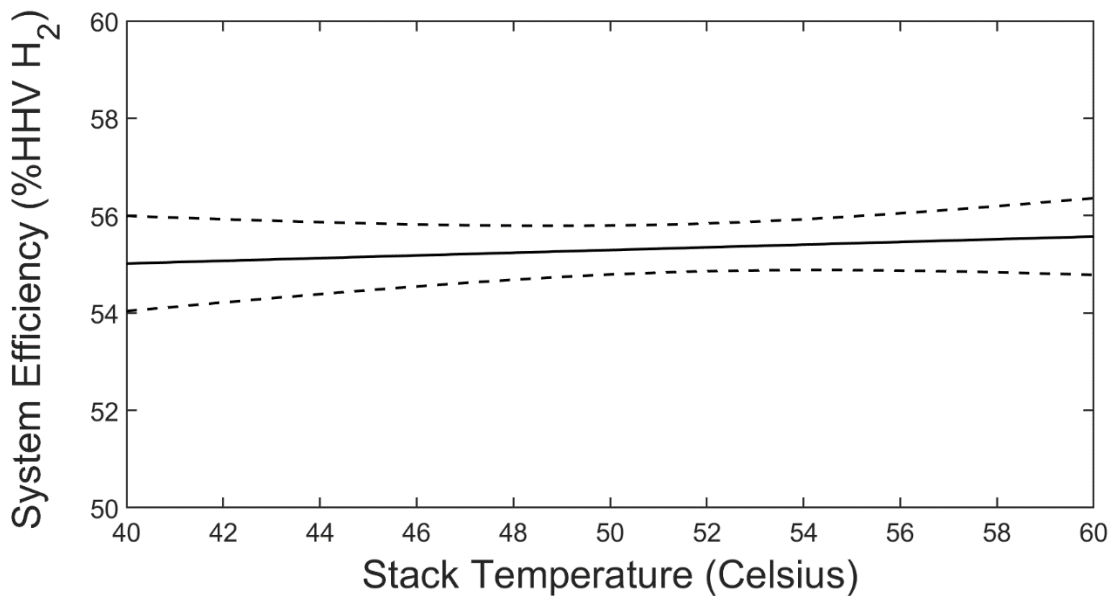


Figure 56. ANOVA prediction of stack temperature influence on system efficiency, dashed lines depict 95% confidence intervals ($j = 1 \text{ A/cm}^2$, $P_{H_2} = 30 \text{ barg}$, $P_{O_2} = 1.5 \text{ barg}$).

There is a stronger influence on overall system efficiency from H₂ pressure and, to a lesser extent, O₂ pressure. The distribution of data for these two factors was left unmodified. Figures Figure 57 and Figure 58 show these distributions below.

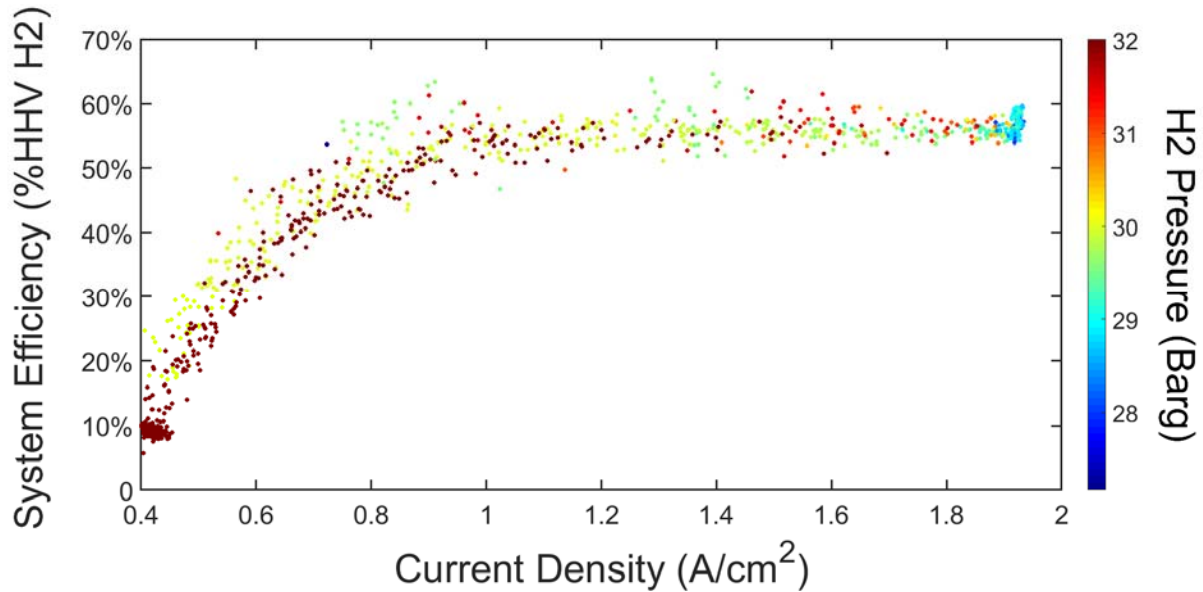


Figure 57. System efficiency versus current density with H₂ pressure distribution.

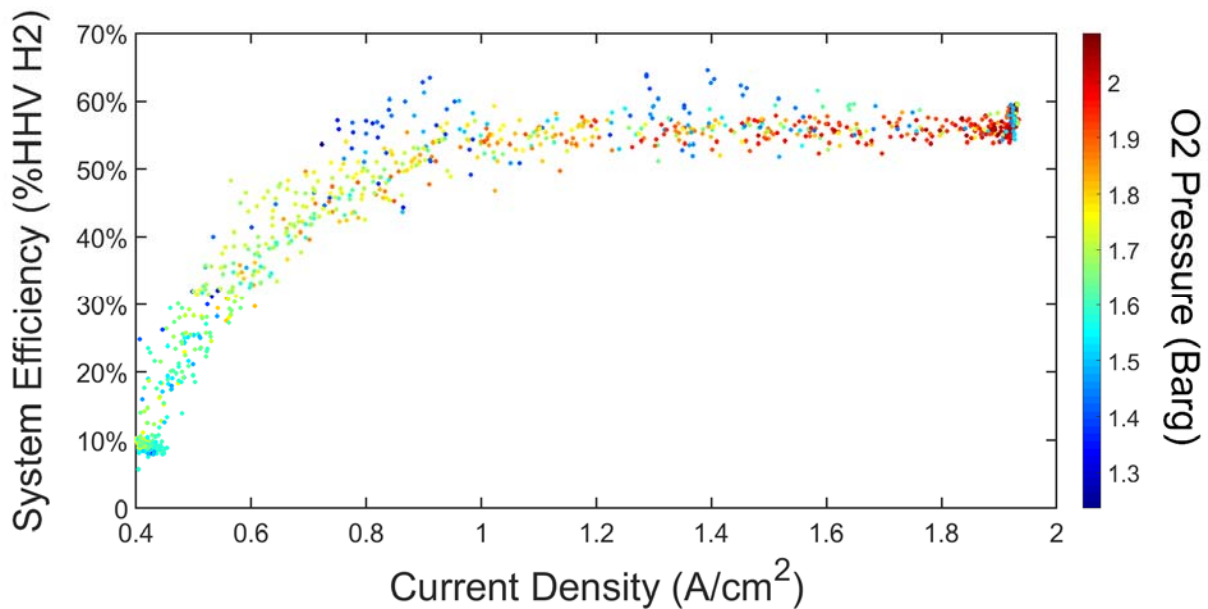


Figure 58. System efficiency versus current density with O₂ pressure distribution.

The ANOVA results for the entire range of system efficiency considered are summarized below in Table 8. The full range of system efficiency responses resulted in a much better fit for the ANOVA model prediction with an R^2 value of 0.85. Both current density and H_2 pressure showed significant influence on system efficiency. O_2 pressure as well seemed to have an influence, although due to the uncontrollable nature of the oxygen pressure, the effects are not nearly as clear. These three terms comprise the ANOVA model.

Table 8. Results of ANOVA analysis on system efficiency, all data points & stack temperature excluded.

	Sum of Squares	Degrees of Freedom	Mean Square	F Value	P-value (Prob > F)
A-Current Density	1.398E+11	1	1.398E+11	1677.1253	<0.0001
D-H_2 Pressure	2.634E+09	1	2.634E+09	31.6038	<0.0001
F-O_2 Pressure	2.506E+08	1	2.506E+08	3.0066	0.0834
Model	3.149E+11	3	1.050E+11	1259.3299	<0.0001

Std. Dev.	9129.4467	R^2	0.8528
Mean	26969.3660	Adjusted R^2	0.8521
C.V. %	33.8512	Predicted R^2	0.8507
		Adeq Precision	116.9948

The predicted effects of varying H₂ and O₂ pressure on system efficiency are shown below in figures Figure 59 and Figure 60 respectively. Hydrogen pressure has a clear negative correlation with system efficiency that grows at lower current density regimes.

Interestingly, O₂ pressure has a positive correlation with system efficiency. The overlapping confidence intervals suggest that this trend could be in large part arbitrary. There is already a strong correlation of high oxygen pressure with high current density as well, which obscures effective analysis of the effects of oxygen pressure.

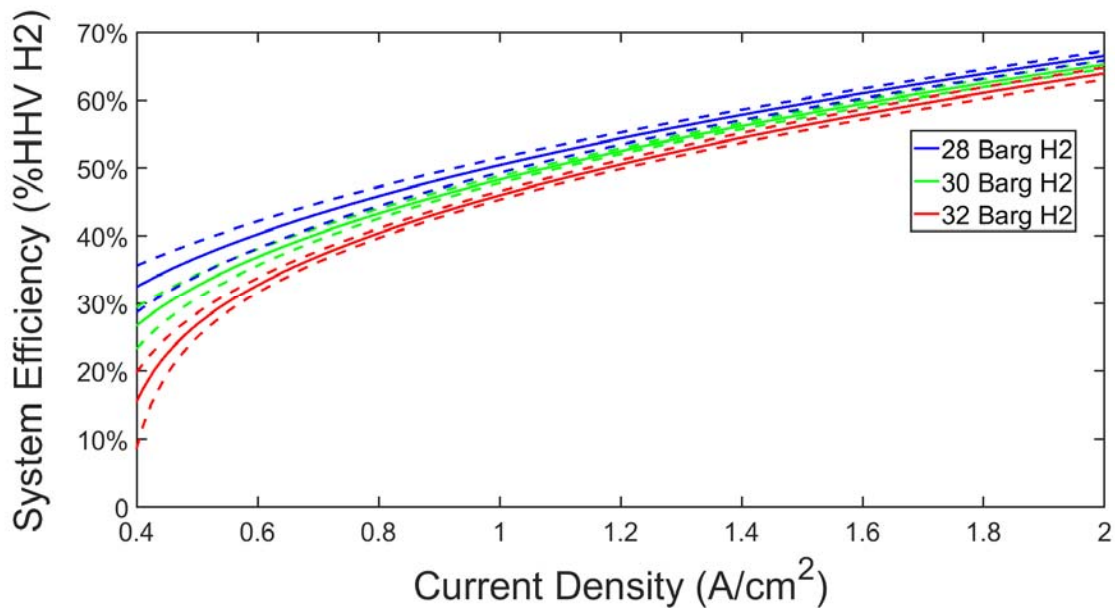


Figure 59. ANOVA prediction of H₂ pressure influence on system efficiency, dashed lines depict 95% confidence intervals ($P_{O_2} = 1.5$ barg).

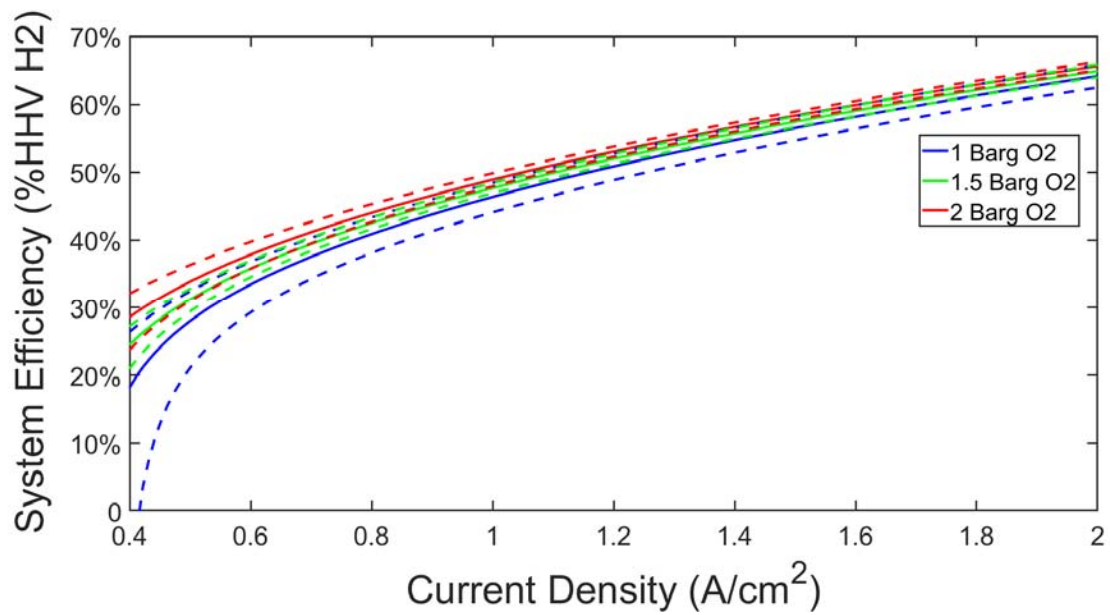


Figure 60. ANOVA prediction of O₂ pressure influence on system efficiency, dashed lines depict 95% confidence intervals ($P_{H_2} = 30$ barg).

4.5.3 Effects of Operating Conditions on H₂ losses

Several factors outside of the efficiency of the electrolysis process can influence the overall system efficiency. Previously established during the sustained part load operation testing was the contribution of hydrogen gas losses to lower system efficiencies as load condition decreases. It is reasonable then to look for matching trends with respect to system efficiency for the measured hydrogen losses. Figure 61 and Figure 62 show the distribution of hydrogen and oxygen pressure respectively for % of hydrogen loss versus current density.

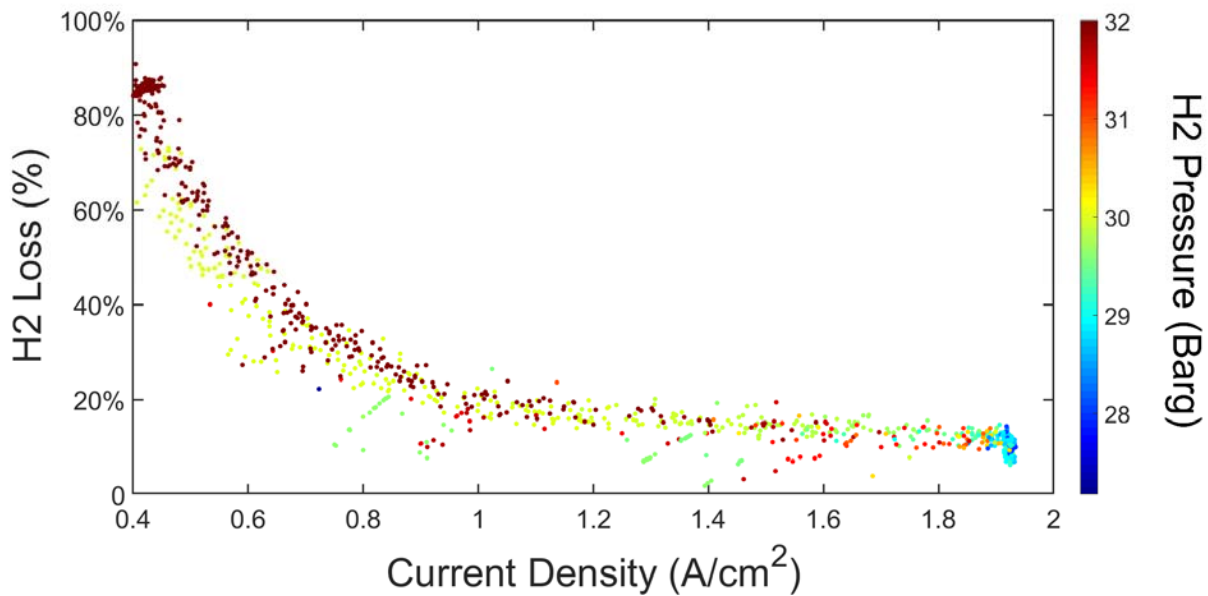


Figure 61. %H₂ loss versus current density with H₂ pressure distribution.

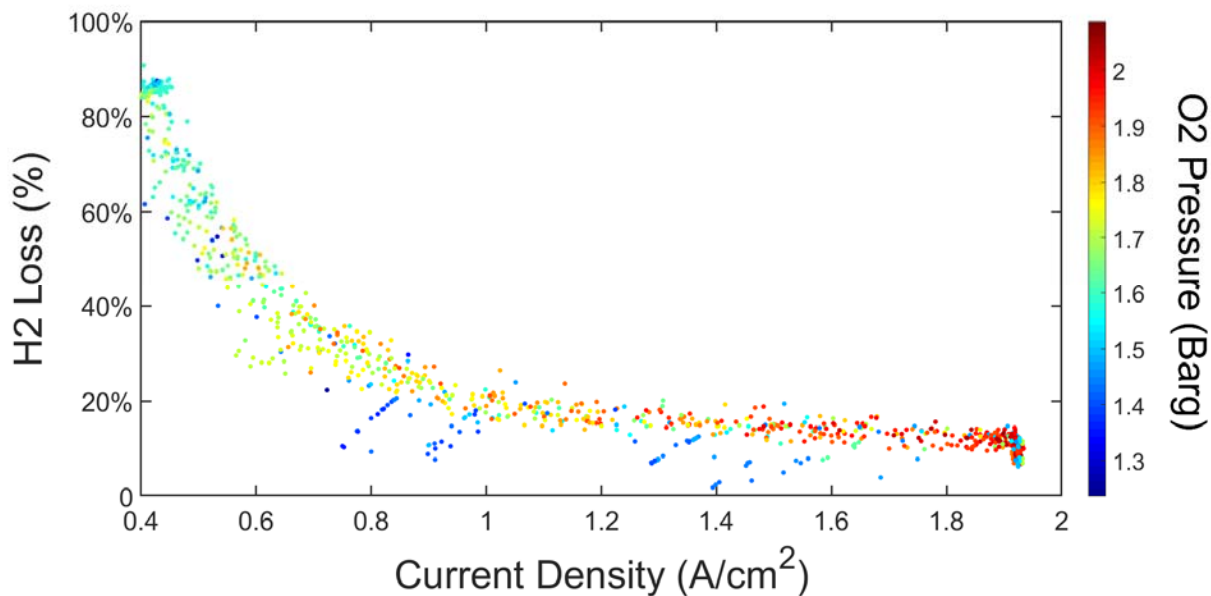


Figure 62. %H₂ loss versus current density with O₂ pressure distribution.

The ANOVA results for %H₂ loss are summarized below in Table 9, and closely mirror the results of the system efficiency analysis. The model fit is slightly stronger, and the H₂ pressure significance was found to be higher while the O₂ pressure significance decreased. Figure 63 and Figure 64 show the model correlation for H₂ and O₂ pressure respectively. The confidence intervals for the H₂ pressure variation tightened considerably, and in combination with the clear distribution of higher H₂ losses at higher H₂ pressures observed in Figure 61, it is certain that higher H₂ pressures lead to greater H₂ losses. O₂ pressure does not clearly impact the hydrogen losses.

Table 9. Results of ANOVA analysis on %H₂ loss.

	Sum of Squares	Degrees of Freedom	Mean Square	F Value	P-value (Prob > F)
A-Current Density	1.1498	1	1.1498	4118.7081	< 0.0001
D-H₂ Pressure	0.0111	1	0.0111	39.6783	< 0.0001
F-O₂ Pressure	0.0000	1	0.0000	0.0150	0.902555
Model	2.4138	3	0.8046	2882.0607	< 0.0001

Std. Dev.	0.0167	R ²	0.9299
Mean	0.1765	Adjusted R ²	0.9296
C.V. %	9.4669	Predicted R ²	0.9287
		Adeq Precision	172.4244

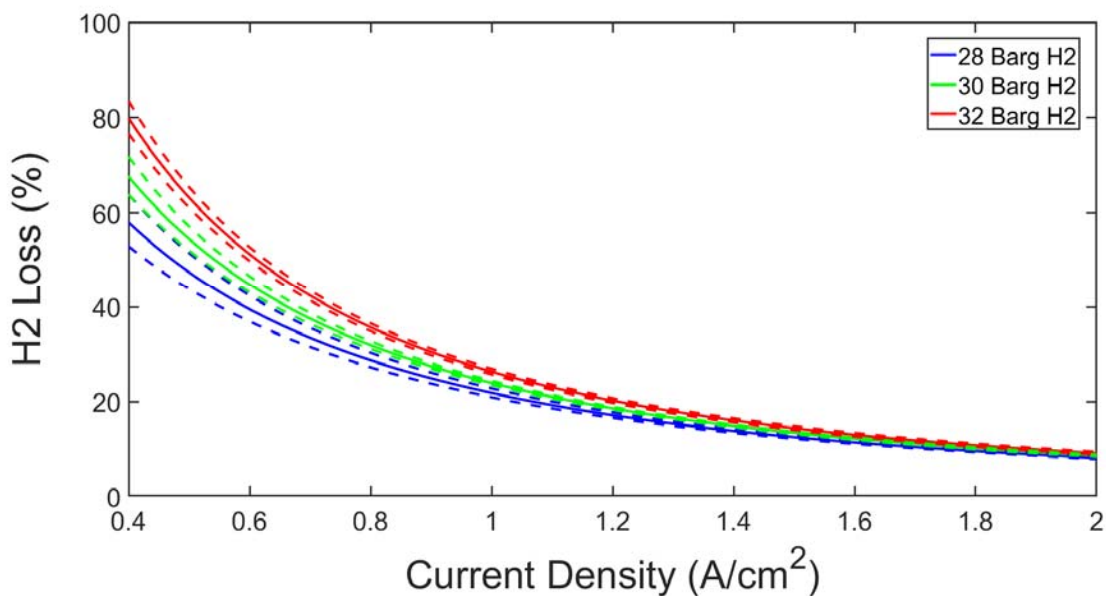


Figure 63. ANOVA prediction of H₂ pressure influence on H₂ efficiency, dashed lines depict 95% confidence intervals (P_{O₂} = 1.5 barg).

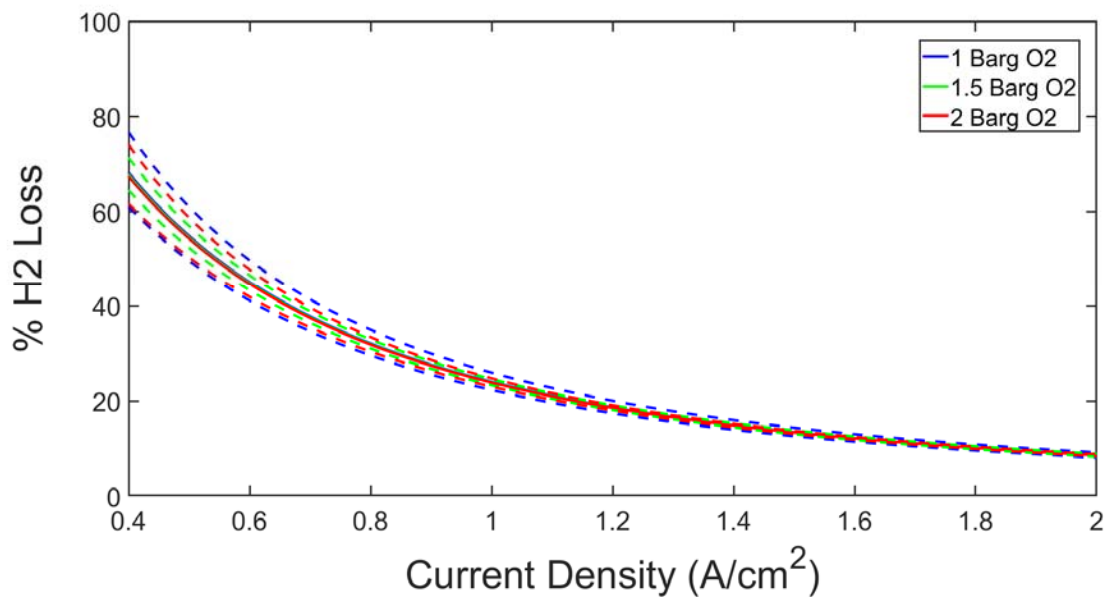


Figure 64. ANOVA prediction of O₂ pressure influence on system efficiency, dashed lines depict 95% confidence intervals ($P_{H_2} = 30$ barg).

4.5.4 Effects of Operating Conditions on AC/DC Power Electronics

The AC/DC power electronics are another significant source of loss in system efficiency that could be influenced by operating conditions. Figure 15 demonstrated a clear correlation between lower ambient temperatures and higher AC/DC power electronics efficiency, although only at 100% load conditions ($\sim 1.92 \text{ A/cm}^2$). In sustained part load testing, no such correlation was found, although the range of ambient temperatures operated were limited. Very little correlation between load condition and AC/DC power electronics efficiency was found in sustained part load testing (Figure 28). Figure 65 shows the observed AC/DC power electronics efficiency versus current density and the distribution of ambient temperatures.

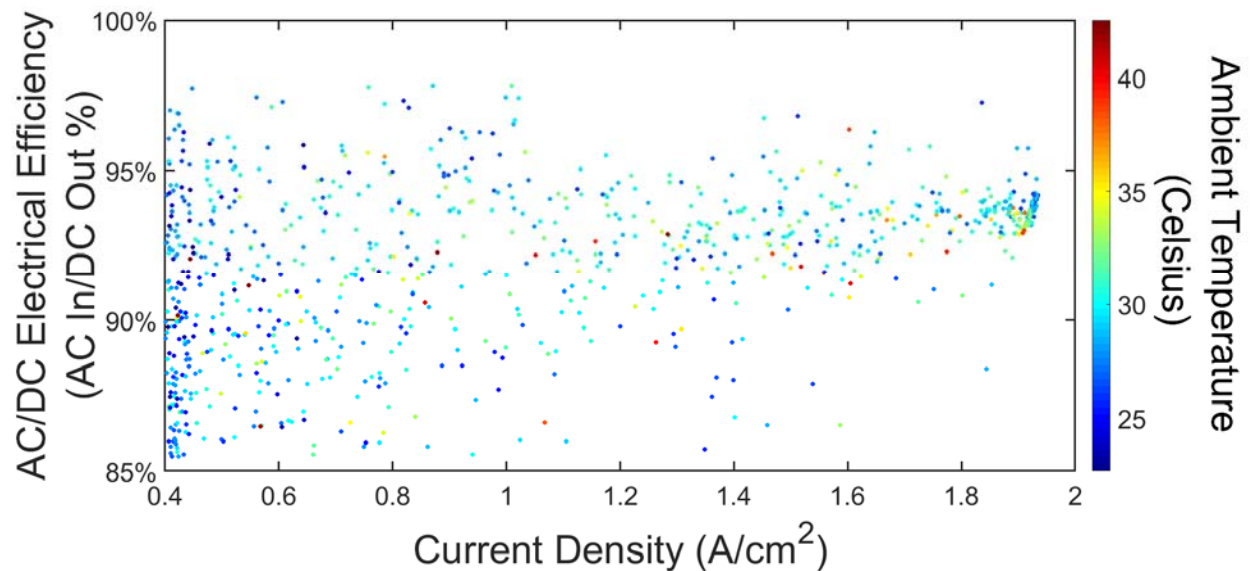


Figure 65. AC/DC power electronics efficiency versus current density with ambient temperature distribution.

In agreement with what was observed in the sustained part load operation, there is an overall poor correlation between lower current densities, ambient temperature, and resulting AC/DC power electronics efficiency (Table 10). Figure 66 shows the ANOVA model prediction, showing a general down trend in AC/DC efficiency with decreasing current density. Lower ambient temperatures are also correlated with higher AC/DC power electronics efficiencies. While the model itself is not a powerful predictor of AC/DC efficiency, the trends in efficiency do appear to be accurate. A cursory glance at the data distribution (Figure 65) suggests that ambient temperature is weighted to be lower at lower current densities and that this may influence the ANOVA analysis. A closer examination of the data shows that the average ambient temperature for the high current density regime, low current density regime, and entirety of the points is around 28 degrees Celsius.

Table 10. Results of ANOVA analysis on AC/DC power electronics efficiency.

	Sum of Squares	Degrees of Freedom	Mean Square	F Value	P-value (Prob > F)
A-Current Density	1177.9947	1	1177.9947	123.8344	< 0.0001
H-Ambient Temperature	28.5512	1	28.5512	3.0014	0.0837
Model	1246.3817	2	623.1909	65.5117	< 0.0001

Std. Dev.	3.0843	R ²	0.1671
Mean	91.0731	Adjusted R ²	0.1646
C.V. %	3.3866	Predicted R ²	0.1610
		Adeq Precision	27.1759

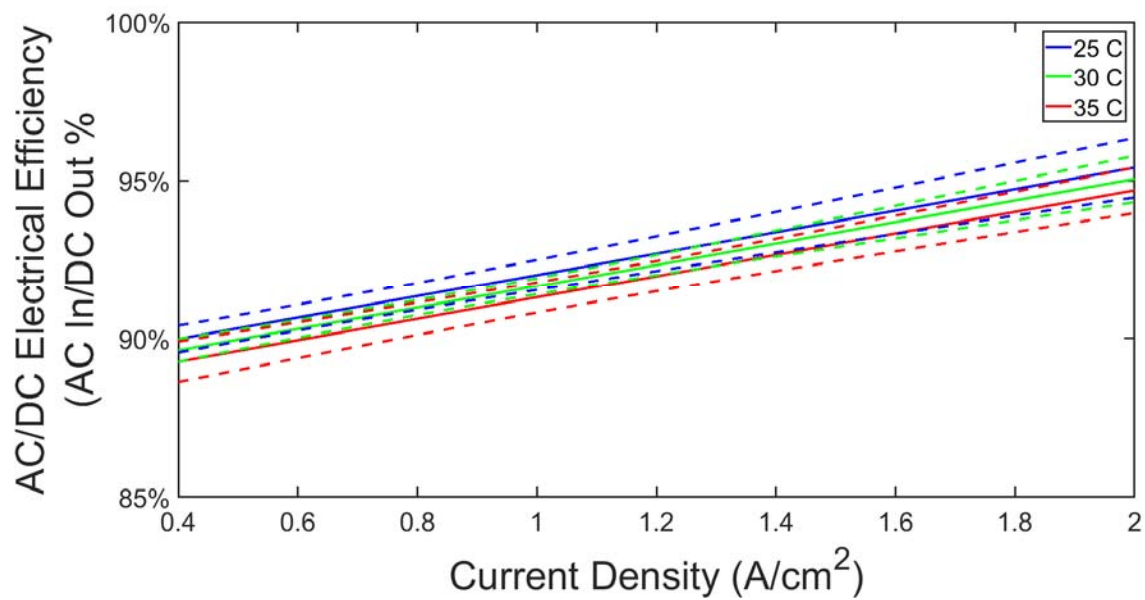


Figure 66. ANOVA prediction of ambient temperature on H_2 efficiency, dashed lines depict 95% confidence intervals.

4.5.5 Synthesis of System Efficiency and Specific Energy Analysis

For steady state benchmarking and sustained part load operation, an energy steps breakdown was shown in Figure 18 and Figure 29 where losses occurred in the electrolyzer and the resulting energy equivalent of hydrogen produced. For giving an equivalent overview of the entire breadth of dynamic testing, Figure 67 shows the specific energy consumption of electrolysis (kWh of electrical energy per kg of hydrogen produced) at the system level. It becomes particularly clear that operating the electrolyzer near the 0.4 A/cm² and lower entails massive losses with specific energy costs in the regime of 400 kWh/kg H₂ and higher (a 6-7x fold increase in energy cost from the rated specific energy consumption of 65 kWh/kg H₂ at full load).

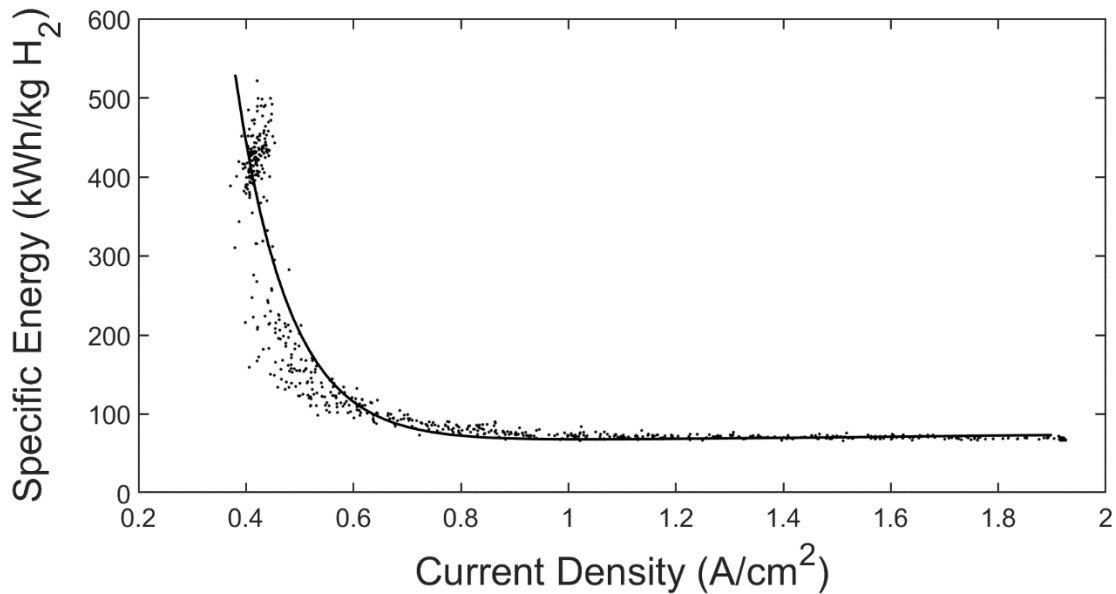


Figure 67. Specific energy cost of electrolyzer system versus current density.

The specific energy consumption of the system can be broken down into four sources of energy consumption – the electrolysis process or ‘stack’ energy consumption, the energy consumption of H₂ loss, energy consumption associated with the AC/DC power electronics, and the energy consumption of the balance of plant. Figure 68 shows this breakdown relative to Figure 67. As

current density decreases, the efficiency of the electrolysis process increases thus the downtrend in specific energy consumption for the stack. AC/DC power electronics and ancillary power consumption losses are roughly on the same order of magnitude and are similar in trend although ancillary power consumption increases steadily while the power electronics consumption remain largely flat. This trend continues until the minimum load condition is hit at roughly 0.4 A/cm² beyond which reductions in hydrogen output just dramatically increase specific energy consumption. Figure 69 shows the percentage share of the total system specific energy consumption.

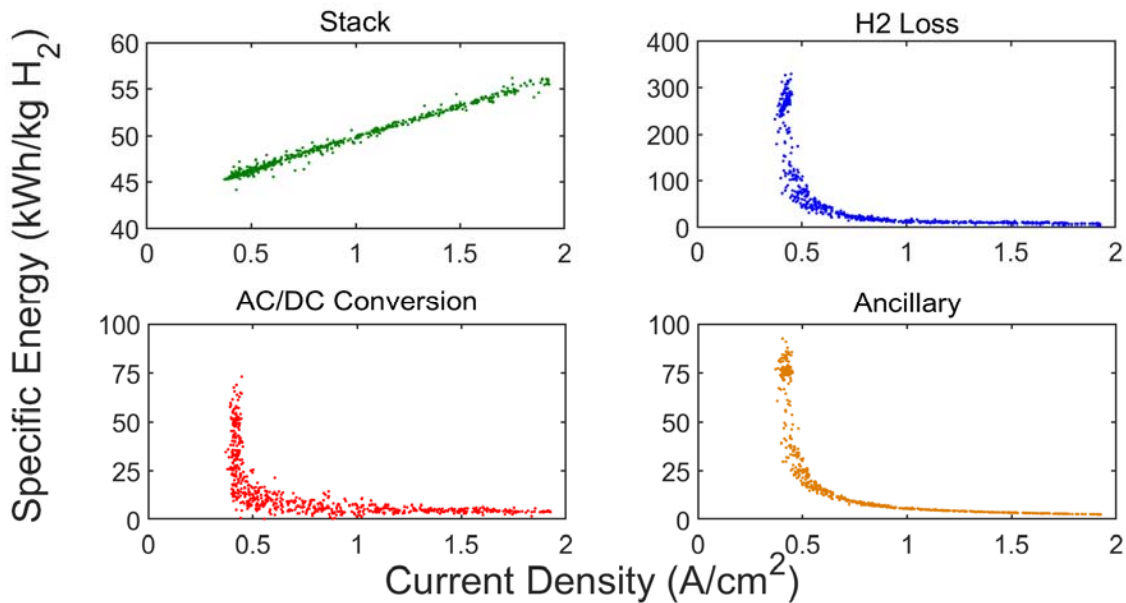


Figure 68. Specific energy consumption of electrolyzer system broken down by sources of energy consumption versus current density.

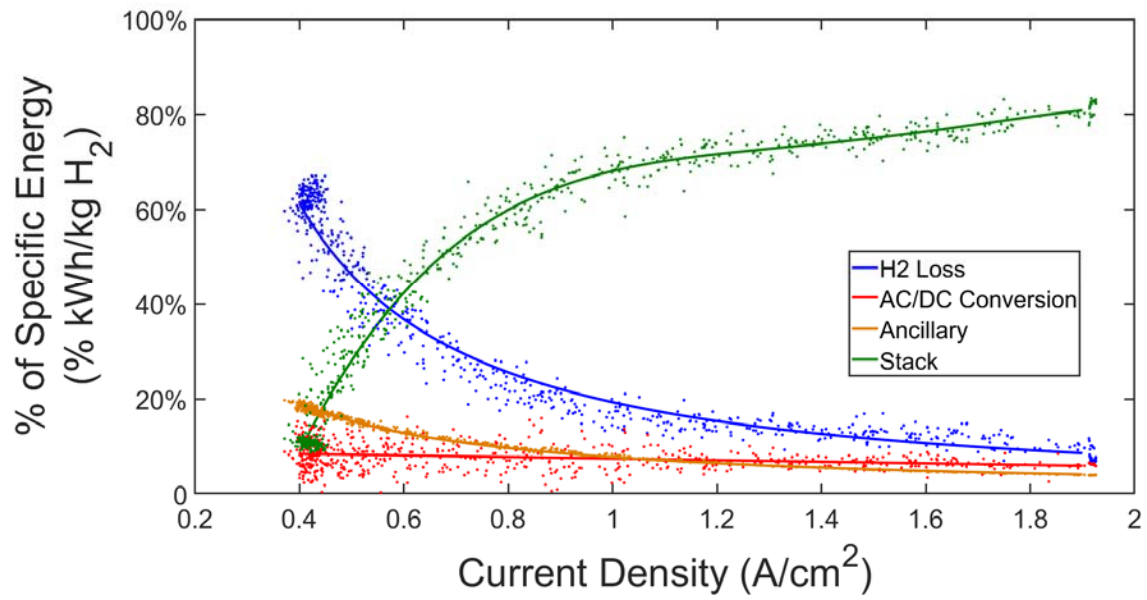


Figure 69. Percentage share of total specific energy consumption of hydrogen production by the electrolyzer system.

4.5.6 Degradation

Hours of operation were included in the ANOVA analysis for all analyzed responses to check for the possibility of degradation effects. Typically, PEM electrolyzer systems are expected to operate with lifetimes of 20,000 + hours, however power cycling of the cell leads to enhanced degradation [75]. Observable degradation is not an expected result nor were degradation mechanisms an aim of this study. Figure 70 shows system efficiency at full load and average mode parameter values versus total hours of operation. A general downtrend suggests that there may be observable degradation, however the large confidence intervals suggest that the downtrend is statistically insignificant.

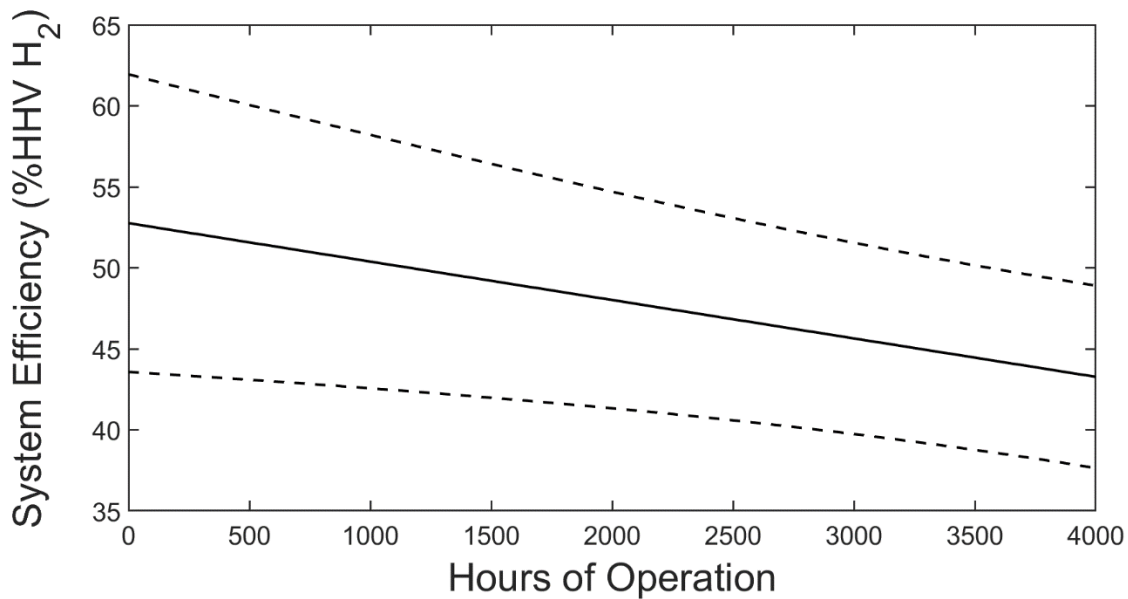


Figure 70. System efficiency versus hours of operation, 95% confidence intervals shown in dashed lines ($j = 1.92 \text{ A/cm}^2$, $P_{\text{H}_2} = 30 \text{ barg}$, $P_{\text{O}_2} = 1.5 \text{ barg}$).

Figure 71 breaks down the mechanisms that contribute to system efficiency and show their trends versus total hours of operation. Out of these, an increase in cell voltage is the only trend

that shows some significance. Tests that involved higher pressures and lower stack temperatures also occurred later in the operational period, which would lead to generally higher cell voltages. Ultimately, there is no clear degradation of the electrolyzer system after 4000 hours of operation.

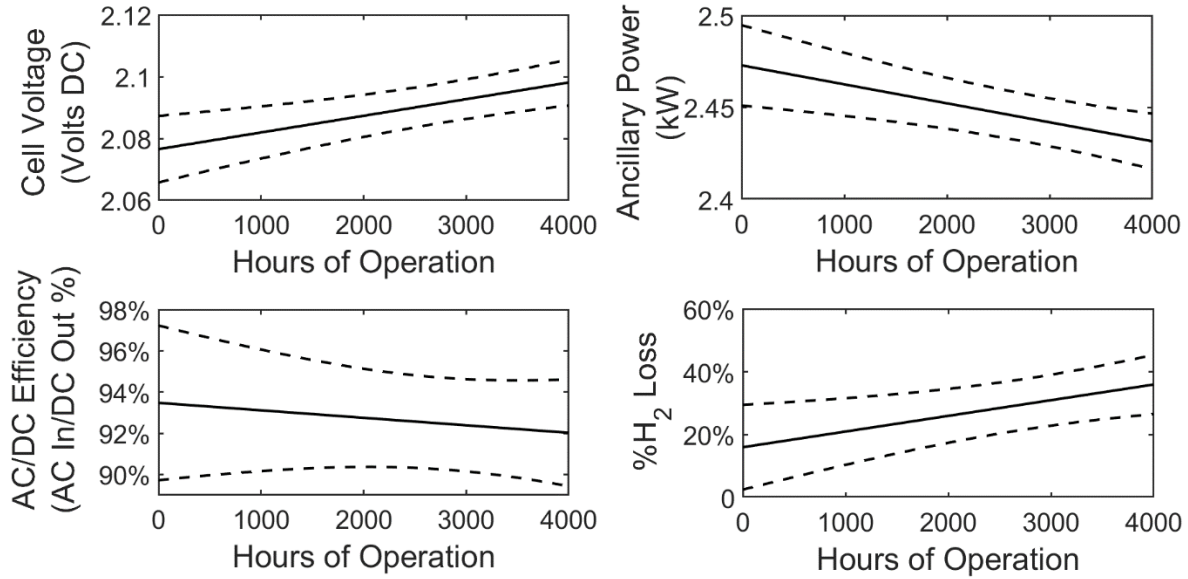


Figure 71. Cell voltage (Top Right), Ancillary Power Consumption (Top Left), AC/DC Efficiency (Bottom Left), %H₂ Loss (Bottom Right) versus hours of operation ($j = 1.92 \text{ A/cm}^2$, $P_{\text{H}_2} = 30 \text{ barg}$, $P_{\text{O}_2} = 1.5 \text{ barg}$, $T_{\text{Stack}} = 55 \text{ Celsius}$, $T_{\text{Ambient}} = 28 \text{ Celsius}$).

5 Hydrogen Injection & Combustion Turbine Impacts

The integration of hydrogen gas into pre-existing natural gas infrastructure is a promising pathway for adoption of power-to-gas. Natural gas in our region is supplied by the Southern California Gas Company (SoCalGas), whose storage facilities hold a net working gas capacity of roughly 3.8 cubic kilometers [76]. These gas storage facilities alone could provide 424 GWh of energy storage capacity in the form of injected hydrogen gas from power-to-gas activities at only 4% H₂ by volume in natural gas. In addition, the blending of hydrogen gas with natural gas results directly in decarbonization of emissions as hydrogen is a carbon free fuel. For these reasons, understanding the properties of hydrogen enriched natural gas and its effects on natural gas infrastructure and end uses is of critical importance for the successful implementation of power-to-gas. Furthermore, the introduction of hydrogen at higher and higher concentrations into existing natural gas infrastructure could provide for an eventually carbon neutral gas-based energy system without significant investment into entirely new infrastructure. Currently, broad studies carried out in the European Union [77] and the United States [78] cite ranges of 5-15% by volume hydrogen in natural gas infrastructure as a reasonable target that involves minimal modification of end use appliances. Concentrations greater than 20-30% were found to be a safety risk without modification of end use appliances [77]. The variation in injection range is a result of the wide variation in natural gas properties across regions, meaning that acceptable hydrogen concentrations will likely have to vary regionally or be set to the lowest of acceptable regional limits to maintain safety throughout the system.

5.1 Variation of Natural Gas Properties with Blended Hydrogen

Natural gas is a mixture of several lighter hydrocarbons, primarily methane, though appreciable amounts of ethane, propane, and butane are often present. In addition to the hydrocarbons, there are also highly variable amounts of impurities in the form of nitrogen, carbon dioxide, and even possibly trace amounts of hydrogen. A mass spectroscopy analysis of natural gas at the Engineering Lab Facility (ELF) at UC Irvine gave the following molar composition (Table 11).

Table 11. Mole fraction of natural gas constituents for Engineering Laboratory Facility – 1993.

% Mole Fraction			
Methane	95.800	Hexane	0.017
Ethane	1.400	Heptane	0.017
Propane	0.400	Octane	0.016
iso-Butane	0.050	Carbon Dioxide	1.900
n-Butane	0.050	Oxygen	0.000
iso-Pentane	0.025	Nitrogen	0.300

When gaseous fuels are interchanged in a combustion process, certain burner parameters may need to be adjusted to maintain the energy throughput, equation (5), and stability, as well as secondary characteristics such as the temperature profile which can influence emissions.

To maintain heat rate, the volumetric heat rate may need to be adjusted to compensate for differences in the heating value of the fuel. The Wobbe index is a commonly used indicator for the interchangeability of fuel gases on the basis of energy throughput. By taking the Bernoulli equation (6) for describing a steady-state, inviscid, incompressible and laminar flow condition from one point in a horizontal flow path to another, and combining with our heat rate expression (5), we can obtain the expression for the Wobbe index - equation (7).

$$\dot{q} = \dot{V} * HHV_{vol} \quad (5)$$

$$P_1 + \frac{\rho \dot{V}_1^2}{2} = P_2 + \frac{\rho \dot{V}_2^2}{2} \quad (6)$$

$$WI = \frac{HHV_{vol}}{\sqrt{SG}} \quad (7)$$

Appreciable differences in Wobbe index for a fuel intended to substitute the design specification fuel indicate that the combustor should be modified to maintain energy throughput at the fuel nozzle. This does not account for other combustion characteristics that are heavily influenced by the fuel gas such as stability (flashback and blow-off), flame length, temperature, and emissions that could also require modification of the combustor when substituting fuel gases. Wobbe Index then, accounts for the ability of a fuel gas to offer equivalent energy throughput in the same piping and burner and valve geometries present throughout the system.

Natural gas and hydrogen differ appreciably in density and heat content from one another. Table 12 below summarizes the characteristics of hydrogen and natural gas used throughout this study. Natural gas characteristics are based on the mass spectroscopy analysis from Table 11 above. Hydrogen gas is nearly one tenth the weight of natural gas on average. From a gravimetric standpoint, hydrogen is roughly three times as energy dense, however from a volumetric standpoint, hydrogen has less than a third of the energy density of natural gas. From a Wobbe index standpoint however, the interchangeability of natural gas and hydrogen gas start to appear favorable. Although hydrogen gas delivers less energy per unit volume, it also has a much lower specific gravity, allowing a greater amount of hydrogen to flow through the same orifice. The result is a Wobbe index that is within 10% of natural gas.

Table 12. Hydrogen and Natural Gas Characteristics (1 atm, 20 Celsius)

	Hydrogen [79]	Natural Gas
Density (kg/m ³)	0.083	0.707
Specific Gravity	0.070	0.588
LHV _{mass} (MJ/kg)	119.960	48.262
LHV _{vol} (MJ/m ³)	10.048	34.025
HHV _{mass} (MJ/kg)	141.800	53.552
HHV _{vol} (MJ/m ³)	11.877	37.754
Wobbe Index (MJ/m ³)	45.049	49.235

As hydrogen gas is blended in with natural gas, the volumetric heat content drops dramatically due to the large difference between the two. By itself, natural gas can vary in heating content an appreciable amount. In the case of southern California service territory, this can be observed in a recent LNG interchangeability study carried out by San Diego Gas & Electric (SDG&E) and SoCalGas. The study involved gas chromatograph measurements of pipeline gas at a number of locations across their service territory. The extremity of these measurements for the pipeline gas varied as much as 6.3 MJ/m³ above the national average [80] to 1.1 MJ/m³ below for an observed variation of 7.5 MJ/m³ (higher heating value basis) [81].

When it comes to the addition of hydrogen gas to natural gas, the closest analogue to specifications on fuel gas characteristics for injection to natural gas infrastructure is SoCalGas Rule No. 30 on transportation of customer-owned gas [82]. Rule 30 is intended to regulate the quality of biogas injection to SoCalGas pipelines and includes minimum and maximum limits on both higher heating value as well as Wobbe index. Taking the national average for higher heating value and Wobbe index for natural gas as the baseline, the variation in heating value and Wobbe

Index with the addition of hydrogen can be observed and compared to the limits imposed by Rule 30 as well as to the observed variation in natural gas quality. Figure 72 and Figure 73 show this variation for higher heating value and Wobbe index respectively.

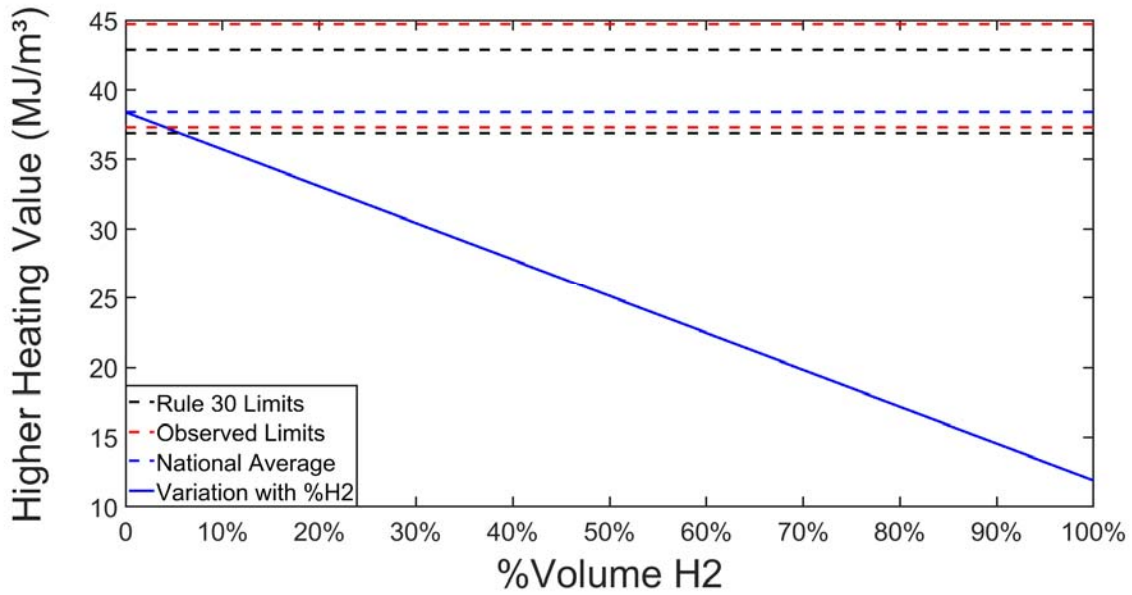


Figure 72. National average for higher heating value of natural gas balanced volumetrically with increasing amounts of hydrogen versus the observed limits of natural gas variation in higher heating value and rule 30 limits.

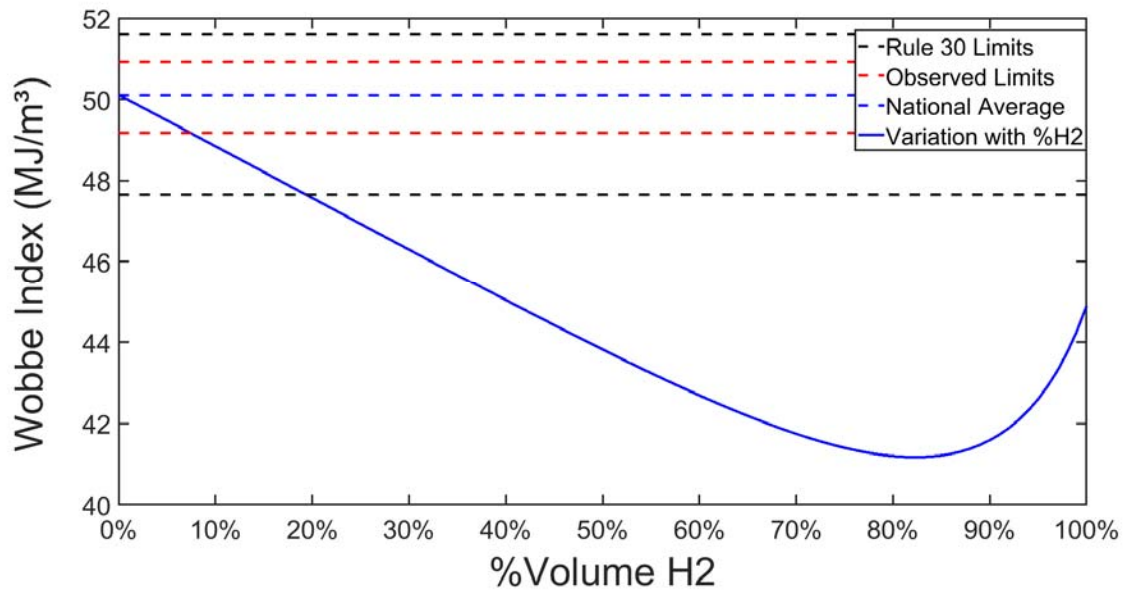


Figure 73. National average for Wobbe Index of natural gas balanced volumetrically with increasing amounts of hydrogen versus observed limits of natural gas variation in Wobbe Index and rule 30 limits.

It is readily apparent that the extent to which hydrogen can be blended with natural gas will be highly depend upon the initial quality of the natural gas. This idea has also been found to apply to other fuel gas interchangeability parameters such as burning velocity, flashback propensity, and yellow tipping [83]. Using the Rule 30 limits as representative limits for the addition of hydrogen, just under 5% by volume H₂ can be blended into natural gas, limited by higher heating value restrictions. On a Wobbe Index basis, this limitation is much closer to 20% by volume.

There is an appreciable difference in the allowable amount of hydrogen gas that can be injected depending upon the initial quality of gas. Table 13 summarizes the different allowable ranges of hydrogen gas by volume, on the same Rule 30 basis, for the two ‘extremes’ of observed natural gas quality.

Table 13. Allowable percentage of hydrogen by volume in natural gas for complying with Rule 30 standards on higher heating value and Wobbe Index

Natural Gas	Higher Heating Value	Wobbe Index
Max. Observed	23%	27%
National Average	5%	19%
Min. Observed	1%	13%

Ultimately, separate standards will need to be set for the addition of hydrogen to natural gas infrastructure based on careful study of its effects across the broad spectrum of natural gas end uses. Heating value and Wobbe Index alone do very little to capture the entirety of a fuel gases behavior for any given combustor. Still, Rule 30 can serve as a representative regulation for future regulation concerning hydrogen addition. In the case of this study, it serves to highlight the extent to which natural gas quality alone varies relative to quality requirements for third party injection of fuel gas to the pipeline.

5.2 Effects of Hydrogen Addition to Natural Gas on Gas Turbine Operation

The mass flow of fuel input to the combustion turbine is controlled via mass flow controller and adjusted automatically to maintain the current electrical load set point. Combustion turbines, especially when paired with heat recovery steam generators (HRSG), commonly use turbine exit temperature (TET) based feedback controls to adjust the incoming fuel mass flow rate for a given electrical load set point while maximizing energy flow to the HRSG [84]. This is the case for the Solar Turbines Titan 130 engine at UCI Central Plant utilized for this study.

Hydrogen has a higher adiabatic flame temperature than natural gas, and as a result tends to burn hotter than natural gas. For this reason, at higher hydrogen concentration regimes the heat input balance approach is not expected to predict the adjusted fuel mass flow for unmodified TET controls on a natural gas engine.

To predict the effects of hydrogen gas addition to the natural gas fired combustion turbine in the relatively low hydrogen concentration regime at which the electrolyzer is injecting, a heat rate balance approach is used, and then compared to observations. Hydrogen gas, being more gravimetrically energy dense, would be expected to cause a decrease in total fuel gas mass flow as a result of its addition to natural gas.

The reduction of natural gas usage in the combustion process by offsetting with hydrogen leads to a direct reduction in the amount of carbon present, ultimately leading to lower carbon dioxide emissions. For stationary power generation, the primary concerns with the addition of even small amounts of hydrogen are the potential impacts on criteria pollutant emissions (CO, NO_x), flame stability (flashback, exceedingly high turbine exit temperatures), the leakage of hydrogen through small cracks, and potentially causing increased degradation by metal embrittlement.

Historical data from UCI Central Plant was used to generate efficiency and heat rate curves for the combustion turbine. For the turbine balance calculations, lower heating value will be used as we are considering only the electrical power generation data for turbine output.

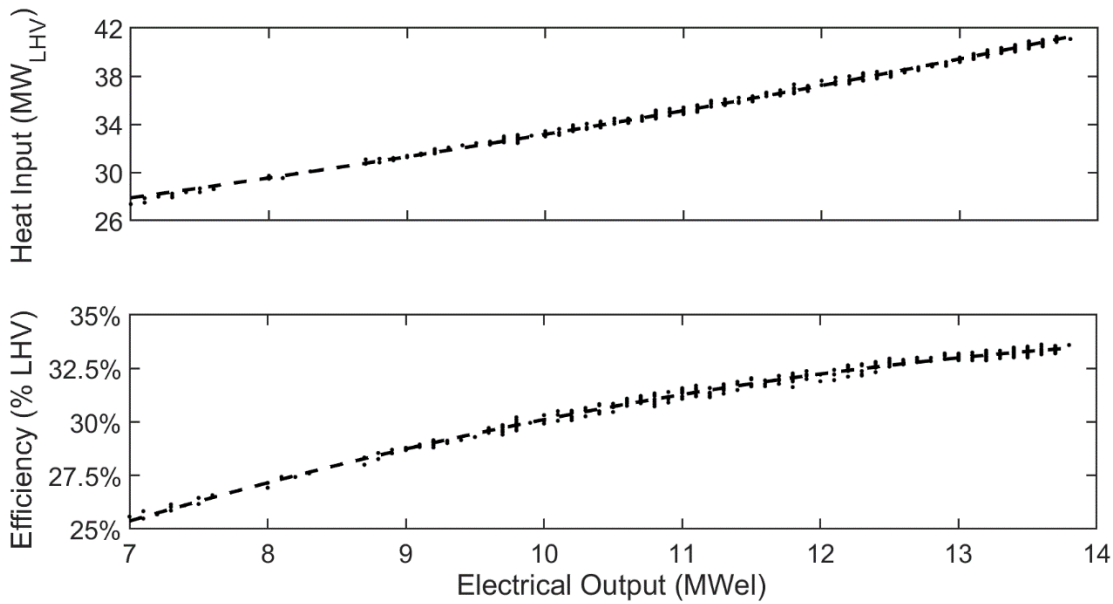


Figure 74. Heat rate (Top) and efficiency (Bottom) versus electrical load curve for UC Irvine Central Plant combustion turbine.

A curve fit of the heat input data versus the electrical output from the turbine was determined with high correlation ($R^2 = 99.73$), shown below in equation (8).

$$Heat_Rate_{LHV} = 18.62e^{0.058 * Electrical\ Output} \quad (8)$$

The total gas flow to the combustion turbine at full load (13.8 MWeI) is roughly 3200 kg/hr natural gas. At the minimum observed load of 7.0 MWeI, this gas flow goes down to approximately 2200 kg/hr natural gas. The predicted fixed heat rate trend of the turbine fuel gas flow as hydrogen is added is shown below in Figure 75.

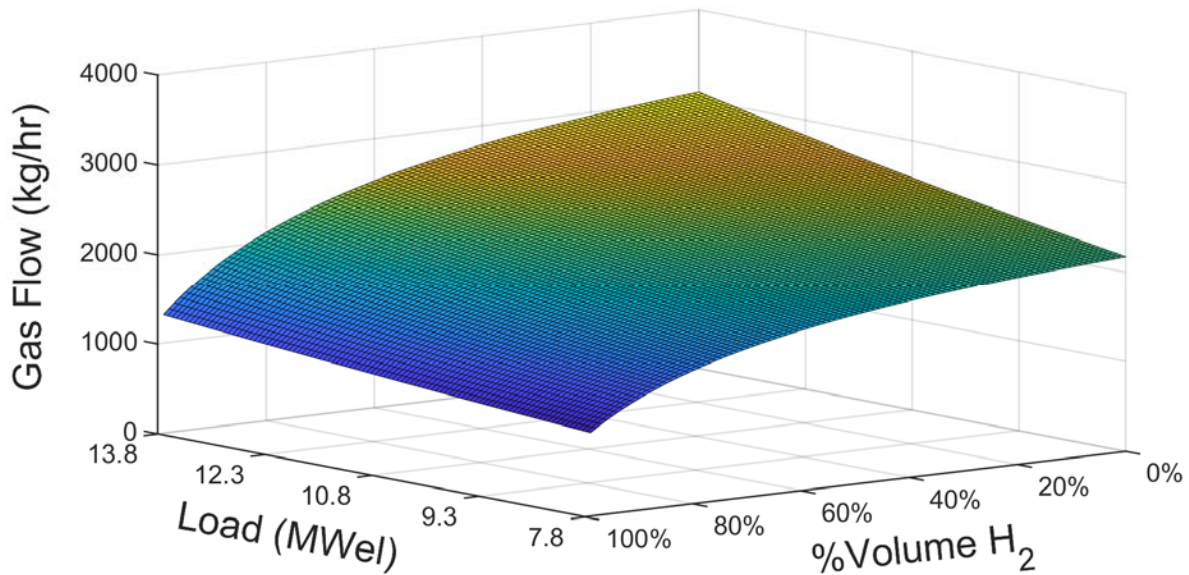


Figure 75. Combustion turbine fuel gas flow versus electrical load and % volume H₂.

Hydrogen's higher gravimetric energy density leads to notable offsets in natural gas mass flow, with each kg of hydrogen replacing 2.45 kg of natural gas on a lower heating value basis. From a volumetric perspective, 1% by volume hydrogen gas corresponds to 3.5 kg of hydrogen, for a net offset of 8.6 kg of natural gas usage.

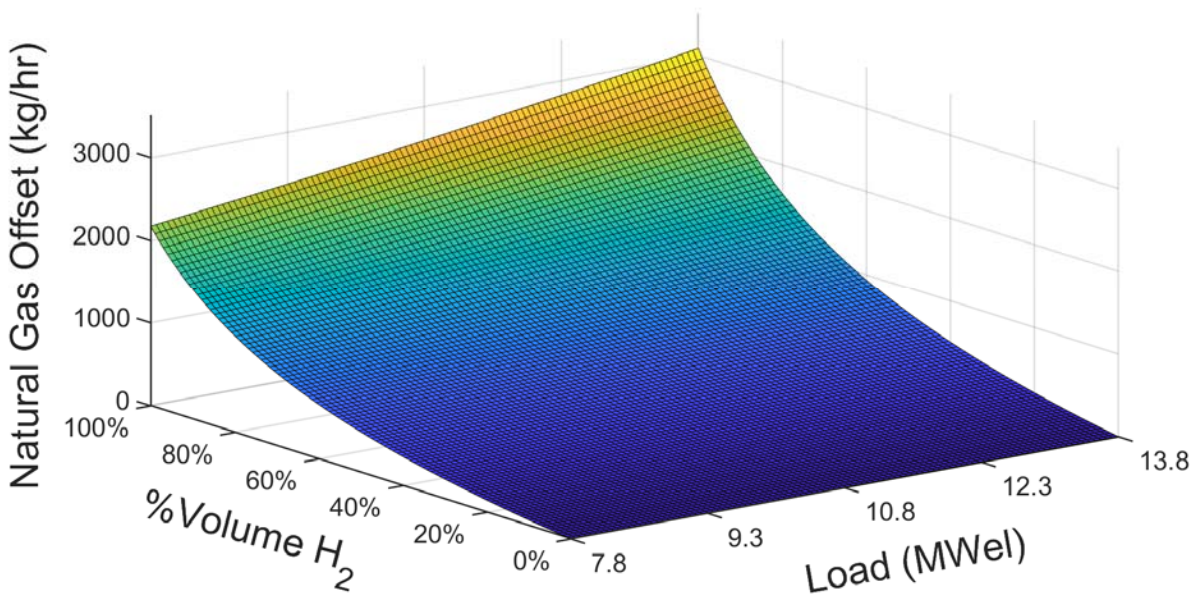


Figure 76. Combustion turbine natural gas offset versus electrical load and % volume H₂.

The reduction in usage of natural gas has a direct and quantifiable effect on net emissions of carbon dioxide. The U.S. EPA provides guidelines for assessing carbon dioxide emissions per unit of a particular fuel, referred to as emissions factors [85]. Using the molar composition of natural gas (Table 11) and the simplified stoichiometric equations for complete combustion, equations (9)-(12), the emissions factor of natural gas can be estimated at 2.67 kg CO₂/ kg Natural Gas (NG). This matches up well with pre-determined emissions factors for natural gas from the EPA which predict 2.69 kg CO₂/kg NG [86].

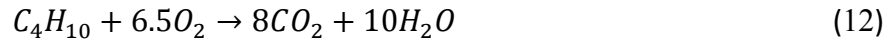


Figure 77 below shows the magnitude of carbon dioxide offset for hydrogen addition across turbine electrical load for fixed heat input. Each kg of hydrogen gas introduced ends up displacing 6.54 kg of carbon dioxide emissions. The reduction in carbon dioxide per increment of percentage by volume H₂ increases at higher hydrogen concentrations due to hydrogens lower density.

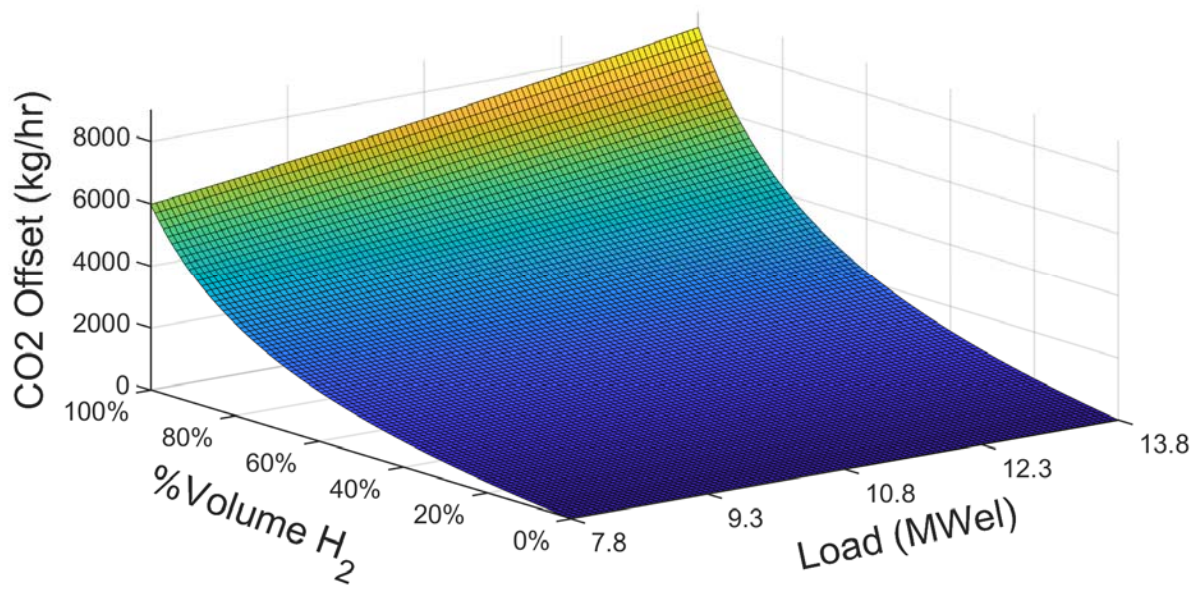


Figure 77. Combustion turbine carbon dioxide offset versus electrical load and % volume H₂.

5.3 Statistical Analysis (ANOVA) of Injection of Hydrogen produced by the Electrolyzer System to the Natural Gas Fired Combustion Turbine

Throughout all phases of testing, hydrogen produced by the electrolyzer system was injected downstream into a natural gas pipeline at an injection point within the UCI Central Plant (Figure 8). As the injection point is upstream of the combustion turbine, the entirety of this hydrogen gas is assumed to have been combusted in the turbine. UCI Central Plant personnel provided operational data for the combustion turbine from August 2016 to March of 2018, capturing all turbine operation during hydrogen injection, as well as data between injection for comparison.

At a maximum rate output of 0.91 kg/hr H₂, the magnitude of hydrogen flow from the electrolyzer system relative to the total fuel gas flow to the combustion turbine is several orders of magnitude smaller. Figure 78 below shows the expected range of observed percentage hydrogen gas by volume in the natural gas line as a result of electrolyzer output and turbine load conditions. The maximum expected percentage by volume of hydrogen that the electrolyzer system can achieve in natural gas ranges from 0.33% to 0.46%.

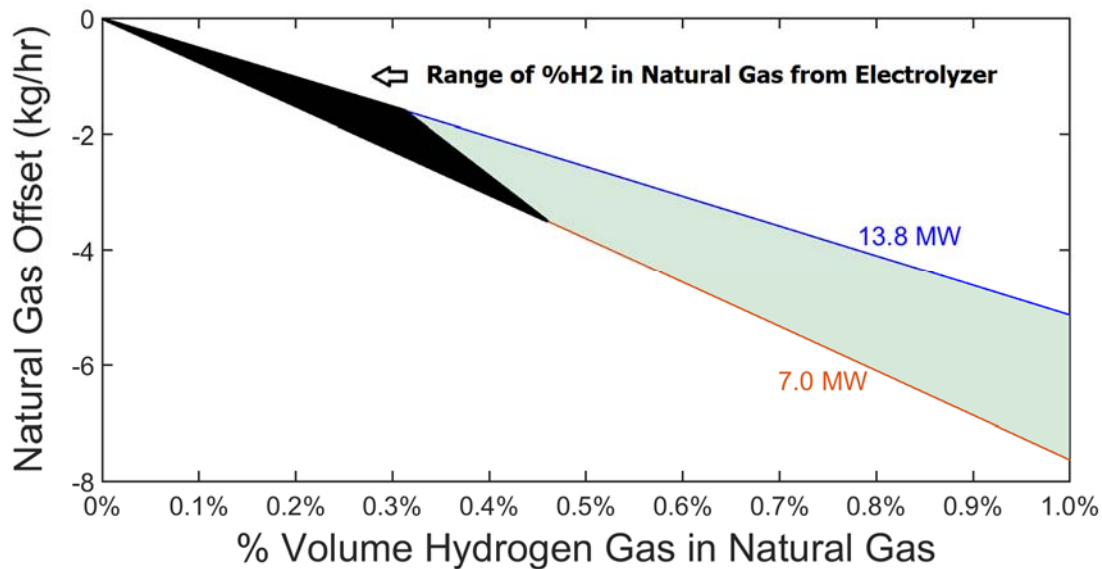


Figure 78. Expected natural gas flow offset with addition of hydrogen gas to the gas turbine fuel input.

Data collected from the turbine was time averaged from 1-minute intervals to hourly intervals and matched with hydrogen flow to the injection point. Effects of interest on turbine operation due to hydrogen addition is its influence on emissions. Emissions of carbon dioxide can be inferred from measured total fuel gas flow to the combustion turbine. Emissions of the criteria pollutants carbon monoxide and NO_x are monitored as well. Criteria pollutant emissions are only measured downstream of their respective catalytic clean-up processes, and as such, the 'raw' emissions from the combustion process are not available and the direct effect of hydrogen addition on these emissions is not observable. Due to the prevalence of these downstream emissions clean-up measures, it is still of great interest whether or not hydrogen influences the end emissions result. Despite the large population of data, there was an imbalance that influenced statistical analysis via ANOVA. No hydrogen injection was carried out on turbine set points below 9.3 MW_{el}, but data was collected on electrical set points as low as 7.0 MW_{el} with no hydrogen injection. As a result, the population that is considered below was orthogonalized to get rid of that particular imbalance. Figure 79 below shows the two populations of turbine data.

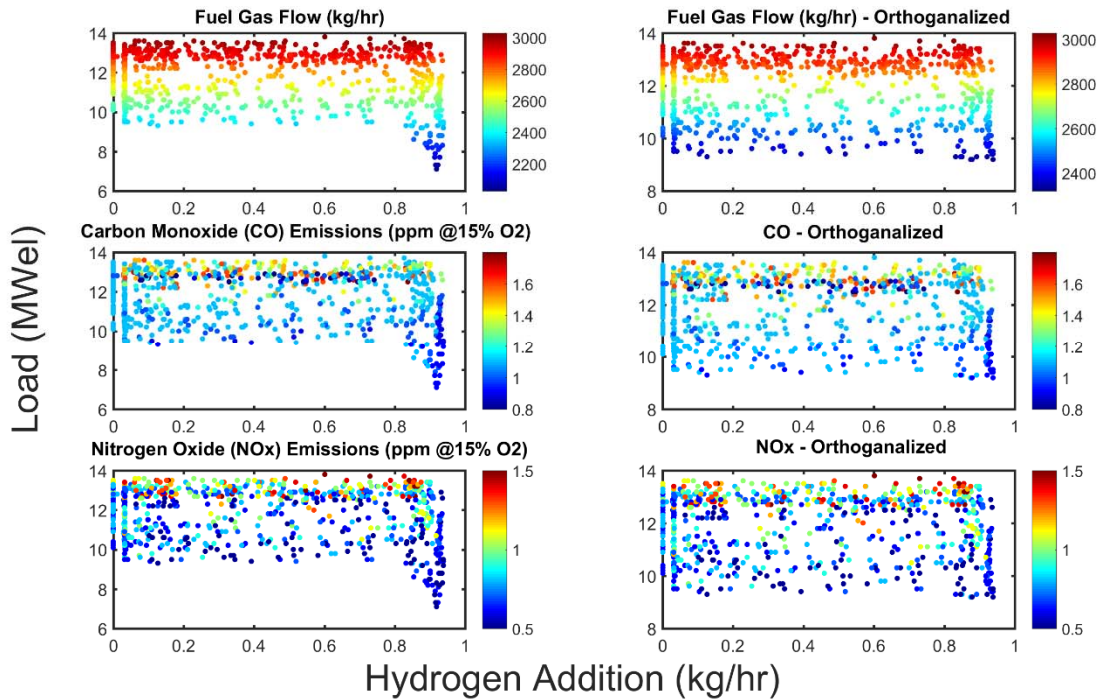


Figure 79. Population of turbine operation data versus hydrogen addition via injection from electrolyzer system throughout test period, all points (left) and orthogonalized input used for ANOVA (right).

The observed correlations of hydrogen addition (kg/hr) and turbine load (MW_{el}) with the three responses of interest (Total Fuel Gas Flow (kg), NOx (ppm @ 15% O₂), and CO (ppm @15% O₂)) are displayed in Figure 80. In all cases, turbine load is overwhelmingly more influential as a predictor, not surprising given the marginal amount of hydrogen addition. The slight negative correlation of hydrogen addition associated with all responses is interesting, but too small to be of significant meaning except potentially in the case of total gas flow.

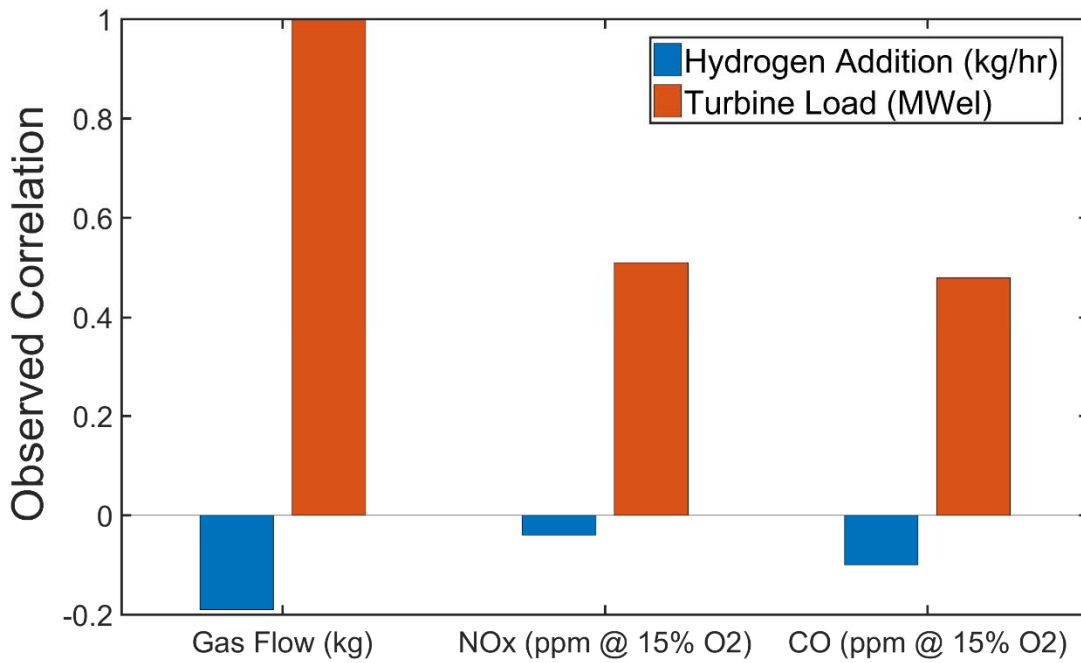


Figure 80. Observed correlation for turbine injection of hydrogen from electrolyzer system and turbine load against total fuel gas flow, NOx, and CO emissions using ANOVA analysis.

5.3.1 Effects of Hydrogen Addition on Gravimetric Gas Flow to Turbine

The results of the ANOVA analysis for total gas flow are summarized below in Table 14. The correlation of load versus gas flow is several orders of magnitude higher than hydrogen addition. Furthermore, the f-value of the hydrogen addition factor is so low relative to electrical load, and even relative to the SCR temperature factor, that the observed trend due to hydrogen addition (Figure 81) is highly uncertain.

Table 14. Summary of ANOVA analysis of the effects of hydrogen injection from the electrolyzer system, turbine electrical load, and SCR temperature on emissions of carbon monoxide post catalytic reduction from the combustion turbine.

	Sum of Squares	Degrees of Freedom	Mean Square	F Value	P-value (Prob > F)
A-H2	0.0000	1	0.0000	1.2678	0.2605
B-Load	4.5866	1	4.5866	142573.5349	<0.0001
C-SCR Temp	0.0121	1	0.0121	376.7809	<0.0001
Model	5.6285	3	1.8762	58319.2711	< 0.0001

Std. Dev.	187.943	R-Squared	0.9956
Mean	2735.136	Adj R-Squared	0.9956
C.V. %	0.2311	Pred R-Squared	0.9955
		Adeq Precision	785.1796

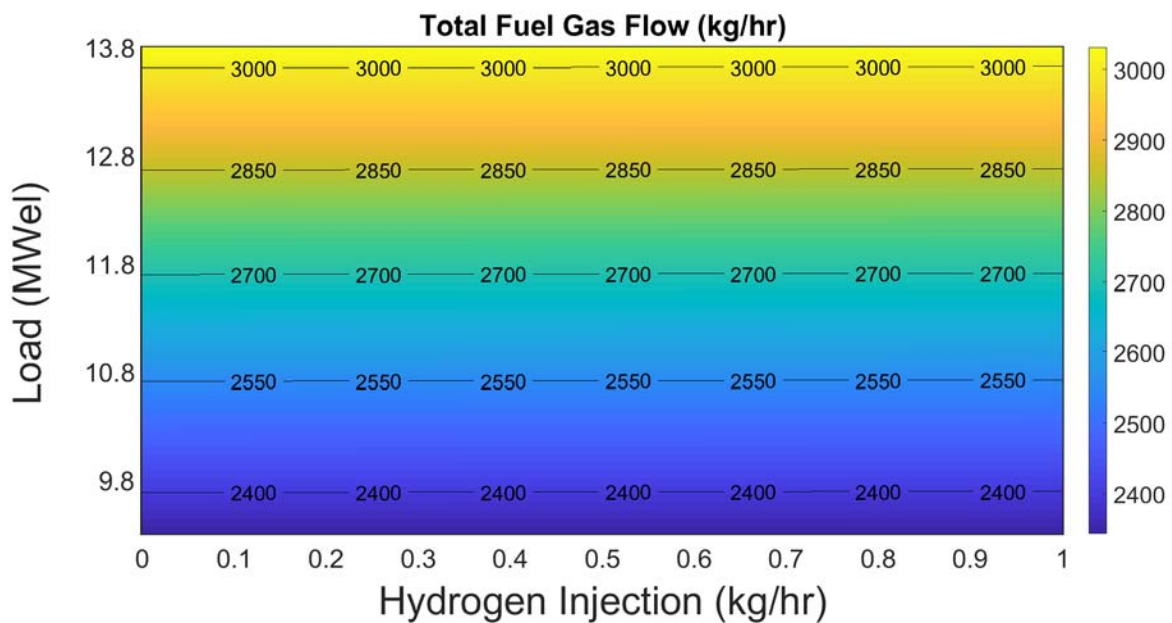


Figure 81. Contour plot of ANOVA predictive model for combined influence of turbine load and hydrogen injection on total fuel gas flow.

The predicted trend from the statistical model matches well with the expected variation in total fuel gas flow within the range measured (Figure 82). The average in natural gas offset predicted

from the ANOVA analysis per kg of hydrogen addition is 2.50 kg, however the 95% confidence intervals are relatively wide, with a lower range of 0.75 kg of natural gas offset per kg of hydrogen, and an upper range of 4.25 kg.

Extending the model outwards, the ANOVA prediction matches the prediction from the fixed heat rate prediction reasonably well (Figure 83). This suggests that at least for the lower ranges of hydrogen mixtures we are considering here in this study, for the predicted impact on fuel gas flow and by extension the reduction in carbon dioxide emissions due to hydrogen blending in natural gas, we can use a fixed heat rate calculation to predict the average effect of hydrogen addition. ANOVA analysis as a statistical tool only predicts significant means within the population and is not reliable for precise calculations. In this case, due to the low correlation, there is a large variation in gas flow for a given electrical load that is not accurately explained by the predicted effects of hydrogen injection, and more likely due to uncontrollable factors (of which there are many in the case of the combustion turbine).

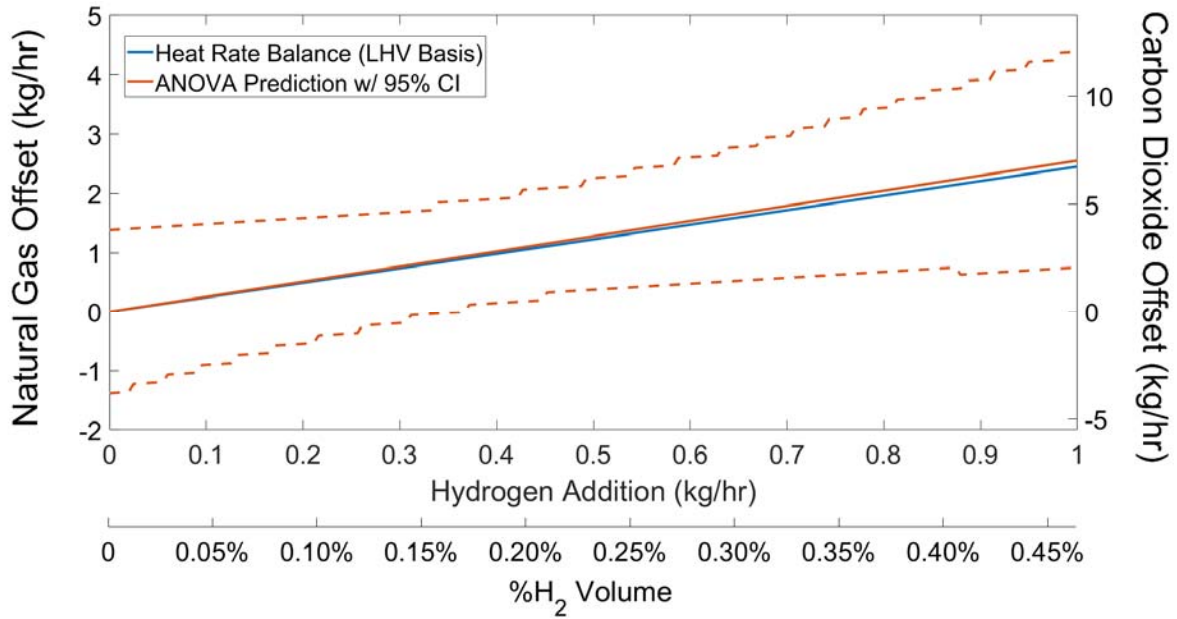


Figure 82. ANOVA predicted model with 95% confidence interval versus fixed heat rate prediction for offset of natural gas flow with the addition of hydrogen within range of testing (Turbine Load = 11.8 MW_{el}).

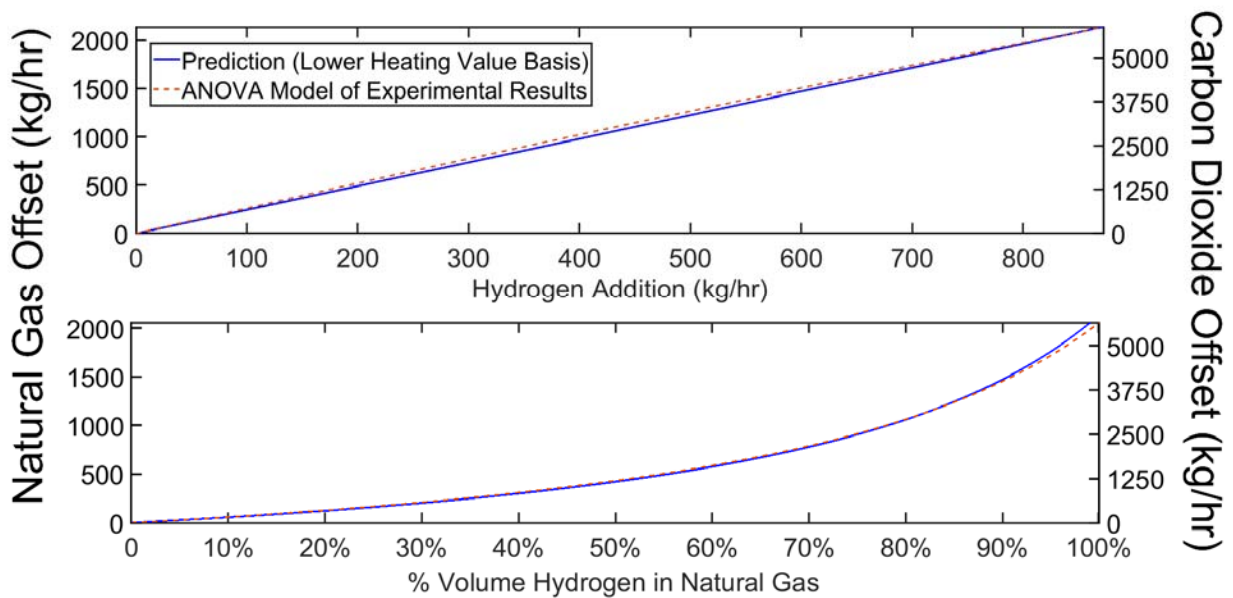


Figure 83. ANOVA predicted model versus fixed heat rate prediction for offset of natural gas flow with the addition of hydrogen up to 100% hydrogen (Turbine Load = 11.8 MW_{el}).

5.3.2 Effects of Hydrogen Addition on Carbon Monoxide (CO) Emissions

In the case of the criteria pollutant emissions, the accuracy of the ANOVA prediction improved appreciably with the inclusion of the selective catalytic reduction system (SCR) temperature. The ANOVA results are summarized below in Table 15. The amount of hydrogen being injected did not have anywhere near as much influence as load and SCR temperature.

The trend predicted by the ANOVA model for the addition of hydrogen is shown below in Figure 84. The range of carbon monoxide emissions (from 1 ppm to 1.4 ppm) is so limited that it is difficult to draw any real conclusions, when compounded with the limited range of hydrogen addition, as to the effects of hydrogen addition on such emissions.

Table 15. Summary of ANOVA analysis of the effects of hydrogen injection from the electrolyzer system, turbine electrical load, and SCR temperature on emissions of carbon monoxide post catalytic reduction from the combustion turbine.

	Sum of Squares	Degrees of Freedom	Mean Square	F Value	P-value (Prob >F)
A - H₂ (kg/hr)	0.0110	1.0000	0.0110	1.8491	0.1743
B - Load (MWel)	2.3612	1.0000	2.3612	398.6190	< 0.0001
C - SCR Temp (Celsius)	4.2247	1.0000	4.2247	713.2296	< 0.0001
AB	0.0257	1.0000	0.0257	4.3341	0.0377
AC	0.0387	1.0000	0.0387	6.5324	0.0108
BC	1.9609	1.0000	1.9609	331.0528	< 0.0001
A²	0.0912	1.0000	0.0912	15.4011	0.0001
B²	0.0492	1.0000	0.0492	8.3045	0.0041
C²	5.8618	1.0000	5.8618	989.6097	< 0.0001
Model	10.0496	9.0000	1.1166	188.5114	< 0.0001

Std. Dev.	0.0770	R-Squared	0.6815
Mean	0.8899	Adj R-Squared	0.6779
C.V. %	8.6483	Pred R-Squared	0.6699
		Adeq Precision	84.9563

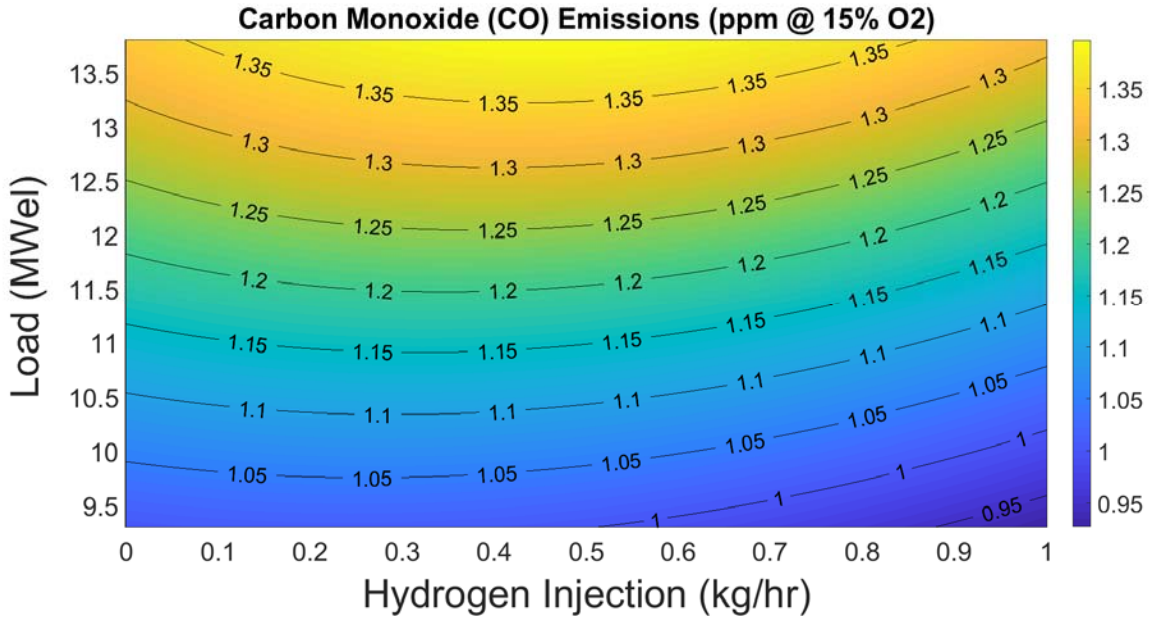


Figure 84. Contour plot of ANOVA predictive model for combined influence of turbine load and hydrogen injection on carbon monoxide emissions (SCR Temperature = 592 Celsius).

5.3.3 Effects of Hydrogen Addition on Emissions of Nitrogen Oxides (NO_x)

Table 16 summarizes the results of the ANOVA analysis on NO_x emissions. Given the low f-value and poor correlation, observed variation in NO_x emissions that is attributed to hydrogen addition is more likely due to other, uncontrollable factors.

The predicted trend for NO_x emissions as a function of hydrogen injection across load conditions is plotted in Figure 85. High loads correlated to higher NO_x concentrations is an expected result that matches up with similar studies on gas turbine emissions, as is the trend of increasing NO_x emissions with the addition of hydrogen observed at lower loads. However, at the higher load conditions, a downtrend in emissions is observed. This runs counter to observations made on unmodified natural gas fired turbines of similar scale when hydrogen was introduced, although the studies on these situations are limited [87] [88].

Table 16. Summary of ANOVA analysis of the effects of hydrogen injection from the electrolyzer system, turbine electrical load, and SCR temperature on emissions of nitrogen oxides (NO_x) post catalytic reduction from the combustion turbine.

	Sum of Squares	Degrees of Freedom	Mean Square	F Value	P-value (Prob >F)
A – H ₂ (kg/hr)	0.4293	1.0000	0.4293	5.3220	0.0213
B - Load (MWel)	30.3714	1.0000	30.3714	376.5170	< 0.0001
C - SCR Temp (Celsius)	11.2504	1.0000	11.2504	139.4723	< 0.0001
AB	1.4372	1.0000	1.4372	17.8166	< 0.0001
AC	0.0029	1.0000	0.0029	0.0365	0.8485
BC	15.5867	1.0000	15.5867	193.2298	< 0.0001
Model	4.7770	3.0000	1.5923	81.5634	< 0.0001

Std. Dev.	0.2840	R-Squared	0.4212
Mean	1.3543	Adj R-Squared	0.4169
C.V. %	20.9711	Pred R-Squared	0.4125
		Adeq Precision	56.8407

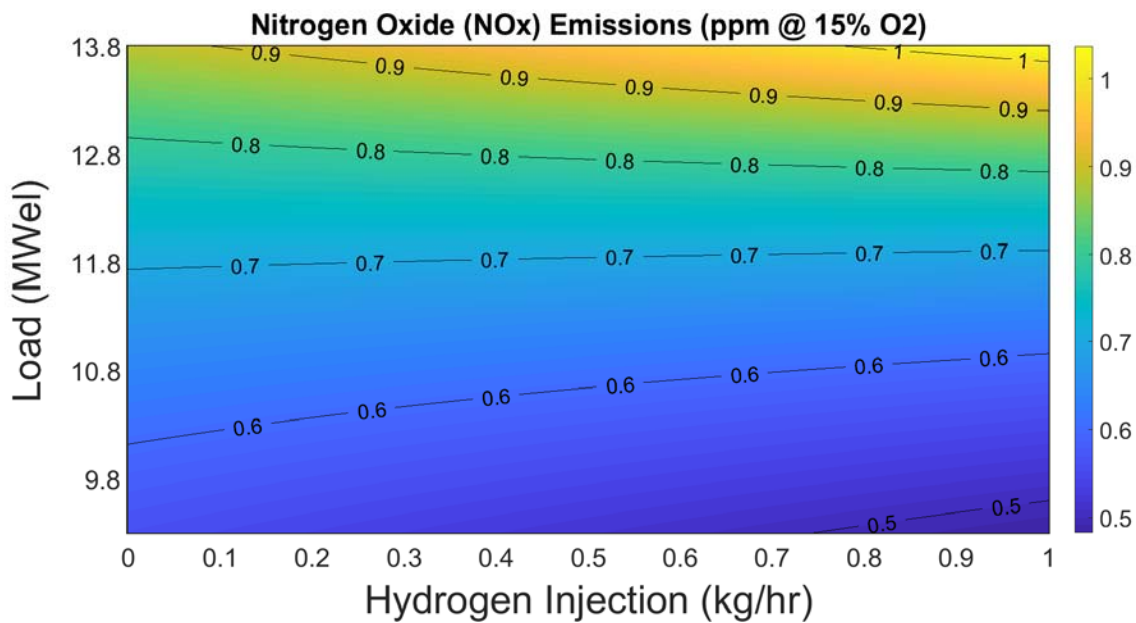


Figure 85. Contour plot of ANOVA predictive model for combined influence of turbine load and hydrogen injection on nitrogen oxides (NO_x) emissions (SCR Temperature = 592 Celsius).

5.4 High Throughput Hydrogen Injection Test

With a maximum observed hydrogen concentration of 0.38% by volume during operation of the electrolyzer system, it was desired to temporarily boost the hydrogen throughput to the injection point and observe the effects on turbine operation in the presence of relatively appreciable amounts of hydrogen.

Through discussion with UCI Central Plant Personnel and Solar Turbines, a maximum allowable limit of 4% by volume hydrogen in natural gas was determined. Due to the possibility of complications involving an essential campus resource, care had to be taken to avoid interrupting campus operations. As a result, the tests were confined to a one-day testing period to be carried out on a previously scheduled turbine shutdown.

To get the most information possible out of the limited test duration, a wide range of load conditions coinciding with the test period was desired. As load influences the responses of interest immensely (emissions of criteria pollutants & total fuel gas flow), repeated test points at a given load are also important. The ability to control the gas turbine load was given through approval from UCI Central Plant personnel, to whatever extent was possible given campus load conditions. Ancillary central plant equipment such as absorption chillers, could be turned off and on by the operator, at request, to impact the total campus load for roughly 1 MW of flexibility in load.

To otherwise maximize the range of turbine load conditions, the test schedule was set for two four-hour periods, from 6 AM to 10 AM to capture the campus ramping from mid-range to high load conditions, and 12 PM to 4 PM to capture minimum load conditions that occur as campus solar PV resources are at their peak. While these test periods seek to give us the broadest range of points possible, a review of June 2017 showed that on average the electrical load was 10.5

MW from 6 AM to 10 AM, and 11 MW from 12 PM to 4PM. Actual load conditions experienced will depend largely on uncontrollable factors.

Normally, for the purposes of eliminating noise in the ANOVA analysis, the level of hydrogen injection would be varied arbitrarily. In this case, to maintain stable operation at the turbine and avoid a premature shut-off, hydrogen output is ramped up and down sequentially between levels. Figure 86 shows the planned hydrogen output test points. Each test point is held at 15 minutes, and repeated twice, for a total test time of two hours during each four-hour period. This is to give a buffer for each four-hour test period.

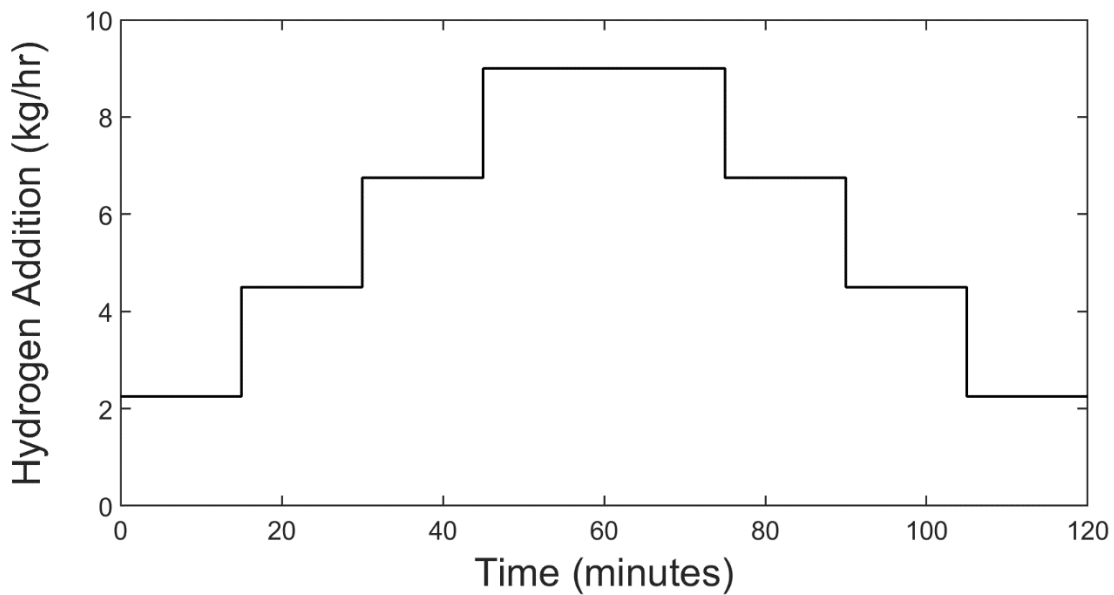


Figure 86. Planned hydrogen injection rates for high throughput hydrogen injection.

5.4.1 High Throughput Hydrogen Injection System

A separate injection system was constructed solely for this test. The total amount of hydrogen needed to accomplish the test points is 22.5 kg, with a maximum flow rate spec of 9 kg/hr. The maximum flow rate was determined by readily available equipment, specifically the Sierra Hi-Trak 840 mass flow controller (P/N#: 840H-4-OV1-SV1-D-V4-S4-HP), chosen for the injection system (Figure 87). This flow controller is a scaled-up version of the Sierra Hi-Trak 840H used in the electrolyzer dispatch. The primary difference between the two being a motor driven valve to allow for higher hydrogen throughputs (rated up to 60 SCFM H₂) at the high pressures needed for the injection process.



Figure 87. Sierra Hi-Trak 840 mass flow controller utilized in high throughput hydrogen injection testing.

Calibration of the flow controller was complicated by the large amounts of gas required, and the lack of ability to calibrate ‘in-situ’ at the Central Plant injection point. Calibrating ex-situ posed the issue of venting large amounts of hydrogen gas without construction of a proper calibration system. Additionally, the cost of the hydrogen needed to carry out multiple rounds of calibration was prohibitive. The decision was made to confirm the linearity of the flow controller and rated flow range using nitrogen gas due to its availability and its inert nature. The same control system used to dispatch the flow controller for electrolyzer testing was applied here with very little modification due to the similarity in flow controller operation.

A wide range of options for meeting the hydrogen supply were considered, including liquid tankers, gaseous trailer tanks, and gaseous cylinders. Due to restrictions in siting large, concentrated quantities of hydrogen gas, particularly near the natural gas compressor intake co-located with the injection point, gaseous cylinder ‘six-packs’ were selected to meet supply requirements. A 7’x 16’ area of concrete pad was available for siting of the cylinders, which could accommodate 10 size 300 six-packs of hydrogen gas cylinders.



Figure 88. Siting of the six-pack hydrogen cylinders at the UCI Central Plant on concrete pad space.

At the maximum cylinder pressure of 2400 psig (165.5 barg), the total hydrogen capacity of the 60 size 300 cylinders of H₂ is rated at 36.6 kg H₂. With a minimum pressure requirement of 500 psig (34.5) to ensure sufficient pressure drop through the injection system at maximum flow rate, only 28.4 kg of the H₂ is ‘usable’ from the cylinders. Airgas also cautioned that due to the size of the order, size 300 cylinder six packs may need to be substituted with the smaller size 200 six-packs. Each size 200 six pack substituting a size 300 six pack would result in a 0.5 kg H₂ loss, for a possible usable minimum of 23.6 kg H₂ in the event that all six packs are size 200s. As it turned out, Airgas was unable to provide any size 300 six-packs in the end, and total hydrogen supply was rated at the above 23.6 kg H₂.



Figure 89. Pressure regulator and cylinder manifold used in high throughput hydrogen testing.

To reduce the complexity of the injection system, as well as save cost on pressure regulation, all cylinders were manifolded on the high-pressure side, with a single high flow pressure regulator downstream of the cylinder manifold. On the day of testing, the original pressure regulator failed, venting large amounts of hydrogen, and was swapped out with the pressure regulator shown in Figure 89 above. No complications occurred with the second pressure regulator.

Relief valve lines were installed up and downstream of the mass flow controller to ensure that lines can be cleared of gas in the event of a flow controller failure. A summary of the entire injection system layout can be found below in Figure 90.

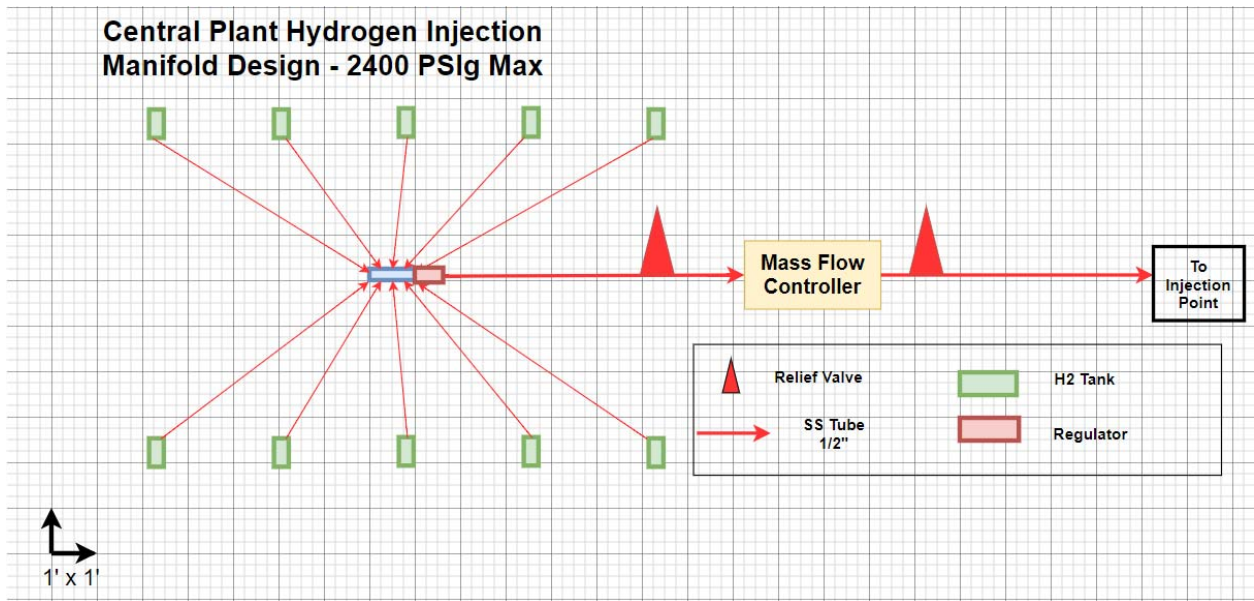


Figure 90. Injection system simplified process flow diagram.

5.4.2 Test Results

The one-time high throughput test was carried out on June 22nd, 2018. The day before, the injection system was leak tested at working pressures, and all system components were tested at low flow conditions (< 1 kg/hr H₂). On the day of testing, leakage on the output side of the flow controller required that portion of the system to be taken off site and tightened up before proceeding. After reinstalling the flow controller, hydrogen injection commenced at 9:07 AM. Final leakage rates were found to be negligible with respect to the injection rate measurements, estimated at 3 grams H₂ per minute downstream of the flow controller. Leakage upstream of the flow controller was mitigated to the point that it was no longer noticeable through conventional leak testing, but it is likely that small amounts of leakage persisted on the high-pressure side.

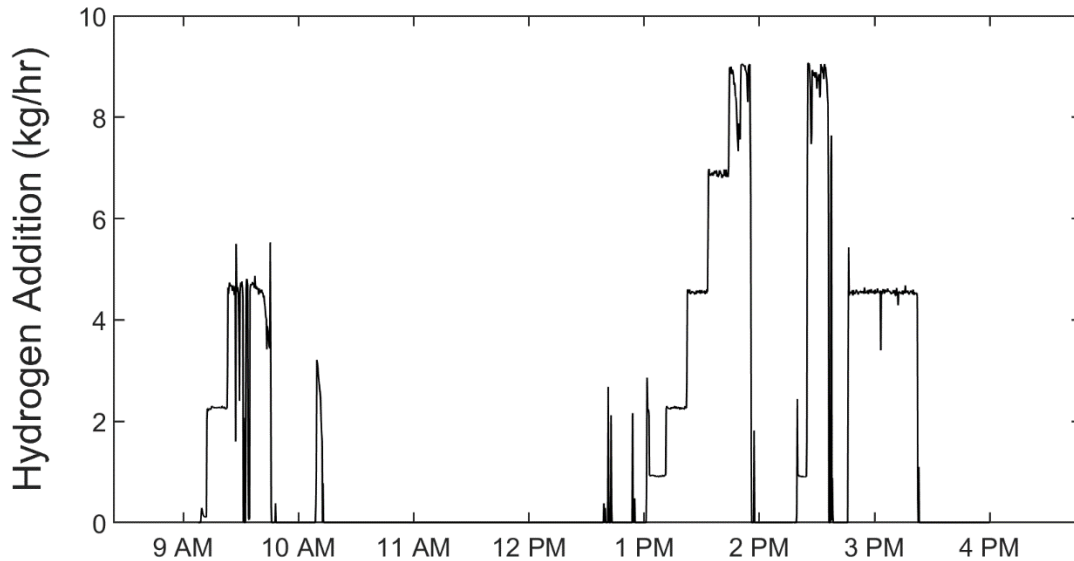


Figure 91. Hydrogen output (kg/hr) from mass flow controller for high throughput hydrogen injection test on June 22nd, 2018.

Figure 91 below shows the hydrogen injection during the day of testing. At 4.6 kg/hr, the pressure regulator prematurely experienced lock out, and could not handle any higher flows while continuing to regulate pressure. The faulty regulator was removed from the line at 10:30

AM, and a new regulator was identified and reinstalled at approximately 12:25 PM. Testing continued at 1 PM, and the new regulator was able to handle the entire flow regime. At maximum flow (9.1 kg/hr H₂) six packs were dropping from full pressure to minimum injection pressure in under 3 minutes. Only one six pack was open at a time during testing to limit the amount of hydrogen that would escape in the event of a critical injection failure. These two factors combined meant that at full flow, the pressure regulator had to be actively adjusted to maintain output pressure and by extension the flow rate. Additionally, cylinders had to be opened in-situ to keep up with the flow rate. For this reason, the maximum flow regime periods were relatively unstable. A total of 11.5 kg of H₂ was injected, far short of the expected 23.6 kg of H₂ available with all size 200 cylinders. All cylinders were observed to be somewhat short of the 2000 psig ‘full’ rating, and some cylinders were exhausted during the pressure testing of the lines and the initial pressure regulator failure. Combined with a small amount of leakage upstream of the flow controller, this likely accounts for the disparity in hydrogen amounts.

Due to higher than average temperatures and high relative humidity with respect to weather, the campus load remained higher than average throughout the day. Figure 92 shows the turbine electrical load and fuel gas flow for the duration of the injection testing. The minimum load set point for the day was 11 MW_{el}, during which the average minimum fuel gas flow was 2562 kg/hr. From 2 PM to 4 PM the Central Plant operator was able to take one adsorption chiller down to step down the load to the 11 MW_{el} mark for a short period of time, and then ramped up the chiller in the stepwise pattern shown to 11.8 MW_{el}. The shutdown schedule proceeded on

time; spin-down began at approximately 3:30 PM.

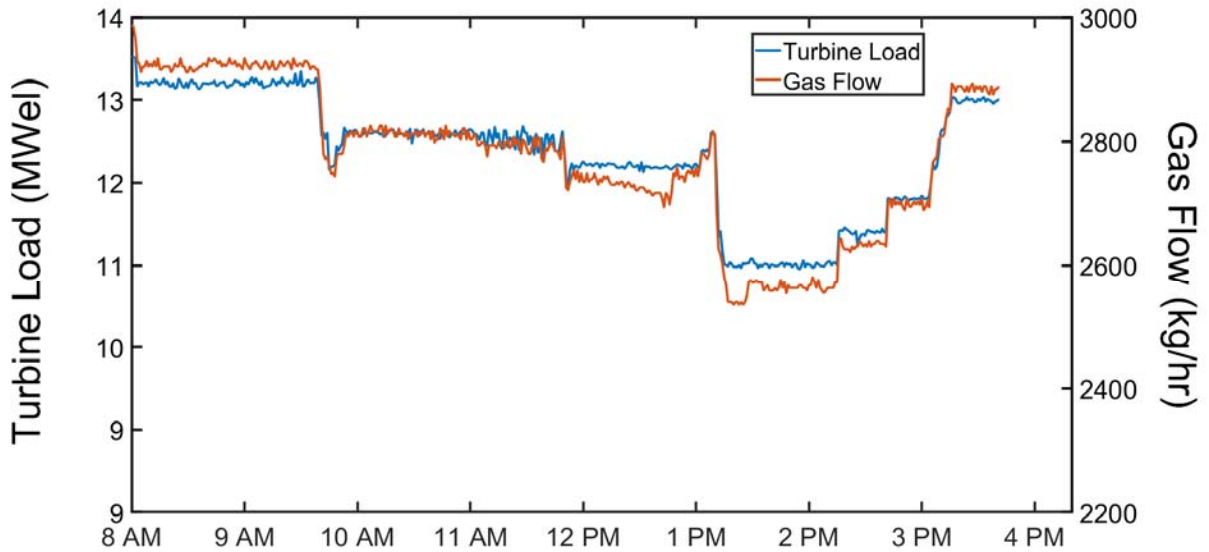


Figure 92. Turbine electrical load and gas flow during high throughput hydrogen injection test on June 22nd, 2018.

The resulting volumetric concentrations of hydrogen in balance with natural gas is shown below in Figure 93. A maximum observed concentration of 3.4% by volume fell well short of the 4% by volume upper limit, largely due to the limited range of turbine load on the day of testing. The total range of data matches poorly with the expectations set in Figure 86, however given the nature of the test this was not an unexpected result.

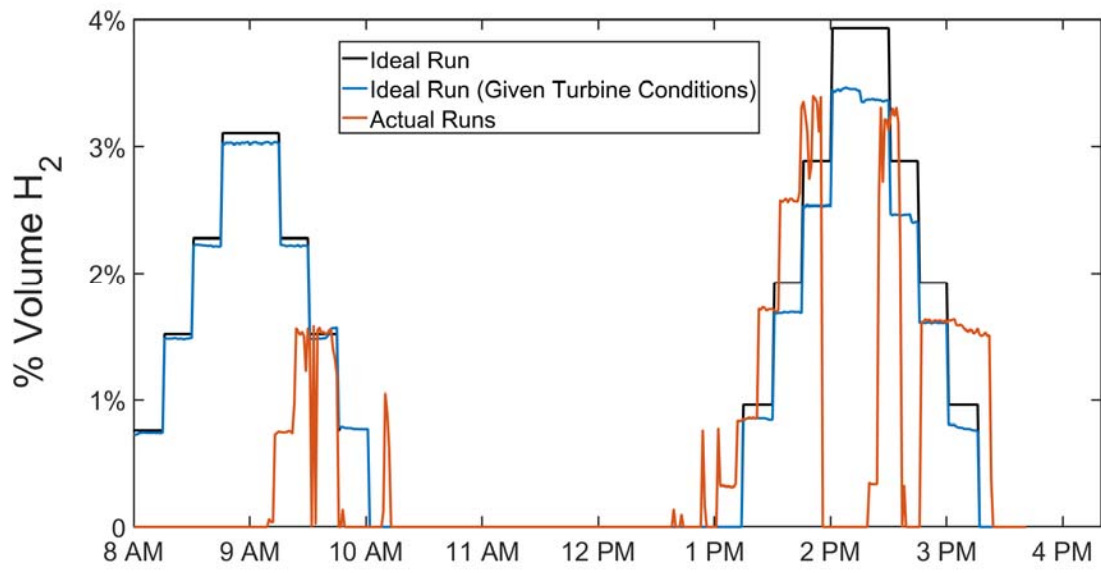


Figure 93. Percentage of hydrogen in fuel gas flow to combustion turbine at UCI Central Plant during high throughput hydrogen injection test on June 22nd, 2018.

5.4.3 Effects of Hydrogen Addition on Gravimetric Gas Flow to Turbine

Similar to what was previously observed from the electrolyzer-based injection testing, the influence of hydrogen addition on the natural gas fuel flow remains questionable, even at sustained flow rates of ten times larger than the electrolyzer output. Table 17 displays the results of the ANOVA for the observed variation in fuel gas flow. The load condition of the turbine again dominates as the predicting variable, and the SCR temperature was included in the analysis as its variation better explained the small variations in fuel gas flow at sustained load conditions. As a result, the addition of SCR temperature helped reduce obfuscation of the predicted effects that hydrogen addition had on fuel gas flow.

Table 17. Summary of ANOVA analysis of the effects of hydrogen injection from the high throughput hydrogen injection testing on net gravimetric fuel gas flow.

	Sum of Squares	Degrees of Freedom	Mean Square	F Value	P-value (Prob >F)
A – H₂ (kg/hr)	55.3801	1.0000	55.3801	1.5490	0.2352
B - Load (MWel)	2.73E+05	1.0000	2.73E+05	7624.6844	< 0.0001
C - SCR Temp (Celsius)	212.1363	1.0000	212.1363	5.9337	0.0300
AC	121.4296	1.0000	121.4296	3.3965	0.0882
Model	316047	4.0000	79012	2210	< 0.0001

Std. Dev.	5.9792	R-Squared	0.9985
Mean	2722.6169	Adj R-Squared	0.9981
C.V. %	0.2196	Pred R-Squared	0.9974
		Adeq Precision	114.7212

Figure 94 displays the trend in fuel gas flow as a function of turbine load and hydrogen addition as predicted by the ANOVA model. At zero hydrogen addition, the total amount of fuel gas flow for a given load condition was observed to be higher on average than what was found in the

larger injection study (Figure 81). Given that the high throughput testing was carried out on the last day of preceding scheduled quarterly maintenance, when turbine performance is generally at its lowest, this is to be expected. The range of turbine load conditions observed was limited as well, narrowing the study to the range of 11 MW_{el} to 13.2 MW_{el}.

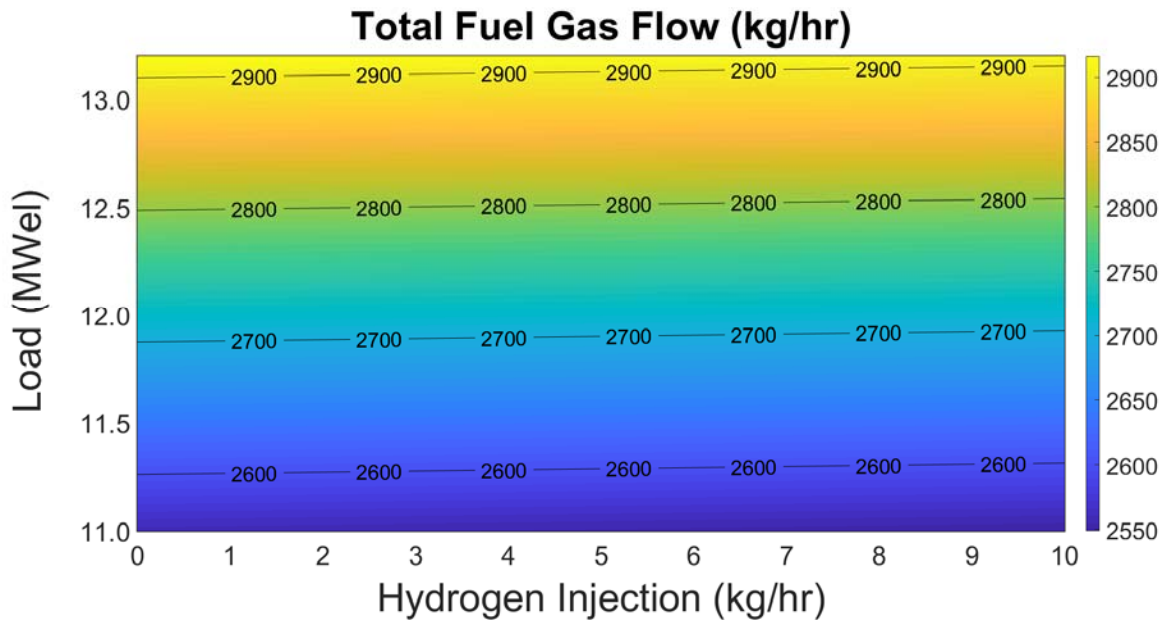


Figure 94. Contour plot of ANOVA predictive model for combined influence of turbine load and hydrogen injection on total fuel gas flow for high throughput hydrogen testing.

The predicted offset in natural gas as a result of the ANOVA analysis is shown below, compared against the heat balance prediction (Figure 95). Unfortunately, the wide range of hydrogen injection did not result in a stronger trend for hydrogen addition influencing fuel gas flow. The agreement is not as strong as what was previously observed in the electrolyzer injection study, but the general trend is similar. The 95% confidence intervals are much larger, giving an average offset of 1.9 kg of natural gas usage per kg of H₂ added, varying from 0.04 kg up to 3.75 kg of natural gas for the highest confidence intervals around 2.2 kg/hr hydrogen flow rate. This is lower than what was previously observed, but within the wide range of uncertainty previously

observed as well. The wide uncertainty range can be seen as a result of the low significance of hydrogen addition in predicting fuel gas flow.

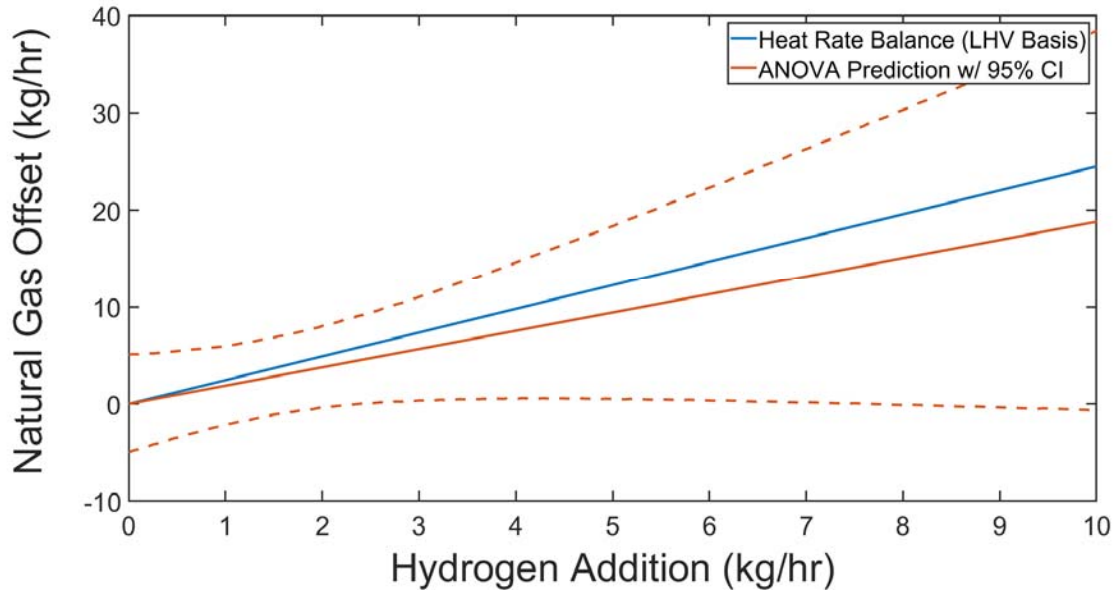


Figure 95. Predicted natural gas offset due to hydrogen injection from ANOVA analysis with 95% confidence intervals versus expected natural gas offset on a lower heating value basis for high throughput hydrogen testing.

5.4.4 Effects of Hydrogen Addition on Carbon Monoxide (CO) Emissions

Emissions of carbon monoxide did not vary appreciably throughout the day of testing, only varying between 1.05 and 1.08 ppm @ 15% O₂ (as opposed to historical observations varying between 0.6 up to 1.5 ppm @ 15% O₂). As a result, no correlation of significance for CO emissions can really be drawn outside of the definite positive correlation with turbine load. For posterity, the results of the ANOVA analysis are shown below in Table 18. The contour plot of the ANOVA model for the effects of turbine load and hydrogen addition is shown in Figure 96. This lack of observed variation in emissions reinforces the supposition that hydrogen addition in the ranges studied does not have any influence on carbon monoxide emissions for a combustion turbine with catalytic clean-up.

Table 18. Summary of ANOVA analysis of the effects of hydrogen injection from the high throughput hydrogen injection testing on post catalytic clean-up carbon monoxide emissions.

	Sum of Squares	Degrees of Freedom	Mean Square	F Value	P-value (Prob >F)
A – H₂ (kg/hr)	0.0001	1.0000	0.0001	2.8022	0.1223
B - Load (MWel)	0.0005	1.0000	0.0005	13.3244	0.0038
C - SCR Temp (Celsius)	< 0.0001	1.0000	0.0000	0.0753	0.7888
AB	< 0.0001	1.0000	0.0000	0.6445	0.4391
AC	0.0001	1.0000	0.0001	1.6531	0.2249
BC	0.0001	1.0000	0.0001	4.1257	0.0671
Model	0.0012	6.0000	0.0002	5.7336	0.0063

Std. Dev.	0.0060	R-Squared	0.7577
Mean	1.0675	Adj R-Squared	0.6256
C.V. %	0.5638	Pred R-Squared	0.3030
		Adeq Precision	8.2863

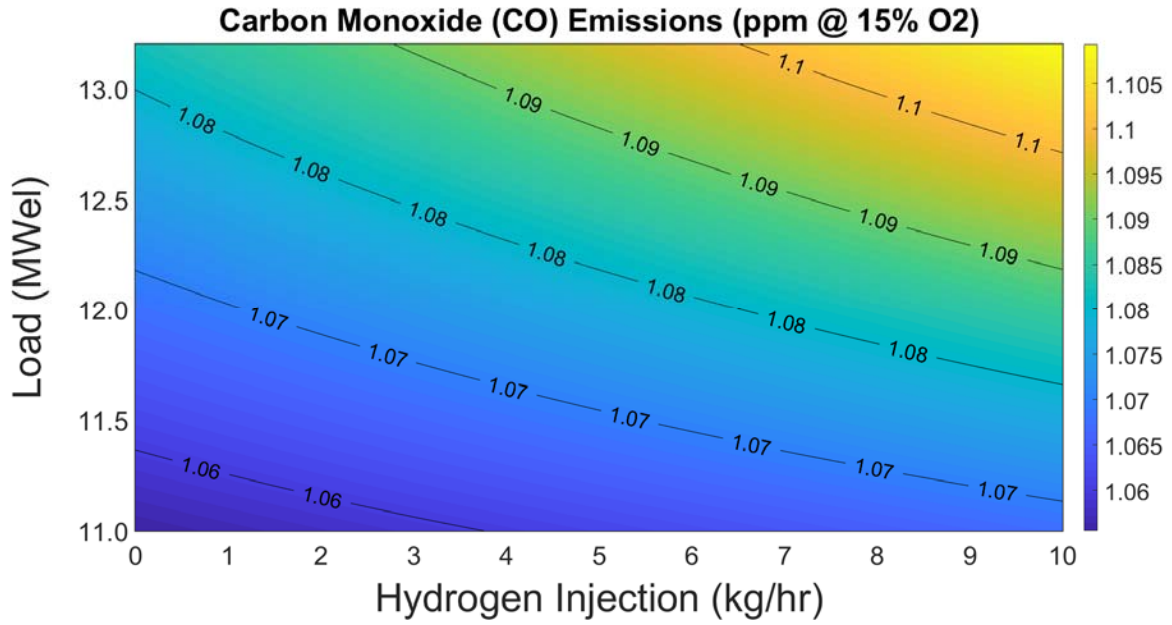


Figure 96. Contour plot of ANOVA predictive model for combined influence of turbine load and hydrogen injection on carbon monoxide emissions for high throughput hydrogen testing.

5.4.5 Effects of Hydrogen Addition on Emissions of Nitrogen Oxides (NO_x)

Emissions of nitrogen oxides did not vary appreciably throughout the day of testing, limited to an observed range of 0.5 to 0.8 ppm @ 15% O₂. For this reason, no significant correlation for the factors of interest had any appreciable impact on nitrogen oxide emissions. Table 19 summarizes the ANOVA analysis for nitrogen oxide emissions, with no stand-out variables for explaining the variance in nitrogen oxide emissions. Figure 97 shows the contour plot of nitrogen oxide emissions as a function of turbine load and hydrogen addition as predicted by the ANOVA model. The trends shown in Figure 97 are highly likely to not be indicative of the actual effects of these factors on nitrogen oxide emissions due to the low strength of the model. This result reinforces the previous results that hydrogen addition does not have any impact on the ultimate nitrogen oxide emissions and combined with the results for the carbon monoxide emissions, does not affect emissions of criteria pollutants from the combustion turbine and its pollution controls.

Table 19. Summary of ANOVA analysis of the effects of hydrogen injection from the high throughput hydrogen injection testing on post catalytic clean-up nitrogen oxide emissions.

	Sum of Squares	Degrees of Freedom	Mean Square	F Value	P-value (Prob >F)
A – H₂ (kg/hr)	0.4293	1.0000	0.4293	5.3220	0.0213
B - Load (MWel)	0.0188	1.0000	0.0188	4.8218	0.0504
C - SCR Temp (Celsius)	0.0161	1.0000	0.0161	4.1237	0.0672
AB	0.0494	1.0000	0.0494	12.6690	0.0045
AC	0.0019	1.0000	0.0019	0.4907	0.4982
BC	0.0131	1.0000	0.0131	3.3539	0.0942
Model	0.1020	6.0000	0.0170	4.3590	0.0170

Std. Dev.	0.0624	R-Squared	0.7039
Mean	0.6032	Adj R-Squared	0.5424
C.V. %	10.3506	Pred R-Squared	0.4079
		Adeq Precision	7.0258

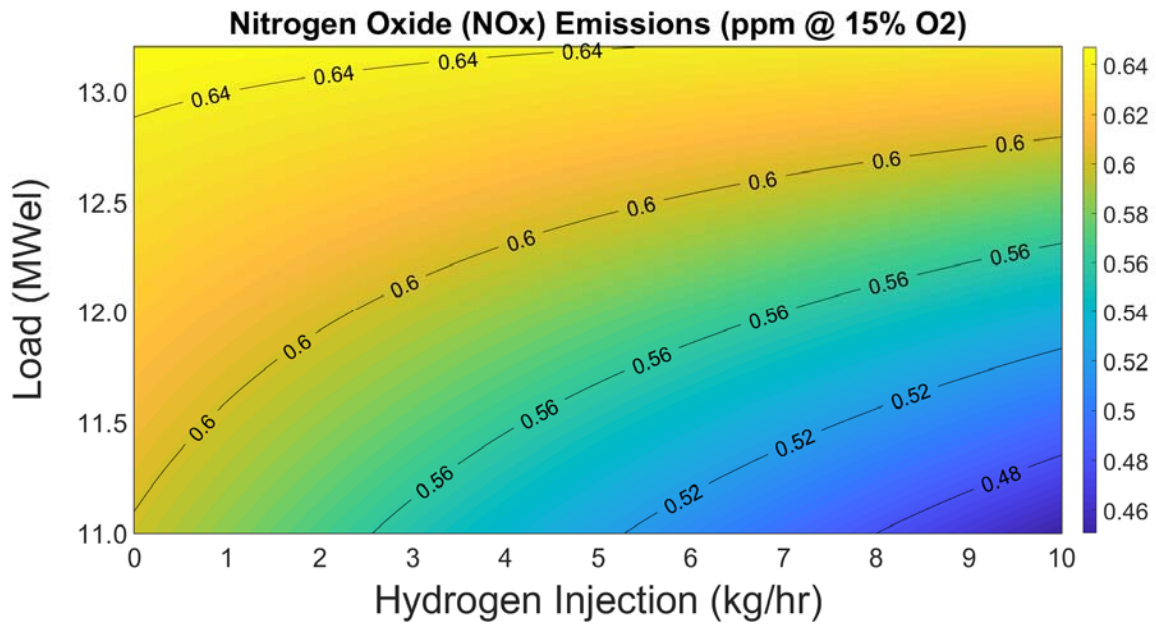


Figure 97. Contour plot of ANOVA predictive model for combined influence of turbine load and hydrogen injection on nitrogen oxide emissions for high throughput hydrogen testing.

6 Semi-empirical Thermodynamic Model of PEM Stack

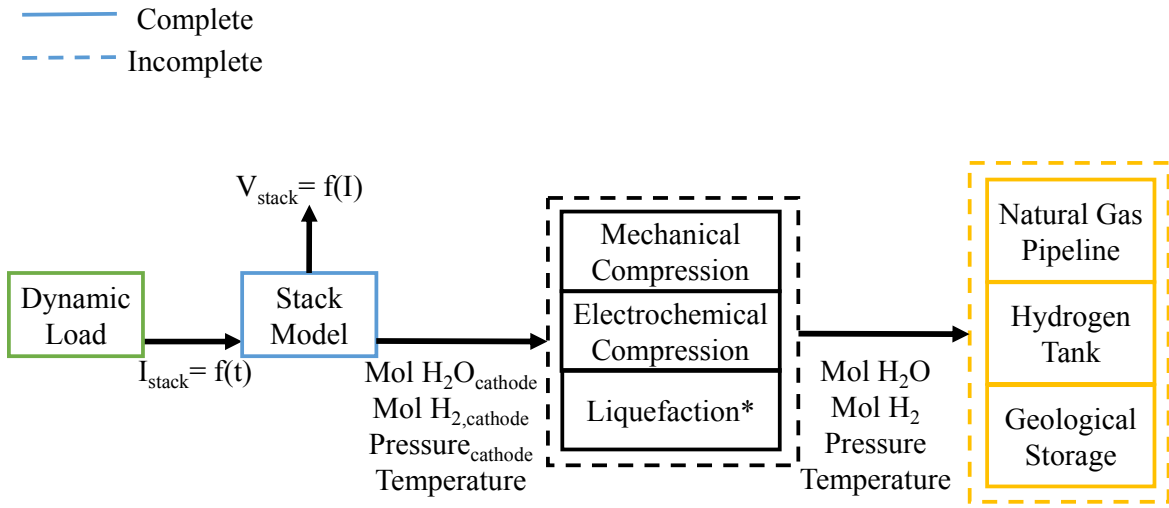
A steady-state stack model is developed that incorporates 0-D species transport. This is accomplished by creating an overall ‘pseudo’ steady-state electrolyzer model, wherein the electrochemical response is assumed to be fast enough in PEM electrolyzers such that transient effects would be minimal on the time scales of interest for our application. This is apparent from the results of the electrolyzer system dynamic operation testing.

Due to the presence of a chiller for thermal management on the electrolyzer considered in this modeling effort, the stack model is assumed isothermal. Additionally, a pressure regulator maintains relatively even pressure on the hydrogen side, and experimental measurements have demonstrated that the anode side sees very little variation in pressure, so an isobaric condition is utilized at each respective electrode. This allows for pressure-driven transport phenomena across the electrolytic membrane to be analyzed, and species transport out of the cells can still be determined by molar balance in and out of the cell by assuming zero storage. For modeling efforts seeking to incorporate a PEMEZ model, this approach should allow for a realistic scenario wherein a real electrolyzer system would operate based on temperature, pressure, and power set points, and would be expected to deviate very little from the set points during operation. In combination with the mass transport models, also provide a more accurate system efficiency and species output than a simplified electrochemical model.

A dynamic load model sends a current value to the electrochemical based stack model at a time t . Operating pressures, stack temperature, and water flow rate are set in the stack model. For the exercising of the stack model to compare against experimental data, the pressures of the cathode and anode, as well as the stack temperature, that were measured alongside the current, will be sent to the stack model to assess how accurate the electrochemical model is. The stack model

returns the cell voltage, species transport out of the anode and out of the cathode, and the pressure and temperature of the cathode outlet stream. With the current balance of plant on the C10 electrolyzer, temperature and pressure deviate very little from the set points, such that this model can capture with modest accuracy the output and efficiency of the electrolyzer stack with a fixed temperature and pressure against the slight deviations experienced by the system.

This PEM electrolyzer stack model can be applied in a number of applications for power-to-gas studies, providing information on the mass flows out of a PEM system based on dynamic electrical load inputs. Modern PEM systems utilize the pressure regulators, thermal conditioning, and power electronics that justify the isobaric, isothermal, and DC current based input assumptions of the model, making it flexible in application across the spectra of PEM systems. Figure 98 shows the information flow of the model as well as possible applications of the model, such as integration with hydrogen compression or liquefaction systems for application to pipeline injection, tank filling (for applications in back-up power and vehicle fueling), and geological storage.



*Separate 'Storage' Model for liquid tank

Figure 98. Semi-Empirical PEM Stack Model with Possible Applications for future studies.

6.1 Steady State Electrochemical Model

Cell voltage of a PEM electrolyzer can be stated as the sum of the open-circuit voltage E_{OCV} , the activation overvoltage η_{act} , the Ohmic overvoltage η_{ohmic} , and the concentration overvoltage η_{conc} .

$$E_{cell} = E_{OCV} + \eta_{act} + \eta_{ohmic} + \eta_{conc} \quad (13)$$

Open-circuit voltage refers to the minimum electrical work needed to start the electrolysis process and can be defined for a PEM electrolyzer by the Nernst equation as shown in equation (14),

$$E_{OCV}(T, P) = E_{rev}(T) + \frac{RT}{2F} \left[\ln \left(\frac{P_{H_2, cathode} P_{O_2, anode}^{0.5}}{a_{H_2O, anode}} \right) \right] \quad (14)$$

where R is the ideal gas constant, F is the Faraday constant, P_{H_2} is the partial pressure of produced hydrogen in the cathode, P_{O_2} is the partial pressure of produced oxygen in the anode, and $a_{H_2O, anode}$ is the activity of reactant liquid water being fed to the anode. E_{rev} is a thermodynamic property that can be expressed as the change in Gibbs free energy associated with the dissociation of water reaction (equation (15)). In the case of electrolysis, Gibbs free energy is representative of the electrical work available to drive the reaction.

$$E_{rev} = \frac{\Delta G^\circ}{2F} \quad (15)$$

The dissociation of water into hydrogen and oxygen, equation (16), can be carried out through the application of electrical work, heat or a combination of the two. Electrolysis in a PEM

electrolyzer system is accomplished largely with electrical work input due to the low operating temperature limits required to maintain water in a primarily liquid state. Equation

(17) describes the relationship between Gibbs, enthalpy, and entropy that determines the ability of the reaction to use electrical work and heat to run the reaction.



$$\Delta G = \left[H_{H_2}(T_{cath}) + \frac{1}{2}H_{O_2}(T_{an}) - H_{H_2O}(T_{an}) \right] - T_{avg} \left[S_{H_2}(T_{cath}, P_{H_2}) + \frac{1}{2}S_{O_2}(T_{an}, P_{O_2}) - S_{H_2O}(T_{an}, P_{H_2O}) \right] \quad (17)$$

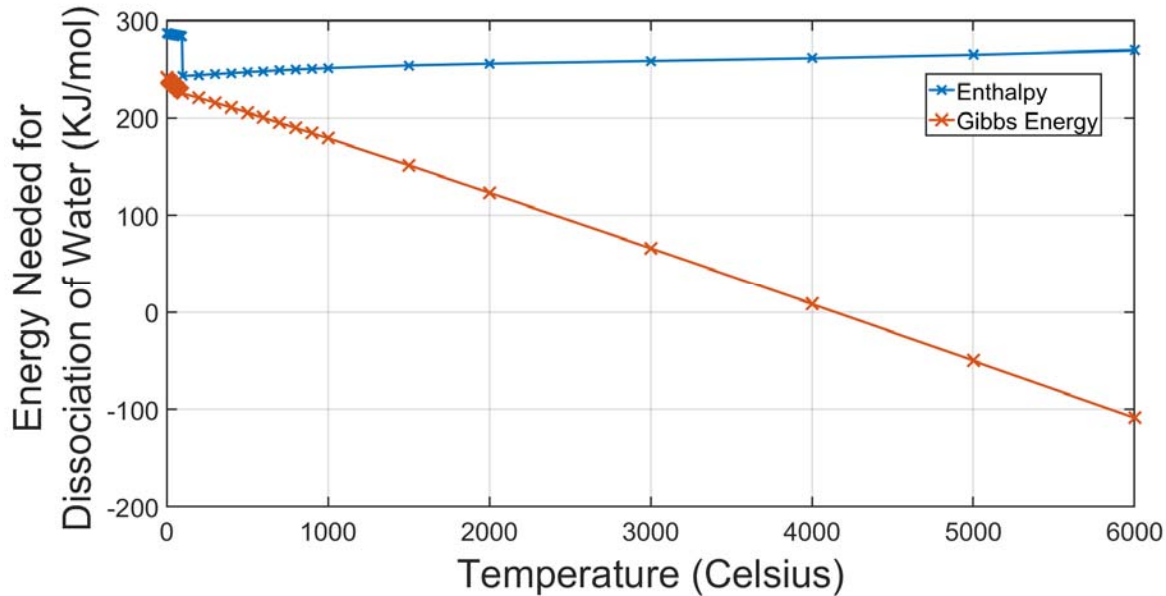


Figure 99. Energy requirement for dissociation of water reaction versus temperature.

Figure 99 demonstrates that as system temperature increases, more heat can be utilized in the dissociation of water. This illustrates an interesting advantage of high temperature electrolyzers which can achieve much higher electrical efficiencies due to the increased availability of heat.

Pyrolysis of water, where water dissociates entirely by way of heat addition, occurs at roughly 4000°C.

Open-circuit voltage can be determined from the Gibbs free energy,

$$E_{OCV}(T, P) = \frac{\Delta G(T, P)}{2F} \quad (18)$$

Alternatively, we can use the expression,

$$E_{rev}(T) = E_{std} - 0.0009(T_{avg} - T_{std}) \quad (19)$$

Equation (19) is a popular option in modeling literature, where T_{std} is typically taken as 298 K, at which E_{std} is 1.23 V [89] [90] [91] [92] [93]. The use of the empirical relationship combined with the Nernst equation saves the need for extensive thermodynamic lookup tables. For electrolysis involving liquid water as the reactant and in absence of the need to model temperature fluctuations across the cell structure, this relationship accurately describes E_{OCV} within $\pm 0.2\%$ and will be used moving forward.

Combining the expressions, we arrive at equation (20) for determining E_{OCV} , using $T_{std} = 25^\circ\text{C}$.

$$E_{OCV}(T, P) = 1.228 - 0.0009(T_{avg} - 298.15) + \frac{RT}{2F} \left[\ln \left(\frac{P_{H2,cathode} P_{O2,anode}^{0.5}}{a_{H2O,anode}} \right) \right] \quad (20)$$

The activation overpotential η_{act} represents the kinetic losses as an added voltage required to start the reactions. Electrochemical reactions occur at the interface between electrode and electrolyte. It is at this interface that the characteristic charge transfers occur, which results in the build of an electric field through which the ionic species move. In the case of PEM electrolysis, this charged species takes the form of a proton. The losses associated with this are difficult to quantify as they

are highly dependent on not only the reaction taking place but also properties of the catalyst, current density, and activity of reactants at the reaction sites [33] [94]. These reaction sites are at the triple phase boundaries where catalyst, electrode, and electrolyte are in contact.

The Butler-Volmer equation (21) describes the ability for applied overvoltage to lower the kinetic barrier of the reaction, biasing the forward or reverse directions based on the applied voltage.

$$j = j_0 \left(\exp \left(\frac{2\alpha F \eta_{act}}{RT} \right) - \exp \left(\frac{-2(1 - \alpha) F \eta_{act}}{RT} \right) \right) \quad (21)$$

η_{act} refers to the applied overpotential to overcome activation losses. The resulting current density is j , and j_0 is the exchange current density. Exchange current density describes the rate of exchange between products and reactants at equilibrium. Higher exchange current densities lead to lower activation losses. The charge transfer coefficient α is a symmetry coefficient describing the bias in charge transfer towards the forward or reverse reaction due to applied potential and is typically found between 0.2 and 0.5. Both α and j_0 are largely functions of cell structure that influences the availability of reaction sites, reactants, and the activation barrier energy, but also have shown dependence on temperature [95] [96] [97].

Rearranging for the activation overpotential gives the following relationships for the anode and cathode activation losses in equations (22) & (23).

$$\eta_{act,an} = \frac{RT}{2\alpha_{an}F} \sinh^{-1} \left(\frac{j}{2j_{o,an}} \right) \quad (22)$$

$$\eta_{act,cath} = \frac{RT}{2\alpha_{cath}F} \sinh^{-1} \left(\frac{j}{2j_{o,cath}} \right) \quad (23)$$

To further simplify these expressions, literature often assumes that the charge transfer coefficient is equivalent to the symmetry factor $\alpha_{an}=\alpha_{cath}=0.5$ [98] [94] [99] [100]. This assumption holds true especially well at the higher operating temperature range of PEMEZ on the order of 60°C [101]. Combining (22) & (23) gives equation (24) for η_{act} , leaving the exchange current density of the anode and cathode respectively left to be determined.

$$\eta_{act} = \frac{RT}{F} \sinh^{-1} \left(\frac{j}{2j_{o,an}} \right) + \frac{RT}{F} \sinh^{-1} \left(\frac{j}{2j_{o,cath}} \right) \quad (24)$$

The Ohmic overpotential refers to the losses due to charge transport, which in the case of PEM electrolyzers is dominated by the protonic membrane resistance given by equation (25,

$$\eta_{ohmic} = \frac{\delta_{mem}}{\sigma_{mem}} j \quad (25)$$

Where δ is the thickness of the membrane, taken as 178 μm for Nafion™ 117. Membrane proton conductivity, σ (S/cm), has been found to vary with temperature and with membrane water content λ . Two empirical relations for conductivity that are prevalent in the modeling literature originate from Kopitzke et al. [102], equation (26), and Springer et al. [103], equation (27).

$$\sigma_{mem} = 2.29 \exp \left(-\frac{7829}{RT} \right) \quad (26)$$

$$\sigma_{mem} = (0.005139\lambda_{mem} - 0.00326) \exp \left(1268 \left(\frac{1}{303} - \frac{1}{T} \right) \right) \quad (27)$$

Concentration overpotential, η_{conc} , occurs due to mass transport limitations, typically resulting from diffusion limitations in moving reactants from the bulk flow to the reaction sites.

Concentration overpotential depends strongly on current density, as well as on reactant activity and electrode structure. This overpotential can be modeled by defining a limiting current density

parameter j_L , and by ignoring the cathode concentration limits as the anode effects are far more dominant equation (28) [104].

$$\eta_{conc} = \frac{RT}{2\alpha_{an}F} \ln\left(\frac{j_L}{j_L - j}\right) \quad (28)$$

Literature reports values of j_L around 6 A/cm² [104] [105]. This results in a negligible contribution to cell voltage for current densities ranges of practical interest (<10 mV at 2 A/cm²) and as such the literature value will be used in the model and not be determined experimentally. The complete electrochemical description being used following the assumptions made in the previous section is then,

$$E_{cell} = 1.228 - 0.0009(T - 298.15) + \frac{RT}{2F} \left[\ln\left(\frac{P_{H_2,cathode} P_{O_2,anode}^{0.5}}{a_{H_2O,anode}}\right) \right] \\ + \frac{RT}{F} \sinh^{-1}\left(\frac{j}{2j_{o,an}}\right) + \frac{RT}{F} \sinh^{-1}\left(\frac{j}{2j_{o,cath}}\right) + \frac{\delta}{\sigma_{mem}} j \quad (29)$$

Isothermal conditions are assumed in the stack due to the presence of heat exchangers controlling the temperature of the recirculating feed water. Stack temperature, T, is measured in the feed water at the oxygen-water separator which serves as a recirculation tank, taking in water at the stack outlet and feeding water to the circulation pump upstream of the feed water heat exchanger.

In electrolyzer systems utilizing a back-pressure regulator on the gas outlets, the outlet pressure varies very little. Isobaric conditions are assumed in the anode and cathode for this reason.

Measurements from the operation of a Proton OnSite C10 electrolyzer indicate that the pressure in the anode tends to increase slightly with current density (1.0 barg up to 2.3 barg), due to the lack of a back-pressure regulator on the oxygen outlet. On the cathode side of the C10, pressure deviates very little from the back-pressure regulator setting on the outlet.

The absolute pressure of the anode and cathode are measured at the oxygen-water and hydrogen-water phase separators respectively. It is assumed that predominantly water vapor and hydrogen are present in the gaseous phase in the cathode as oxygen crossover reacts to form water in the presence of platinum catalyst on the cathode side [44]. Water vapor, oxygen and potentially trace amounts of hydrogen gas are found in the gaseous phase in the anode. Finally, it is assumed that the partial pressure exerted by liquid water is equivalent to the saturated vapor pressure of water, which is a function of the temperature.

$$P_{H_2O,cath} = P_{H_2O,an} = P_{H_2O,sat}(T) = 6.1078 \times 10^{-3} \exp \left[17.2694 \left(\frac{T - 273.15}{T - 34.85} \right) \right] \quad (30)$$

$$P_{H_2,cathode} = P_{cathode} - P_{H_2O,sat} \quad (31)$$

$$P_{O_2,anode} = P_{anode} - P_{H_2O,sat} - P_{H_2,anode} \quad (32)$$

$$P_{H_2,anode} = y_{H_2,an} * P_{anode} \quad (33)$$

Where $y_{H_2,an}$ is the mole fraction of hydrogen in the anode.

Molar flows in the cell considered in the model are shown below in Figure 100.

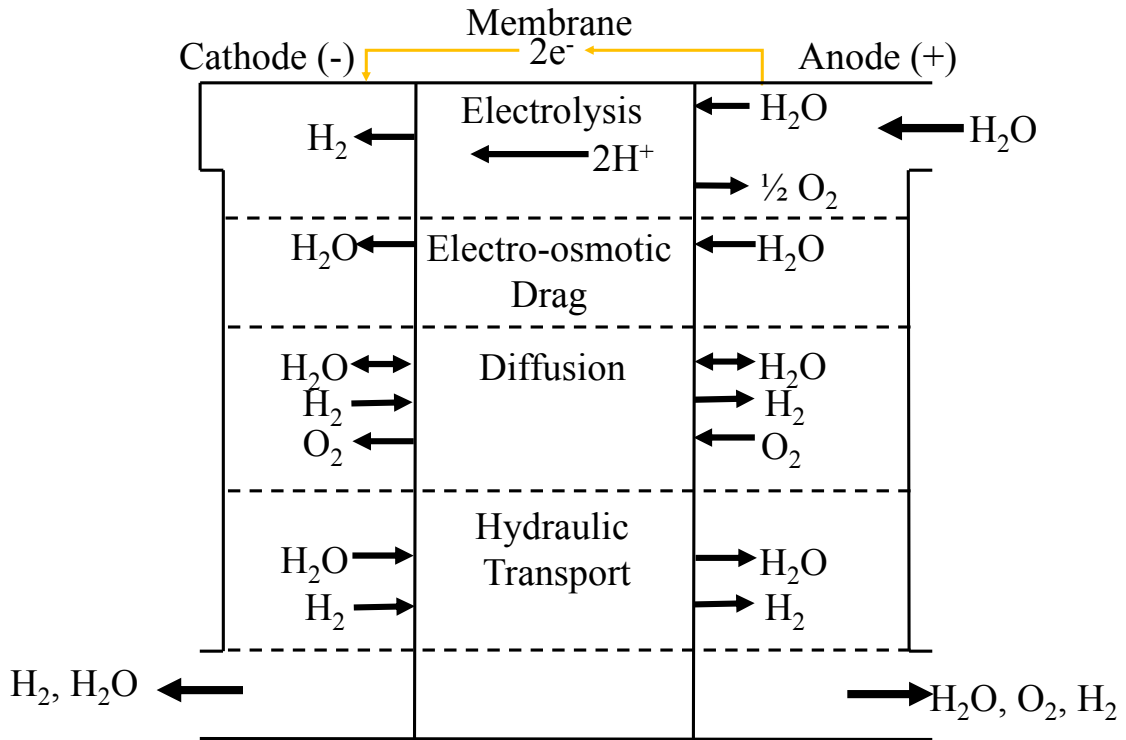


Figure 100. Species Transport in PEM Electrolyzer

6.1.1 Water Transport

On the anode side liquid water circulates continuously in great excess of the amount of water needed as a reactant. At the anode, water is consumed and oxygen is generated at a rate proportional to the current density. Hydrogen is generated at the cathode in like manner.

$$\dot{N}_{H_2O,react,an} = \frac{jA}{2F} \quad (34)$$

$$\dot{N}_{O_2,prod,an} = \frac{jA}{4F} \quad (35)$$

$$\dot{N}_{H_2,prod,cath} = \frac{jA}{2F} \quad (36)$$

Water enters the cathode by transport through the electrolyte layer from the anode side. The transport of water to the cathode in PEM electrolysis stacks can be described through three transport mechanisms; electro-osmotic drag, diffusion, and permeation or ‘hydraulic’ transport [106]. Figure 100 in the previous section shows these transport mechanisms with respect to water and other species in the stack.

Electro-osmotic drag describes the phenomena of water molecules transporting along with the movement of protons across the membrane. Thus, molar flow associated with electro-osmotic drag can be described by a proportionality with proton flow across the membrane, which is a function of current (37).

$$\dot{N}_{H_2O,eo} = n_{eo} \frac{jA}{F} \quad (37)$$

Where n_{eo} is the electro-osmotic drag coefficient, which represents the number of water molecules dragged across the electrolyte membrane per proton. This quantity can be chosen by referencing experimental studies in literature (as is often the case in PEM fuel cell studies) [90]

[107], and other experimental studies have proposed fitting the parameter as a function of membrane water content such as the widely cited Springer et al.(38) [108] [45], or if experimental data is available, an analytical model such as the one proposed in this section can be combined with measurements in cathode water flow to determine a fit [106]. The Springer equation was formulated using measurements in PEM fuel cell conditions, where humidified gases are present with some liquid water in the channels, as opposed to the completely inundated with liquid water conditions present in a PEM electrolysis cell. For this study, experimental data is used to determine the best fit for n_{eo} .

$$n_{eo} = 0.0029\lambda_m^2 + 0.05\lambda_m - 3.4 \times 10^{-19} \quad (38)$$

The pressure difference between the two electrodes in a PEM electrolyzer tends to oppose the water transport due to electro-osmotic drag. Hydraulic transport of water through a membrane by pressure gradient can be determined using Darcy's law (equation (39)).

$$\dot{N}_{H_2O,perm} = \frac{\rho_{H_2O} A K_D \nabla P}{\mu_{H_2O}} \quad (39)$$

Where K_D is the permeability coefficient, or 'Darcy' constant', ∇P is the pressure gradient, and μ is the dynamic viscosity of water. Some modeling studies considering high pressure PEM electrolyzer systems (where high pressure is comparable in range to the electrolyzer system considered in this thesis), ignore hydraulic transportation effects [72] [43]. Focused testing on Nafion membranes immersed in liquid water (conditions purposefully comparable to use in a PEM electrolysis cell) showed the presence of hydraulic transport and provided measurements of K_D and water content (λ_m) across a range of water temperatures [109].

Dynamic viscosity of liquid water is solely a function of temperature (seen in equation (40)) [110].

$$\mu_{H_2O} = 0.6612(T - 229)^{-1.562} \quad (40)$$

Diffusion transport occurs due to different water concentrations at the surface of the electrolytic membrane. This diffusion transport can be described as shown below in equation (41) [111],

$$\dot{N}_{H_2O,diff} = \frac{AD_{eff}}{\delta_{mem}} (C_{H_2O,cat} - C_{H_2O,an}) \quad (41)$$

where D_{eff} is the membrane water diffusion coefficient and terms $C_{H_2O,cat}$ and $C_{H_2O,an}$ refer to the concentrations of water in mol/cm³ at each electrode, A is the active area, and δ_{mem} is the thickness of the electrolyte membrane. $\delta_{mem} = 0.0178$ cm for Nafion 117 membranes [112]. For correcting the diffusion coefficient, the Bruggeman equation can be applied in the case of the randomized porous fiber membrane (42)

$$D_{eff} = \varepsilon^{1.5} D_w \quad (42)$$

Where the dimensionless value ε is a function of the void fraction of the electrolyte,

$$\varepsilon = \frac{1}{1 - \varphi} \quad (43)$$

For Nafion 117, the void fraction is often taken as $\varphi = 0.3$ [107] [106] [113]. Measurements on similar Nafion membranes submerged in liquid water showed void fractions of $\varphi = 0.30$ to 0.39 [109]. Since the variation in diffusion transport in water was less than 0.1% going from $\varphi = 0.3$ to $\varphi = 0.39$ void fraction, the value of $\varphi = 0.3$ was identified as a reasonable value.

For a membrane at maximum humidification, liquid water diffusivity D_w can be calculated from equation (44) [106],

$$D_w = (0.256 \times 10^{-4}) \left(\frac{T}{273.15} \right)^{1.823} \quad (44)$$

for liquid water with an assumed activity of 1, the concentrations of water in each electrode are purely a function of temperature (45) & (46). Due to the elevated pressure in the cathode compartment, water activity is nearly one at all times. On the anode side, the mole fraction of water is overwhelmingly dominant due to the excessive feed water pumped through the stack on that side. As a result, diffusion transport is effectively zero in the absence of a temperature difference. Diffusion transport has been determined to be orders of magnitude lower than electro-osmotic drag [90] [43] and permeation [106] in previous studies of PEM electrolyzer water transport. Diffusion transport is retained in the model for future additions such as spatial dimensions and heat transfer.

$$C_{H_2O,ch,an} = \frac{\rho_{H_2O}(T_{an})}{MM_{H_2O}} \quad (45)$$

$$C_{H_2O,ch,cath} = \frac{\rho_{H_2O}(T_{cath})}{MM_{H_2O}} \quad (46)$$

Our overall membrane water transport equation is then,

$$\dot{N}_{H_2O,mem} = \dot{N}_{H_2O,diff} + \dot{N}_{H_2O,Perm} + \dot{N}_{H_2Oeo} \quad (47)$$

6.1.2 Hydrogen Gas Transport

Hydrogen gas is produced in the cathode at an elevated pressure relative to the anode. This elevated pressure combined with the higher hydrogen concentrations leads to both diffusive and pressure-driven transport of hydrogen across the electrolytic membrane to the anode. This is undesirable due to hydrogen loss and safety issues given the lower explosive limit (LEL) hydrogen is 4% in O₂ and air [114].

For diffusive transport, we can apply Fick's law once again;

$$\dot{N}_{H_2,diff} = \frac{D_{H_2}}{\delta_{mem}} (C_{H_2,cat} - C_{H_2,an}) \quad (48)$$

Where D_{H_2} is the diffusion coefficient. For gases, we can also restate this relation using partial pressures and the diffusive permeability of hydrogen gas through Nafion 117, $\varepsilon_{H_2,diff}$.

$$\dot{N}_{H_2,diff} = \frac{\varepsilon_{H_2,diff}}{A\delta_{mem}} (P_{H_2,cat} - P_{H_2,an}) \quad (49)$$

And for pressure-driven transport, driven by the pressure gradient from cathode to anode,

$$\dot{N}_{H_2,Perm} = \frac{\varepsilon_{H_2,perm}}{A\delta_{mem}} (P_{H_2,cat} - P_{O_2,an}) \quad (50)$$

where $\varepsilon_{H_2,perm}$ is the permeability coefficient. A recent study of hydrogen gas cross-over in PEM cells indicated that the gas permeability of Nafion 117 is independent of pressure, and as a result is a purely diffusive transport process ($\varepsilon_{H_2,perm} = 0$) [115].

The partial pressure of hydrogen at the cathode-electrolyte interface can be characterized by,

$$P_{H_2,cat} = P_{cat} + A_{H_2}j - P_{H_2O,cat} \quad (51)$$

where P_{cat} is the absolute cathode pressure, measured in the electrolyzer, A_{H_2} is the hydrogen partial pressure enhancement factor, j is the current density, and $P_{H_2O,cat}$ is the partial pressure of water vapor in the cathode, calculated by equation (30).

For a net hydrogen transport across the membrane of,

$$\dot{N}_{H_2,mem} = \dot{N}_{H_2,diff} = \frac{\varepsilon_{H_2,diff}}{\delta_{mem}} (P_{cat} + A_{H_2}j - P_{H_2O,cat} - P_{H_2,an}) \quad (52)$$

The values for parameters $\varepsilon_{H_2,diff}$ and A_{H_2} are estimated from experimental measurements in section 6.3.2.

6.1.3 Oxygen Gas Transport

Oxygen gas is produced at the lower pressure anode side of the cell. As such, there is no pressure driven transport of oxygen to the cathode, but there is still a concentration gradient driving diffusion transport. We can apply a similar treatment to the hydrogen gas transport above to arrive at,

$$\dot{N}_{O_2,diff} = \frac{\varepsilon_{O_2,diff}}{A\delta_{mem}} (P_{O_2,an}) \quad (53)$$

Assuming negligible cathodic partial pressures of oxygen gas due to the high reactivity of oxygen in the cathode.

6.1.4 Overall Molar Balance

The molar balance for the cathode side flow is simplified by the high reactivity of cathode oxygen. In the model, molar transport of oxygen gas to the cathode is calculated and assumed to

react completely with hydrogen gas, consuming 2 moles of hydrogen and producing 2 moles of water for every mole of oxygen.

$$\dot{N}_{O_2,cath,out} = n(\dot{N}_{H_2,diff}) \quad (54)$$

$$\dot{N}_{H_2,cath,out} = n(\dot{N}_{H_2,prod,cath} - \dot{N}_{H_2,diff} - \dot{N}_{H_2,Perm}) - 2\dot{N}_{O_2,cath,out} \quad (55)$$

$$\dot{N}_{H_2O,cath,out} = n(\dot{N}_{H_2O,cath,in} + \dot{N}_{H_2O,mem}) + 2\dot{N}_{O_2,cath,out} \quad (56)$$

$$\dot{N}_{O_2,cath,out} = n(\dot{N}_{O_2,prod,an} - \dot{N}_{O_2,diff}) \quad (57)$$

$$\dot{N}_{H_2,an,out} = n(\dot{N}_{H_2,diff} + \dot{N}_{H_2,Perm}) \quad (58)$$

$$\dot{N}_{H_2O,an,out} = n(\dot{N}_{H_2O,an,in} - \dot{N}_{H_2O,mem}) \quad (59)$$

Table 20 summarizes the values of key parameters associated with the species transport.

Table 20. Identified Stack Parameters associated with species transport

A (cm²)*	213.68	δ_{mem}(cm)	0.0178
δ_{an}* (cm)	0.13	ϵ_{mem}	0.3 [71]
ϵ_{an}* 	0.50	n (#cells)	65
δ_{cath}* (cm)	0.13	$\epsilon_{O_2,diff}$ (mol/cm s bar)	2.00×10^{-11} [44]
ϵ_{cath}* 	0.65	$\epsilon_{H_2,perm}$(mol/cm s bar)	0 [115].

*Values provided by Proton Onsite, specific to the C10 Electrolyzer Stack

6.2 Electrochemical Parameter Identification

Experimental data from the 60kW C10 electrolyzer was used in conjunction with the electrochemical model to determine the unknown electrochemical parameters; membrane conductivity, cathodic exchange current density, and anodic exchange current density. This was accomplished by using the trust region methods for parameter identification available in the Matlab optimization toolset. A similar approach has been used in [96] [99], and has proven effective when a wide range of experimental data is available.

Data for four different temperature set points (40C, 45C, 50C, 55C) at 30 barg cathodic pressure was used for the parameter fitting. Anodic pressure cannot be fixed, however it varied very little. The average anodic pressure of 1.6 barg was used in the parameter identification. As temperature is not perfectly controlled by the chiller, and anodic pressure did deviate, only I-V points that occurred at ± 1 Celsius from the desired temperature reading, and ± 0.2 barg at the anode, were included. As the electrolyzer was not able to vary the cathode pressure over a large range, the effects of pressure on these parameters were not examined, however previous studies in this area only found slight influences of pressure on these parameters, even with ranges of 7 barg up to 70 barg in the cathode [107]. The influence of pressure on the Nernst voltage described completely any additional overvoltage correlated with higher partial pressures of hydrogen or oxygen gas in the cathode and anode respectively.

The results of the curve fit are shown below in Figure 101,

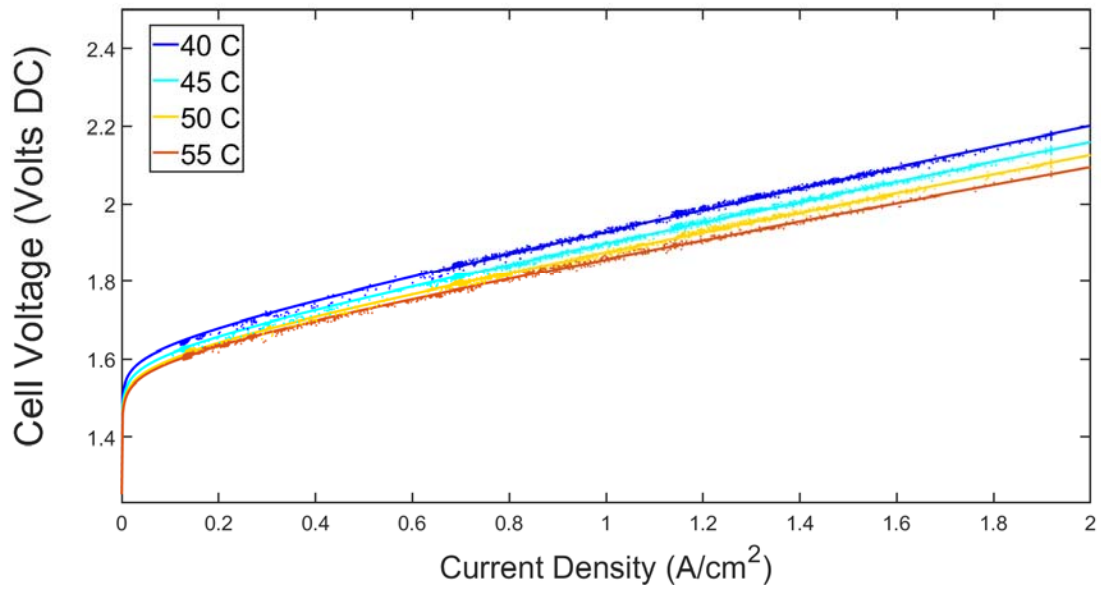


Figure 101. Fitted polarization curve agreement with input experimental data

The resulting values for each parameter are displayed in Figure 102. The strong dependence on temperature for the anode exchange current density and membrane conductivity agrees well with literature, as does the low temperature dependence in this small temperature range in the case of cathodic exchange current density [96] [99] [107].

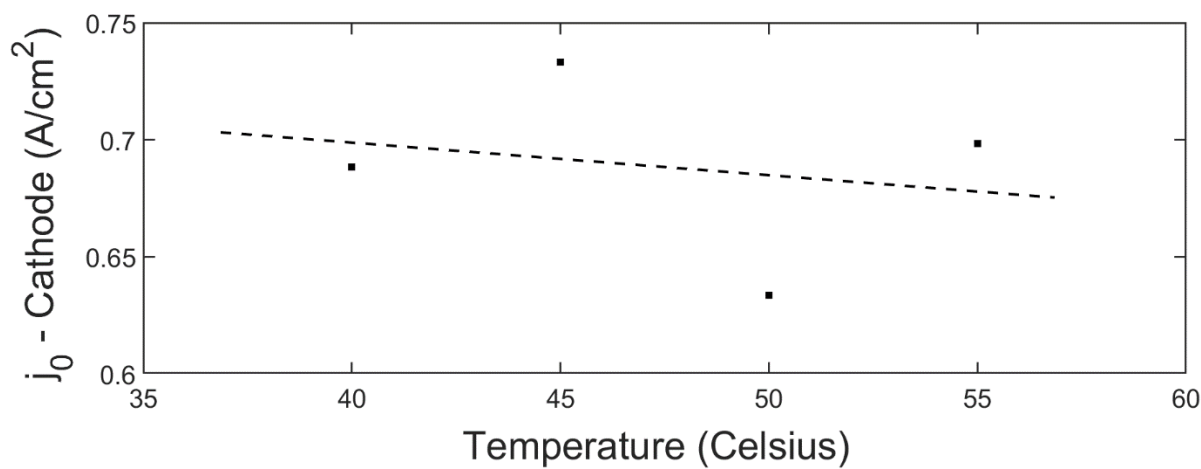
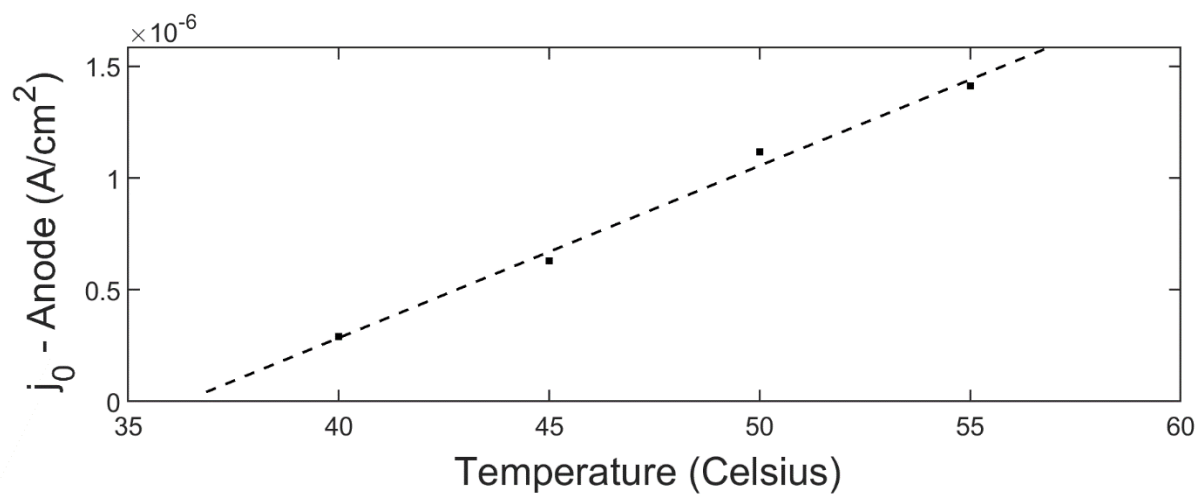
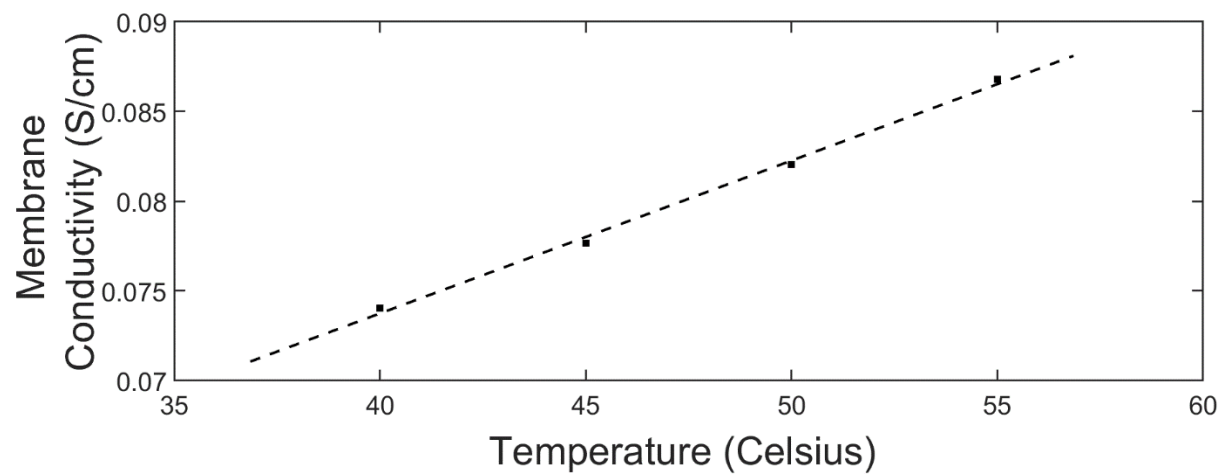


Figure 102. Dependence of electrochemical parameters on temperature

Using the Springer relationship for conductivity (eq. (27)), we can attempt to estimate the water content present in the membrane from our temperature vs. conductivity relationship. Rearranging and solving for λ_{mem} , we obtain a value of $\lambda_{mem} \approx 13$. This result matches poorly with studies of Nafion membranes in-situ for PEM water electrolysis [102] [116]. Most models choose to use “inundated” water content values of $\lambda_{mem} > 20$ [95] [71], which have been observed ex-situ of electrolysis with membranes measured after being submersed in liquid water – the closest analogue to PEM electrolysis conditions [45] [117] [118]. This highlights the potential inaccuracy of the Springer equation when applied to PEM electrolyzer operating conditions, as the equation was developed for PEM fuel cell operating conditions, where liquid water concentrations are lower.

For the final electrochemical model, membrane conductivity and anode exchange current density were determined using the linear fit correlation with temperature found above. The mean of the cathode exchange current densities was used to determine the final cathode exchange current density.

$$\sigma_{mem} = 0.000852T + 0.03967 \text{ [Siemens/cm]}$$

$$j_{o,an} = 7.703426 \times 10^{-8}T - 2.7966 \times 10^{-6} \text{ [A/cm}^2\text{]}$$

$$j_{o,cath} = 0.688356 \text{ [A/cm}^2\text{]}$$

Figure 103 shows the contribution of the various overvoltage to the polarization curve using the final fitted parameters for average stack operating conditions. Activation overpotential at the anode dominates at low current density due to the slower kinetics of the oxygen evolution reaction (OER), and Ohmic overpotential takes up an increasing share at higher current densities due to the linear Ohmic losses.

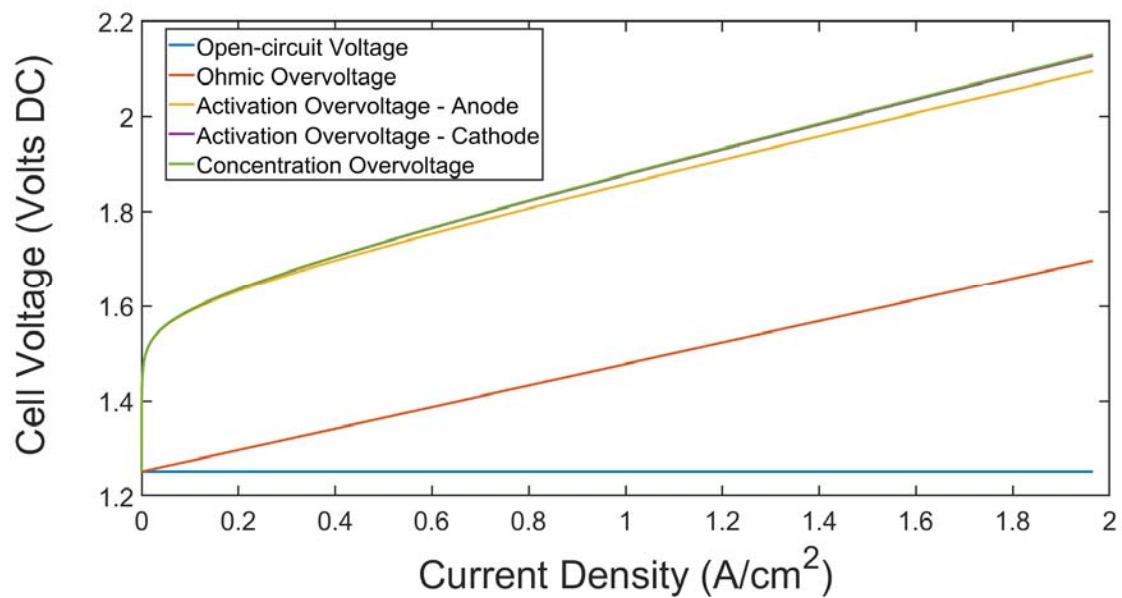


Figure 103. Breakdown of additive overvoltage contributions to polarization curve using experimentally determined parameters ($T_{stk} = 55\text{ C}$, $P_{cath} = 30\text{ barg}$, $P_{anode} = 1.6\text{ barg}$).

6.3 Membrane Species Transport Parameters Identification

Using the transport models in conjunction with experimental data, certain fitting parameters for species transport across the electrolyte membrane were determined.

6.3.1 Water Transport

The electrolyzer net water consumption is rated at an approximated 2.4 gal/hour, yet consumption at full power is measured at approximately 3 gal/hour (Table 1). The rated water consumption specification from the OEM matches with the amount of water required to carry out electrolysis at full stack throughput. This excess water consumption occurs through two mechanisms. Water is lost in the system to the environment, via evaporation due to elevated temperatures and forced convection at the oxygen-water phase separator chamber. Some water that is pumped to the stack on the anode side crosses the electrolytic membrane to the cathode side through electro-osmotic drag and diffusion transport processes. On the cathode side, the hydrogen-water phase separator collects liquid water and periodically drains back to the oxygen-water phase separator. Water vapor is transported along with the hydrogen gas to heat exchangers and then a pressure swing adsorption process. Water purged from the adsorption process is sent to the hydrogen vent stack and not recovered.

Figure 104 shows the observed water consumption in gallons per hour for a given day of operation against the average operating current density. At lower current densities, the discrepancy between water consumption for electrolysis and the total system consumption narrows. At lower current densities, the amount of humid oxygen vented from the anode side is lower. Additionally, the transport of water to the cathode side into the hydrogen stream is a function of current density (electro-osmotic drag).

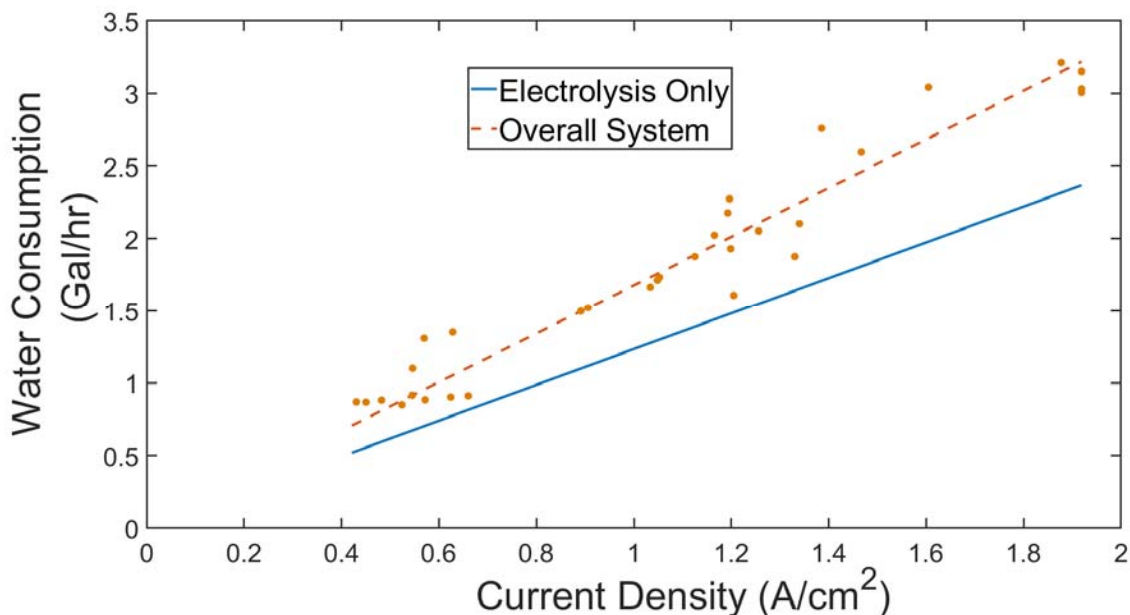


Figure 104. Water consumption of electrolysis process and observed total system water consumption.

Quantifying the amount of water lost to the environment through evaporation with forced convection, as is the case in the oxygen-water phase separator tank, is outside the scope of this study. However, it is fairly trivial to estimate the losses due to water vapor entrained in the hydrogen gas product stream.

The pressure swing adsorption (PSA) process that terminates the hydrogen drying process removes essentially all water vapor from the product stream and purges the water to the atmosphere instead of recovering it. Assuming fully saturated conditions due to the large amount of liquid water present and elevated temperatures, we can refer to expression (30) to calculate the vapor pressure of water for an average temperature of 55 Celsius. Taking an average pressure of 30 barg on the cathode product side, and 1.5 barg on the anode side, the mols of water vapor present per mol of respective gas on each side can be estimated as 0.0196 mol H₂O(g)/mol H₂ and 0.0233 mol H₂O(g)/mol O₂ on average. At full throughput, this loss of water vapor is

equivalent to 0.15 gallons per hour of water expelled to the atmosphere, only accounting for ~1.5% of the total electrolyzer water consumption.

Net water transport from the cathode side was estimated from the fill and drain cycles of the 'A300' hydrogen-water phase separator tank (Figure 105). The A300 periodically fills until reaching the 'L3' water level (measured by float-based level switch). Once the water level reaches L3, a solenoid valve-orifice assembly opens, draining liquid water until 'L1' is reached. Knowing the inner diameter of the A300 and the height difference from L1 to L3 state, the estimated volume of water between L1 and L3 is approximately 0.05 gallons. Hydrogen gas saturated with water vapor continues on to a heat exchanger and subsequently the pressure swing adsorption dryers. Condensed water from the heat exchange process is returned to the A300 as well.

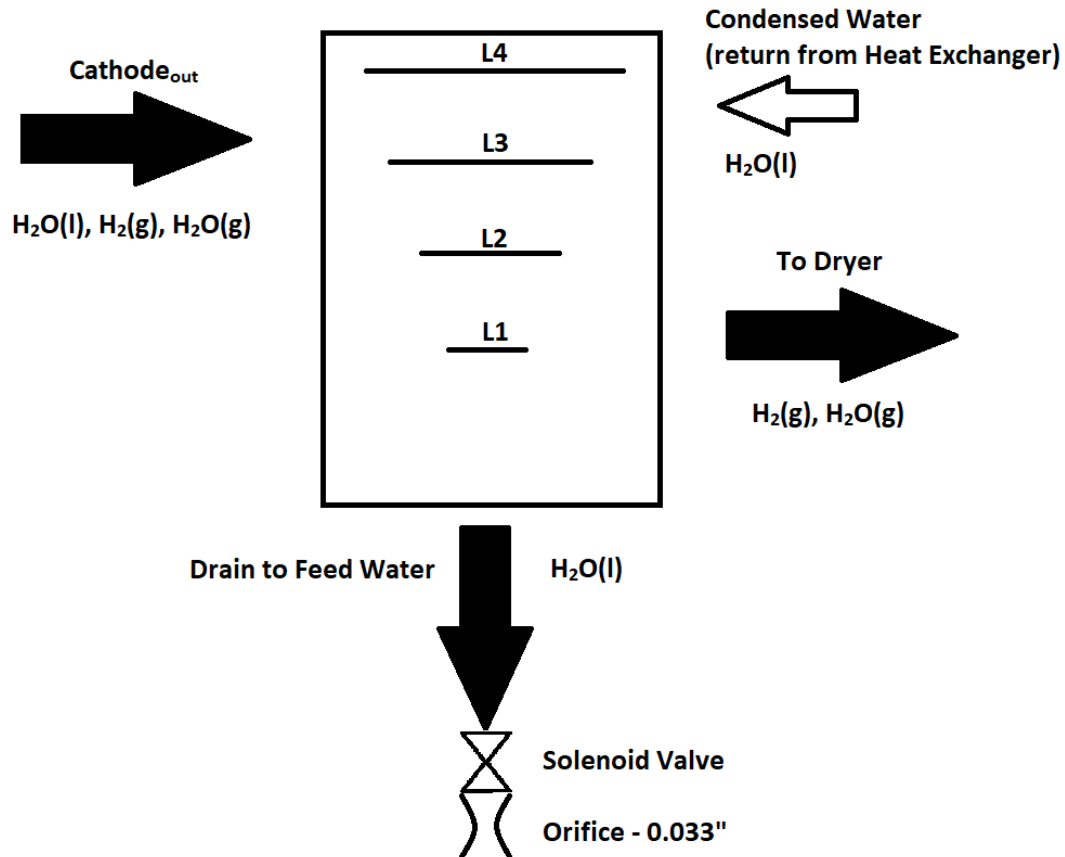


Figure 105. A300 hydrogen-water phase separator schematic.

During fill periods, the liquid water flow out of the cathode can be estimated from the level switch data (Figure 106). From these data, assuming very little condensed phase water continues to the dryers, the total flow rate of water from the cathode can be estimated (Figure 107).

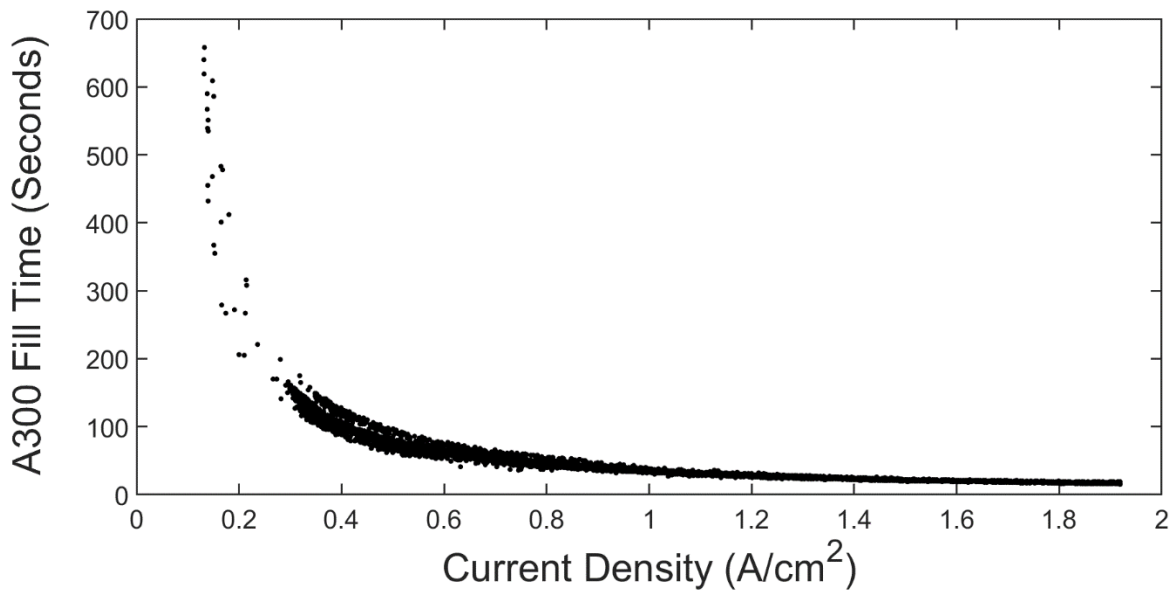


Figure 106. A300 fill time vs. current density.

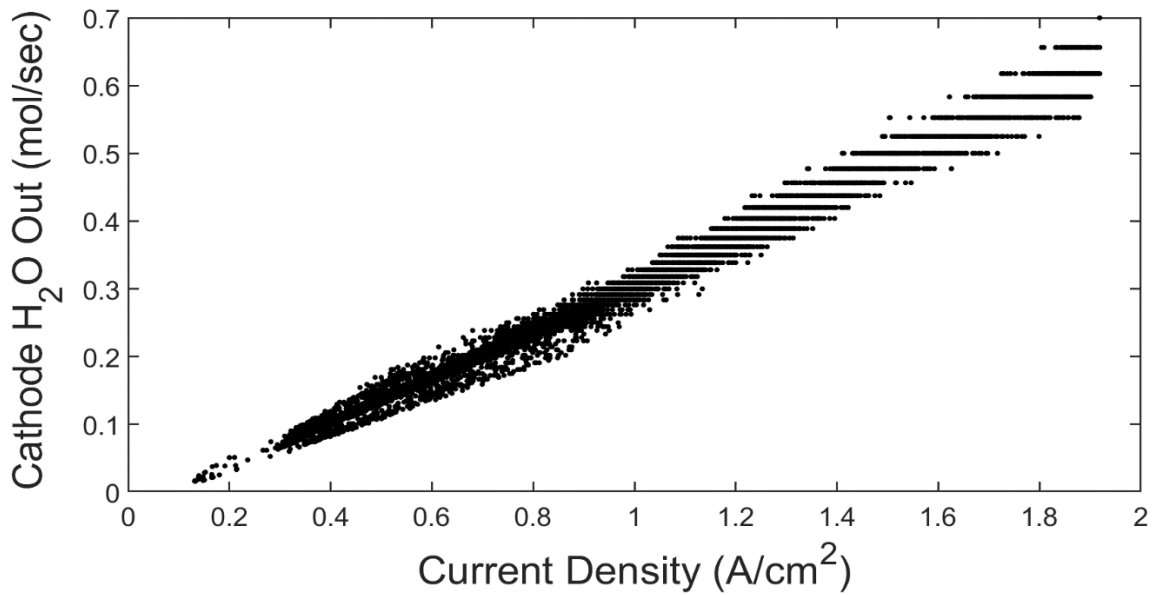


Figure 107. Cathode water out molar flow rate – estimate from A300 fill time.

Due to the 1-second resolution of the level switch data, a wide range of flow rates is observed. Using linear regression and ANOVA techniques, the average variation in cathode flow rate due to variations in pressure differential in the stack can be extracted. The results of the ANOVA based linear regression are summarized in Table 21 below. A significant linear correlation was found for the pressure differential in the stack, although the magnitude of its impact was relatively small (Figure 108).

Table 21. ANOVA Results for cathode water flow rate.

	Sum of Squares	Degrees of Freedom	Mean Square	F Value	P-value (Prob > F)
A-Current Density	268.1036	1	268.1036	1.1138E+06	< 0.0001
B-Pressure Differential	0.0591	1	0.0591	245.5750	< 0.0001
Model	1246.3817	2	295.7079	1.2285E+06	< 0.0001

Std. Dev.	0.0155	R²	0.9933
Mean	0.3237	Adjusted R²	0.9933
C.V. %	4.7931	Predicted R²	0.9933
		Adeq Precision	2910.9971

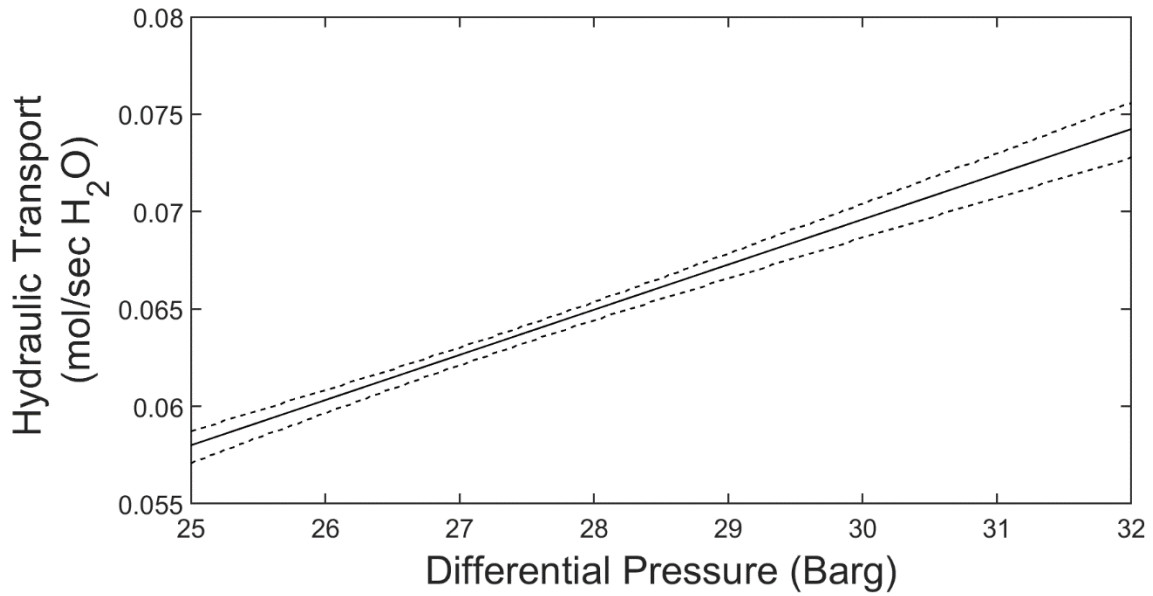


Figure 108. Estimated hydraulic transport of water across cell stack with 95% confidence intervals.

Using our relationship for hydraulic transport across the cell stack as a function of the pressure differential (equation (39)), the Darcy constant K_D can be estimated to be in the range of $2.671 - 2.739 \times 10^{-16} \text{ cm}^2/\text{sec}$, weighted most closely to a value of $2.712 \times 10^{-16} \text{ cm}^2/\text{sec}$.

To complete the description of the membrane water transport, all that remains is the determination of the electro-osmotic drag coefficient n_d . By applying the analytical model, the electro-osmotic drag transport can be isolated.

$$\dot{N}_{H_2O,eo} = \dot{N}_{Observed} - \dot{N}_{H_2O,diff} + \dot{N}_{H_2O,Perm}$$

Major influencing factors are determined through ANOVA, with the results summarized below in Table 22. Some influence was also attributed to the pressure differential, even after accounting for variations due to hydraulic transport, however the influence was several orders of magnitude lower than current density and stack temperature.

Table 22. ANOVA results for influencing factors on electro-osmotic water transport in the membrane.

	Sum of Squares	Degrees of Freedom	Mean Square	F Value	P-value (Prob > F)
A-Current Density	73.0105	1	73.0105	2.5052E+05	< 0.0001
C-Stack Temperature	0.3373	1	0.3373	1157.3674	< 0.0001
Model	85.3164	2	42.6582	1.4637E+05	< 0.0001

Std. Dev.	0.0155	R²	0.9933
Mean	0.3237	Adjusted R²	0.9933
C.V. %	4.7931	Predicted R²	0.9933
		Adeq Precision	2910.9971

The resulting transport attributed to electro-osmotic drag for the measured range of operating temperatures is shown below in Figure 109. The linear regression fits for the different operating temperatures show a clear increasing trend in electro-osmotic drag transport with temperature. The positive effective of temperature on electro-osmotic drag in PEM electrolysis has been studied in a similar fashion by Medina & Santarelli [106], and Li et al. [42]. The associated n_{eo} coefficient fit is shown in Figure 110.

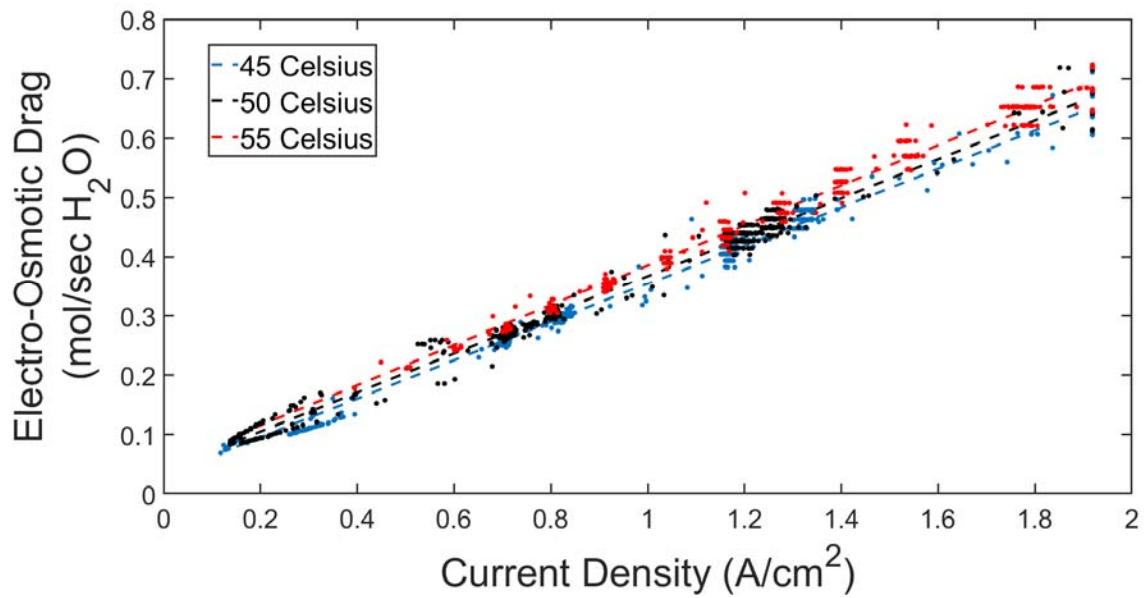


Figure 109. Electro-osmotic drag transport versus current density at different stack operating temperatures with linear regression trend lines.

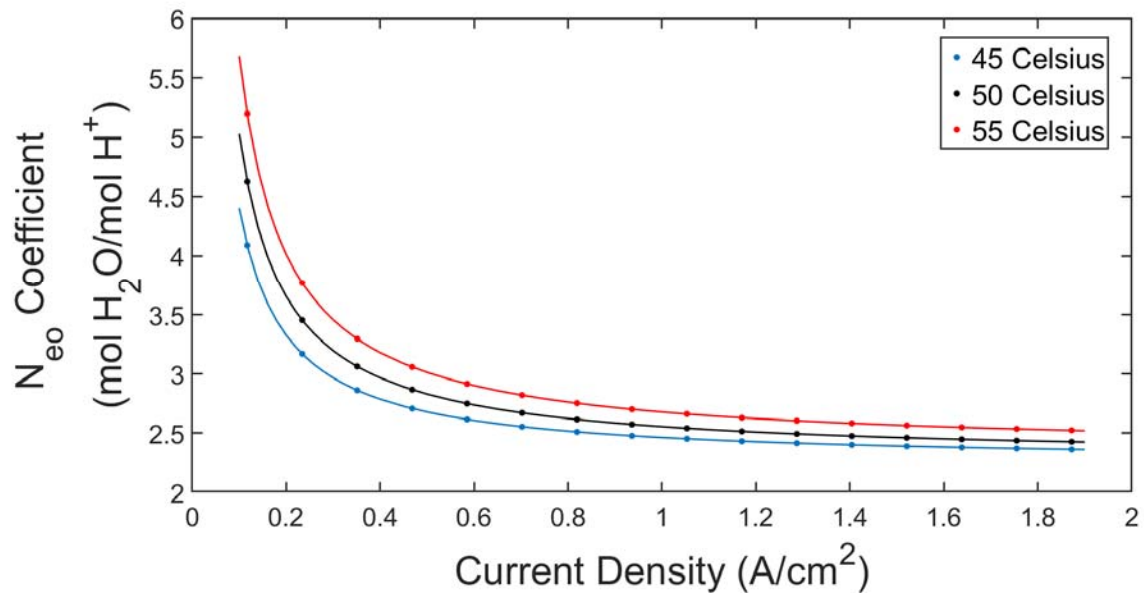


Figure 110. Electro-osmotic drag coefficient as a function of current density and operating temperature.

The relationships between n_{eo} , current density, and temperature are compared to other studies of membrane water flow rate, the aforementioned Medina & Santarelli [106] and Li et al. [42].

Medina & Santarelli studied the pressure effects of water transport, providing measurements of membrane water transport at 7 barg H_2 and 70 barg H_2 at current densities of 0.25 A/cm² and 1 A/cm² for a differential pressure PEMEZ system. Li et al. provided water transport measurements for PEMEZ operating at 1 barg H_2 at very low current density in a single cell. Kim et al. used the experimental data from Medina & Santarelli to create a regression model for use in a PEMEZ model operating at 30 barg H_2 . Most models for PEMEZ use an assumed n_{eo} value, and these model estimates are included for comparison as well [40] [71].

The comparison of this studies n_{eo} measurements against the aforesaid literature values are shown below for current density and temperature for Figure 111 and Figure 112 respectively.

The variation in current density matches Medina & Santarelli, albeit loosely, as their measurements did not include any midpoints between their high and low current density measurements. Li et al. did not show any variation with current density at ambient pressure conditions, a result that also matches other ex-situ studies of liquid submersed membrane electrode assemblies (MEA) imitating PEM electrolysis conditions at ambient [119] [120]. Kim et al.'s proposed regression model based off of Medina & Santarelli shows fairly good agreement with this study's estimations as well. It can be seen that decreasing H_2 pressures lead to a lower and lower slope in the n_{eo} vs. j relationship, with ambient studies showing very little to no slope, suggesting that the current density dependency is a combined effect with cathodic pressure.

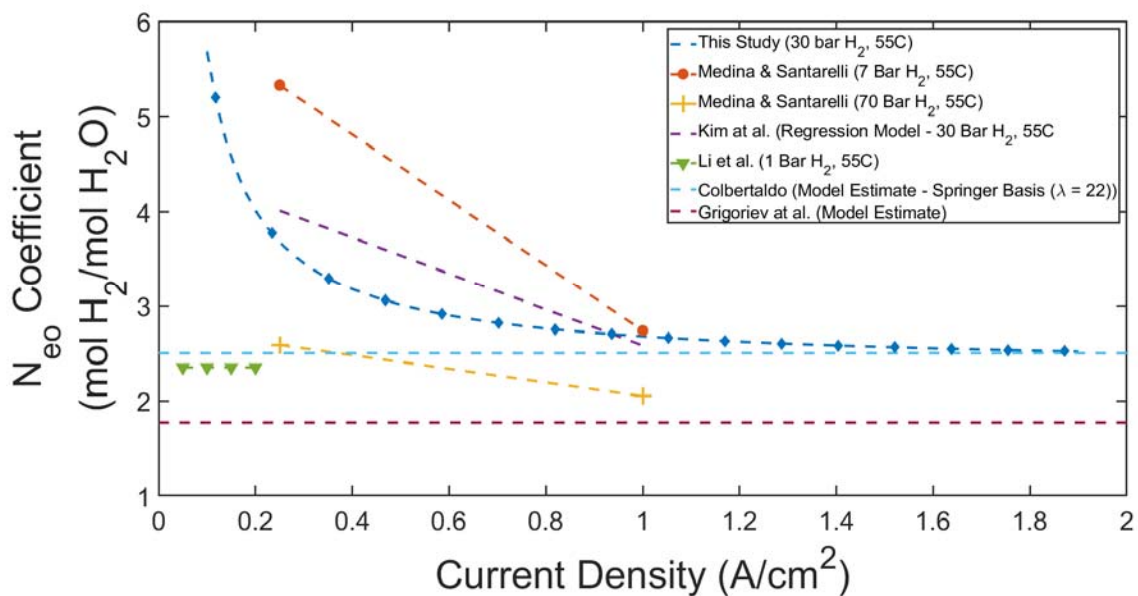


Figure 111. Comparison of electro-osmotic drag coefficient vs. current density measurements in this study to values found in literature.

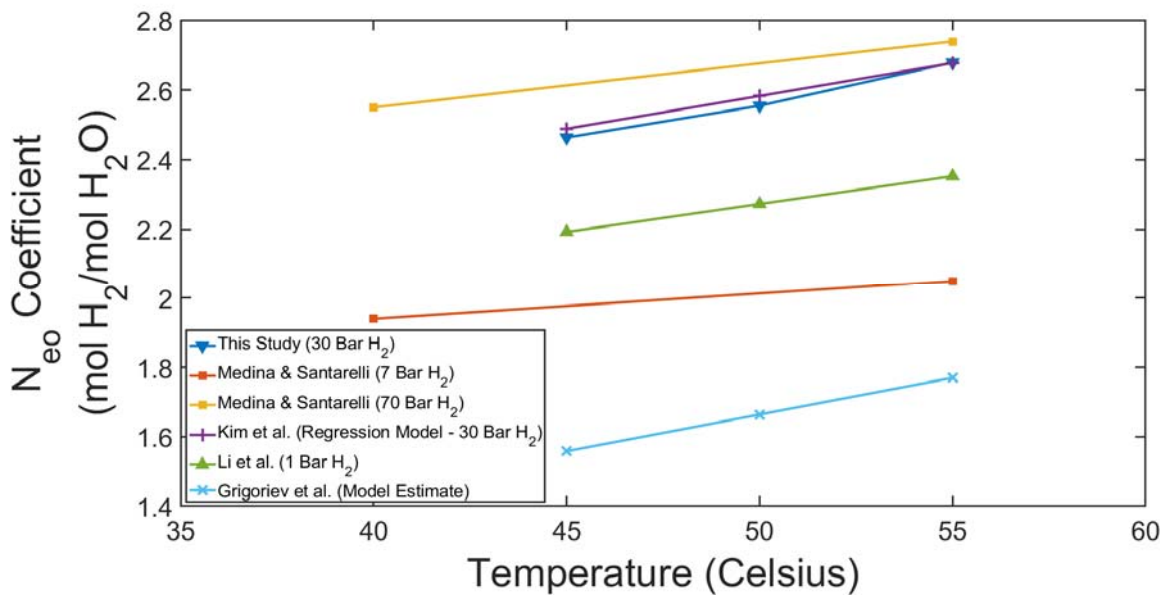


Figure 112. Comparison of electro-osmotic drag coefficient vs. temperature measurements in this study to values found in literature.

6.3.2 Product Hydrogen Loss & Gas Cross-Over

From a system perspective, there are several pathways through which product hydrogen loss occurs. Generated hydrogen can be predicted from Faraday's law of electrolysis (36). Some losses occur due to cross-over of gaseous species in the electrolyzer stack. Dissolved hydrogen gas in the water flow from the cathode is circulated back to the anode feed water. Higher pressures in the cathode compartment lead to appreciable quantities of hydrogen in the cathode water, however near ambient pressures combined with long residence times at large volume tanks in the water recovery loop leads to much of the hydrogen dissipating to the atmosphere before it makes its way back to the anode feed water. A significant source of hydrogen loss comes from the operation of the PSA dryer system. Throughout operation, a slipstream of dry hydrogen from the working bed is flowed through inactive bed to purge accumulated moisture. Some product hydrogen is also likely lost due to leakage through the joints in the process piping. The end result of these effects is that the product hydrogen measured at the system outlet is far lower than the hydrogen generated due to electrolysis. These loss pathways are summarized in equation (60) and Figure 113 below.

$$\dot{m}_{H_2,produced} = \dot{m}_{H_2,generated} - \dot{m}_{H_2,soluble} - \dot{m}_{H_2,Dryer} - \dot{m}_{H_2,Leakage} \quad (60)$$

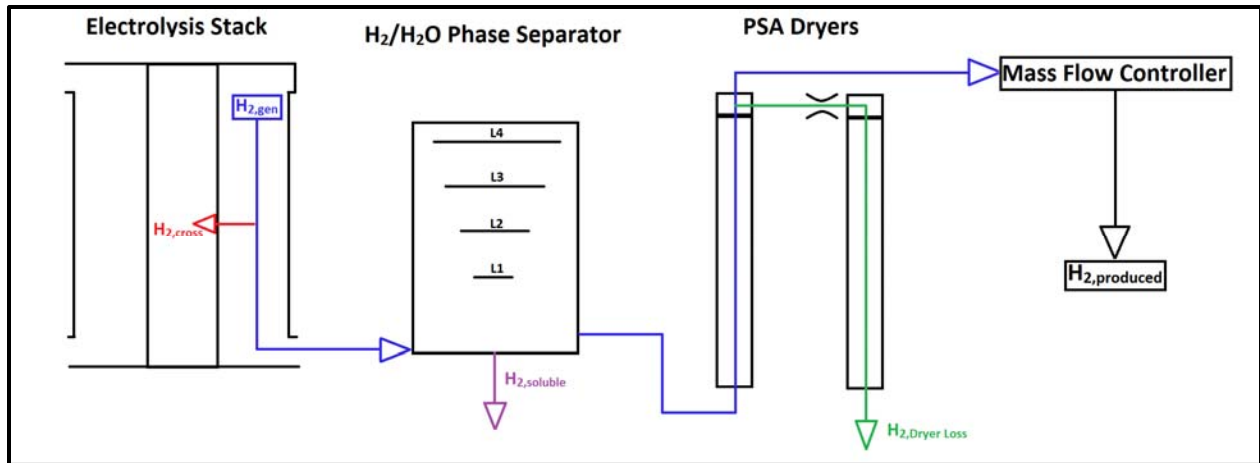


Figure 113. Product hydrogen loss pathways.

6.3.2.1 Solubility

The contribution of dissolved hydrogen in the cathode water recovery stream to overall hydrogen losses was estimated using Henry's Law for steady state conditions. The Henry's Law constant was determined as $K_H = 75253 \text{ bar} \cdot \frac{\text{mol } H_2O}{\text{mol } H_2}$, interpolated from experimental data for the temperature range of interest from two studies of pressure dependence on hydrogen solubility in pure water [121] [122]. In combination with the drain valve behavior data used to estimate the cathode water flow rate out, the net hydrogen loss to this mechanism can be estimated. The amount of dissolved hydrogen gas that contributed to the observed concentration in the anode due to feed water recirculation is determined using solubility of hydrogen at atmospheric pressures.

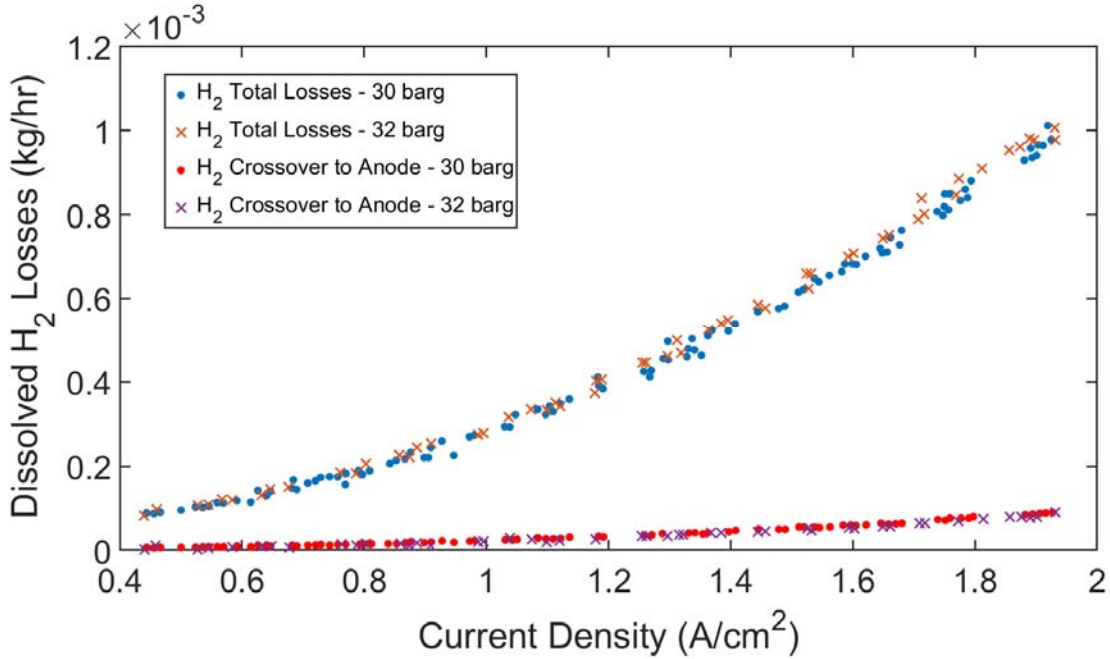


Figure 114. Hydrogen loss & hydrogen transport to the anode due to dissolved hydrogen entrained in water recovered from the cathode outlet.

Figure 114 shows the estimated hydrogen loss to the cathode water recovery process. Sustained part load operation was used to establish as close to steady state conditions as possible, for hydrogen pressure set points of 30 barg and 32 barg. At most, approximately 1 gram per hour is lost, equivalent to 0.1% of the generated hydrogen flow. Of this loss, an estimated 0.09 grams per hour at most is transported to the anode. The concentration of anodic hydrogen attributable to transport of dissolved hydrogen can be estimated from equation (61). Figure 115 below shows the estimated contribution of this transport mechanism to anodic hydrogen concentration versus measurements of hydrogen concentration in the anode.

$$\%H_{2,an,sol} = \frac{\dot{m}_{H_2,sol,an}}{\dot{m}_{H_2,sol,an} + \dot{m}_{O_2,gen}} = \frac{\dot{m}_{H_2,sol,an}}{\dot{m}_{H_2,sol,an} + \frac{n_{cells}jA}{4F}} \quad (61)$$

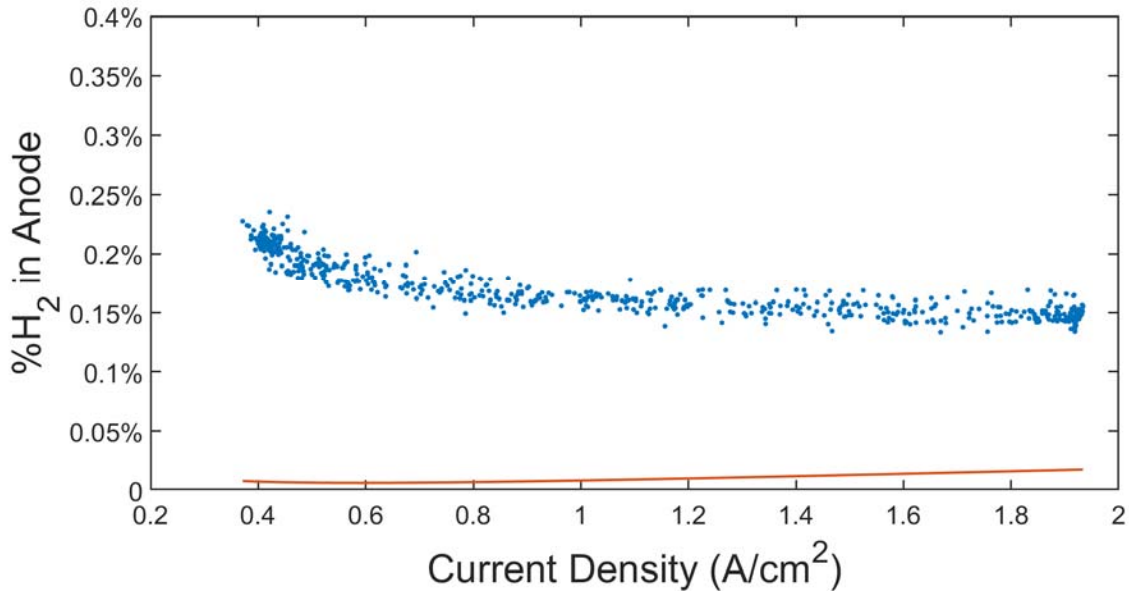


Figure 115. Estimated percentage of hydrogen content in anode due to solubility versus observed values.

6.3.2.2 Orifice/Dryer

Hydrogen loss to the PSA dryer beds is flow restricted by an 0.18 mm orifice, rated at a maximum nominal flow rate of 13.8 SLPM H₂ at 30 barg H₂, equivalent to 0.0744 kg H₂/hr.

Since the downstream pressure is effectively atmospheric, choked flow conditions are established, and the dryer flow as a function of varying hydrogen pressure can be estimated using equation (62) from Crowl & Louvar [123].

$$\dot{m}_{H_2,Orifice} = C_d A_o P_{H_2} \sqrt{\left[\frac{k G_c M_{H_2}}{RT} \right] \left[\frac{2}{k+1} \right]^{\frac{k+1}{k-1}}} \quad (62)$$

For the rated flow rate of 0.0744 kg H₂/hr at 30 barg, the discharge coefficient is determined to be C_d = 0.42. Using the relation between hydrogen pressure and orifice mass flow, the dryer losses are estimated as a function of H₂ pressure and orifice flow uptime (~roughly 91.5% of the time on average). Figure 116 below shows the predicted losses due to solubility of hydrogen in recovered cathode water as well as dryer losses versus the generated hydrogen output (Faradaic basis) and the observed hydrogen output. It can be seen that the estimated system losses account for the majority of the discrepancy in hydrogen output from the observed measurements.

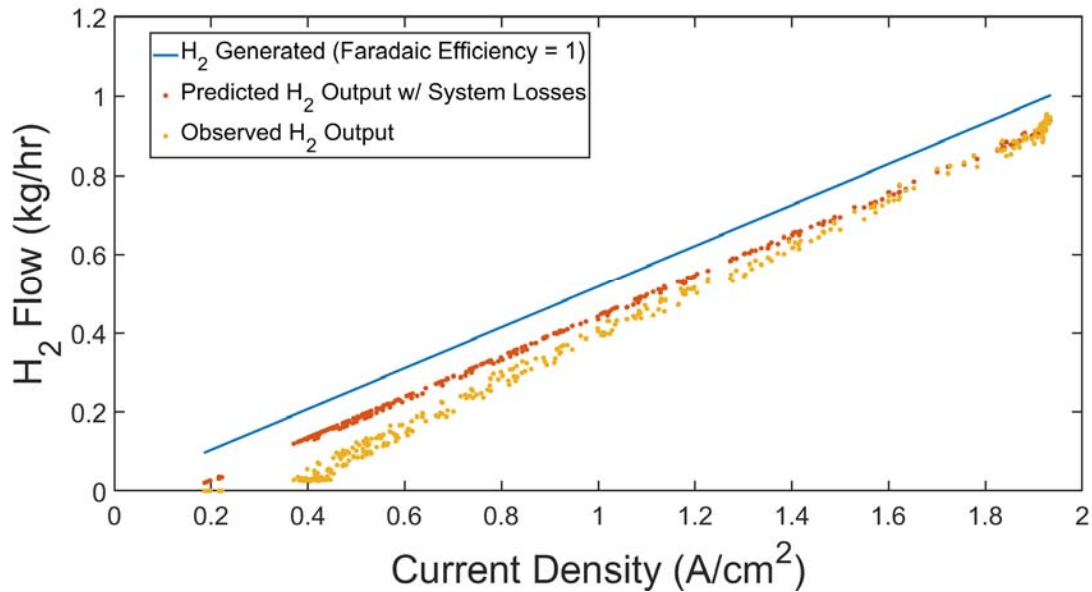


Figure 116. Comparison of net generated hydrogen at stack versus predicted hydrogen output after dryer and solubility losses versus observed hydrogen output.

6.3.2.3 *Cross-over*

Cross-over of product gaseous species in the electrolyzer cell stack occurs as a result of the chemical potential gradient across the polymer electrolyte, which itself is a result of the pressure gradient. Mass transport of gaseous species across the electrolyte is primarily driven by diffusion [44] [124]. In the case of the C10 electrolyzer system, which operates at pressure differentials of as much as 30 barg from cathode to anode, safety is considered a potential concern, particularly at low current densities where oxygen production slows down in the anode, while pressure-driven diffusion of hydrogen remains relatively constant, leading to higher concentrations of hydrogen gas in oxygen gas. The lower explosive limit of hydrogen gas is 4% by volume in O₂ and air [114], requiring stringent mitigation of mixing for the two product gas species.

Hydrogen content in the anode stream is measured by combustible gas detector at the oxygen-water phase separator tank for purposes of safety. The combustible gas sensor requires regular calibration, as well as having relatively poor error range ($\pm 10\%$ accuracy at 25 Celsius), and as such the measurements are not an accurate measure of hydrogen gas present. Hydrogen concentration in the anode side is typically around 0.16% on a volumetric basis, equating to roughly 4% of the LEL of H₂ in oxygen or air. At lower current densities, an increase in hydrogen concentration is observed as the rate of oxygen production drops, while hydrogen transport across the electrolyte to the anode remains relatively constant, reaching concentrations as high as 0.25% by volume, or 6.25% of the LFL of H₂, well within safety limits.

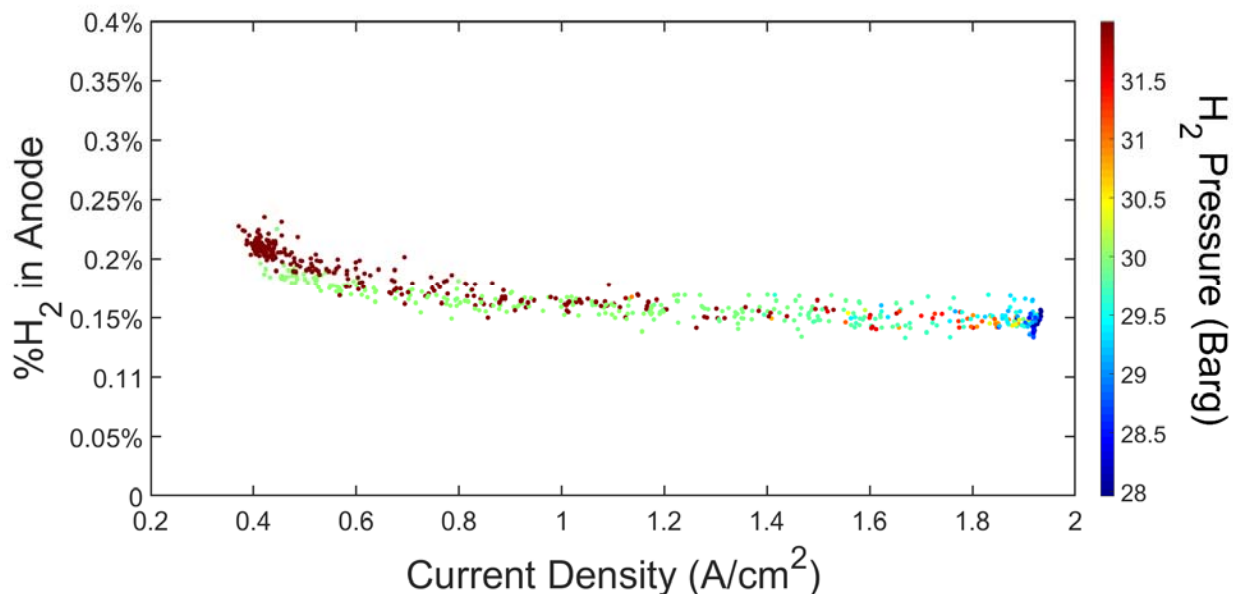


Figure 117. Observed percentage of hydrogen gas in the anode product stream.

While not of initial interest to this study, it became clear as the study progressed that the amount of hydrogen gas that is lost to cross-over in the stack increases with increasing hydrogen pressures and ultimately could reach prohibitive levels for reasons of both efficiency and safety when projecting PEM electrolyzer systems out to higher H₂ pressures. As a result, the initial test bed was not designed with quantifying this cross-over phenomena in mind.

The amount of hydrogen gas that crosses over from the cathode to the anode in the electrolyzer stack is estimated via two different approaches; a ‘top-down’ estimate and a ‘bottom-up’ estimate. In the ‘top-down’ estimate, hydrogen losses unaccounted for by the dryer and dissolved hydrogen gas losses are assumed to be accounted as cross-over losses. In the ‘bottom-up’ estimate, the anodic hydrogen content is used to estimate the concentration of hydrogen exiting the anode stream.

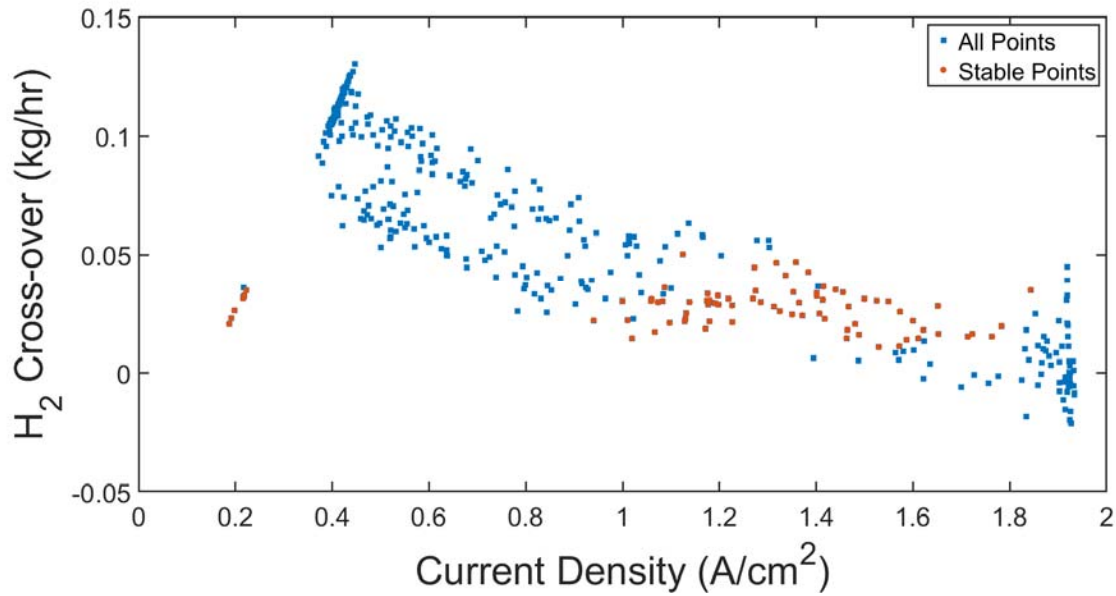


Figure 118. Observed ‘unaccounted’ for hydrogen losses, with stable points utilized for the top-down estimate of hydrogen cross-over.

Figure 118 shows the ‘unaccounted’ for hydrogen losses considered for the top-down estimate of hydrogen gas cross-over losses. Due to the transient nature of the pressure driven controls, points that were collected with high pressure transience over the sampling period were eliminated for this analysis. This occurred primarily in two regimes. At operating conditions below 1 A/cm², the average pressure downstream was typically higher than the upstream pressure, resulting in likely greater but unquantifiable losses to the dryer orifice. The exception to this regime occurred at ‘zero-flow’ points, where the pressure regulator remained closed; Figure 118 illustrates these points in the lower left. At near full out operating conditions, H₂ pressure fluctuated dramatically, similarly impacting estimations of dryer orifice loss. The points ultimately used are highlighted in Figure 118.

As described by equation (52), two coefficients, diffusive permeability, $\varepsilon_{H_2} \left[\frac{\text{mol}\cdot\text{sec}}{\text{cm}\cdot\text{bar}} \right]$, and the H₂ partial pressure enhancement coefficient, $A_{H_2} \left[\frac{\text{bar}\cdot\text{cm}^2}{\text{amp}} \right]$, are needed to describe the hydrogen

diffusion transport across the membrane as a function of the partial pressure of hydrogen and the current density. Linear regression was used to fit the two coefficients to the experimental data, resulting in $\varepsilon_{H_2} = 1.76 \times 10^{-10} \left[\frac{\text{mol}\cdot\text{sec}}{\text{cm}\cdot\text{bar}} \right]$ and $A_{H_2} \approx 0$. A H_2 partial pressure enhancement factor of near zero occurred due to lack of correlation with current density, suggesting effective mass transport of hydrogen species away from the electrode-electrolyte interface (Figure 119). As a result, hydrogen cross-over was estimated to only be a function of the partial pressure of hydrogen in the cathode, as was found to be the case in the majority of the literature reviewed concerning gas gross-over in PEM electrolysis [124] [125] [115]. This correlation with the 95% confidence intervals is displayed below in Figure 119.

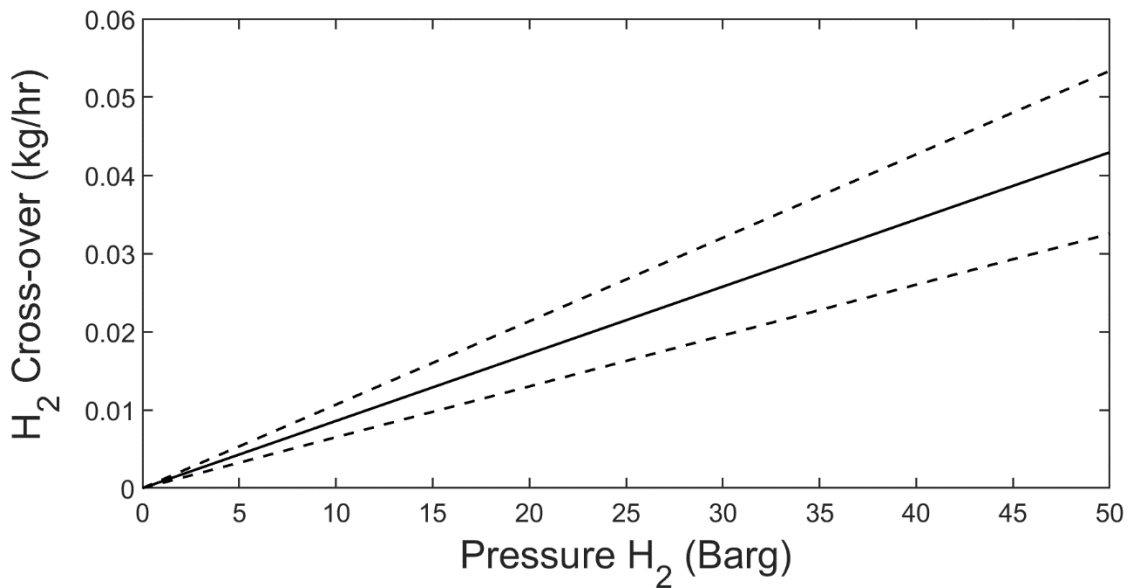


Figure 119. Top-down estimate of H_2 cross-over, function of cathodic H_2 pressure; $\varepsilon_{H_2} =$

$$1.76 \times 10^{-10} \left[\frac{\text{mol}\cdot\text{sec}}{\text{cm}\cdot\text{bar}} \right]. \text{ 95\% confidence intervals in dashed lines.}$$

The end result of the top-down estimate is shown below in Figure 120. The trend of hydrogen concentration varying with current density is similar to what was actually observed (Figure 117),

however there is a two order of magnitude separation between the top-down estimated hydrogen concentration and the measured hydrogen concentrations.

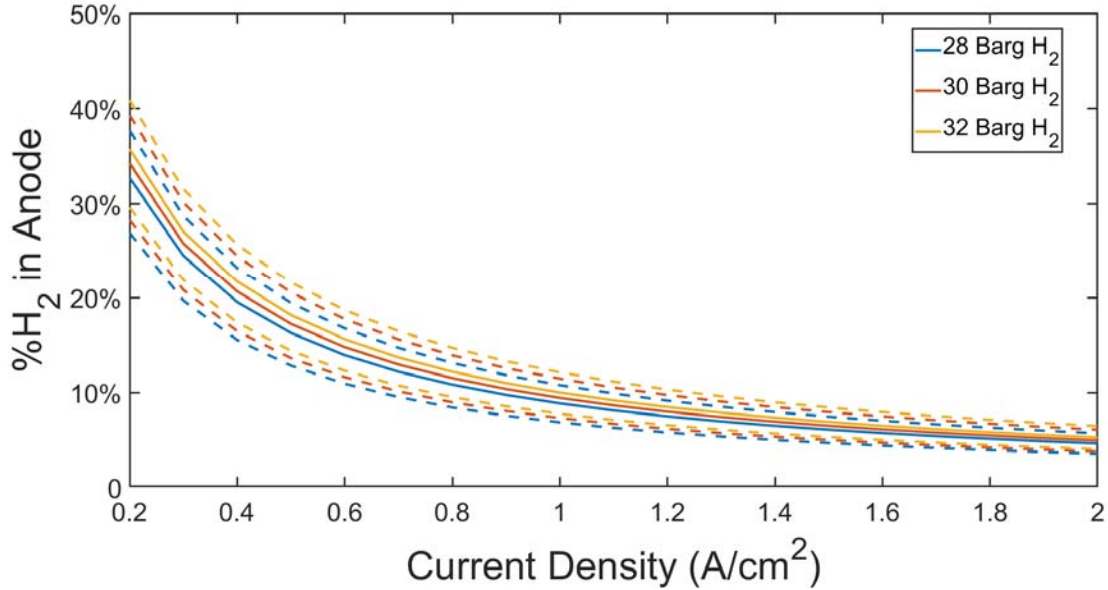


Figure 120. Percentage of hydrogen gas in anode predicted by top-down estimate of hydrogen gas cross-over.

From a 'bottom-up' perspective, the amount of hydrogen cross-over can be estimated using the observed hydrogen concentration values in the anode (Figure 117). Figure 121 shows the points used for the bottom-up estimate of hydrogen cross-over parameters. There is a clear enhancement in cross-over from higher pressures as expected and likewise observed in the top-down estimate. There is a far stronger agreement with the linear correlation between cross-over and current density described by the pressure enhancement factor A_{H_2} .

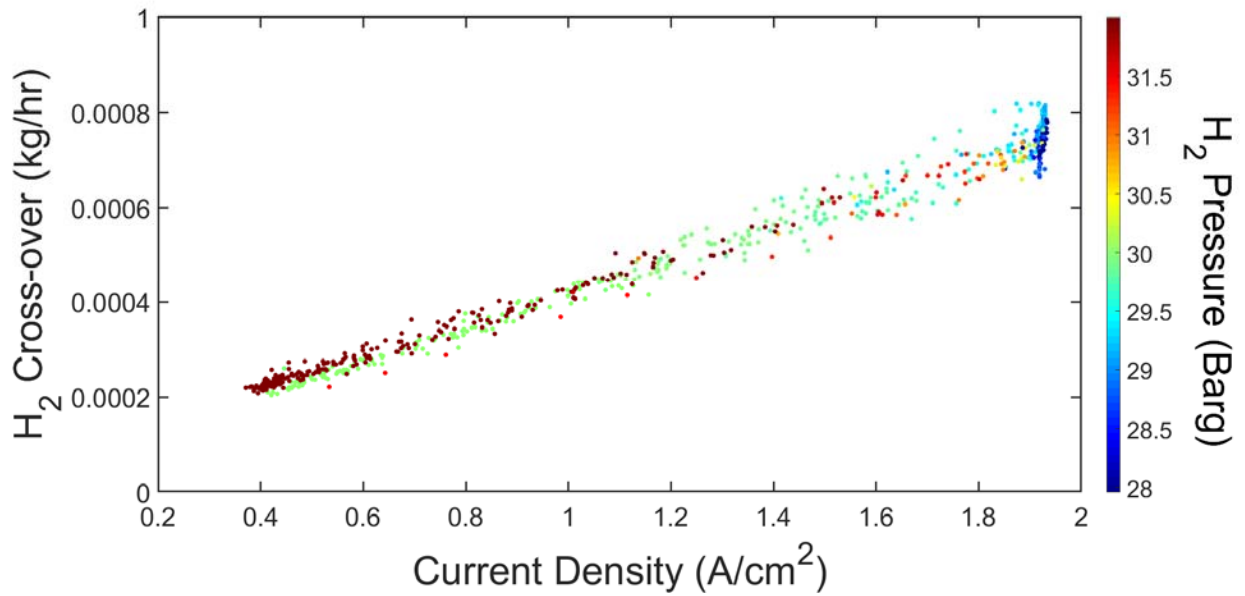


Figure 121. Bottom-up estimate for H₂ cross-over in kg/hr, with pressure correlation.

Linear regression fitting of the bottom-up estimate results in parameter fits of $\epsilon_{H_2} = 4.47 \times 10^{-13} \left[\frac{\text{mol}\cdot\text{sec}}{\text{cm}\cdot\text{bar}} \right]$ and $A_{H_2} = 154.34 \left[\frac{\text{bar}\cdot\text{cm}^2}{\text{amp}} \right]$. The relationship between cross-over, hydrogen pressure and current density predicted by these parameters is shown below in Figure 122.

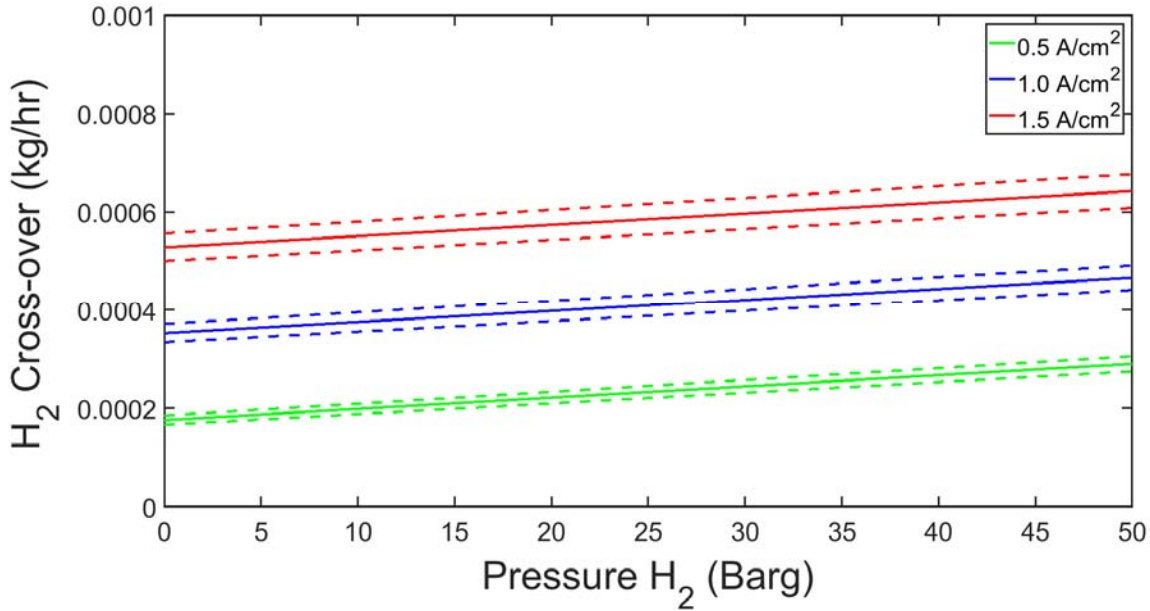


Figure 122. Bottom-up estimate of H₂ cross-over, function of cathodic H₂ pressure and current density; $\epsilon_{H_2} = 4.47 \times 10^{-13} \left[\frac{\text{mol}\cdot\text{sec}}{\text{cm}\cdot\text{bar}} \right]$ and $A_{H_2} = 154.34 \left[\frac{\text{bar}\cdot\text{cm}^2}{\text{amp}} \right]$. 95% confidence intervals in dashed lines.

The value obtained for pressure enhancement factor A_{H_2} is two orders of magnitude higher than what was observed by Schalenbach et al. where the correction factor was proposed [44], and similarly the diffusion coefficient was two orders of magnitude lower than what was observed.

Both methods of gas cross-over estimation suffer from a few limitations. The top-down estimate very likely overestimates cross-over by not accounting for hydrogen leakage in the system, outside of the cell stack. Additionally, the combined rated measurement error of the current transducers (used to calculate Faradaic hydrogen production) and the mass flow meter (used to measure the system hydrogen output) is ~ 0.02 kg/hr, on the same order of magnitude as the ‘unaccounted for’ hydrogen loss used in the top-down cross-over estimate. However, the repeatability of hydrogen measurements through multiple rounds of calibrations over the testing

period suggests that this measurement error range is much tighter than the specified error for both the current transducers and mass flow meter. Furthermore, sustained ‘zero-flow’ operation demonstrated a repeated consistent H₂ loss that follows the predicted trend, while taking the flow meter measurement error out of the equation.

The bottom-up estimate relied on two assumptions. First, that hydrogen gas in the anode was largely inert. For IrO₂ catalyst typically employed in PEMEZ anodes, it is assumed that no hydrogen reacts electrochemically with oxygen [44], or that there is no secondary catalytic combustion of hydrogen in the anode stream, through the use of gas recombiners [125] [124]. Secondly, it is supposed that the timescale on which measurements are taken in the anode is long enough such a steady state condition in the oxygen-water phase separator volume is achieved. At the lowest oxygen flow rate, the amount of time for the volume to be fully exchanged is 3 minutes 15 seconds, and all measurements used were made at sustained 10-minute intervals. Some transients occurred due to dryer operation during testing, which could have had minor undue influence on the results, however these cases did not result in noticeable outliers.

Given that the assumptions for the bottom-up estimate could be invalid (particularly lack of catalytic conversion of anodic hydrogen gas), in addition to the lack of agreement in the resulting transport parameters with current literature, the top-down estimate parameters of $\varepsilon_{H_2} = 1.76 \times 10^{-10} \left[\frac{\text{mol}\cdot\text{sec}}{\text{cm}\cdot\text{bar}} \right]$ and $A_{H_2} \approx 0$ are selected for the analytical electrolyzer model. This will serve as an over-estimate of hydrogen gas cross-over in the stack but reflects the trend properly and is likely close in magnitude.

No significant hydrogen leakage was identified in process piping, which was leak tested intermittently throughout the testing period using visual and pressurization methods. At low part

load conditions, particularly in the regime below $\sim 1 \text{ A/cm}^2$ where pressure began to fluctuate (and was entirely eliminated from the top-down estimate for this reason), ambient hydrogen concentration in the electrolyzer cabinet began to climb, suggesting losses of hydrogen mass flow to the pressure regulation manifold, which could partially explain the large discrepancy in hydrogen loss to gas cross-over below the 1 A/cm^2 load condition, in addition to difficulty in estimating orifice flows with high transience inlet pressure conditions.

6.4 Model Validation

The analytical model using the empirically obtained fitting parameters was exercised against experimental data. The winter and spring solar load following scenarios, as well as the wind load following scenarios were selected for model validation.

The model is setup in a fashion such that the cathode and anode pressures, as well as the stack temperature, are fed as inputs with the stack current. The model inputs used are the electrolyzer system set points, rather than the measured values, to reflect the accuracy of the model when being exercised for analysis, such as in a particular load following application, potentially further integrated with one of the end uses highlighted above (Figure 98). The output of the model is then compared against the actual electrolyzer system behavior with the given set points, to highlight the difference that a more robust model (incorporating dynamics and/or controls) would make.

In modern electrolyzer systems, the cathode pressure and stack temperatures are typically tightly controlled by pressure regulation and heat exchanger systems respectively. In the case of a differential pressure electrolyzer such as the C10 system, the anodic pressure is typically left to vary freely within a small range of pressure. The variation of this anodic pressure was found to have very little impact on system operation. In equilibrium pressure systems, the anodic pressure would be similarly regulated such that the ‘set point’ parameter approach is valid.

For the comparison of the model results to the electrolyzer system, estimated losses to the hydrogen dryer system are deducted from the model output to compare against the observed hydrogen output. Additionally, net system power consumption is estimated by the model using a 92.5% efficiency for the AC/DC power electronics and a flat 2.5kW_{el} power demand to ancillary services. These numbers are derived from the results of section 4.5.

6.4.1 Winter & Spring Load Following

The winter and solar load following cases were selected for validating the solar PV load following capabilities as the two seasonal profiles encapsulate the two ‘extremes’ of solar PV dynamics observed from the physical load following tests.

Table 23 summarizes the results of the model versus the data. It can be seen that the set point approach is a fair assumption in this case, as the system stack temperature and pressures did not depart significantly from the set points. The analytical model does not account for cathodic water recovery, and thus projects dramatically greater water consumption. The percentage of cathodic water recovery is determined from this discrepancy. The model closely matched the actual system performance, with very little deviation in the projected efficiency on both the stack and system efficiency, as well as the hydrogen output.

Table 23. Solar load following cases with analytical model using set points and input current versus actual system behavior.

	Winter		Spring	
	Actual	Model	Actual	Model
Stack Temp (Celsius)	55.08	55	55.04	55
Cathode Pressure (Barg)	29.98	30	29.71	30
Anode Pressure (Barg)	1.72	1.5	1.83	1.5
H2O Cons. (Gallons)	80.98	360.32	166.58	751.52
Cathode Water Recovery	94.99%	--	94.66%	--
Total kg H2 Prod.	21.75	21.98	45.96	46.92
kWh/kg Stack (Faradaic)	50.32	50.29	53.10	52.97
kWh/kg System	76.31	76.48	73.19	73.67

Figure 123 and Figure 124 show the predicted stack power consumption versus the experimental data for the winter and spring solar load following cases respectively. Figure 125 shows the polarization curve agreements between data and model for these cases. These figures highlight the accuracy of the electrochemical model and the parameters obtained from fitting in determining the cell voltage.

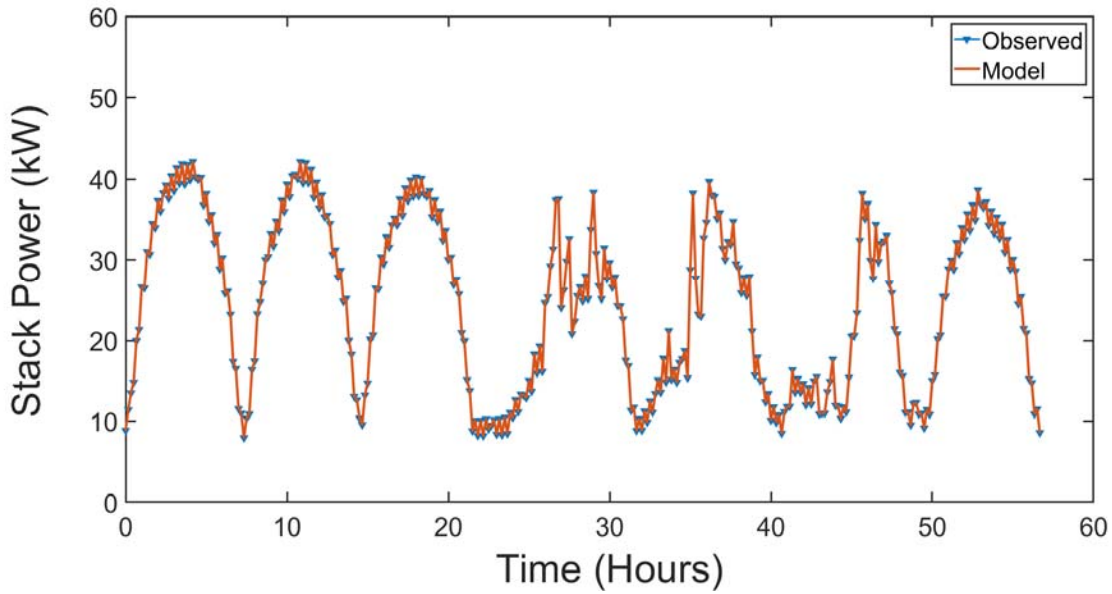


Figure 123. Stack power consumption for winter solar load following, observed data versus analytical model fit.

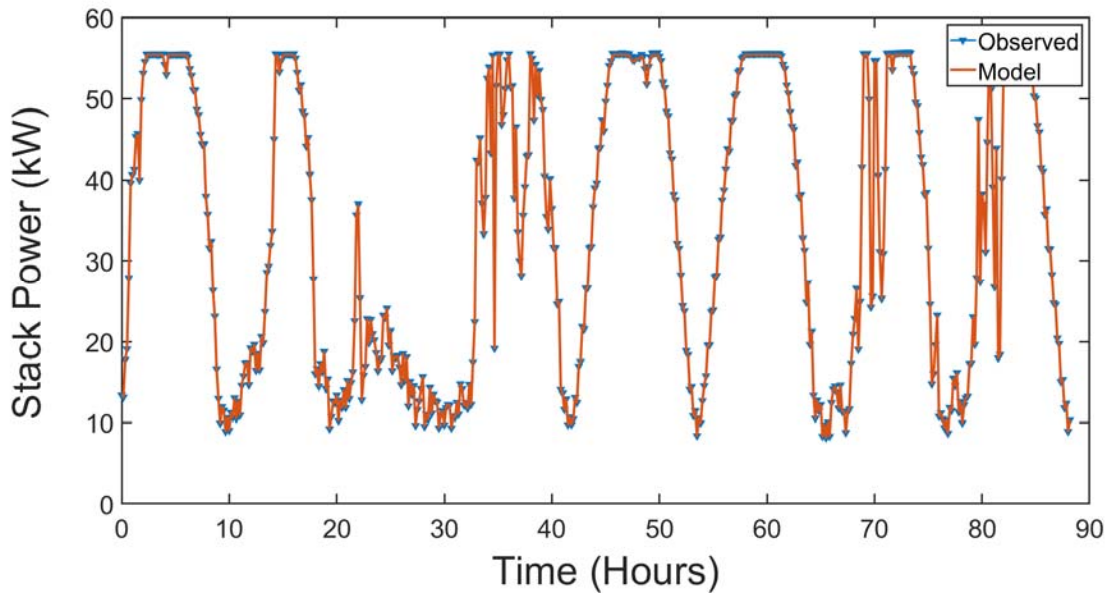


Figure 124. Stack power consumption for spring solar load following, observed data versus analytical model fit.

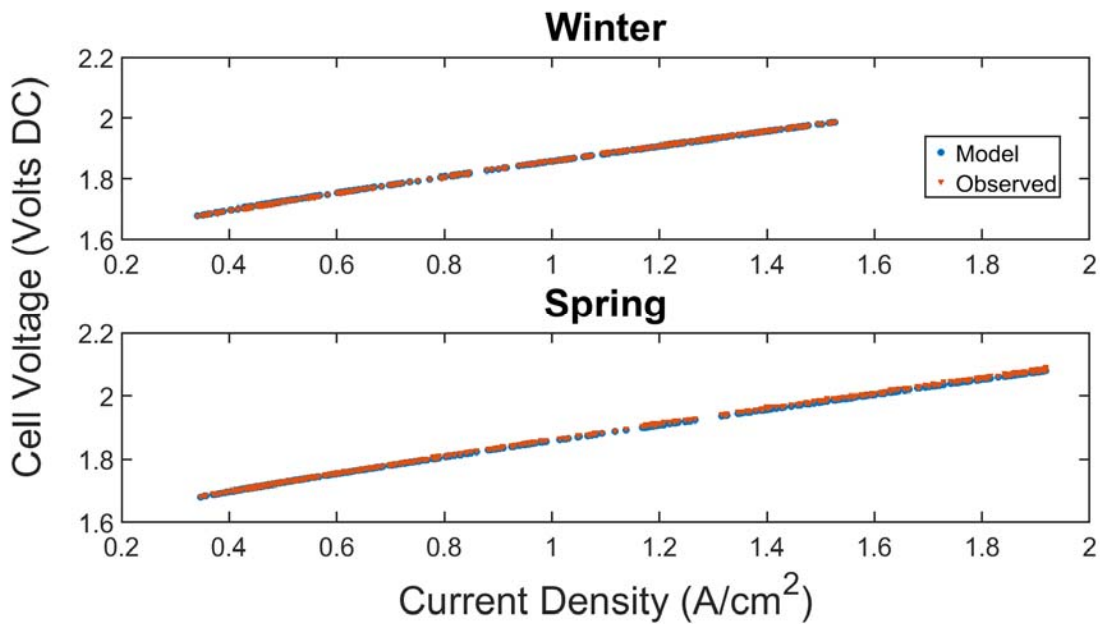


Figure 125. Polarization curve fits for winter and spring solar load following, observed data versus analytical model fit.

Net hydrogen production of the electrolyzer system matched well for the solar load following cases between the model and observations. One-hour averages of measured hydrogen output

were included in Figure 126 showing the agreement between model and data. This was to highlight that while the hydrogen output deviated from the model prediction on a minute to minute basis, over longer time-scales the model prediction agreed well. An increasing degree of departure between the model and data is noticeable at increasingly lower current densities, corresponding to the ‘unstable’ system pressure region of operation where hydrogen flow losses to the orifice dryer becomes difficult to estimate accurately.

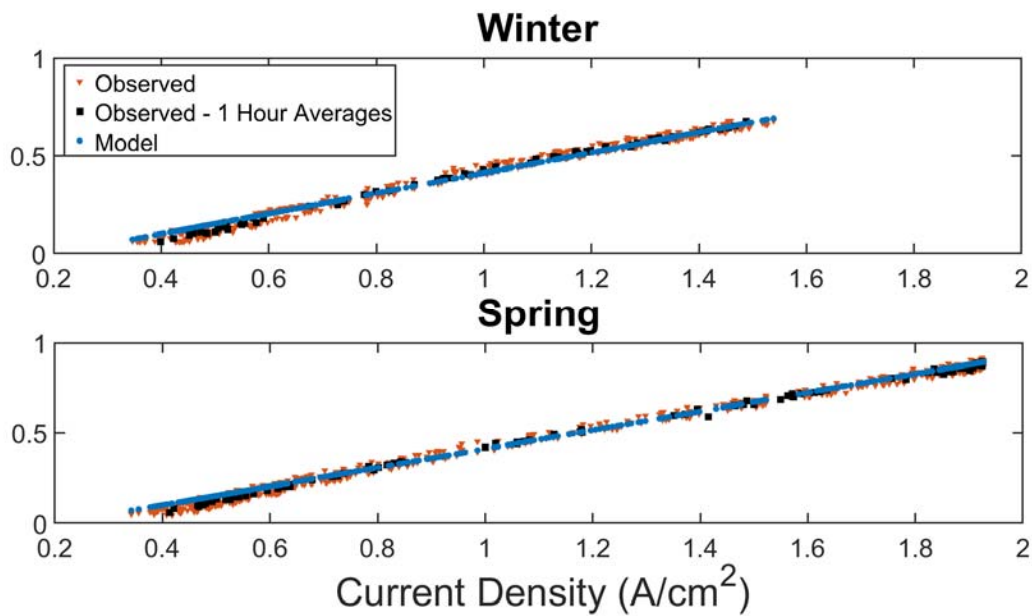


Figure 126. System hydrogen output versus stack current density for winter and spring solar load following, observed data versus model fit with 1-hour averaged observed data.

6.4.2 Wind Load Following

The exercising of the analytical model with the wind load following data provides for a wider range of load conditions than the solar load following case as well as a higher hydrogen pressure set point (32 barg in this case versus 30 barg in the solar load following cases). Table 24 summarizes the results of the model runs for two extremes of wind load following, and figures Figure 127 and Figure 128 show the agreement in stack power consumption for the two profiles. As opposed to the solar load following scenario, there is a noticeable departure in accuracy for hydrogen output and system efficiency particularly for the low load condition first wind case. Additionally, a nearly 1 barg difference in set point pressure versus average observed pressure can be seen in the high load wind case two. At higher flow throughputs, the pressure regulation system sees pressures closer to the injection point pressure rather than the system set point.

Table 24. Wind load following case with analytical model using set points and input current versus actual system behavior.

	Wind - 1		Wind - 2	
	Actual	Model	Actual	Model
Stack Temp (Celsius)	55.09	55	55.09	55
Cathode Pressure (Barg)	31.99	32	31.17	32
Anode Pressure (Barg)	1.70	1.5	1.79	1.5
H2O Cons. (Gallons)	80.50	374.49	151.52	820.85
Cathode Water Recovery	85.91%	--	89.87%	--
Total kg H2 Prod.	14.10	21.00	47.44	50.36
kWh/kg Stack (Faradaic)	47.47	47.39	52.43	52.21
kWh/kg System	147.12	96.94	82.70	77.76

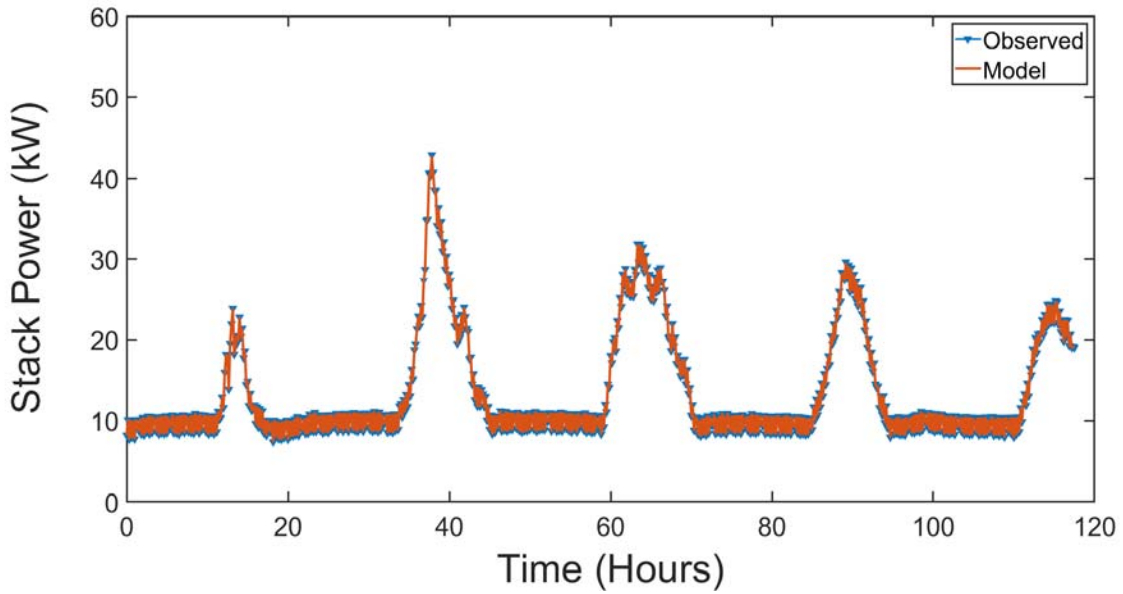


Figure 127. Stack power consumption for first half of wind load following, observed data versus analytical model fit.

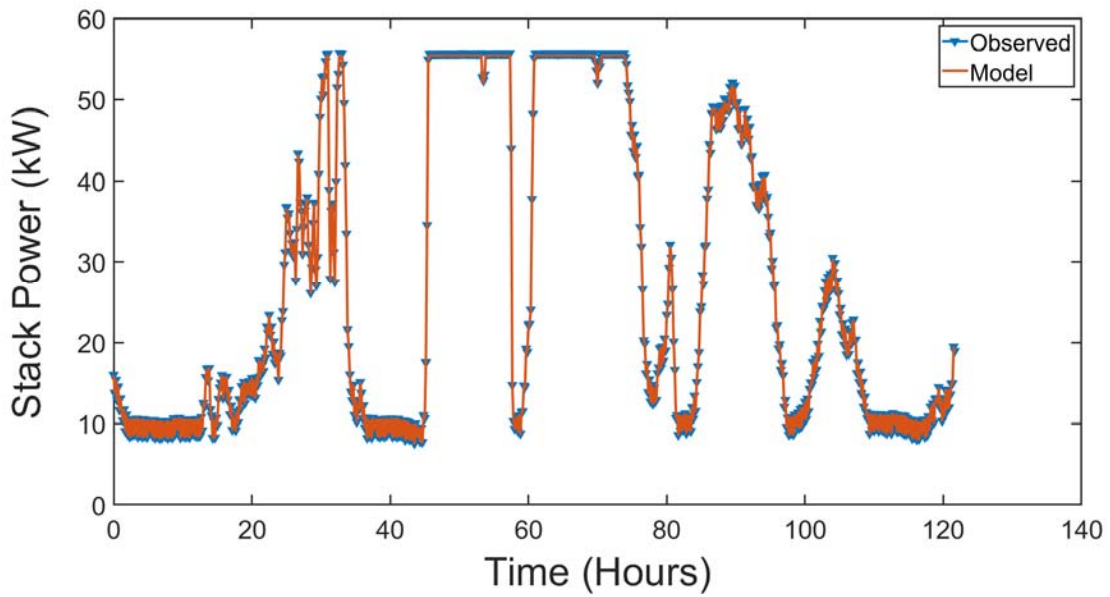


Figure 128. Stack power consumption for second half of wind load following, observed data versus analytical model fit.

Figure 129 shows the polarization curve agreement for the wind load following cases. Some departure can be seen at the higher load condition as opposed to the near perfect agreement from solar load following, but the cell voltage prediction is still accurate to within 0.5% error.

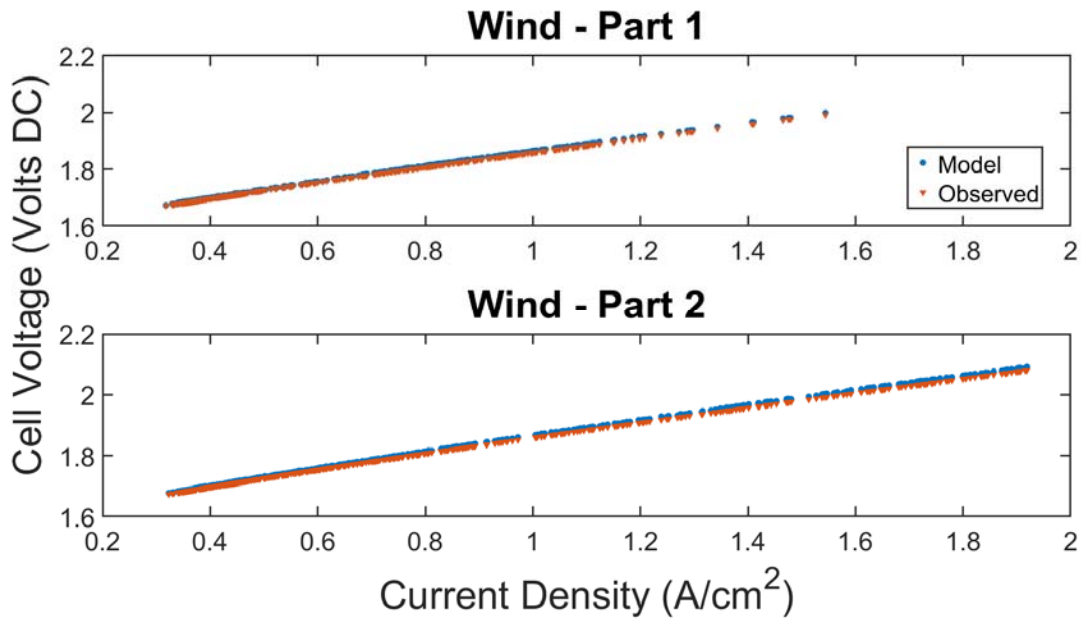


Figure 129. Polarization curve fits for wind load following, observed data versus analytical model fit.

The more extreme deviation in hydrogen output prediction by the model versus measured system performance at the low load condition can be seen in Figure 130. Once again, particularly from a longer time scale averaged perspective, the hydrogen output prediction remains fairly accurate until 0.7 A/cm^2 and below. The end result is a nearly 33% over prediction in hydrogen output for the first wind case of 14 kg H₂ measured output versus a predicted 21 kg of H₂ where the system is operating below the 0.7 A/cm^2 current density regime for 60% of the run time.

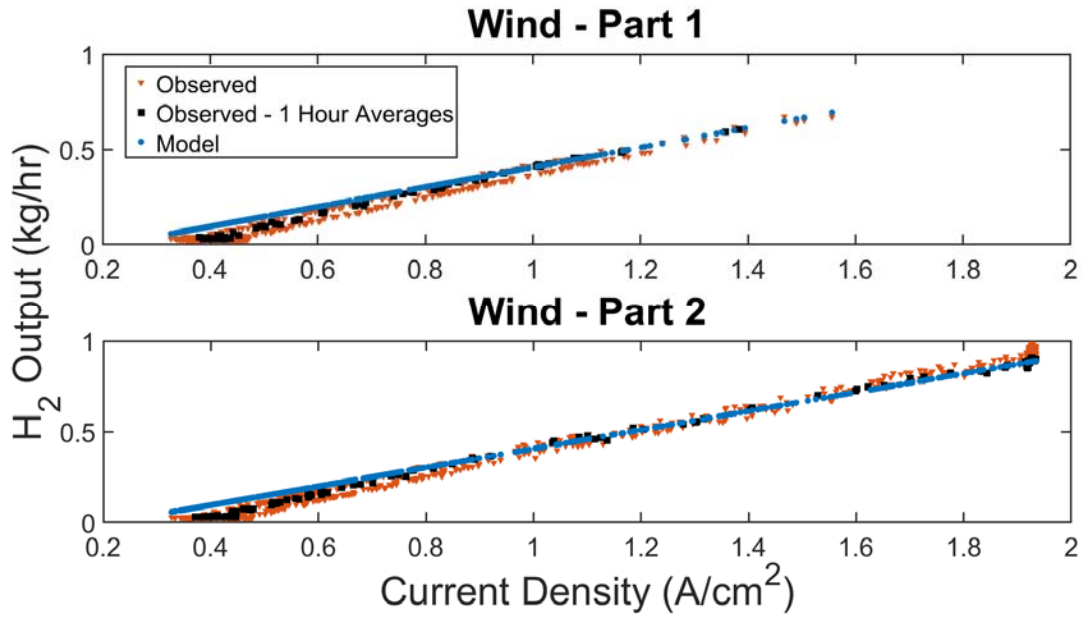


Figure 130. System hydrogen output versus stack current density for wind load following, observed data versus model fit with 1-hour averaged observed data.

6.5 Electrochemical Compression

An important aspect of hydrogen production by electrolysis is the product gas pressure of the hydrogen. Electrolyzer systems can both produce and compress hydrogen electrochemically. For most commercial electrolyzers this hydrogen compression typically does not exceed 30 barg (as is the case for the C10 electrolyzer system at the center of this study). Higher operating pressures are limited by safety and efficiency concerns due to gas cross-over in the membrane.

Furthermore, accelerated chemical degradation in the stack assembly at elevated operating pressures in PEM electrolyzers is a concern [126]. Pressures of 170 barg and 350 barg H₂ (ambient pressure on O₂ side) have been demonstrated by PEM electrolyzer original equipment manufacturers Proton OnSite (now NEL) [127] and Giner [128] respectively.

Ideal electrochemical compression can be characterized as an ideal isothermal compression process, demonstrated by Maclay [129]. Ideal isothermal compression is given by equation (63) from Cengel & Boles [130], where P₂ is the outlet pressure, P₁ is the inlet pressure, R is the specific gas constant (hydrogen gas constant in this case), and T is the temperature.

$$W_{comp, isothermal} = RT \ln\left(\frac{P_2}{P_1}\right) \quad (63)$$

By isolating the voltage increase due to an increase in hydrogen pressure from the Nernst equation (64) [98], and noting the relation between voltage change and work (eq. 65), where Q is the charge and ΔV is the voltage change going from P₁ to P₂, it is evident that the two expressions are equivalent.

$$\Delta V = E_{OCV}(T, P_{2,cathode}) - E_{OCV}(T, P_{1,cathode})$$

$$\Delta V = \frac{RT}{2F} \left[\ln \left(\frac{P_{2,cathode} P_{O_2,anode}^{0.5}}{a_{H_2O,anode}} \right) \right] - \frac{RT}{2F} \left[\ln \left(\frac{P_{1,cathode} P_{O_2,anode}^{0.5}}{a_{H_2O,anode}} \right) \right] \quad (64)$$

$$\Delta V = \frac{RT}{2F} \ln \left(\frac{P_2}{P_1} \right)$$

$$W = \Delta V \times Q = \Delta V \times 2F \quad (65)$$

In the case of using natural gas infrastructure for the compression and transport of hydrogen, common types of compressors include reciprocating, centrifugal, and to a lesser extent, rotary engines [131]. For compression of hydrogen, reciprocating compressors offer the best efficiency as they only suffer from sealing issues, whereas centrifugal engines require far higher tip speeds and/or rotor circumferences to make up for the lighter hydrogen molecules, and rotary engines suffer from severe leakage issues [132]. These mechanical compression methods are typically considered as adiabatic compression processes when taken as a single compression step [130].

The work to compress hydrogen adiabatically is given by equation (66). The constant k is the ratio of specific heats, which is 1.41 for hydrogen gas.

$$W_{comp,adiabatic} = \frac{kRT_1}{k-1} \left[\left(\frac{P_2}{P_1} \right)^{(k-1)/k} - 1 \right] \quad (66)$$

From an ideal, thermodynamic perspective, isothermal compression of hydrogen gas is a less work intensive process, Figure 131 compares the specific work requirement for compression of hydrogen gas for both processes.

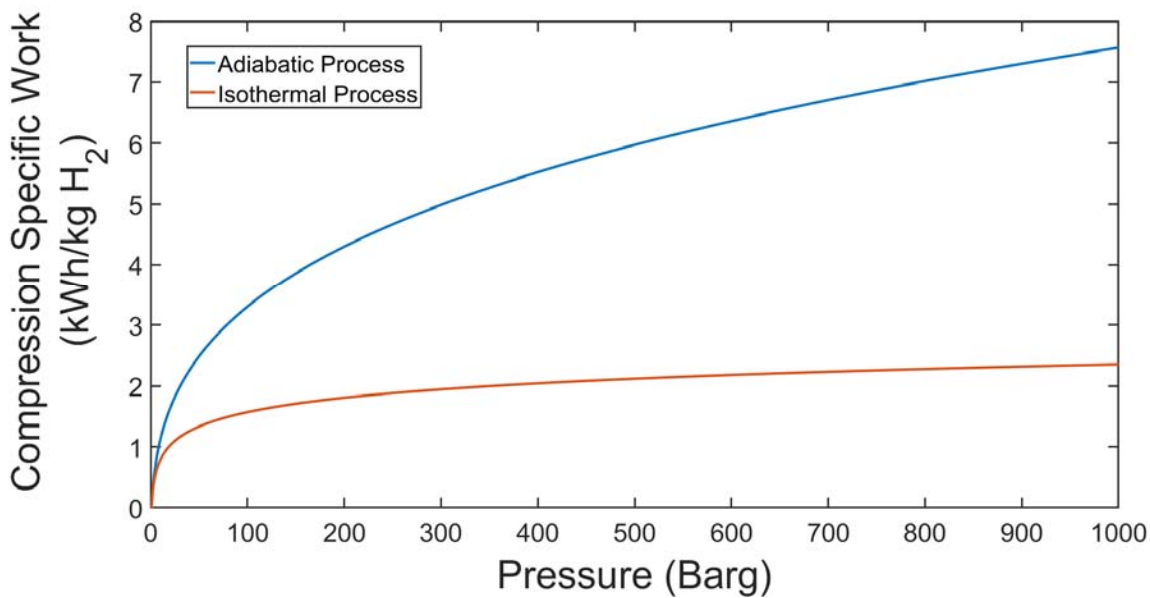


Figure 131. Work requirements for adiabatic vs. isothermal compression of hydrogen gas.

To overcome the limitations of adiabatic compression, mechanical compression processes are often split into stages, with intercooling of the gases in between, bringing the overall process closer to an isothermal compression. Each additional stage adds system complexity and cost considerations however. Furthermore, external mechanical compression suffers from part load efficiency losses & and sizing constraints as a result. Further reason to explore the use of electrochemical compression for hydrogen produced through electrolysis.

Electrochemical compression in a PEM electrolyzer stack leads to penalties in the form of both the aforementioned voltage increase, but also in reduced Faradaic efficiencies as a result of product gas losses to cross-over phenomena. Using the developed analytical model, the effective work requirement of electrochemical compression can be compared against the ideal case. Figure 132 shows this comparison for the range of 0 to 50 barg, where the departure from ideal compression is limited.

Figure 132. Specific work for electrochemical compression of hydrogen gas in PEM electrolyzer stack. ($T_{stack} = 55$ Celsius, $P_{anode} = 0$ barg, $j = 1$ A/cm²).

The cell overvoltage as a sole function of hydrogen pressure is shown in Figure 133. Included as well is the ANOVA mode of cell voltage as a function of hydrogen pressure (Section 4.5.1) for the range of pressures measured. The agreement in cell voltage change attributable to hydrogen pressure observed suggests that the Nernst equation captures the effects of hydrogen pressure, at least for the lower pressures observed. At higher pressures, kinetic improvements could potentially occur, however the kinetics of the hydrogen evolution reaction (HER) at the cathode side are orders of magnitude faster than the oxygen evolution reaction (OER) on the anode side, such that improvements due to elevated hydrogen pressures would largely be negligible. For pressurized electrolysis with equal pressures at the anode and cathode, noticeable kinetic improvements could occur.

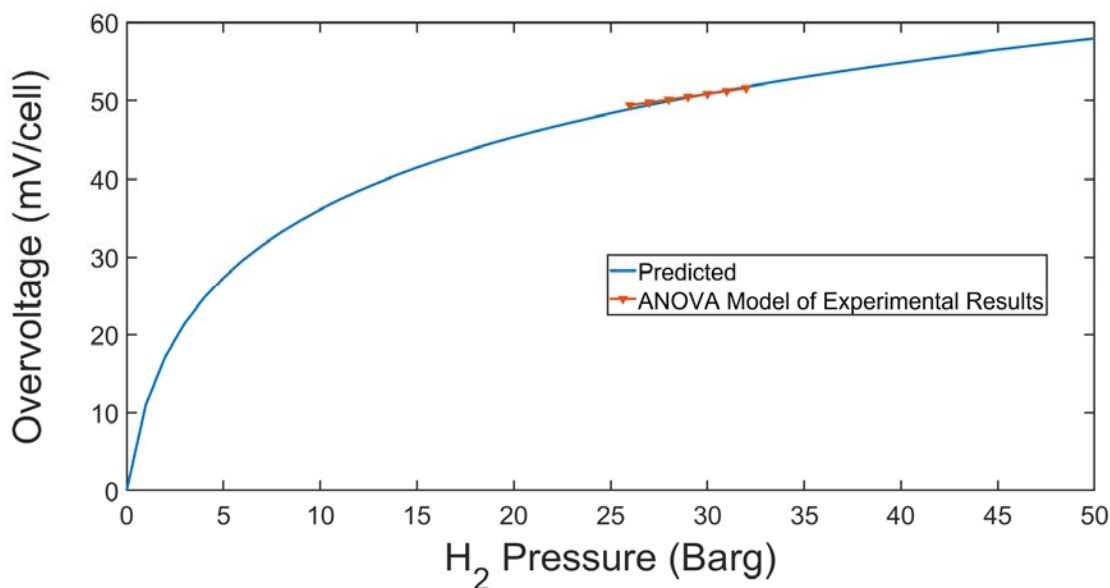


Figure 133. Predicted overvoltage due to increasing hydrogen pressure versus observed average variation using ANOVA on cell voltage measurements.

The extent to which electrochemical compression via electrolysis is effective is limited by gas cross-over losses, which become increasingly prohibitive at lower current densities in the stack. This has implications for the effective part load capabilities of high-pressure PEM electrolysis. The specific energy requirement of hydrogen production across the effective pressure range several load conditions is plotted below (Figure 134). It can be seen that down to 50% load condition, hydrogen pressures of up to 100 barg are within reasonable efficiency ranges, with specific energy requirements of roughly 60 kWh/kg H₂. However, beyond that point it becomes more efficient to operate the stack at increasing current densities to offset the hydrogen losses to cross-over. Operating pressure is also limited by the need to prevent explosive mixtures of hydrogen in oxygen in the anode stream, but this can be prevented by other methods such as the use of gas combiners/catalytic combustors.

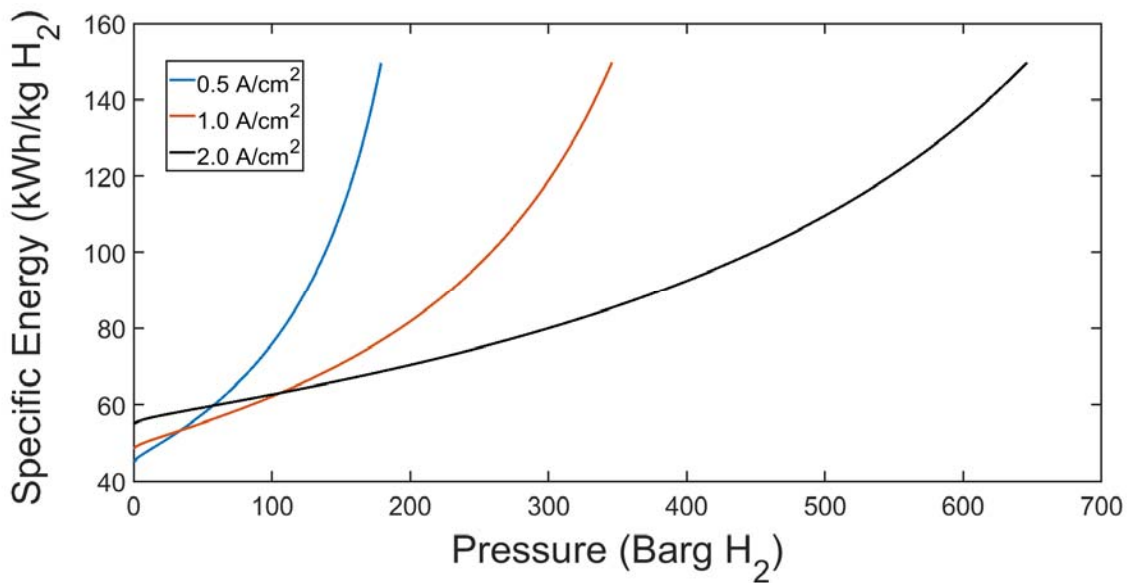


Figure 134. Specific energy of hydrogen production for increasing pressures in the PEM electrolyzer system at several load conditions.

As a result of its similarity to isothermal compression, it is expected that compression during the electrolysis step would be a competitive option due to higher efficiency and reduced system

complexity. It is evident however that for very high pressures and/or for electrolyzer systems that are not operating at near full capacities, this form of compression may not be effective.

For the end use case of integration with natural gas pipeline infrastructure or dedicated hydrogen pipeline infrastructure, the US DoE funded the development of an advanced centrifugal hydrogen compressor capable of boosting 350 psig (24 barg) hydrogen gas to >1000 psig (69 barg) at capacities exceeding 100,000 kg H₂/day [133]. A design for a six-stage centrifugal compressor-based system was developed rated at 240,000 kg H₂/day for a discharge pressure of 1285 psig (88 barg) with a total hydrogen efficiency of 98% HHV H₂ [134]. Such a system could be integrated with a large-scale electrolysis plant outputting at 24 barg, boosting the output for pipeline injection to 88 barg. This integration case for the ideal and actual specific compression work of the electrolyzer system is compared against using solely electrochemical compression to output hydrogen at 88 barg in Figure 135 below. It can be seen that even for the actual electrochemical compression case, the compression of hydrogen solely during the electrolysis step is predicted to be more efficient in addition to reducing system complexity by having to size the mass throughput of the compressor system.

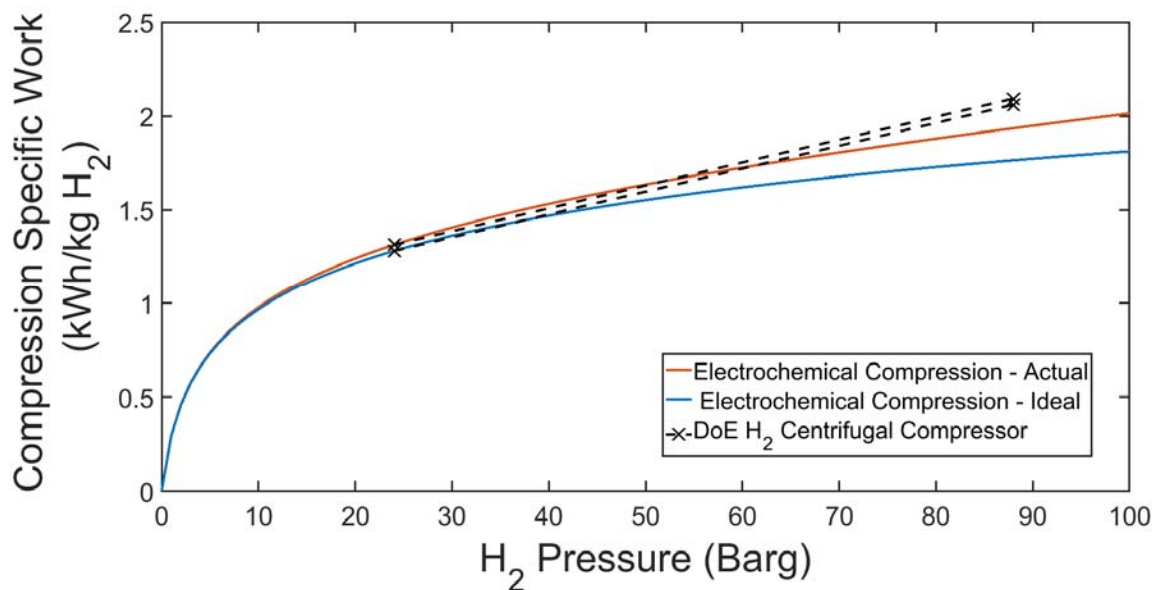


Figure 135. Integration of state-of-the-art H₂ centrifugal compressor design with electrolysis plant for pipeline end-use versus compression solely performed during electrolysis step for ideal and actual electrochemical compression ($j = 2 \text{ A/cm}^2$, $T_{stack} = 55 \text{ Celsius}$).

For higher pressure hydrogen applications such as vehicle refueling, compression during the electrolysis step is highly ineffective, however external electrochemical compressors show promise in this regime. An external hydrogen electrochemical compressor compresses hydrogen through a PEM style electrochemical cell, eliminating safety concerns of mixing hydrogen in oxygen gas. These compressors have been demonstrated performing single-stage compression of hydrogen from ambient pressure to 800 barg [135].

HyET Hydrogen Energy Efficiency Technologies is one such manufacturer of the electrochemical hydrogen compressor technology who have published performance data for optimal conditions for single-step compression of hydrogen from 10 barg to 450 barg [136].

There are still parasitic losses present with respect to back diffusion of hydrogen gas to the low-pressure side, as can be observed with the increasing work requirement with higher hydrogen mass flows (Figure 136).

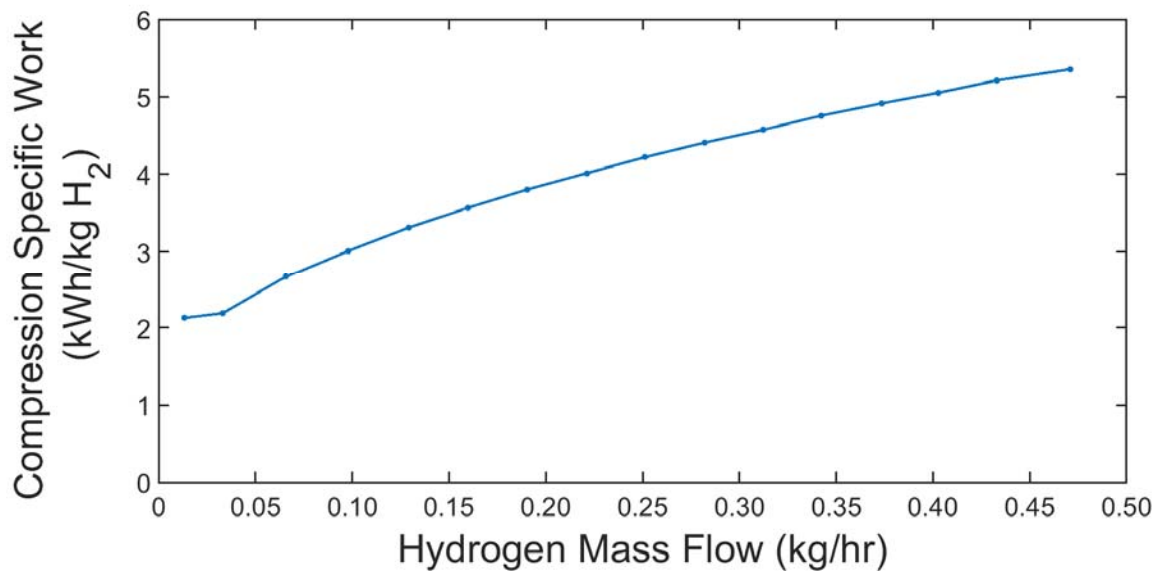


Figure 136. Compression work for HyET electrochemical compressor vs. hydrogen mass flow rate [136].

Taking the scenario of a small hydrogen fueling station at a capacity of 200 kg/day, whose hydrogen supply is maintained on-site by a PEM electrolyzer, the implementation of external electrochemical compression with an electrolyzer system versus compression solely accomplished in an electrolyzer system can be compared. As the available data for the HyET system covers compression from 10 to 450 barg, the station storage pressure will be set to 450 barg. For a fueling station supplying H35 fueling services (350 barg fueling) this is a reasonable final storage pressure [137].

The external electrochemical compressor and electrolyzer systems are scaled up in size by number of electrochemical cells to meet the demand capacity of 200 kg H₂/day (maximum rated flow rate of 8.33 kg H₂/day) at their maximum rated output. Many hydrogen refueling station analysis have employed polytropic expression assumptions in modeling on-site hydrogen compression for refueling [138] [139] [140]. Polytropic compression representative of a typical

diaphragm compressor employed at a hydrogen fueling station with a value of $n_p = 1.6$ and an isentropic efficiency of 80% is also compared against the two cases [52].

The results of this comparison are shown below in Figure 137. Specific energy consumption of hydrogen is strongly dependent on system output for the electrolyzer compression only case due to Faradaic inefficiencies of part-load high pressure electrolyzer operation. The polytropic compression assumption does not likely capture the part load capability of a fixed size diaphragm compressor, however its performance is predicted to be fairly comparable at the full load condition point to the electrolyzer system. The external electrochemical compressors stand out in this application, with specific energy costs of just under 60 kWh/kg H₂.

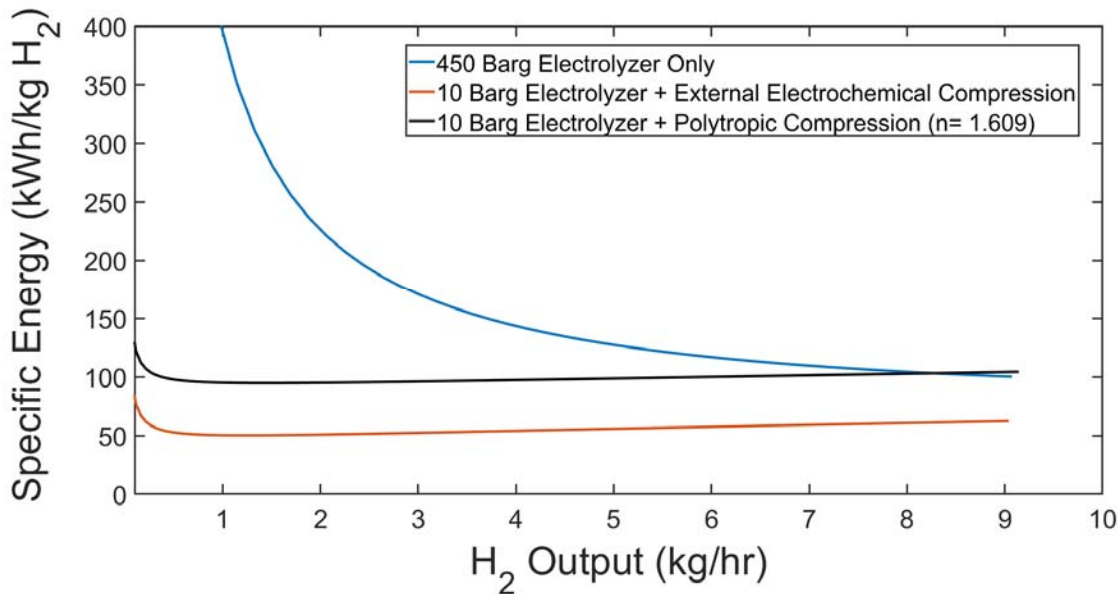


Figure 137. Performance comparison for electrolyzer system with compression in supplying 200 kg/day H₂ at 450 barg intended to be representative of a hydrogen fueling station.

7 Summary, Conclusions & Recommendations

7.1 Summary & Observations

Over 4000 hours of operation of a commercially available 60kW PEM electrolyzer system integrated with the UC Irvine Central Plant's natural gas system and combustion turbine were

achieved. Of the 4000 hours of operation, 1000 hours of steady state benchmarking, several hundred hours of sustained part load operation, and over 2000 hours of VRES load following were accomplished. The control of the PEM electrolyzer system for dynamic dispatch response to VRES load following was accomplished using a mass flow controller on the hydrogen process connection from the PEM electrolyzer system, without any physical modifications to the system itself. VRES load following was demonstrated for both a solar PV system across a wide range of conditions, and for aggregated wind turbine resources. The data acquired from the dynamic operation of the electrolyzer system indicates that PEM electrolyzers can operate under extreme power transients on a second-to-second time scale, not only at a stack level but from an overall system level, using a relatively simple and unobtrusive control strategy. The successful installation and integration of the electrolyzer system, the steady state benchmarking and dynamic operation, and the characterization of the electrolyzer system performance in conjunction with the mass flow controller approach comprise the first half of the current work, and fulfill objectives 1-4.

Analysis of the electrolyzer system included benchmarking of the overall electrolyzer system including water consumption, power electronics, ancillary system power consumption, hydrogen drying components, and the electrolysis process itself. Dynamic operation of the electrolyzer system across the available range of operating parameters allowed for extended characterization of part load performance that is essential to the success of such a system in power-to-gas applications where lower equipment capacity factors are expected due to the intermittency of solar and wind resources. Use of ANOVA techniques through Design Expert software provided insight as to the primary influencing operating conditions on the effectiveness of the electrolyzer system and its components. The experimental analysis indicated relatively stable system

efficiency down to 50% load condition (1 A/cm^2 at the stack). Exceedingly poor performance below 30% load condition (0.6 A/cm^2) primarily due to high percentage losses of the hydrogen product, providing a recommended minimum operating condition, rather than the rated 10% minimum load condition. The increasing discrepancy between the measured hydrogen output and the amount of hydrogen produced according to the Faradaic relation at lower current densities explained the large drop off in system efficiency. This hydrogen loss was thoroughly analyzed and broken down into several pathways that were implemented into the analytical model.

The analytical model was developed in Matlab. It provides a configurable electrolyzer system model that takes in a load profile (in the form of stack current) and system operating set points, and outputs the net electrical consumption of the stack and the species transport. Matlab optimization techniques and steady state experimental data were used in conjunction to estimate stack electrochemical and membrane transport parameters of the C10 electrolyzer system. The accuracy of the model using the set point approach and semi-empirical fitting techniques was validated against the VRES load following runs.

The PEM electrolyzer system analytical model was further exercised to characterize the real electrical work required to pressurize the hydrogen in the electrolysis step to pressurize as high as 32 barg. The model was further exercised to compare this electrolysis based electrochemical compression to a state-of-the-art centrifugal compressor for pipeline integration of hydrogen as well as to external electrochemical compression and polytropic compression for end-use in hydrogen refueling stations. This analysis showed that electrolysis based electrochemical compression could already be better suited from an efficiency standpoint for pressures as high as 90 barg, eliminating the need for external mechanical compression systems and reducing the complexity of hydrogen pipeline integration. For higher pressure applications, further

improvements in mitigating hydrogen gas cross-over in the PEM electrolyzer stack is required, however external electrochemical compression provides an attractive alternative. In either case, extra measures will need to be taken to ensure that combustible mixes of hydrogen in oxygen do not occur due to hydrogen cross-over to the anode. The development of the analytical model and the results obtained from its use accomplished objectives 5-7 and leave only the combustion turbine impacts of hydrogen addition to be determined.

The impacts of hydrogen injection from the electrolysis process for the entirety of the testing period was assessed using ANOVA analysis due to the incredible number of variables that influence turbine operation and the large amount of data gathered throughout the testing period. Hydrogen addition showed a high likelihood that it offset 2.5 ± 1.75 kg of natural gas per kg added, with the average prediction of 2.5 kg lining up very closely with the predicted offset given by heat balance methods. No significant impact was shown on emissions of carbon monoxide and nitrogen oxides, taken after the turbine exhaust catalytic clean-up systems.

A higher throughput hydrogen test was designed, built, and carried out at the end of the testing period, increasing maximum hydrogen throughput from 0.9 kg/hr to 9.0 kg/hr. A maximum observed concentration of 3.4% H₂ in natural gas was sustained to the combustion turbine for 15 minutes without any complications. Results from the high throughput hydrogen test were limited due to the limited time duration of the testing period combined with the complications associated with the injection system and the available hydrogen supply. ANOVA analysis of the results showed similar results as to what was found with the longer term, lower throughput hydrogen addition testing.

Observations from steady state electrolyzer operation

- A slight ‘break-in’ effect of the PEM stack was observed with an increasing maximum stack current observed during the first 1000 hours of operation. This was determined to not be due to the power electronics as the stack DC power supply was replaced at 600 hours with no change in the break-in trend.
- The stack AC/DC power electronics exhibited consistently higher efficiencies at lower ambient temperatures, matching expected temperature derating for DC power supplies, although at this scale the phenomenon is not well documented. This variation in AC/DC power electronics efficiency explained the diurnal trend in system efficiency observed, where the system performed better at night due to lower ambient temperatures.
- OEM rated system efficiency was 57.1% HHV H₂. Sustained system efficiency measured at full load conditions was around 58.5% HHV H₂ on average, increasing from 57.47% up to around 60% HHV H₂ across the sustained full load runs during the first 1000 hours.
- The power consumption of the chiller unit providing cold water to the electrolyzer system heat exchangers was measured at 17 kWh/kg of H₂ produced, leading to a net hydrogen production efficiency of 46.5% HHV H₂ on average for sustained full load operation.
- The OEM rated water consumption rate was specified at approximately 2.4 gals/hr. Actual measured water consumption at full load was found to be 3 gal/hr. The difference is water losses to the ambient through venting of humid gases and evaporation.

Conclusions from dynamic electrolyzer operation

- At full throughput, the hydrogen flow rate out of the electrolyzer system would swing dramatically, but this flow pattern vanished at lower load conditions. An inverse pattern in stack current was observed, where stack current was constant at full load condition, and ramped intermittently to carry out purge processes with the additional hydrogen flow.
- The mass flow controller accurately controlled the hydrogen output as expected but resulted in erratic power consumption profiles at part load on minute-to-minute time-scales. On a ten-minute time-scale basis, the system power consumption profile began to smooth to the desired result.
- Ancillary power consumption was found to be constant across all load conditions at 2.5 kW_{el}, and as such consumed an increasingly large share of the power going to hydrogen production.
- The efficiency of the AC/DC power electronics did not vary on average with the system load condition. The range of observed efficiencies did increase with lower load conditions, due to the high transients in stack current.
- The electrolyzer system successfully load-followed four weeks of solar PV, each week taken from a different season. The two extremes in transients and capacity factor were the seasons of winter and spring which the electrolyzer system accomplished without issue.
- Electrolyzer system capacity factor did not lead to significant impacts on system efficiency between the different solar load following cases, which remained in the regime of 51-53% HHV H₂. Overall capacity factors highlighted the issue with coupling energy storage systems solely with PV, with electrolyzer capacity factor going as low as 15.89% in the winter case and only as high as 38.07% for a 1:1 scale between the two systems.

- Three weeks of aggregated wind farm load following operation were carried out successfully in one continuous run, and achieved a minimum H₂ output of 0.03 kg/hr, system power consumption of 14 kW_{el}, and minimum sustained current density of 0.14 A/cm².
- Lower minimum load conditions combined with lower overall system capacity factors during the wind load following operation lead to system efficiencies as low as 31.07% HHV H₂ for one week, but as high as 51.35% for another.
- A novel control strategy was developed involving turning off the electrolyzer system when the control signal went below 14 kW_{el} of total power consumption (corresponding to the minimum sustained power consumption for the system). This novel control strategy lead to dramatically improved system efficiency even when considering start-up times and hydrogen losses to system start-up and shutdown. System efficiency with this control strategy was around 55-56% HHV H₂ consistently, only requiring 10 power cycles per week for the wind load following profiles. The trade-off for the improvement in system efficiency (11% improvement on average) was a loss of capacity factor on the order of 10%.
- Dynamic response of PEM electrolyzers is more than sufficient to meet even the most extreme power transients in a VRES load-following capacity, and likely at shorter time-scales by proper design and control of the AC/DC conversion equipment (e.g., for voltage support or frequency regulation). The stack was observed ramping >90% maximum operating current regularly both up and down on a second-to-second basis. This transient was far more often correlated to interactions between the mass flow control dispatch and

the pressure management system rather than control signal transients, leading to undesirable dynamics that could impact system degradation in the long term.

Observations from effects of operating conditions on electrolyzer system

- Performance of the electrolysis process itself was most influenced by current density, temperature, and hydrogen pressure. Stack current density reduces the efficiency of the process largely due to Ohmic losses in the cell stack. Higher operating temperatures improves stack efficiency largely through improving the conductivity of the electrolyte and reducing the reversible voltage of electrolysis. Increasing hydrogen pressure increases the reversible voltage, leading to lower efficiency.
- System level efficiency was most influenced by current density and hydrogen pressure, as well as oxygen pressure to a lesser extent. A positive correlation between current density and oxygen pressure made the influence of oxygen pressure unlikely.
- Hydrogen losses were most influenced by current density and hydrogen pressure. The congruency between hydrogen loss and system efficiency influencing factors is a result of the dominance of hydrogen loss as a source of efficiency loss. At lower current densities, the proportion of hydrogen produced versus hydrogen lost increases. The majority of hydrogen loss was associated with dryer operation, controlled by an orifice flowing a slipstream of hydrogen from the active dryer bed to the inactive bed to regenerate the bed. As a result, hydrogen losses to the dryers are a function of hydrogen pressure, and largely fixed regardless of system load condition.
- Characterization of electrolyzer system losses across all load conditions showed that while at load conditions of 50% and higher ($>1 \text{ A/cm}^2$), the majority of the energy that goes into producing hydrogen goes to the stack. Below this load condition, hydrogen

losses and ancillary power demands begin to take an increasing share of energy input. Below 0.6 A/cm^2 , the amount of energy input towards producing hydrogen climbs exponentially, with observed specific energies as high as $500 \text{ kWh}_{\text{el}}/\text{kg H}_2$ at 0.5 A/cm^2 , as opposed to $100 \text{ kWh}_{\text{el}}/\text{kg H}_2$ at 0.6 A/cm^2 .

- No statistically significant degradation of system efficiency or system components was observed during the 4000 hours of operation. It is slightly likely that there was some degradation in the cell stack, although only on the order of $25 \pm 20 \text{ mV/cell}$.

Observations from hydrogen injection to natural gas fired turbine

- The regular variation in composition that occurs in pipeline natural gas heavily influences the extent to which hydrogen can be blended into natural gas using current Southern California Gas Rule 30 standards for customer owned gas injection. Using the national average for natural gas quality, up to 19% H_2 by volume hydrogen can be blended with natural gas on a Wobbe Index basis. Based off measured pipeline values in the southern California region, this amount could vary from 13% up to 27% by volume H_2 . On a higher heating value basis using Rule 30, this amount could vary 1% up to 23% by volume H_2 .
- On a lower heating value basis, one kg of hydrogen offsets the energy throughput of 2.45 kg of natural gas. Assuming complete combustion, the combustion of 1 kg of natural gas results in the emission of 2.67 kg of CO_2 . Thus, the net offset on an energetic basis, is 6.54 kg of CO_2 per kg of H_2 .
- Hydrogen concentrations as high as 0.46% by vol H_2 in natural gas to the combustion turbine were observed over the 4000 hours of electrolyzer system operation. The one-

time high throughput hydrogen testing achieved sustained concentrations as high as 3.4% by volume H₂ without any adverse effects on turbine operation.

- ANOVA analysis across 1 hour sustained hydrogen injection data from the electrolyzer operation (n = 1000) showed an average offset of 2.5 ± 1.75 kg natural gas per kg of H₂. Analysis of the results for the one-time high throughput hydrogen testing showed average offsets of 1.9 ± 1.85 kg natural gas per kg of H₂.
- The addition of hydrogen gas to the natural gas fuel feed to the combustion turbine did not have any statistically significant influence on the final stack emissions of carbon monoxide and nitrogen oxides.

Observations from semi-empirical thermodynamic model of PEM stack

- Sustained part load operation data at varying operating temperatures and 30 barg cathode pressure was used with trust region optimization methods was used to determine values for electrolytic membrane conductivity (σ_{mem}), anodic exchange current density ($j_{\text{o,an}}$), and cathodic exchange current density ($j_{\text{o,cath}}$). Membrane conductivity was found to vary linearly with operating temperature, for a range of 0.074 S/cm up to 0.087 S/cm from 40 Celsius to 55 Celsius. Anodic exchange current density also showed a strong linear variation with temperature, increasing from 2.92×10^{-7} amp/cm² at 40 Celsius up to 1.41×10^{-6} amp/cm². Cathodic exchange current density did not show any temperature dependence, and varied very little from the average value of 0.688 A/cm².
- The Darcy constant for water permeability (K_D) of the membrane was determined by assessing the average effect of varying pressure differentials had on observed cathode water output using ANOVA. A linear correlation with a high statistical significance for a

slight variation in water transport solely due to pressure differential gave a Darcy constant of 2.712×10^{-16} cm²/sec.

- After isolating the pressure-driven transport of water, the electro-osmotic drag coefficient, n_{eo} , was determined using linear regression techniques. The coefficient varied with temperature and current, agreeing with results found in another study of high-pressure electrolysis water transport. The variation with current density was not observed in any studies carried out on ambient condition electrolysis, suggesting an interaction between current density and elevated operating pressures. Other studies concerning this interaction only displayed low and high point measurements and did not capture the non-linear relationship observed in this study. For utilization in the analytical model, only the relation between temperature and electro-osmotic drag coefficient was used. At 55 Celsius, this value was $n_{eo} = 2.68$ mol H₂O/mol H⁺.
- Discrepancies between the measured hydrogen output versus the Faradaic hydrogen output, referred to as hydrogen losses, were characterized as a result of three mechanisms; losses to dissolved hydrogen gas in cathodic water, losses to the PSA dryer regeneration process, and losses to gas cross-over in the electrolysis stack.
- Losses to dissolved hydrogen gas in cathode water were determined to be orders of magnitude lower than what was observed based upon Henry's Law estimations.
- Hydrogen losses to the PSA dryer were characterized using the rated orifice output at nominal conditions in combination with orifice flow relations and measurements of inlet pressure and valve condition at the dryer orifice over time, using only sustained periods of time where inlet pressure was constant. At nominal conditions, the dryer losses were rated at 0.744 kg/hr H₂, explaining the majority of hydrogen loss in the operation of the

electrolyzer. Low part load operation where the system pressure became less stable due to erratic stack current throughput led to increasing hydrogen losses that were attributed to unsteady orifice flow conditions.

- A top-down estimate of hydrogen losses to gas cross-over was used for the remaining discrepancy, providing an overestimation of hydrogen losses to that particular mechanism. Due to the regular pressure testing of the hydrogen process piping, the assumption that minimal hydrogen loss went to leakage rather than gas cross-over was justified. Cross-over parameters for hydrogen gas were fit against this experimental data using linear regression, giving a diffusive permeability value of $\epsilon_{H_2}=1.76 \times 10^{-10} \left[\frac{\text{mol}\cdot\text{sec}}{\text{cm}\cdot\text{bar}} \right]$ and a partial pressure enhancement factor of $A_{H_2} \approx 0 \left[\frac{\text{bar cm}^2}{\text{amp}} \right]$.
- A bottom-up estimate of hydrogen losses using combustible gas concentration sensing in the anode outlet was carried out and compared against the top-down estimate. The two estimates differed by nearly two orders of magnitude. As the bottom-up estimate relied on the assumption that there was no catalytic combustion of hydrogen in oxygen on the anode outlet, it was determined that the top-down estimate provided a result closer to reality. Fitted transport parameters for hydrogen cross-over from the bottom-up estimate were $\epsilon_{H_2}=4.47 \times 10^{-13} \left[\frac{\text{mol}\cdot\text{sec}}{\text{cm}\cdot\text{bar}} \right]$ and $A_{H_2} \approx 154.34 \left[\frac{\text{bar cm}^2}{\text{amp}} \right]$.
- The semi-empirical stack model with fitted electrochemical and transport parameters was combined with relationships for hydrogen dryer orifice loss and AC/DC power electronics losses and exercised against the VRES load following cases using only the stack current, temperature, and pressure set points as inputs. Power consumption of the system and stack were accurately modeled, as was hydrogen output for load conditions

where orifice losses to the dryer were accurate ($j > 0.7$ amps/cm²). For an electrolyzer system utilizing current control rather than mass flow control (the more realistic scenario moving forward), this would not be expected to be an issue.

- The analytical model was used to characterize the electrolysis based electrochemical compression of hydrogen gas. The actual compression losses matched very closely with isothermal compression, only requiring ~ 0.1 kWh_{el}/kg H₂ more than isothermal compression at of hydrogen from 0 barg to 30 barg (a 7% increase).
- The modeled increase in electrical work due to increasing hydrogen pressure was compared against ANOVA predicted variation from the electrolyzer operating conditions study and showed good agreement.
- The performance of the electrolysis based electrochemical compression was compared against the performance of a state-of-the-art centrifugal hydrogen compressor design specs for hydrogen pipeline integration. Electrochemical compression during the electrolysis step showed favorable performance aspects over an integration of first stage compression in the electrolysis step followed by second stage compression in the centrifugal compressor.
- The performance of the electrolysis based electrochemical compression was assessed for the high-pressure end-use application of hydrogen refueling (450 barg H₂). It was shown that this application is ill-suited to the current projected capabilities of electrolysis based electrochemical compression. Performance data from external electrochemical compression systems did show attractive performance characteristics for the integration of external electrochemical compression with first stage electrolysis based electrochemical compression, over the integration of electrolysis-based compression with

a general polytropic compression model (selected from hydrogen refueling station literature), and the compression of hydrogen solely in the electrolyzer.

7.2 Conclusions

- **PEM electrolyzer systems can ramp their stack utilization in a highly transient manner and overall the system is capable of load following dynamic VRES generation.**

The potential for electrolyzer systems to not only load following VRES and provide load balancing services, but also to further participate in ancillary grid services such as frequency regulation, hinges on the system being able to respond on timescales up to the order of milliseconds. The PEM electrolyzer at the stack level displayed the capability to ramp power 100% of its rated output on a second to second basis. At the system level, the electrolyzer system demonstrated ramping to match the transients of solar and wind on a minute to minute timescale. Modifications in system architecture, particularly the removal of the H₂ PSA dryer system, could lead to a very flexible system matching the transient capabilities of the stack.

- **Stack load condition is the strongest influence on PEM electrolyzer performance, from both a system and stack perspective. Temperature of the stack influences stack performance noticeably, while cathode pressure shows a much stronger influence on overall system performance.**

ANOVA analysis across the breadth of data highlights the influence of stack current density as the primary factor in efficiency at both the stack and system level. As the stack accounts for the bulk majority of power consumption, this means that the system load condition is the primary determinant for performance for the range of operating

conditions the system allows. Following current density, stack temperature has the next greatest effect on performance at the stack level, due to temperatures positive effects on reversible voltage, membrane conductivity, and exchange current density. The influence of elevated cathode and anode pressures are negligible on stack performance. From an overall system performance perspective, the impact of stack temperature was not as strong as an influence as cathode pressure. This is due to the pressure dependence of the hydrogen loss at the PSA H₂ dryer and to a lesser degree the crossover of hydrogen gas in the stack. Operating the system at higher temperatures to achieve better performance also puts less load on the thermal management system, which in this study was an external chiller system. Higher cathode pressures mean less compression through less efficient external means such that the efficiency loss to the PEM system is an overall efficiency gain.

- **Operation of PEM electrolyzers at low load conditions leads to severe performance drop-offs.**

While stack efficiency improves at lower current densities, losses to at the system level increase as current density goes down. This is due to fixed losses in the form of ancillary power consumption, and purely pressure dependent hydrogen gas losses. Down to 0.8 A/cm², roughly 50% load condition, system efficiency is relatively flat as the performance gains in the stack offset system losses. Beyond this point system losses begin to heavily outweigh the stack performance gain. This leads to an effective minimum operating point of 25% load condition.

- **Modern electrolyzer system controls make it possible to predict effectively system power consumption and species transport with a simple isobaric and isothermal**

analytical model.

Control systems that hold pressures and temperatures to set points established at system start-up mean that for the purposes of analytical modeling of PEM electrolyzer systems, a simple thermodynamic and electrochemical transport model can capture accurately metrics of interest (species output, system power consumption) with a semi-empirical approach to parameterization. Such a model can be applied to larger system's studies of P2G electrolyzer utilization, giving a more accurate picture of the efficacy of these system's by taking into account output purity, performance dependence on load condition, and capabilities of electrochemical compression via electrolysis.

- **Electrochemical compression via PEM electrolysis is an effective way to compress hydrogen in the 1 to 100 barg pressure range, making it an attractive choice for pipeline integration.**

Due to the near isothermal nature of electrochemical compression, the capability to compress hydrogen via electrolysis provides a great opportunity for performance. Furthermore, electrochemical compression uses no moving parts, minimizing maintenance as compared to traditional mechanically-driven methods. Being able to curtail entirely external compressors, or reduce the amount of compression performed externally depending on the application, reduces system complexity as well.

Electrochemical compression via electrolysis is limited by the pressure-dependent cross-over of hydrogen gas in the stack, making it unsuitable for high pressure (> 100 barg) applications and potentially limited to even lower pressures in the absence of catalytic gas reduction in the anode to keep H_2 in O_2 concentrations in a safe range.

- **The addition of hydrogen to a natural gas fired gas turbine shows no significant effects on emissions and operation up to 0.5% by volume H₂ in the long term, and up to 3.4% by volume H₂ in the short term.**

Over 3000 hours of H₂ injection testing at quantities up to 0.5% by volume H₂ in natural gas showed no significant impacts on emissions of criteria pollutants (CO, NO_x) from the natural gas fired turbine at the UCI Central Plant. Short-term higher throughput testing up to 3.4% by volume H₂ in natural gas gave similar results, not showing any appreciable impact on emissions of criteria pollutants. There was an appreciable impact on emissions of CO₂ by extension through the measured reduction in total fuel gas flow and thus reduction in natural gas usage, with a much more definite influence observed over the long-term due to the large amount of ‘noise’ that has to be filtered through with studies of complex systems such as the gas turbine.

7.3 Recommendations

This study served to highlight the current technical viability of the power-to-gas energy storage concept when using commercially available equipment. As this study was centered on a pilot plant of an emerging energy storage concept, much of the recommendations concern the need for more concentrated studies of certain aspects of the power-to-gas plant.

- Large, controllable AC/DC power electronics for dynamic dispatch of electrolysis stacks are needed for more effective dispatch of electrolyzer systems. The mass flow control dispatch of electrolyzer systems developed and deployed in this work is not recommended as an accurate or effective long-term control strategy.
- Thermal conditioning requirements of PEM electrolyzer systems should be considered from a system efficiency perspective.
- Electrolyzer system configurations for pipeline injection end-use are needed for eliminating the large parasitic loss to PSA drying of hydrogen gas, as only certain high purity applications of hydrogen need such extensive drying.
- Electrolyzer system load following of high power transients should deploy the control strategy developed herein to turn off the system rather than idle (or operate at low production levels) when the load following signal goes below a determined minimum system power consumption requirement of the system.
- Consider the use of hybrid energy storage systems, integrating electrolyzer system and battery, enabling higher capacity factors for both systems.
- Due to the rapid dynamic response capabilities of the PEM stack, proper AC/DC power electronics could enable a number of electrical grid ancillary service capabilities.

- Construction of larger power-to-gas plants is needed to better assess the impacts of hydrogen end-use by producing appreciable amounts of hydrogen, additionally larger PEM electrolyzer systems would mitigate balance of plant inefficiencies, particularly from hydrogen drying.
- Limits on acceptable hydrogen quantities in natural gas for the entire spectrum of natural gas end-uses is needed.
- Begin introducing renewable hydrogen gas incrementally into the natural gas system in increasing quantities as end-use suitability is assessed and approved to see immediate carbon emission offsets.
- More focused studies are needed on in-situ gas cross-over in PEM electrolyzer stacks, particularly in pressurized electrolysis. Special attention should be paid to ensure combustible mixtures of hydrogen gas in the anode are avoided.
- Consideration of effective part load range for pressurized PEM electrolysis is needed for use of such systems in power-to-gas for flexible load following applications.
- For pipeline integration, high pressure electrolyzers alone can effectively produce and pressurize hydrogen to desired levels rather than increasing system complexity by addition of external compression systems.
- Research and development on high pressure electrolysis (400+ barg H₂) could result in highly effective and simple systems for production and utilization of power-to-gas pathways for fueling applications, current capabilities of high-pressure electrolysis are not effective for pressures past 100 barg.

8 Bibliography

- [1] L. Bird, D. Lew, M. Milligan, M. E. Carlini, A. Estanqueiro, D. Flynn, E. Gomez-Lazaro, H. Holttinen, N. Menemenlis, A. Orths, P. Eriksen, C. J. Smith, L. Soder, P. Sorensen, A. Altiparmakis, Y. Yasuda and J. Miller, "Wind and solar energy curtailment: A review of international experience," *Renewable and Sustainable Energy Reviews*, no. 65, pp. 577-586, 2016.
- [2] P. Beiter, K. Haas and S. Buchanan, 2014 Renewable Energy Data Book, United States Department of Energy, November 2015.
- [3] "California State Assembly Bill 350, Clean Energy and Pollution Reduction Act of 2015," October 7, 2015.
- [4] California Energy Commission, "Staff draft report on renewable power in California: status and issues.," Publication No. CEC-150-2011-02, August 2011.
- [5] D. León, "SB 100. California Renewables Portfolio Standard Program: emissions of greenhouse gases.," California State Legislature, Sacramento, CA, 2018.
- [6] L. Bird, J. Cochran and X. Wang, "Wind and solar energy curtailment: experience and practices in the United States.," National Renewable Energy Laboratory, NREL/TP-6A20-60983, Golden, CO, Us, 2014.
- [7] Energy and Environmental Economics., "Investigating a higher renewables portfolio stand in California," San Francisco, CA., 2014.
- [8] C. Budischak, D. Sewell, H. Thomson, L. Mach, D. E. Veron and W. Kempton, "Cost-minimized combinations of wind power, solar power and electrochemical storage, powering the grid up to 99.9% of the time," *Journal of Power Sources*, no. 225, pp. 60-74, 2013.
- [9] B. Elliston, M. Diesendorf and I. MacGill, "Simulations of scenarios with 100% renewable electricity in the Australian National Electricity Market," *Energy Policy*, no. 45, pp. 606-613, 2012.
- [10] T. Ackermann, *Wind Power in Power Systems*, West Sussex PO19 8SQ, England: John Wiley & Sons, Ltd, 2005.

- [11] D. Devaraj and R. Jeevajyothi, "Impact of fixed and variable speed wind turbine systems on power system voltage stability enhancement," in *IET Conference on Renewable Power Generation*, Edinburgh, 2011.
- [12] B. Parsons, M. Milligan, B. Zavadil, D. Brooks, B. Kirby, K. Dragoon and J. Caldwell, "Grid impacts of wind power: A summary of recent studies in the United States," in *European Wind Energy Conference and Exhibition*, Madrid Spain, 2003.
- [13] D. Burke and M. O'Malley, "Factors Influencing Wind Energy Curtailment," *IEEE Transactions on Sustainable Energy*, vol. 2, no. 2, pp. 185-193, 2011.
- [14] CAT Projects, "Report: Investigating the Impact of Solar Variability on Grid Stability," Australian Renewable Energy Agency, 2015.
- [15] B. Tarroja, F. Mueller and S. Samuelsen, "Solar power variability and spatial diversification: implications from an electric grid load balancing perspective," *International Journal of Energy Research*, no. 37, pp. 1002-1016, 2013.
- [16] J. D. Eichman, F. Mueller, B. Tarroja, L. S. Schell and S. Samuelsen, "Exploration of the integration of renewable resources into California's electric system using the Holistic Grid Resource Integration and Deployment (HiGRID) tool," *Energy*, no. 50, pp. 353-363, 2013.
- [17] California ISO, "What the duck curve tells us about managing a green grid," CommPR, Folsom, CA, 2016.
- [18] P. Denholm, M. O'Connell, G. Brinkman and J. Jorgenson, "Overgeneration from Solar Energy in California: A Field Guide to the Duck Chart," National Renewable Energy Laboratory, 2015.
- [19] California Independent System Operator (CAISO), "Flexible and Renewable Resources Fast Facts," 2013.
- [20] B. Tarroja, F. Mueller, J. D. Eichman and S. Samuelsen, "Metrics for evaluating the impacts of intermittent renewable generation on utility load-balancing," *Energy*, no. 42, pp. 546-562, 2012.
- [21] N. Kumar, P. Besuner, S. Lefton, D. Agan and D. Hilleman, "Power Plant Cycling Costs," NREL/SR-5500-55433, Sunnyvale, California, 2012.
- [22] M. Beaudin, H. Zareipour, A. Schellenberg and W. Rosehart, Energy Storage for Smart Grids (Ch1. Energy Storage for Mitigating the Variability of Renewable Electricity

Resources), Department of Electrical and Computer Engineering, University of Calgary, 2500 University Drive NW, Calgary, Alberta, Canada T2N 1N4: Elsevier Inc., 2015.

- [23] G. Gahleitner, "Hydrogen from renewable electricity: An international review of power-to-gas pilot plants for stationary applications," *International Journal of Hydrogen Energy*, no. 38, pp. 2039-2061, 2013.
- [24] P. Schulze, J. Holstein, A. v. d. Noort and J. Knijp, "Power-to-gas in a decarbonized european energy system based on renewable energy sources," DNV GL, 2017.
- [25] J.-P. Maton, L. Zhao and J. Brouwer, "Dynamic Modeling of compressed gas energy storage to complement renewable wind power intermittency," *International Journal of Hydrogen Energy*, no. 38, pp. 7867-7880, 2013.
- [26] T. Estermann, M. Newborough and M. Sterner, "Power-to-gas systems for absorbing excess solar power in electricity distribution networks," *International Journal of Hydrogen Energy*, no. 41, pp. 13950-13959, 2016.
- [27] W. H. Zhu, Y. Zhu and B. J. Tatarchuk, "Self-discharge characteristics and performance degradation of Ni-MH batteries for storage applications," *International Journal of Hydrogen Energy*, no. 39, pp. 19789-19798, 2014.
- [28] M. Muller, L. Viernstein, C. N. Truong, A. Eiting, H. C. Hesse, R. Witzmann and A. Jossen, "Evaluation of grid-level adaptability for stationary battery energy storage system applications in Europe," *Journal of Energy Storage*, no. 9, pp. 1-11, 2016.
- [29] X. Luo, J. Wang, M. Dooner and J. Clarke, "Overview of current development in electrical energy storage technologies and the application potential in power system operation," *Applied Energy*, no. 137, pp. 511-536, 2015.
- [30] A. H. Zimmerman, "Self-Discharge Losses in Lithium-Ion Cells," *IEEE AESS Systems Magazine*, pp. 19-24, February 2004.
- [31] A. A. Akhil, G. Huff, A. B. Currier, B. C. Kaun, D. M. Rastler, S. B. Chen, A. L. Cotter, D. T. Bradshaw and W. D. Gauntlett, "DOE/EPRI Electricity Storage Handbook in Collaboration with NRECA," Sandia National Laboratories, 2015.
- [32] S. Schiebahn, T. Grube, M. Robinus, V. Tietze, B. Kumar and D. Stolten, "Power to gas: Technological overview, systems analysis and economic assessment for a case study in Germanyq," *International Journal of Hydrogen Energy*, vol. 40, pp. 4285-2494, 2015.

- [33] EG&G Technical Services, Fuel Cell Handbook, 7th Ed, Morgantown, West Virginia 26507-0880: U.S. Department of Energy, Office of Fossil Energy, National Energy Technology Laboratory, 2004.
- [34] P. Millet, N. Mbemba, S. Grigoriev, V. Fateev, A. Aukauloo and C. Etievant, "Electrochemical performances of PEM water electrolysis cells and perspectives," *International Journal of Hydrogen Energy*, no. 36, pp. 4134-4142, 2010.
- [35] S. Siracusano, V. Baglio, N. Briguglio, G. Brunaccini, A. Di Blasi, A. Stassi, R. Ornelas, E. Trifoni, V. Antonucci and A. A.S., "An electrochemical study of a PEM stack for water electrolysis," *International Journal of Hydrogen Energy*, no. 37, pp. 1939-1946, 2012.
- [36] M. Felgenhauer and T. Hamacher, "State-of-the-art of commercial electrolyzers and on-site hydrogen generation for logistic vehicles in South Carolina," *International Journal of Hydrogen Energy*, no. 40, pp. 2084-2090, 2015.
- [37] M. Carmo, D. L. Fritz, J. Mergel and D. Stolten, "A comprehensive review on PEM water electrolysis," *International Journal of Hydrogen Energy*, vol. 38, no. 12, pp. 4901-93, 2013.
- [38] B. Han, S. M. Steen III, J. Mo and F. Y. Zhang, "Electrochemical performance modeling of a proton exchange membrane electrolyzer cell for hydrogen energy," *International Journal of Hydrogen Energy*, vol. 40, no. 22, pp. 7006-7016, 2015.
- [39] F. Z. Aouali, M. Becherif, H. S. Ramadan and M. Emziane, "Analytical modelling and experimental validation of proton exchange membrane electrolyser for hydrogen production," *International Journal of Hydrogen Energy*, vol. 42, no. 2, pp. 1366-1374, 2017.
- [40] S. A. Grigoriev and A. A. Kalinnikov, "Mathematical modeling and experimental study of the performance of PEM water electrolysis cell with different loadings of platinum metals in electrocatalytic layers," *International Journal of Hydrogen Energy*, vol. 42, no. 3, pp. 1590-1597, 2017.
- [41] Z. Abdin, C. J. Webb and E. M. Gray, "Modelling and simulation of a proton exchange membrane (PEM) electrolyser cell," *International Journal of Hydrogen Energy*, vol. 40, no. 39, pp. 13243-13257, 2015.
- [42] X. Li, S. Qu, H. Yu, M. Hou, Z. Shao and B. Yi, "Membrane water flow rate in electrolyzer cells with a solid polymer electrolyte (SPE)," *Journal of Power Sources*, vol. 190, pp. 534-537, 2009.

- [43] B. Lee, K. Park and H.-M. Kim, "Dynamic Simulation of PEM Water Electrolysis and Comparison with Experiments," *International Journal of Electrochemical Science*, vol. 8, pp. 235-248, 2013.
- [44] M. Schalenbach, M. Carmo, D. L. Fritz, J. Mergel and D. Stolten, "Pressurized PEM water electrolysis: Efficiency and gas crossover," *International Journal of Hydrogen Energy*, vol. 38, pp. 14921-14933, 2013.
- [45] H. Gorgun, "Dynamic modelling of a proton exchange membrane (PEM) electrolyzer," *International Journal of Hydrogen Energy*, vol. 31, pp. 29-38, 2006.
- [46] H. Kim, M. Park and K. S. Lee, "One-dimensional dynamic modeling of a high pressure water electrolysis system for hydrogen production," *International Journal of Hydrogen Energy*, vol. 38, no. 6, pp. 2596-2609, 2013.
- [47] P. Olivier, C. Bourasseau and B. Bouamama, "Dynamic and multiphysics PEM electrolysis system modelling: A bond-graph approach," *International Journal of Hydrogen Energy*, vol. 42, no. 22, pp. 14872-14904, 2017.
- [48] B. Laoun, A. Khellaf, M. W. Naceur and A. M. Kannan, "Modeling of solar photovoltaic polymer electrolyte membrane electrolyzer direct coupling for hydrogen generation," *International Journal of Hydrogen Energy*, vol. 41, no. 24, pp. 10120-10135, 2016.
- [49] R. Sarrias-Mena, L. M. Fernández-Ramírez, C. A. García-Vázquez and F. Jurado, "Electrolyzer models for hydrogen production from wind energy systems," *International Journal of Hydrogen Energy*, vol. 40, no. 7, pp. 2927-2938, 2015.
- [50] A. Saadi, M. Becherif and H. S. Ramadan, "Hydrogen production horizon using solar energy in Biskra, Algeria," *International Journal of Hydrogen Energy*, vol. 41, no. 47, pp. 21899-21912, 2016.
- [51] M. Blal, B. Ali, B. Amhed, B. Ahmed, L. Salah and D. Rachid, "Study of hydrogen production by solar energy as a tool of storing and utilization of renewable energy for desert areas," *International Journal of Hydrogen Energy*, vol. 41, no. 45, pp. 20788-20806, 2016.
- [52] L. Zhao and J. Brouwer, "Dynamic operation and feasibility study of a self-sustainable hydrogen fueling station using renewable energy sources," *International Journal of Hydrogen Energy*, vol. 40, no. 10, pp. 3822-3837, 2015.

- [53] J. D. Maclay, J. Brouwer and G. S. Samuelsen, "Dynamic analyses of regenerative fuel cell power for potential use in renewable residential applications," *International Journal of Hydrogen Energy*, vol. 31, no. 8, pp. 994-1009, 2006.
- [54] E. Özgirgin, Y. Devrim and A. Albostan, "Modeling and simulation of a hybrid photovoltaic (PV) module electrolyzer PEM fuel cell system for micro-cogeneration applications," *International Journal of Hydrogen Energy*, vol. 40, no. 44, pp. 15336-15342, 2015.
- [55] M. Ç. a. M. S. G. G. Genç, "Cost analysis of wind electrolyzer fuel cell system for energy demand in Pinarbasi-Kayseri," *International Journal of Hydrogen Energy*, vol. 37, no. 17, pp. 12158-12166, 2012.
- [56] Ł. B. D. W. a. K. D. J. Kotowicz, "Hydrogen generator characteristics for storage of renewable-generated energy," *Energy*, vol. 118, pp. 156-171, 2017.
- [57] T. Ramsden, K. Harrison and D. Steward, "NREL Wind-to-Hydrogen Project Renewable Hydrogen Production for Energy Storage & Transportation," NREL/PR-560-47432, Golden,CO, 2009.
- [58] J. Eichman, K. Harrison and D. Steward, "Novel Electrolyzer Applications: Providing More Than Just Hydrogen," NREL/TP-5400-61758, Golden, CO, 2014.
- [59] M. Santarelli, P. Medina and M. Cali, "International Journal of Hydrogen Energy," *Fitting regression model and experimental validation for high-pressure PEM electrolyzer*, vol. 34, no. 6, pp. 2519-2530, 2009.
- [60] J. Mergel, M. Carmo and D. Fritz, Status on technologies for hydrogen production by water electrolysis, D. Stolten and V. Scherer, Eds., Weinheim, Germany: WILEY-VCH, 2013.
- [61] J. D. Maclay, J. Brouwer and S. G. Samuelsen, "Experimental results for hybrid energy storage systems coupled to photovoltaic generation in residential applications," *International Journal of Hydrogen Energy*, vol. 36, no. 19, pp. 12130-12140, 2011.
- [62] University of California Irvine, "UC Irvine's Combined Heat and Power Plant," 2010.
- [63] Irvine Ranch Water District, "2017 Water Quality Report," Irvine Ranch Water District, Irvine, CA, 2017.

- [64] United States Geological Survey, "USGS Water," U.S. Department of the Interior, 28 December 2016. [Online]. Available: <https://water.usgs.gov/owq/hardness-alkalinity.html>. [Accessed 20 October 2017].
- [65] I. Alaefour, S. Shahgaldi, A. Ozden, X. Li and F. Hamdullahpur, "The role of flow-field layout on the conditioning of a proton exchange membrane fuel cell," *Fuel*, vol. 230, pp. 98-103, 2018.
- [66] J. R. Vang, S. J. Andreasen, S. S. Araya and S. K. Kaer, "Comparative study of the break in process of post doped and sol-gel high temperature proton exchange membrane fuel cells," *International Journal of Hydrogen Energy*, vol. 39, no. 277, pp. 14959-14968, 2014.
- [67] S. Thomas, S. S. Araya, J. R. Vang and S. K. Kaer, "Investigating different break-in procedures for reformed methanol high temperature proton exchange membrane fuel cells," *International Journal of Hydrogen Energy*, Vols. In Press, Corrected Proof, 2018.
- [68] V. B. Silva and A. Rouboa, "Hydrogen-fed PEMFC: Overvoltage analysis during an activation procedure," *Journal of Electroanalytical Chemistry*, vol. 671, pp. 58-66, 2012.
- [69] Fumatech Functional Membranes for Fuel Cells and Batteries, *PEM Fuel Cells - PEM Water Electrolysis*, Bietigheim-Bissingen: BWT Group.
- [70] Z. Qi and A. Kaufman, "Quick and effective activation of proton-exchange membrane fuel cells," *Journal of Power Sources*, vol. 114, pp. 21-13, 2002.
- [71] P. Colbertaldo, S. L. Alaez Gomez and S. Campanari, "Zero-dimensional dynamic modeling of PEM electrolyzers," in *Energy Procedia*, Cardiff, UK, 2017.
- [72] T. Yigit and O. F. Selamet, "Mathematical modeling and dynamic Simulink simulation of high-pressure PEM electrolyzer system," *International Journal of Hydrogen Energy*, vol. 41, pp. 13901-13914, 2016.
- [73] S. D. Leon-Aldaco, J. Calleja-Gjumlich, H. Jimenez-Grajales and F. Chan-Puc, "Experimental Assessment of Derating Guidelines Applied to Power Electronics Converters," *Journal of Applied Research and Technology*, vol. 11, no. 1, pp. 103-114, 2013.
- [74] CUI Inc, "Design Considerations for Thermal Management of Power Supplies," Tualatin, Oregon 97062, 2014.

- [75] V. Fateev, "High pressure PEM electrolyzers: efficiency, life-time and safety issues," Fraunhofer ISE, Freiburg, Germany, 2013.
- [76] U.S. Energy Information Administration (EIA), ""Natural Gas Annual Respondent Query System (EIA-191)", " US Department Of Energy, Washington, DC 20585, 2013.
- [77] H. De Vries, O. Florisson and G. Tiekstra, "Safe Operation of Natural Gas Appliances Fueled with Hydrogen/Natural Gas Mixtures (Progress Obtained in the NaturalHY-Project)," KEMA (Keuring van Elektrotechnische Materialen te Arnhem), Brussels, 2007.
- [78] M. W. Melaina, O. Antonia and M. Penev, "Blending Hydrogen into Natural Gas Pipeline Networks: A Review of Key Issues," National Renewable Energy Laboratory. U.S. Department of Energy, Golden, Colorado, 2013. NREL/TP-5600-51995 .
- [79] National Institute of Standards and Technology (NIST), "NIST Chemistry WebBook, SRD 69," US Department of Commerce, 2017. [Online]. Available: <https://webbook.nist.gov/cgi/cbook.cgi?ID=C1333740&Mask=1#Thermo-Gas>. [Accessed 2017].
- [80] NGC+ Interchangeability Working Group, "White Paper on Natural Gas Interchangeability and Non-Combustion End Use," Federal Energy Regulatory Commission, 2005.
- [81] Sempra Energy Utilites, San Diego Gas & Electric, Southern California Gas Company, "LNG Interchangeability Study," SoCalGas, 2003.
- [82] Southern California Gas Company, "Rule No. 30; Transportation of Customer-Owned Gas," California Public Utilites Commission, Sacramento, 2017.
- [83] H. de Vries, A. V. Mokhov and H. B. Levinsky, "The impact of natural gas/hydrogen mixtures on the performance fo end-use equipment: Interchangeability analysis for domestic appliances," *Applied Energy*, vol. 208, pp. 1007-1019, 2017.
- [84] A. Ordys, A. Pike, M. Johnson, R. Katebi and M. Grimbale, *Modelling and Simulation of Power Generation Plants*, Springer, 1994.
- [85] EPA Center for Corporate Climate Leadership, "Greenhouse Gas Inventory Guidance: Direct Emissions from Stationary Combustion Sources," US Environmental Protection Agency, 2016.
- [86] US Environmental Protection Agency, "Emission Factors for Greenhouse Gas Inventories," 2014.

- [87] Nilsson, Brackmann, Abou-Taouk, Larfeldt and Moell, "Hydrogen addition to flames at gas turbine relevant conditions," in *Energiforsk*, 2017.
- [88] Larfeldt, Larsson and Andersson, "Co-firing with hydrogen in industrial gas turbines," Siemens, SGC Report 2013.
- [89] A. R. Balkin, "Modeling a 500W Polymer Electrolyte Membrane Fuel Cell," Sydney, 2002.
- [90] F. Marangio, M. Santarelli and M. Cali, "Theoretical model and experimental analysis of a high pressure PEM water electrolyser for hydrogen production," *International Journal of Hydrogen Energy*, vol. 3, no. 34, pp. 1143-1158, 2009.
- [91] A. Roy, S. Watson and D. Infield, "Comparison of electrical energy efficiency of atmospheric and high-pressure electrolysers," *International Journal of Hydrogen Energy*, vol. 14, no. 31, pp. 1964-1979, 2006.
- [92] D. Ghribi, A. Khelifa, S. Diaf and M. Belhamel, "Study of hydrogen production system by using PV solar energy and PEM electrolyser in Algeria," *International Journal of Hydrogen Energy*, vol. 20, no. 38, pp. 8480-8490, 2013.
- [93] K. S. Agbli, M. C. Pera, D. Hissel, O. Rallires, C. Turpin and I. Doumbia, "Multiphysics simulation of a PEM electrolyser: energetic macroscopic representation approach," *International Journal of Hydrogen Energy*, vol. 2, no. 36, pp. 1382-1398, 2011.
- [94] R. O'hayre, S.-W. Cha, W. Colella and F. B. Prinz, *Fuel Cell Fundamentals*, 3rd ed., New York: Wiley, 2013.
- [95] N. V. Dale, M. D. Mann and H. Salehfar, "Semiempirical model based on thermodynamic principles for determining 6kW proton exchange membrane electrolyzer stack characteristics," *Journal of Power Sources*, no. 185, pp. 1348-1353, 2008.
- [96] C. Y. Biaku, N. V. Dale, M. D. Mann, H. Salehfar, A. J. Peters and T. Han, "A semiempirical study of the temperature dependence of the anode charge transfer coefficient of a 6kW PEM electrolyzer," *International Journal of Hydrogen Energy*, no. 33, pp. 4247-4254, 2008.
- [97] M. Espinosa-Lopez, C. Darras, P. Poggi, R. Glises, P. Baucour, A. Rakotondrainibe, S. Besse and P. Serre-Combe, "Modelling and experimental validation of a 46 kW PEM high pressure water electrolyzer," *Renewable Energy*, no. 119, pp. 160-173, 2018.
- [98] J. Larminie and A. Dicks, *Fuel Cell Systems Explained*, 2nd ed., New York: Wiley, 2003.

- [99] K. Harrison, E. Hernandez-Pacheco, M. Mann and H. Salehfar, "Semiempirical model for determining PEM electrolyzer stack," *Journal of Fuel Cell Science & Technology*, vol. 3, pp. 220-3, 2006.
- [100] S. Chan and Z. Xia, "Polarization effects in electrolyte/electrode-supported solid oxide fuel cells," *Journal of Applied Electrochemistry*, no. 32, pp. 339-447, 2002.
- [101] M. Ni, M. K. Leung and D. Y. Leung, "Energy and exergy analysis of hydrogen production by a proton exchange membrane (PEM) electrolyzer plant".
- [102] R. W. Kopitzke, C. A. Linkous, H. R. Anderson and G. L. Nelson, "Conductivity and Water Uptake of Aromatic-Based Proton Exchange Membrane Electrolytes," *Journal of the Electrochemical Society*, vol. 147, no. 5, pp. 1677-1681, 2000.
- [103] T. E. Springer, T. a. Zawodzinski and S. Gottesfeld, "Polymer electrolyte fuel cell model," *Journal of the Electrochemical Society*, vol. 134, no. 8, pp. 2334-2342, 1991.
- [104] R. Garcia-Valverde, N. Espinosa and A. Urbina, "Simple PEM water electrolyser model and experimental validation," *International Journal of Hydrogen Energy*, vol. 37, no. 2, pp. 1927-1938, 2012.
- [105] M. W. Bernardi, M. Dawn and Verbrugge, "Mathematical model of a gas diffusion electrode bonded to a polymer electrolyte," *Journal of the American Institute of Chemical Engineers*, vol. 37, no. 8, pp. 1151-1163, 1990.
- [106] P. Medina and M. Santarelli, "Analysis of water transport in a high pressure PEM electrolyzer," *International Journal of Hydrogen Energy*, vol. 35, pp. 5173-5186, 2010.
- [107] M. G. Santarelli, M. F. Torchio and P. Cochis, "Parameters estimation of a PEM fuel cell polarization curve and analysis of their behavior with temperature," *Journal of Power Sources*, vol. 159, pp. 824-835, 2006.
- [108] S. Dutta, S. Shimpalae and J. Zee, "Numerical Prediction of mass-exchange between cathode and anode channels in pem fuel cell.," *Internation Journal of Heat & Mass Transfer*, vol. 44, pp. 2029-42, 2001.
- [109] Q. Duan, H. Wang and J. Benziger, "Transport of liquid water through Nafion membranes," *Journal of Membrane Science*, vol. 392, pp. 88-94, 2012.
- [110] E. Birgersson, M. Nojonen and M. Vynnycky, "Analysis of a two-phase non-isothermal model for a PEFC," *Journal of Electrochemical Society*, vol. 152, pp. 1021-1034, 2005.

- [111] R. Bird, W. Stewart and E. Lightfoot, *Transport Phenomena* 2nd ed., John Wiley & Sons, 2002.
- [112] FuelCellsEtc, "Nafion Membrane Comparison Table," FuelCellsEtc: Commercial Fuel Cell Components, [Online]. Available: <https://www.fuelcellsetc.com/store/DS/nafion-comparison-chart.pdf>.
- [113] J. Amphlett, R. Baumert, R. Mann, B. Peppley and P. Roberge, "Performance modelling of the Ballard Mark IV solid polymer electrolyte fuel cell," *Journal of Electrochemical Society*, vol. 142, pp. 1-15, 1995.
- [114] National Aeronautics and Space Administration, "Safety Standard for Hydrogen and Hydrogen Systems," Office of Safety and Mission Assurance, Washington, DC 20546, 1997.
- [115] M. Schalenbach, T. Hoefner, P. Paciok, M. Carmo, W. Lueke and S. Detlef, "Gas Permeation through Nafion. Part 1: Measurements," *The Journal of Physical Chemistry*, vol. 119, pp. 25145-25155, 2015.
- [116] H. Ito, T. Maeda, A. Nakano and H. Takenaka, "Properties of Nafion membranes under PEM water electrolysis conditions," *International Journal of Hydrogen Energy*, vol. 36, pp. 10527-10540, 2011.
- [117] T. Zawodzinski, C. Derouin, S. Radzinski, R. Sherman, V. Smith, T. Springer and et al, "Water uptake by and transport through Nafion 117 membranes," *Journal of the Electrochemical Society*, vol. 140, pp. 1041-1047, 1993.
- [118] K. Broka and P. Ekdunge, "Oxygen and hydrogen permeation properties and water uptake of Nafion 117 membrane and recast film for PEM fuel cell," *Journal of Applied Electrochemistry*, vol. 27, pp. 117-123, 1997.
- [119] G. Shanhai, Y. Baolian and M. Pingwen, "Experimental Determination of Electro-Osmotic Drag Coefficient in Nafion Membrane for Fuel Cells," *Journal of the Electrochemical Society*, vol. 153, no. 8, pp. 1443-1450, 2006.
- [120] M. Ise, K. D. Kreuer and J. Maier, "Electroosmotic drag in polymer electrolyte membranes: an electrophoretic NMR study," *Solid State Ionics*, vol. 125, pp. 213-223, 1999.
- [121] U. Jauregui-Haza, E. Pardillo-Fontdevila, A. Wilhelm and H. Delmas, "Solubility of Hydrogen and Carbon Monoxide in Water and some Organic Solvents," Centro de

Química Farmacéutica, Apdo. 16042, C. Habana, Cuba, Ecole Nationale Supérieure d'Ingenieurs en Arts Chimiques et Technologiques, 118 route de Narbonne, 31077,, 2004.

- [122] R. Wiebe, V. Gaddy and C. J. Heins, "Solubility of Hydrogen in Water at 25 C from 25 to 1000 Atmospheres.," Fertilizer and Fixed Nitrogen Investigations, Bureau of Chemistry and Soils, Washington, D. C., 1932.
- [123] D. A. Crowl and J. F. Louvar, *Chemical Process Safety: Fundamentals with Applications* (3rd Edition), Prentice Hall, 2011.
- [124] S. Grigoriev, V. Poremskiy, S. Korobstev, F. Fateev, F. Aupretre and P. Millet, "High-pressure PEM water electrolysis and corresponding safety issues," *International Journal of Hydrogen Energy*, vol. 36, pp. 2721-2728, 2011.
- [125] S. A. Grigoriev, P. Millet, S. V. Korobtsev, V. I. Poremskiy, M. Pepic, C. Etievant, C. Puyenchet and V. Fateev, "Hydrogen safety aspects related to high-pressure polymer electrolyte membrane water electrolysis," *International Journal of Hydrogen Energy*, vol. 34, no. 14, pp. 5986-5991, 2009.
- [126] M. Hamdan, "High Pressure PEM Electrolysis: Status, Key Issues, and Challenges," in *Electrolytic Hydrogen Production Workshop*, NREL, Golden, Colorado, 2014.
- [127] K. E. Ayers, E. B. Anderson, C. B. Capuano, B. D. Carter, L. T. Dalton, G. Hanlon, J. Manco and M. Niedzwiecki, "Research Advances Towards Low Cost, High Efficiency PEM Electrolysis," in *ECS Transactions*, 33, 2010.
- [128] T. Norman, "High Efficiency Large PEM Electrolyzers," Giner, Inc., Newton, Ma. 02466, 2016.
- [129] J. D. Maclay, "Solar Hydrogen Production and Reversible Fuel Cells for Residential Power".
- [130] Y. A. Cengel and M. A. Boles, *Thermodynamics: An Engineering Approach* 8th Edition, New York, NY: McGraw Hill Education, 2015.
- [131] P. W. Parfomak, "Energy Storage for Power Grids and Electric Transportation: A Technology Assessment," Congressional Research Service, 2012.
- [132] A. Witkowski, A. Rusin, M. Majkut and K. Stolecka, "Comprehensive analysis of hydrogen compression and pipeline transportation from thermodynamics and safety aspects," *Energy*, vol. 141, pp. 2508-2518, 2017.

- [133] US Department of Energy Hydrogen Program, "Annual Merit Review and Peer Evaluation Report," December 2010.
- [134] F. A. D. Bella, "Development of a Centrifugal Hydrogen Pipeline Gas Compressor: Final Report (Technical Memorandum NO. 1785)," Concepts NREC, April 16, 2015.
- [135] HyET Hydrogen Efficiency Technologies, "HyET electrochemical hydrogen compressor reaches 800 bar rating," *Fuel Cells Bulletin*, vol. 2011, no. 9, p. 8, 2011.
- [136] P. Bouwman, "Advances in Electrochemical Hydrogen Compression And Purification," *ECS Transactions*, vol. 75, no. 14, pp. 503-510, 2016.
- [137] J. Andrews and J. Alazemi, "Automotive hydrogen fuelling stations: An international review," *Renewable and Sustainable Energy Reviews*, vol. 48, pp. 483-499, 2015.
- [138] E. Dursun, B. Acarkan and C. Kilic, "Modeling of hydrogen production with a stand-alone renewable hybrid power system," *International Journal of Hydrogen Energy*, vol. 37, pp. 3098-3107, 2012.
- [139] S. S. Deshmukh and R. F. Boehm, "Review of modelign details related to renewably powered hydrogen systems," *Renewable & Sustainable Energy Reviews*, vol. 12, pp. 2301-2330, 2008.
- [140] M. Raju and S. K. Khaitan, "System simulation of compressed hydrogen storage based residential wind hybrid power systems," *Journal of Power Sources*, vol. 210, pp. 303-320, 2012.
- [141] J. Aghaei and M.-I. Alizadeh, "Demand response in smart electricity grids equipped with renewable energy sources: a review," *Renewable and Sustainable Energy Reviews*, no. 18, pp. 64-72, 2013.
- [142] J. Nam and M. Kaviany, "Effective Diffusivity and water-saturation distribution in single- and two-layer PEMFC diffusion medium," *International Journal of Heat & Mass Transfer*, vol. 46, pp. 4595-4611, 2003.